RESPONSIVE NANOSTRUCTURES FOR CONTROLLED ALTERATION OF INTERFACIAL PROPERTIES

A Dissertation
Presented to
The Academic Faculty

by

Ren David Geryak

In Partial Fulfillment
of the Requirements for the Degree
Doctor of Philosophy in the
School of Materials Science and Engineering

Georgia Institute of Technology
December 2017

COPYRIGHT © 2017 BY REN DAVID GERYAK

RESPONSIVE NANOSTRUCTURES FOR CONTROLLED ALTERATION OF INTERFACIAL PROPERTIES

Approved by:

Dr. Vladimir Tsukruk, Advisor
School of Materials Science and Engineering
Georgia Institute of Technology

Dr. Dong Qin
School of Materials Science and Engineering
Georgia Institute of Technology

Dr. Meisha Shofner
School of Materials Science and Engineering
Georgia Institute of Technology

Dr. Andrei Fedorov
School of Mechanical Engineering
Georgia Institute of Technology

Dr. Nancy Kelley-Loughnane
Airman Systems Directorate
Wright Patterson Air Force Base

Date Approved: [August 17, 2017]

ACKNOWLEDGEMENTS

I would like to thank my friends, family, and colleagues for their support and guidance.

TABLE OF CONTENTS

LIST OF TABLES

LIST OF FIGURES

SUMMARY

Responsive materials are a class of materials that are capable of “intelligently” changing properties upon exposure to a stimulus. Silk ionomers are introduced as a promising candidate of biopolymers that combine the robust, biocompatible properties of silk fibroin with the responsive properties of poly-l-lysine (PL) and poly-l-glutamic acid (PG). These polypeptides can be assembled using the well-known technique of layer-by-layer processing, allowing for the creation of finely tuned nanoscale multilayers coatings, but their properties remain largely unexplored in the literature.

Thus, this research explores the properties of silk ionomer multilayers assembled in different geometries, ranging from planar films to three-dimensional microcapsules with the goal of created responsive systems. These silk ionomers are composed of a silk fibroin backbone with a variable degree of grafting with PG (for anionic species) or PL or PL-block- polyethylene glycol (PEG) (for cationic species). Initially, this research is focused on fundamental properties of the silk ionomer multilayer assemblies, such as stiffness, adhesion, and shearing properties. Elastic modulus of the materials is considered to be one of the most important mechanical parameters, but measurements of stiffness for nanoscale films can be challenging. Thus, we studied the applicability of various contact mechanics models to describe the relationship between force distance curves obtained by atomic force microscopy and the stiffness of various polymeric materials. Beyond considerations of tip size, we also examine the critical regions at which various commonly used indenter geometries are valid. Following this, we employed standard AFM probes and colloidal probes coated with covalently bonded silk ionomers to examine the friction and adhesion

between silk ionomers layers. This technique allowed us to compare the interactions between silk ionomers of different chemical composition by using multilayer films containing standard silk ionomers or silk ionomers grafted with polyethylene glycol PEG. This led to the unexpected result that the PEG grafted silk ionomers experienced a higher degree of adhesion and a larger friction coefficient compared to the standard silk ionomers.

Next, we move to microscale responsive systems based on silk ionomer multilayers. The first of these studies looks at the effect of assembly pH and chemical composition on the ultimate properties of hollow, spherical microcapsules. This study shows that all compositions and processing conditions yield microcapsules that show a substantial change in elastic modulus, swelling, and permeability, with maximum changes in property values (from acidic pH to basic pH) of around a factor of 6, 1.5, and 5, respectively. In addition, it was discovered that the use of acidic pH assembly inverts the permeability response (i.e. causes a drastic reduction in permeability at higher pH), whilst the use of PEG largely damps any observable trend in permeability, without adversely affecting the swelling or elastic modulus responses. In the second part of these studies, we constructed tri-component photopatterned arrays for the purpose of creating self-rolling films. This study demonstrated that the ultimate geometry of the final rolled shape can be tuned by controlling the thickness of various components, due to the creation of a stress mismatch at high pH conditions. Additionally, it was revealed that pH-driven, semi-reversible delamination of silk ionomers from polystyrene exhibited a change in both magnitude and wavelength with the addition of methanol treated silk fibroin as a top layer.

Finally, we showcase examples of biologically compatible systems that incorporate non-polymeric materials in order to generate tunable optical behavior. In one study, we

fabricated composite nanocellulose-silk fibroin meshes that contained genetically engineered bacteria that acted as chemically sensitive elements with a fluorescent response. The addition of silk fibroin was found to drastically improve the mechanical properties of the cellulose composite structures, safely contain the bacteria to prevent efflux into the medium, and protect the cells from moderate ultraviolet radiation exposure. The final study concludes with the creation of a self-assembled segmented gold-nickel nanorod array used as a responsive element when anchored into a hydrogen-bonded polymer multilayer. Because of the mild tethering conditions and the magnetic nickel component, the nanorods were able to tilt in response to an external magnetic field. This, in turn, allowed for the creation of a never before reported magnetic-plasmonic system capable of continuously-shifting multiple surface polariton scattering peaks (up to 100 nm shifts) with nearly complete reversibility and rapid (<1 s) response times.

Overall, this research develops the understanding of the fundamental properties of several different species of silk ionomers and related polymeric materials. This understanding is then utilized to fabricate pH-responsive systems with drastic changes in modulus, permeability, and geometry. In the end, the research prototypes two types of systems with optical responses and chemical/magnetic stimuli, using materials that are chemically (i.e. silk fibroin-based) or structurally (i.e. multilayers) translatable to future work on silk ionomers. These projects all serve the purpose of advancing the understanding of materials and assembly strategies that will allow for the next generation of bioinspired responsive materials.

CHAPTER 1. INTRODUCTION

Biological systems are well known for their ability to adapt to environmental cues and react in a way that appears to "intelligently" shift materials properties to produce a desired outcome (e.g. muscle fibers, neurons, virons). Responsive polymeric and hybrid systems, which are sensitive to environmental conditions, mimic biological systems and have been used for biological and chemical sensing, actuation, adaption, and reconfiguration.[1,2] These synthetic approaches have demonstrated an impressive degree of ingenuity, but much of the design space for such materials remains unexplored.

In this light, continued work on reconfigurable polymeric and hybrid systems shows great promise in bringing further advancement well beyond the traditional field of responsive polymer morphologies, microstructures, and surfaces as discussed in multiple reviews and papers.[3,4,5,6] In this research, the focus is primarily centered on the use of biomaterials and hybrid nanostructures which respond to changes in pH conditions, chemical environment, and magnetic field. First, we discuss the need for biocompatible materials and some examples used in this study.

1.1 Natural Biomaterials

1.1.1 Biocompatibility

Materials have a number of unique challenges when used in a biological system. Naturally, most applications will have to contend with the typical issues of corrosion due to the ubiquitous presence of aqueous media. The salt concentration of human blood is roughly 150 mM[7] (within the range of concentrations found in brackish water[8]), and cell culture

solutions will generally span the range of 10^{-3} – 10^{-1} M.[9] In addition, materials may be exposed to a large range of pH (particularly if placed into the digestive system) and a wide variety of enzymes.[10,11] Even for applications that allow for the gradual breakdown of the materials, it is important to consider the toxicity of the materials and their degraded byproducts for the surrounding organisms.[12] This can be especially difficult for applications within animals, where the immune response of the organism will severely limit the choice of materials to avoid complications such as the foreign body response.[13,14]

In the past decades, there has been a trend in moving away from metallic and ceramic materials and towards softer polymeric materials in an attempt to create biomimetic materials. This trend can be illustrated clearly in the transition from the original rigid glass contact lenses to polymethyl methacrylate lenses and finally to the current standard of using lenses based on a hydrogel material (often copolymers based on poly(2-hydroxyethyl methacrylate)).[15] Except in the case of orthopedic implants,[16] hydrogels are capable of closely matching the mechanical properties of surrounding cells and tissue, which prevents stresses due to a mismatch in stiffness.[17,18] In addition, the highly porous nature of hydrogel materials permits a large degree of diffusion, which is essential for any application that might partially or totally cover a cellular surface, due to the need for exchange of nutrients, oxygen, and waste products with their environment.[19]

In many applications, it is not desirable to keep exogenous materials within an organism for an extended duration. Because of this, materials that safely degrade over time are useful for these self-dissolving types of devices. Microencapsulation of drugs is one example of this, as the capsule material is only needed to protect and control the diffusion of payload and should be easily removed after serving its goal.[20] Another example can be seen in the

case of cell scaffolding materials, which provide temporary mechanical support to migrating cells, but would interfere with intercellular connectivity if they remained indefinitely.[21] Related to this, cell encapsulation techniques require materials that can safely contain the cells but will often need to be disintegrated to allow for cell release and growth.[22] The following subsections discuss two biopolymers of particular relevance to this thesis: silk fibroin and cellulose. Many synthetic polymers have been developed for the purpose of biomedical applications, ranging from long lasting varieties like polyether ether ketone (PEEK)[23] and pHEMA[24] to biodegradable varieties such as polylactic acid[25] and polycaprolactone.[26] Compared to naturally derived polymers, these synthetic molecules have the advantage of higher volume of production and easier processing, but have inferior biocompatibility and biodegradability characteristics.[27]

1.1.2 Silk Fibroin (SF)

In recent years, a substantial amount of focus has been placed into the processing strategies and applications of a whole host of biopolymers such as cellulose, chitosan, collagen, hyaluronic acid, and particularly, silk fibroin.[28,29,30]

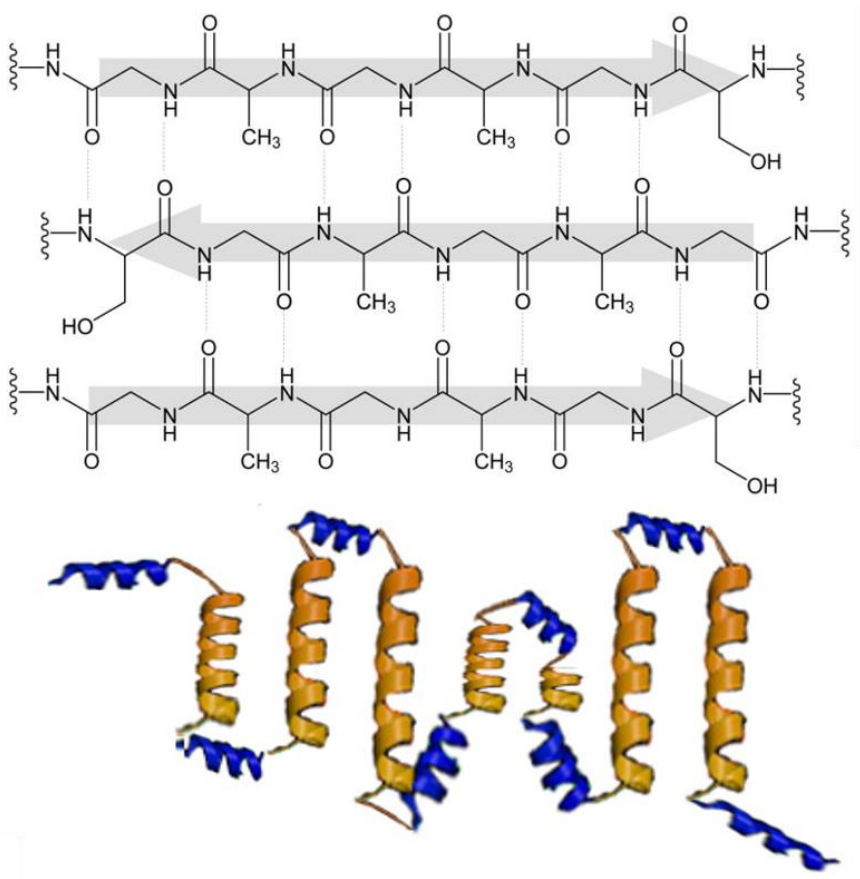

Figure 1.1 (Top) Illustration of β-sheet formation due to GAGAGS in silk fibroin. (Bottom) Cartoon showing the basic structure of silk fibroin. (Top) Ref 35 - Reproduced by permission of The Royal Society of Chemistry (Bottom) courtesy Prof. DL Kaplan

Silk fibroins are a closely related family of structural proteins produced by a number of arthropods, but most notably in the webs of a variety of spider species and in the cocoons of silkworms (*Bombyx mori*). Much of the literature of silk fibroins focuses on the proteins produced by *B. mori* due to a combination of excellent mechanical and biocompatibility properties as well as the large supply of the protein due to the commercial silk textile industry.[31] Silk fibers are spun from the gland of the silkworm and contain a combination of the fibroin proteins and the binding protein, sericin.[32] Solutions of silk fibroin are typically isolated by removing (degumming) the sericin in a boiling alkaline solution (e.g. sodium bicarbonate) and then solubilizing the silk fibroin through a salting-in method

(often with highly concentrated LiBr solutions), which can be dialyzed to obtain a pure silk fibroin solution.[33]

The silk fibroin of *B. mori* exists as a complex of three protein blocks joined by disulfide linkages and hydrophobic interactions, consisting of a 350 kDa heavy chain, a 26 kDa light chain, and a 30kDa p23 chain.[34] The heavy chain consists of twenty different amino acid residues, though more than 90% of these are glycine, alanine, serine, or tyrosine, which comprise 45.9%, 30.3%, 12.1%, and 5.3% of the total residues, respectively.[35] Silk fibroin contains a large number of glycine-serine/glycine-alanine amino acid sequences, particularly the GAGAGS sequence, which allow the molecule to readily form β-sheet crystallites (as shown in Fig. 1.1).[36]

Overall, native silk fibroin typically contains 78% β-sheets/turns (with the remainder being amorphous),[37] though these numbers can vary in the literature and some sources suggest around 14% of the structure consists of 3_1-helices[38] or a significant fraction of α-helices.[39] The structure of the heavy chain contains 12 of these repetitive crystalline segments spaced by 11 repetitive amorphous segments, in addition to two nonrepetitive segments at the N and C terminus.[40] The 151 residue N-terminal domain is a globular protein that appears to control the assembly of silk proteins,[41] while the 58 residue C-terminal domain contains the cysteine residues that allow for disulfide linkages to the light chain.[42] The crystalline segments contain 36-596 amino acids, depending greatly on the position of the domain, whereas the amorphous linker regions constantly have between 42 and 44 amino acids.[36] These crystalline domains in turn, give silk fibroin a large tensile strength and elastic modulus, while the amorphous regions allow for a large elastic strain.[43]

Silk fibers have long been employed for use as use as surgical sutures[44] due to their superior mechanical properties and biocompatibility,[45] though issues[46] with sterilization treatments have prompted the development of composite silk threads.[47,48,49] More recently, electrospun mats composed of silk fibroin (either pure fibroin or in blends) have shown promise as wound dressing materials, particularly with the addition of embedded growth factors to promote wound healing.[50,51] Likewise, scaffolds based on silk fibroin have been successfully deployed in a number of tissue regeneration studies, with most studies focusing on ligament repair applications.[52,53,54] In addition, several drug delivery platforms have been assembled using silk fibroin as the binding polymer.[55,56]

Silk fibroin is an attractive precursor molecule for chemical modifications as it contains multiple reactive amino acid residues (particularly serine and tyrosine) that allow for easy chemical coupling schemes.[35] This has been shown to be an effective method to increase or decrease the β-sheet content,[57] promote increased cellular attachment,[58] and allow for the covalent attachment of drug molecules to the silk surface.[59] The work in this thesis focuses heavily on the processing of a class of silk derivatives called "silk ionomers". These molecules are synthesized by adding a variable amount of cationic (poly-L-lysine) or anionic (poly-L-glutamic acid) to the backbone of a silk fibroin molecule, which gives the molecule a pronounced positive or negative electrical charge.[60] Since their development in 2010, the silk ionomers have been used in multiple reports[61,62] thanks to the combination of biocompatibility with the easy processing associated with polyelectrolytes. Because the charged groups on the silk backbone are weak polyacids or polybases, the charge of the silk molecules will change with pH, allowing for responsive changes in the mechanical properties of silk ionomer based structures.[63] The exact role of these modifications on the

final properties of assembled structures remains largely unanswered, and thus this thesis attempts to expand on this topic while simultaneously utilizing the responsive properties of the silk ionomers to fabricate tunable structures.

1.1.3 Nanocellulose

Cellulose is a structural polysaccharide found in many species of plants, algae, and some species of bacteria.[64] The polymer consists of (1,4)-linked β-D-glucopyranose repeats and is highly stable, both chemically and mechanically, and thus is used by many species as a form of naturally occurring structural reinforcement.[65] Cellulose has long been used by humans as the primary component of textiles and paper and even in the form of biodegradable plastics such as cellophane.[66] Recent research has sought to use nanoscale cellulose due to its mechanical and biocompatible properties, with two major types of cellulose dominating the literature: cellulose nanofibers and cellulose nanocrystals. Cellulose nanocrystals have been utilized as mechanical fillers due to their high stiffness as well as being used as lyotropic liquid crystals due to their stiff, rod-like geometry.[67] Cellulose nanofibers, on the other hand, have presented themselves as attractive materials for wound dressings[68] and cell scaffolding,[69] as hydrated meshes of the nanofibers are compliant, but exceptionally stable in most biological environments.

Cellulose nanofibers can be fabricated using a top-down or bottom-up approach in a laboratory setting. For the former, cellulose fibers from a natural source (e.g. cotton, wood pulp, etc.) is oxidized using a powerful oxidizing agent (e.g. (2,2,6,6-Tetramethylpiperidin-1-yl)oxyl) and sonicated to break down the macroscale fibers into nanofibers of several nm in diameter.[70] In the latter approach, the nanofibers are grown as a biofilm from a natural

cellulose producing bacteria (often *G. xylinum*) before being collected and purified to remove the bacteria and any residual proteins in the matrix.[71] This technique has the advantage of forming a cellulose-based matrix with characteristic pore sizes that allow for growth and migration of mammalian cells,[72] though the fibers formed from the bacteria are much larger (~10^2 nm) than those produced synthetically.[73]

1.2 **Higher order assemblies**

While choice of materials is important for establishing fundamental properties, the ways in which materials are assembled into structures and combined with other materials is of equal importance. The research in this thesis makes use of many types of complicated structures, but the following subsections cover three cases that demand a greater focus in order to explain the nuances of these assemblies. In the first subsection, the use of layer-by-layer (LbL) processing is introduced, which is one of the primary techniques used to fabricate structures throughout the thesis. In the second subsection, the motivation and synthetic methods to produce microcapsules are discussed, which is relevant to the studies performed in Chapter 8. Finally, this section ends with a brief primer on nanorods, which factor into the discussion in Chapter 9 as the primary responsive component added to a multilayer film.

1.2.1 Planar Multilayers

Polyelectrolyte multilayers consist of alternating layers of oppositely charged molecules (typically polymers) arranged in a sandwiched structure. LbL assembly is a popular assembly method by which these films are deposited onto a substrate.[74] The LbL process

requires complementary interactions between the layers in order to prevent desorption once the film is removed from the deposition buffer.

A wide range of weak intermolecular interactions have been shown to be viable as a means of producing LbL films. Among those, Coulombic attractions,[75] hydrogen bonding,[76] host-guest interactions,[77] and hydrophobic interactions[78] have been used most frequently. The ease by which these films are deposited makes them particularly attractive as a means of creating shells on complex surfaces. In addition, the mixed layer structures of these films allow for a large degree of control over changes in composition as the film is grown, thereby allowing a wide range of modifications.[74]

1.2.2 Microcapsules

Microencapsulation is a technique used to suspend a micro-sized suspension of one material into another medium. These components are separated by a (often spherical) membrane that is effectively impermeable to at least one of the components. This technique has the advantage of preventing the diffusion or reaction of the two materials until a specified condition is triggered, sometimes the rupturing of the microcapsules itself.

Microcapsules have found a niche in industrial applications, where they can be used to create more stable dispersions. This technique has long been used in the area of ink manufacturing to produce stable, pressure-sensitive dye dispersions (such as copy paper).[79] In addition, biodegradable microencapsulation has been used as a means to create food color agents with a much longer shelf life than would be achievable with standalone dyes.[80] The ability to entrap volatile chemicals that produce flavoring and fragrances have been used in a wide range of products including food, perfumes, cosmetics, and many others.[81]

One of the more exotic applications is in the area of self-healing materials, which can utilize pressure-sensitive microcapsules to release a healing agent (e.g. a fast-acting polymer and crosslinker mixture) to automatically repair mechanical damage.[82]

The biggest demand for microencapsulation comes from the pharmaceutical industry. This has largely been driven by the desire to develop more effective and nuanced drug delivery platforms.[83] In particular, there has been substantial interest in the synthesis of microcapsule systems which release their content under biologically relevant stimuli (either internally or externally generated) in order to localize the drug release to a desired location.[84] A second, more recent trend is in the design of microcapsule-based systems that function as advanced biosensors. These systems rely on long-term stabilization of an enzyme, Raman label, or other durable transduction molecules to generate a signal in the presence of a specified analyte.[85,86,87]

Microcapsules can be assembled using a number of different processes, each giving different final morphologies to the microcapsules. Some of the most popular techniques are shown in Fig. 1.2 and include LbL, electrospray,[88] and microfluidic gelation.[89] For the purposes of this thesis, LbL assembled structures feature prominently because the technique leads to a high degree of control over microcapsule structure and can be performed without the use of expensive, dedicated assembly devices.

LbL deposition can be used to fabricate hollow microcapsules through stepwise adsorption of the multilayer materials. This is achieved though the deposition of a thin film onto the surface of a solid template particle. Each layer is added through immersion of the template material into a solution containing the adsorbate, followed by rinsing in an appropriate

buffer, and then immersion into another adsorbate solution (or, rarely, a solution to modify the adsorbed material into a stable film). While this is often performed through centrifugation and rinsing of the particles, a continuous flow processing technique has also been used for this purpose.[90] This process can be repeated an arbitrary number of times to increase the thickness of the microcapsule walls, or the composition the microcapsule can be varied at discrete layer transitions. After the microcapsule films are completely deposited (and any surface treatments or crosslinking steps are performed) the template particle is dissolved, leaving only the film in the form of a hollow microcapsule (shown schematically in Fig. 1.2a).

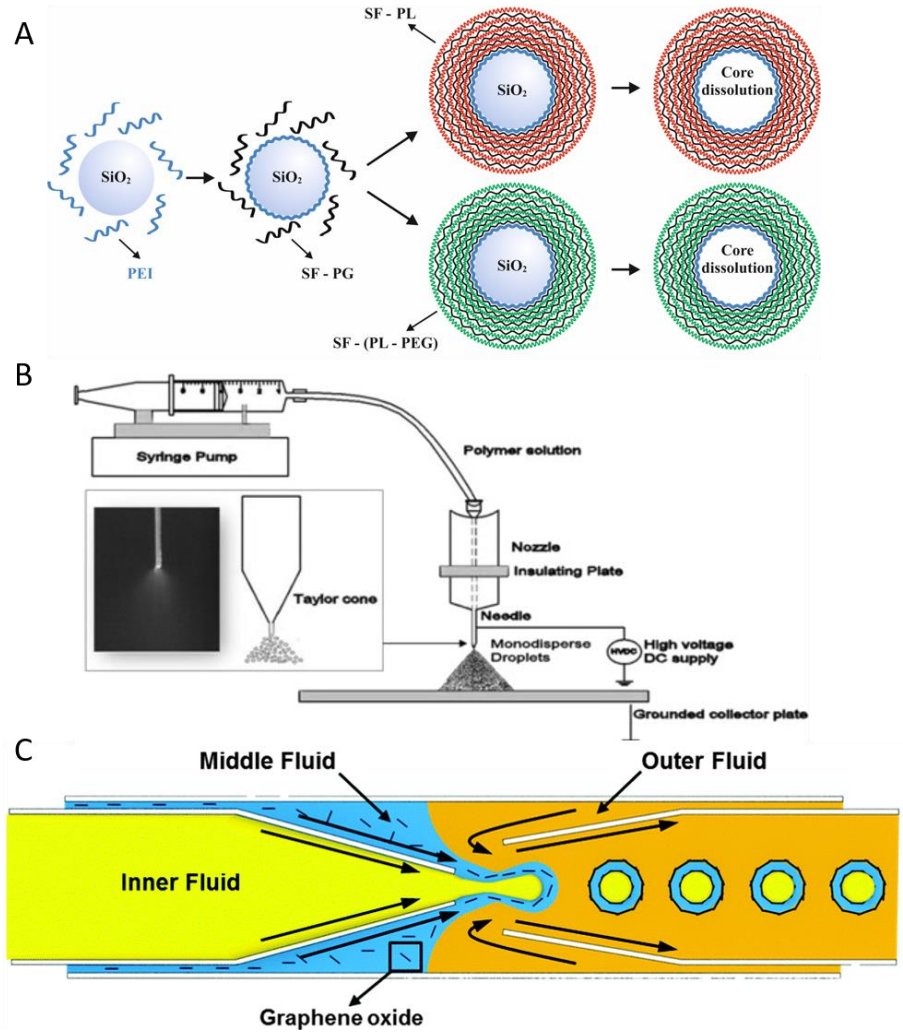

Figure 1.2 Schematics describing typical techniques to fabricate microcapsules via (A) LbL, (B) electrospray, and (C) microfluidic processing. (B), (C) Reproduced from ref 88 and ref 89 with permission from Elsevier and the Royal Society of Chemistry

One of the most important factors in the fabrication of microcapsules starts with the selection of the template particles. These core particles can have sizes ranging from hundreds of nanometers to tens of micrometers, and this size will determine the diameter of the final microcapsule. In addition, the shape of the cores will often be maintained by the microcapsules, allowing for shapes such as spheres and cubes. In fact, the porosity of the template materials will factor into the internal morphology of the microcapsules with smooth, nonporous templates leading to completely hollow microcapsules and porous

templates leading to an internally interconnected microcapsule material. Different template materials will necessitate different etchants, which can impact the microcapsule stability and the compatibility of the microcapsule etching process with their environment (i.e. biocompatibility). Silicon dioxide is a commonly used, nonporous material that is etched with hydrofluoric acid. Calcium carbonate particle can be fabricated in a number of different morphologies including cubic structures, spherical porous structures and can be etched in either a mildly acidic solution or in a chelating agent such as EDTA. Melamine is another spherical nonporous substrate, which can be etched in mildly acidic solutions.

The mechanical stability of microcapsules is important for allowing the microcapsules to remain intact while subjected to shear forces.[91,92] Mechanically robust microcapsules are thus desirable as they can survive being injected into target locations at a relatively fast rate.[93] In addition, many applications will involve further shear forces (e.g. due to blood flow or muscle contraction) and thus the microcapsules must not experience a rapid degradation of their mechanical strength if they are to persist for appropriate timescales.[94] Beyond this, some applications rely on the controlled failure of microcapsules as a means of stimulated release. Simple mechanical shearing can be used in many in vitro applications and usually involves a static, external pressure generating device (e.g. a colloidal indenter).[95] Alternatively, ultrasonic stimulation has shown promise as a means of inducing capsule rupture in vivo due to the large (and benign) penetration of the sonic pressure wavs into tissue.[96] In this case, multiple mechanical properties become extremely relevant, as the microcapsules must efficiently absorb the sonic energy and use the localized pressure gradients to induce a desired failure state.[97,98]

The mechanical stability of microcapsules is determined by numerous factors, including stiffness, tensile strength, geometry, and the applied stress conditions.[99] Of these, the microcapsule geometry and stiffness can be readily measured through the technique of atomic force microscopy (and to some extent, optical microscopy),[100] and thus are the main focus of this thesis. Radius and wall thickness (for hollow microcapsules) are the primary geometric factors that are typically measured,[101] though microstructural properties such as porosity,[102] number/thickness of bilayers (for multilayer structures), [103] and others may all have a large impact as well. Stiffness can be measured via nanoindentation tests by examining the indentation depth of a probe compared to the applied force. [104] Because many microcapsules are swollen composite structures, the stiffness is heavily dependent on the Young's modulus of the microcapsule components in addition to the strength and number of crosslinks (e.g. covalent, electrostatic, physical, etc.) [105] and the swelling ratio of the microcapsule. [106]

The permeability of a microcapsule will determine what sorts of payload it can carry and for what duration it can maintain a concentration gradient. Permeability is typically controlled by altering the microstructure of a membrane to decrease porosity/pore size or increase path length, [107] though there are a number of examples in which repulsive forces (e.g. steric or electrostatic repulsion) are utilized as well. [108,109,] Practically, this means that permeability can be increased by increasing porosity and decreasing the membrane thickness (assuming all other properties remain the same).[110,111] Measuring the permeability requires the use of payloads that can be easily quantified via microscopic or spectroscopic techniques. In the case of large objects such as cells, this can be readily achieved by microscopy techniques to count the number of cells outside of a microcapsule

as a function of time.[112] For slowly diffusing molecules, the permeability can be determined by monitoring the concentration of the analyte in the solution surrounding the microcapsules.[113] For rapidly diffusing molecules, techniques such as fluorescence recovery after photobleaching are more appropriate as they allow for a faster sampling rate.[114]

1.2.3 Nanorods

In contrast to the relatively large (but still microscale) microcapsules, nanorods are typically defined as particles with two roughly equal nanoscale dimensions with a larger length in the third dimension, typically with either a cylindrical or a prolate spheroid geometry.[115] They are valued for their anisotropy, which can cause major changes in their properties versus isotropic nanoparticles, such as nanospheres. One notable example is the case of plasmonic nanorods, which show a polarization dependent optical extinction due to the presence of both transverse and longitudinal excitation modes.[116] In addition, magnetic nanorods demonstrate a preferred magnetization axis (along the long axis) which can be used to cause a rotation in nanorods under static magnetic fields.[117]

Nanorods have been fabricated using many classes of materials including metals,[118] polymers,[119] oxides,[120] and composites.[121] Two common approaches for synthesizing nanorods are the solution based approach and the template based approach. In the former, the nanorods form unto a seed particle (or rarely, spontaneously from solution) and naturally grow into a rod shape. This process can involve various ligands that enhance the growth of the particle along a preferred direction to ensure that the nanorod has a large aspect ratio.[122] In the latter approach, a template is first created to constrain the geometry

of the particles using an inert, insoluble material. This template is then infiltrated with the desired materials, which naturally grow into a rod-like shape due to the template. The template is then removed (i.e. dissolved) and the nanorods can be released into solution.[123] This template-based approach is the technique used in this thesis, and so it will be discussed more thoroughly, though both methods have various advantages and challenges associated with them.

The template material for nanorod synthesis is a nanoporous medium with long and non-branching pores in order to prevent undesirable particle geometries. Two of the most commonly used templates for nanorod synthesis are track-etched membranes and porous aluminum oxide membranes. Track-etched membranes are created though the bombardment of a uniform material with nuclear fission products or heavy ion beams, which create semi-randomly oriented pores.[124] Porous alumina membranes (PAMs) are created through the controlled electrochemical oxidation and controlled etching of polished aluminum. In general, PAMs are preferred as the cylindrical pores created with the technique are all uniformly, vertically oriented and the pore diameter is easily controlled by varying parameters such as voltage, etchant, and temperature.[125] Following this, the nanorods can be assembled using electrochemical deposition, chemical vapor deposition, sol-gel deposition, or polymerization.[126] The electrochemistry based methods cause the nanorods to assemble at the backside of the template, which allows for the alteration of chemistries *in situ*, which in turn allows the nanorod composition to be varied as the nanorod grows, resulting in segmented nanorods.[127] These segmented nanorods are a major part of Chapter 9, where they are used for a combination of magnetic and plasmonic properties derived from their half-nickel/half-gold composition. The use of particles as

responsive materials (along with a discussion of responsive materials in general) will be discussed in the following section.

1.3 **Responsive Materials**

Finally, we turn to a discussion of how different strategies to produce materials that are responsive to various stimuli. The work in this thesis heavily considers the pH responsive properties of silk ionomers, which operate under the principles discussed in subsection 1.3.1. The subsequent subsection (1.3.2) covers the strategies to provide a system with magnetic properties, mostly related to the addition of magnetic particles as in Chapter 9. Finally, the section concludes with a brief discussion on the use of genetically engineered bacteria as chemical sensors, which are relevant to the discussion in Chapter 8.

1.3.1 pH Responsive Materials

Responsive polymers have been subjected to intense theoretical treatments which have resulted in the prediction and discovery of many unique and useful quirks in the behavior of polymeric systems. One area of particular interest is the study of the phase separation behavior of polymer solutions, and the subsequent alteration the conformations of individual macromolecules and their aggregates. Owing to a low entropy of mixing, polymer solutions and blends can be immiscible under certain thermodynamic conditions (*e.g.* temperature and concentration) but show complete miscibility at some critical point (*i.e.* the upper critical solution temperature, or UCST). This result is accounted for under more advanced thermodynamic treatments, most famously the Flory–Huggins solution theory and more recent sophisticated models which have been applied to attempt to explain complex polymeric behavior more completely.[128]

As with most thermodynamic phase boundaries, polymer phase separations can be induced with very slight changes in internal or external thermodynamic parameters. These stimuli alter the overall free energy of the system and methods to alter the entropic term (*via* temperature) and the enthalpic term (*via* pH or solvent quality) have been suggested and are widely explored.[129] From the standpoint of Flory–Huggins theory, the change in solvent is accounted for with a change in the volume fraction of solvent or in the interaction parameter, depending on the specifics of the solvent alteration. In the former case, the resulting changes in the system will be a consequence of the change of the entropic term from the free energy of mixing. In the latter case, the changes will largely be impacted by the change in the enthalpy term of the free energy of mixing as well, assuming that the solvents used are of molecular weights and are much smaller than the polymer.

In order to account for the influence of nature of atomic bonds as well as the various rotational isomers, a generalized equation may be used to connect global chain dimensions with overall dimensions directly related not only to chain and bond parameters N (number of segments) and l (the length of a segment) but also upon thermodynamic parameters embedded in a conversion factor C which is sensitive to chain environment:[130]

$$\langle R_0^2 \rangle = C_\infty N l^2$$

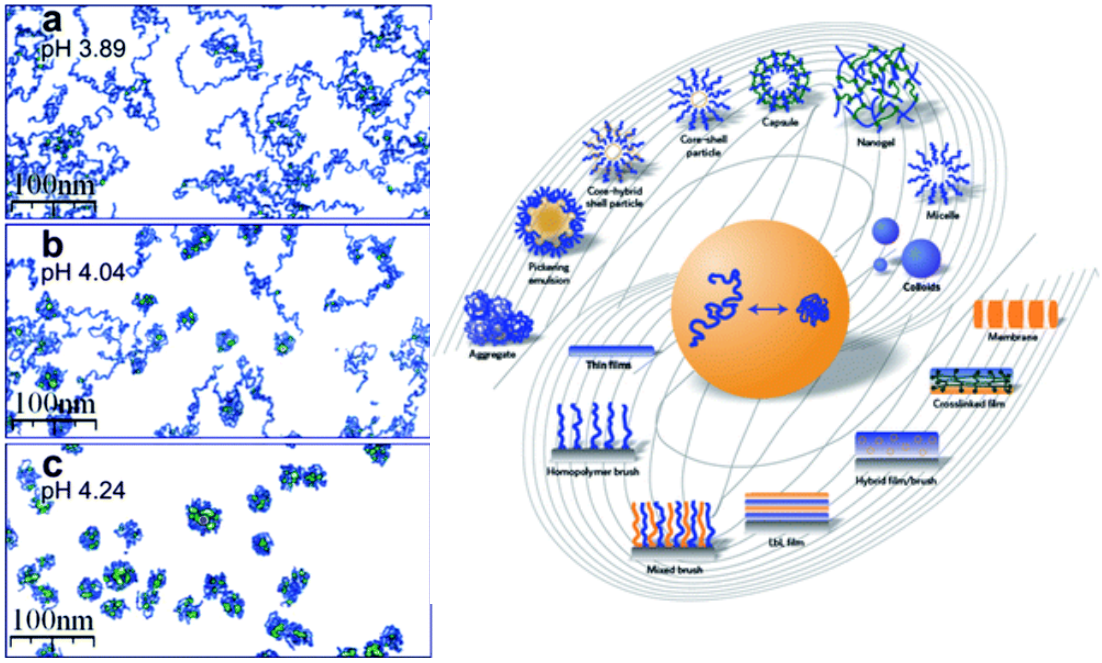

Figure 1.3 (Left) AFM measurements demonstrating different morphologies of a pH responsive polymer at: (a) pH 3.89 (b) pH 4.04; (c) pH 4.24. Reprinted from ref. 132. Copyright (2005) American Chemical Society (Right) Schematic of the many length scales and geometries that have been studied with responsive polymers.. Reprinted from ref. 135. Copyright (2010) Nature Publishing Group

Transformation in chain dimensions (as reflected by *C*) can be exploited to create materials that have distinct "response" (change in macromolecular dimensions) to certain external "stimuli" with corresponding abrupt and dramatic changes in macroscopic dimensions and shapes.[131] An example of this phenomenon can be seen in Fig. 1.3 (Left) which shows the collapse of single macromolecules with dramatic alternation in chain conformation and dimensions as a function of pH conditions and is visualized directly with atomic force microscopy.[132]

Cross-linked polymer gels are particularly interesting from practical viewpoint due to the ease of extracting useful work from their phase-driven responses.[133] From a thermodynamic viewpoint, a gel presents an interesting case as the typical thermochemical results are complicated with the addition of the elastic energy stored within a gel under

deformation, though simplistic solutions, such as the Flory–Rehner equation, have been developed.[134] When applied to gels, these phase changes and molecular dimension changes are referred to as volume-phase transitions. The response towards a stimulus can be widely varied, and depends on the degree and nature of the cross-linking used.

Such a versatile set of phenomena raises the possibility for a range of responsive materials that perform a certain function at an appropriate time or location. In recent years, many complicated designs utilizing responsive polymers have been both proposed and realized. Depending upon design and fabrication conditions a wide variety of individual micro-/nanoparticulated and film-like materials can be made for various applications as has recently been discussed.[135] A wide range of responsive materials and structures can be designed from linear, cross-linked, and branched polymer chains, as core–shell and continuous structures, as unimolecular micelles and colloidosomes, as thin films and nanoscale coatings, as grafted layers and free-standing composite structures (Fig. 1.3 (Right)).

The variation of Columbic interactions can greatly affect the conformation of a polymer chain and its interactions with the surrounding media.[136] When one considers the steady state chain conformation of a polyelectrolyte, the charge carried by the repeat units becomes an important factor to consider. In the case of non-zwitterionic homopolymers, the charge of each repeat unit is the same and so an intra-chain repulsive force will occur, causing an expansion of the overall chain dimensions if ion balance would be altered.

For a charged polymer, the repulsive force between repeat units must take into account the effects of the surrounding medium. The polarizability of the medium, composed

of solvent and dissolved electrolytes, plays an important role in determining the screening length for the polymer chain segments. Adjusting the polarizability of the solvent (through solvent exchange) may not be practical, but it is generally possible to alter the total dissolved ion concentration in a solvent, and thus the screening length may be affected through addition (or subtraction with an appropriate dialysis setup) of a salt solution. Ultimately, this has the effect of reducing the role of Columbic forces in determining the equilibrium state of the polymer.

Polyelectrolyte materials which are widely used to build various responsive nanostructures[137] are commonly divided into two categories: "strong polyelectrolytes" which are fully ionized in solution and "weak polyelectrolytes" which are partially charged according to an equilibrium ratio. While strong polyelectrolytes contain large numbers of charged groups under most experimental conditions, the number of charged groups contained in weak polyelectrolytes may be altered by changing the solvent environment. One of the most ubiquitous methods of controlling the charge contained on a weak polyelectrolyte is through control of the pH of the solution. Many commonly used weak polyelectrolytes are either weak Brønsted acids or bases and thus a critical range of pH values may be obtained from the acid/base dissociation constants of the repeat units.[138] Knowing this pH range, one can tailor a system that responds to relatively minute changes in pH by virtue of the dissociation of the repeat units.

By varying the pH of the solution, one is able to control the conformation of the polymer chains in the solution. As shown in Fig. 1.3, the change in polymer conformation and dimensions can be quite dramatic, leading to a large reduction or increase in the pervaded volume of the polymer chains. The volume change of the polymer chains leads to dramatic

changes in other physical properties such as viscosity, diffusion rate, and light scattering behavior.[139] In the case of a polyelectrolyte gel, the swelling of the gel is dependent on the degree of dissociation of the repeat units. As the pH is adjusted, the swelling ratio and thus the volume of the gel will change depending on the pH value and the dissociation constant of the polymer.

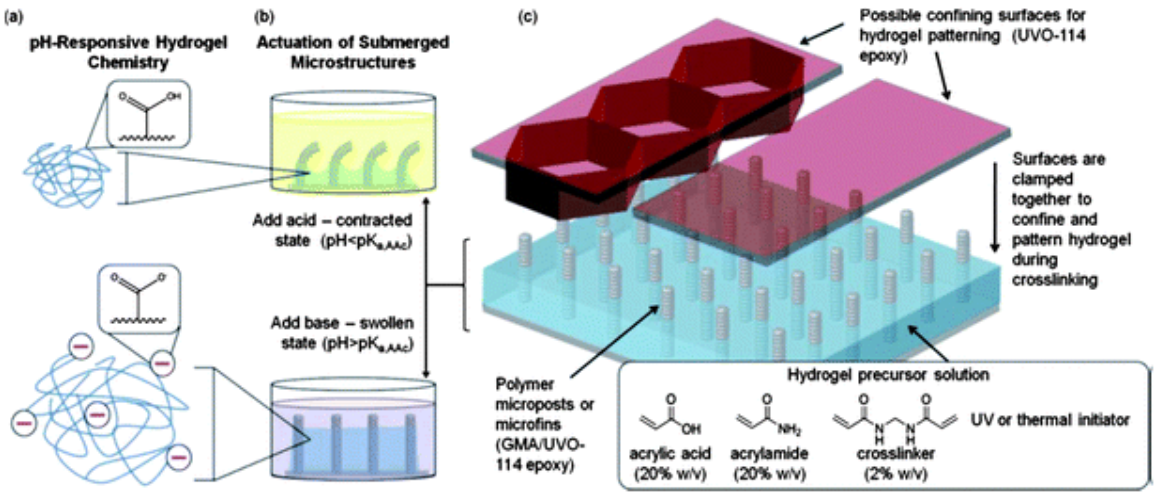

Figure 1.4 Schematic and proposed mechanism of the pillar actuation. (a and b) The hydrogel pillars contract and extend along with the responsive gel matrix when the surrounding solution is acid and basic, respectively, corresponding to the dissociation of the carboxylic acid side group in the polymer. (c) Overall structure of the device, showing the pillar array embedded into the responsive polymer. Reprinted from ref.140. Copyright (2013) John Wiley and Sons

As reported by Aizenberg *et al.* pH responsive polymer gels combined with microfabricated arrays can be used as actuatable structures.[140] By placing flexible polymeric posts (non pH responsive) in a thin film composed of a pH-responsive polymer (poly(acrylic acid-*co*-acrylamide)), the authors were able to cause a reversible and repeatable large-scale collapse in the pillars under a change in the pH of the solution (Fig. 1.4). At low pH, the acid group in the polymer film is protonated, which causes a reduction of the affinity of the gel for the solvent. As the water is expelled from the gel, the polymer attempts to collapse, but is bound to the pillars. As the pillars are

relatively elastic, they are able to bend in order to relieve the elastic strain in the surrounding gel. Upon raising the pH of the solution, and the subsequent swelling of the gel, the stored elastic energy in the pillars is released as the gel continue to expand outwards.

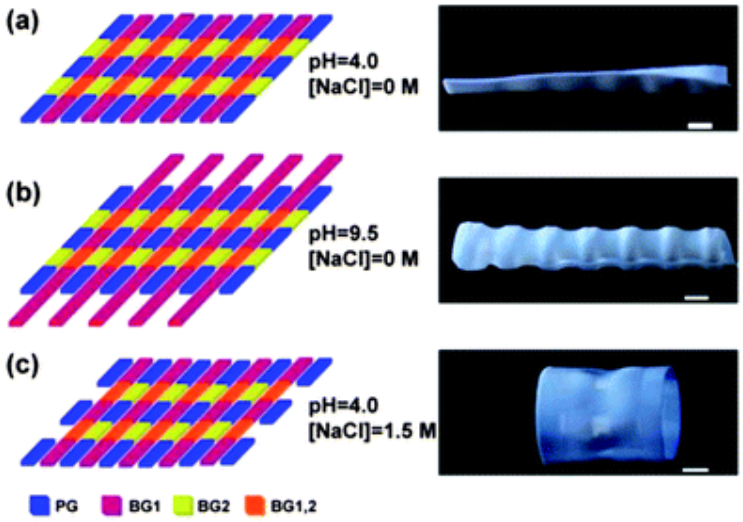

Figure 1.5 Composite structure made of 3 different responsive polymer segments. The morphological changes for different conditions are shown for (a) pH = 4 and [NaCl] = 0 M. (b) At pH = 9. 5 and [NaCl] = 0 M. (c) At pH = 4 and [NaCl] = 1.5 M Reprinted from ref 141. Copyright (2013) American Chemical Society

Through patterning of several different types of polymers (multiphase materials), a more complex actuation response may be garnered. To this end, Kumacheva *et al.* have reported on the synthesis of a composite gel structure which allows for a number of responses for different stimuli.[141] Of particular interest in this report is the design of complex striped ternary composite gel consisting of poly(acrylamide-*co*-butyl methacrylate), poly(acrylamide-*co*-butyl methacrylate)/poly(methacrylic acid), and poly(acrylamide-*co*-butyl methacrylate)/poly(*N*-isopropylacrylamide). The gels were patterned in a specific way to elicit a particular response under various conditions, as shown in Fig. 1.5. In this composite structure, the ionic strength and the pH of the solution may be independently

controlled and each of these stimuli triggers to the swelling or collapse of one of the responsive elements. Due to the orthogonal response of the different elements, the swelling of one polymer is not directly hindered by the state of another polymer. Due to the multiphase nature of this structure, the two stimuli can be varied independently, allowing for a wide number of complex morphologies and multistimuli response.

1.3.2 Magnetic Responsive Materials

Magnetic fields have been used directly on polymeric substances in order to control alignment. Because magnetic fields do not tend to alter the chemical state of a system, they can be used in many systems without concern for causing a secondary reaction in the system. In addition, it is possible to tune an external magnetic field to control both the strength of the field and the gradient of the field across the sample. These features have been used in both fundamental assembly-based applications[142,143] and more applied biomedical schemes[144,145].

Because organic materials tend to have magnetic susceptibility values that are too low to allow for a rapid response in a material, proper inorganic "fillers" are often used as a means to add a magnetic functionality to a polymeric material.[146] This greatly extends the range of magnetic susceptibilities possible in polymeric composites. In addition, controlling the amount of filler can present a strategy to control the degree of magnetic susceptibility in a sample and thus control the responsiveness to an external field. As alluded to previously, one main attraction in using magnetically responsive materials is the ability to align and position a composite material with a high degree of precision. Magnetically assisted

positioning typically requires the presence of a magnetic field gradient in the direction of desired motion.

The effect of a magnetic field on a material depends strongly on the electronic state of the individual atoms in an atom or molecule.[147] In general, atoms that have unpaired electrons are paramagnetic and will align their magnetic moment in the direction of the magnetic field, while atoms with no unpaired electrons are diamagnetic and will opposite the direction of the magnetic field. While diamagnetic materials exhibit a weak repulsion under the influence of an external magnetic field, paramagnetic materials generally exhibit an attraction to the source of the magnetic field. Ferromagnetic materials are similar to paramagnetic materials, but contain additional interatomic interactions which allow them to exhibit a permanent magnetic dipole and a higher magnetic susceptibility.[148]

Ferrogels are magnetically active gels and are typically composed of polymeric gels and magnetic nanoparticles.[149] The ferromagnetic metal or metal oxide (*e.g.* super paramagnetic iron oxide nanoparticles – SPIONs) particles can often be functionalized in a variety of ways to allow the nanoparticle to be covalently bound to the polymer of interest. Once incorporated into the polymer matrix, the nanoparticle endows the results composite with a number of unique properties. As shown in a recent study,[150] this can be used to cause macroscale deformations. By casting a magnetic nanoparticle (magnetite) into a polydimethylsiloxane (PDMS) gel, the authors were able to make a number of complex magnetically actuating structures. Due to the elasticity of the PDMS, shapes such as a cantilever could be made, which deform under a magnetic field and restore their original shape once the field is removed. An example of actuation in molded ferrogels can be seen in Fig. 1.6.[151] Recently, there have been efforts[152] to create magneto-responsive

gels that utilize paramagnetic ions instead of SPIONS, allowing for a wider range of materials to be utilized.

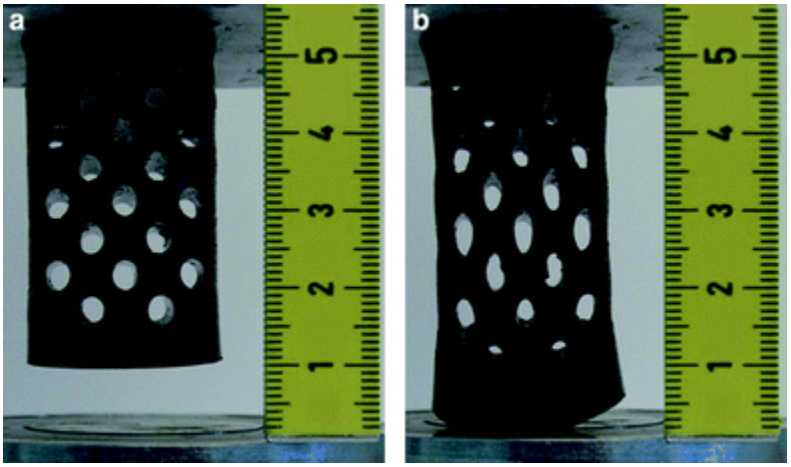

Figure 1.6 Stretching occurs in a highly functionalized hydrogel (60% magnetic nanoparticle). (a) No external magnetic field. (b) Magnetic field is applied. Reprinted from ref.151. Copyright (2009) John Wiley and Sons.

These applications of magnetic structures demonstrate the utility of ferromagnetic materials as responsive media at the macroscale, exerting a large degree of control over these particles at the microscale has been more elusive. One reason for this gap is the difficulty of creating a system that can respond in a coordinated manor without simply aggregating. Recent work[153], demonstrates the ability to control the microscale behavior of such particles, with the end result of a large of control over optical properties. This work suggests that a clever confinement of nanoparticles can allow for sophisticated movement of the particles in a desired fashion.

Recently, several groups have reported on the combination of magnetic materials and plasmonic materials. Surface plasmon resonances occur (primarily in noble metal nanoparticles) when photons are strongly coupled into the electromagnetic field at an interface and cause a localized fluctuation of electron density (called “plasmons”).[154]

Practically this has the effect of increasing the intensity of the electromagnetic near the surface, which is useful for spectroscopic techniques,[155,156] and increases the extinction cross-section of a particle in a (often narrow) region, which can result in a shift in the color of a surface.[157,158] While magnetic and plasmonic properties are often used applications in which the properties are orthogonal (i.e. they do not appreciably interact), some recent publications have shown that the anisotropic response of some particles can be utilized through magnetic control of particle orientation.[159,160]

1.3.3 Engineered Bacteria

While the previous sections have focused on all artificial materials systems, this section will describe hybrid biological/synthetic responsive assemblies. With modern advances in artificial gene transfer, it is now possible to utilize natural, biologic systems as highly sophisticated chemical sensors.[161] The complex cellular machinery that permits living organisms to respond to their environment also leads to many attractive features that are challenging to achieve artificially. Cells naturally have built-in feedback loops to regulate sensing of their environment and the subsequent necessary changes in gene regulation. This can be hijacked away from the naturally occurring stimuli/response pair and substituted for one that enables them to act as sensing elements. In addition, cells can naturally reproduce to ensure a large number of sensors, can sustain and repair themselves using nutrients in their medium, and can be quite resilient against fouling.

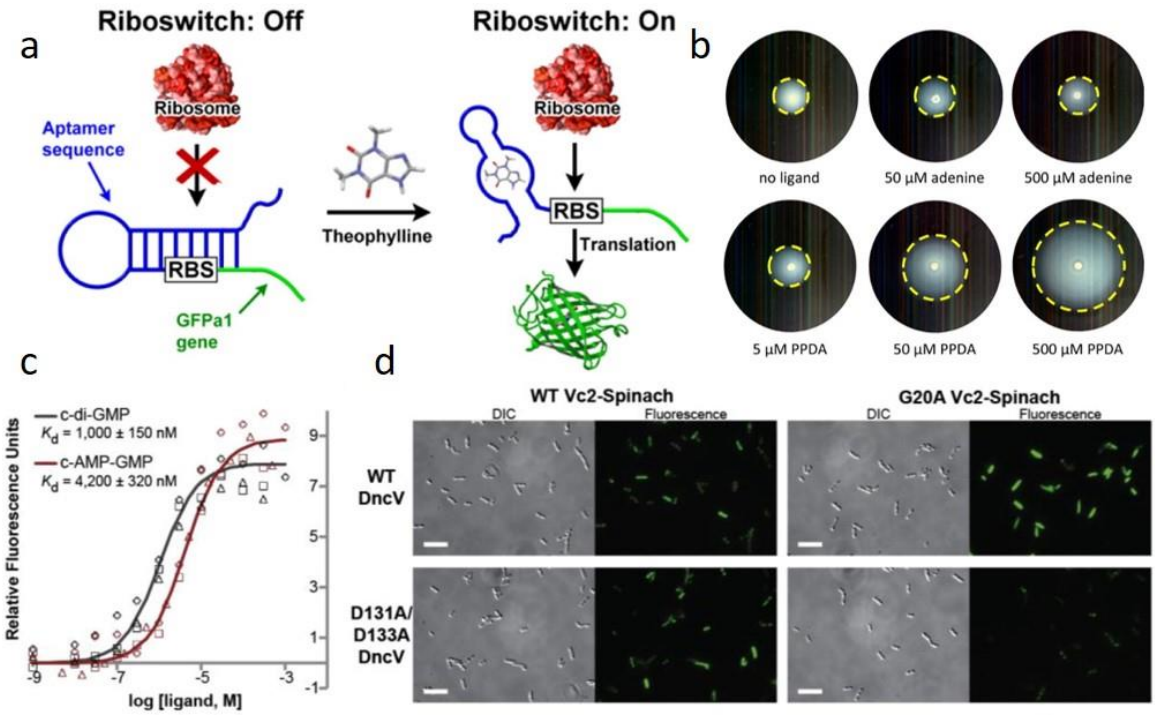

Figure 1.7 (a) Schematic of the functioning of a riboswitch. (b) Control of E. coli motility through riboswitch activation. (c) Fluorescence expression versus analyte concentration in recombinant E. coli. d) Detection of c-AMP-GMP production in top left sample only. (a),(b),(c,d) Adapted with permission from refs 161, 164, 165. Copyright 2015, 2014, 2013 American Chemical Society.

The inserted gene sequences are typically engineered to have an element that allows for increased upregulation of the reporter sequence. This reporter sequence leads to the production of a protein that allows for external observation of the signal, which are often designed for validation with an optical microscopy system. One such type of reporter, luciferases can be found in a number of natural sources (e.g. fireflies, sea pansy, bacteria in the family Vibrionaceae) and catalyzes a light-generating oxidation reaction. Another type of reporter is fluorescent proteins, which can be sourced from a number of different organisms, the most notable of which is green fluorescent protein (GFP) from the jellyfish *Aequorea Victoria*.

Equally important to the insertion of reporter sequences is the proper selection of sensing/regulatory sequences. Some naturally occuring means to detect changes in chemical concentration can be repurposed for use in sensing platforms. Some genes, such as arsR,[162] are evolved to specifically detect the presence of certain chemicals, in the case of arsR this allows the cell to detect arsenic. In other cases, inserted genes can allow cells to detect stress-induced molecular damage, such as the promoter P_{recA},[163] which aids in the detection of damaged DNA segments.

A powerful tool for the development of artificial reporter sequences is the riboswitch, which is schematically shown in Fig. 1.7. These sequences are designed to produce an RNA segment that binds to a transcription region of the bacterial genome directly, as opposed to utilizing the mRNA to synthesize a promotor protein. This riboswitch blocks the activation of the reporter sequence until an analyte binds to the RNA and forces a conformational change that unbinds the sequence. The precise conformation obtained for a specific RNA sequence is easily predicted using simple computational models and allows for the selection of specific RNA molecules that will bind specifically to the target molecule. One group [164]modified that naturally occurring add A-riboswitch to have sensitivity to pyrimido[4,5-d]pyrimidine-2,4-diamine (PDDA) instead of adenine. Another group[165],[166] has shown that various riboswitch schemes can be used to precisely distinguish between the presences of several related compounds, cyclic di-adenosine monophosphate (c-di-AMP), cyclic di- guanosine monophosphate (c-di-GMP), and cyclic guanosine monophosphate-adenosine monophosphate (cGAMP).

While substantial progress has been made in the design of responsive materials, current synthetic materials systems cannot yet match the complexity and elegance of biological

systems. Many types of responsive materials require processing techniques that are not translatable to biologically relevant conditions (e.g. cell encapsulation) or have issues of toxicity in either the materials itself or its degradation products. Many well-known biomaterials, on the other hand, lack the rapid, reversible responsive properties of synthetic materials and are incredibly difficult to process due to environmental sensitivity. Even the hybrid biological/synthetic materials have issues related to long-term viability and containment of biological components. In order to address the pressing need for biologically relevant responsive materials, major research is required to examine to usage, processing strategies, and properties of new types of responsive biomaterials. As will be discussed in Chapter 2, this research has been completed with the goal of addressing the problem of creating and understanding robust, biocompatible responsive systems.

CHAPTER 2. RESEARCH OBJECTIVES

2.1 **Research Goals**

Responsive materials are a key part of next generation technology that seeks to create "intelligent" systems capable of responding and adapting to a diverse range of stimuli, as discussed in the previous chapter. Much like biological organisms, devices assembled using these materials could be designed to adapt to their environmental variability in an autonomous fashion. Because of this, these materials are often used in biomedical applications, as the use of bulky control systems is infeasible or inconvenient to work with, though this also constrains the materials selection further towards biocompatible materials.

With this in mind, silk ionomers (composed of silk fibroin grafted with cationic/anionic polypeptide sequences, as discussed in subsection 1.1.2) are an ideal system to study as they show a large pH-based response (due to moderate pKa values of the side chains) and produce only amino acid fragments as they degrade. Furthermore, they can be customized with a variety of different grafting schemes, allowing for different degrees of ionic character or for charge screening methods such as PEGylation. Beyond the responsive character, the ionic nature of the proteins grants them higher solution based stability than native silk fibroin, as the ability of the molecules to form insoluble β-sheets is severely reduced. Likewise, these proteins behave much like traditional synthetic polyelectrolytes in that conjugation with oppositely charged proteins leads to precipitation from solution. This behavior means that well-established LbL processing can be used to form precisely defined multilayered structures, allowing for facile assembly of nanoscale coatings. In addition, the ability to work with cationic and anionic varieties on the same biopolymer

backbone will allow future applications to take advantage of the same biocompatibility that has long been established for natural silk fibroin.

Despite these attractive qualities, silk ionomers are a relatively new class of naturally derived polymers, and thus the characteristics of the polypeptides have not been studied under a wide variety of different conditions.

First, the properties of the silk ionomers as planar multilayers have not been rigorously studied. Much of the existing body of work on the silk ionomers focuses on large scale, complex three dimensional gels which can complicate the interpretation of the data. In particular, high quality information about the morphology and mechanical properties of nanoscale multilayers of silk ionomers needs to be collected to understand the fundamental nature of the ultimate properties of these films.

Second, more quantitative information is needed about the interaction and stress distributions between different silk ionomer components at different length scales. It is true that the ionic attraction between cationic and anionic species at neutral conditions will play a large role in these interaction, but the highly heterogenous nature of the ~10^5 Da proteins suggests that the actual interactions will be highly complicated. In part, this issue will be ameliorated with the completion of the aforementioned studies of planar film growth. Beyond this, however, quantitative studies of the actual strength of the interfacial energy between multilayers will be needed.

Third, the current literature largely lacks studies relating to the properties of different formulations of silk ionomers, and indeed only a select few have currently been studied. It is essential that we understand how the changes in grafting (grafting density, grafting

length, block co polymer grafting) ultimately affect the properties of final assembled structures in order to rationally guide the development of new varieties of the silk ionomers. Along with this, it is critical to determine how different modifications affect the processing steps needed to build structures (i.e. pH, crosslinking) or conversely, how similar processing conditions can lead to different results due to different grafting species.

Fourth, the interaction of the silk ionomers with other classes of inorganic materials in largely unknown. This lack of understanding leaves a gap in the scientific knowledge needed to create functional composite materials with predictable properties. Some materials such as cellulose nanofibers are attractive one-dimensional reinforcing materials. Likewise, it is important to understand how silk ionomers interact with other polymer species when forming composite multilayer structures.

Last, general strategies for the development of durable, reversible, and rapid responsive systems using magnetic or chemical stimuli require complex systems involving additional (sometimes inorganic or biological) materials that will interact the polymeric components used in the system. Therefore, understanding how magnetic or chemical responsive elements interact with multilayer or composite polymer systems is of vital importance in producing highly advanced responsive materials with wide ranges of stimuli.

While previous work has been undertaken to assemble and study silk ionomer based structures (such as gels and coatings), this research focuses primarily on understanding the nature of these properties and how they might be manipulated by changing chemical compositions, processing conditions, and through the addition of different components. In order to make a priori predictions about silk ionomer behavior, it is essential that we

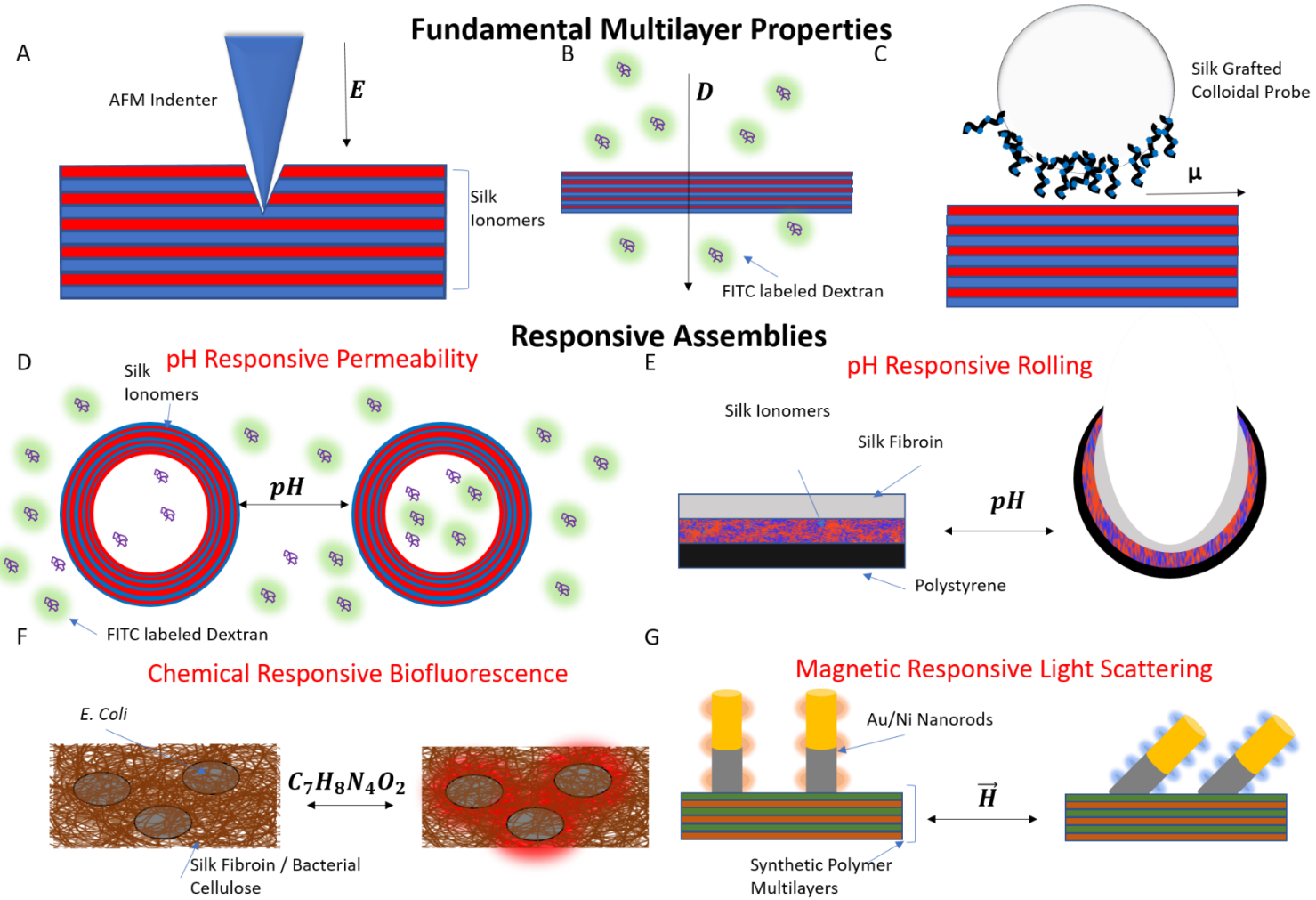

Figure 2.1 Schematic of fundamental studies (A-C) using responsive silk ionomers to determine properties such as (A) Young's modulus of multilayers, (B) friction coefficient between layers, and (C) diffusion coefficient of membranes. Applied responsive structures (D,E) using polymer based composites that utilize silk ionomer based, pH driven responses to alter (D) permeability and (E) macroscale geometry. Composite systems with optical response using (F) encapsulated cells for analyte detection and (G) nanorods for magnetic responsive behavior.

understand the properties of the silk ionomers under these different conditions. In addition, this research focuses on the creation of responsive systems with the ability to respond rapidly and reversibly to pH, chemical analytes, and magnetic fields.

This work focuses on first establishing the fundamental interactions between and mechanical properties of silk ionomers (Fig. 2.1 A-C). Next, it focuses on the application of silk ionomers into responsive systems (Fig. 2.1 D,E) with a particular focus on how the properties of the silk ionomer multilayers affect the overall device performance. Finally, composite based responsive systems are presented (Fig. 2.1F,G) that demonstrate promise for future use with silk ionomers, due to use of silk fibroin or multilayered polymers.

Thus, **the goal of this research** is to develop a deeper understanding of how silk ionomers can be used as responsive material components in a wide variety of applications and with different characteristic dimension scales, but with a primary focus on the impact of nanoscale dimensions. The work will especially focus on how the pH responsive characteristics of the silk ionomers will change fundamental, interfacial materials properties.

The studies presented in this thesis seek to make generalization about the properties of different classes on silk ionomers based changes in these properties and their pH responsiveness. The research presents several strategies to enable biocompatible responsive systems, using the pH responsive silk ionomers or through a combination of highly complex sensing agents (bacterial cell or segmented nanorods).

The specific objectives of this research include:

- Develop and utilize a method to determine the inter-layer interactions present between cationic and anionic components of silk ionomer multilayers and calculate their expected surface energy. Determine what testing methods will allow for proper characterization of such films. In addition, this will be used to quantify the difference in interactions between PEGylated and non-PEGylated varieties of silk ionomer.
- Obtain a critical understanding of the growth and morphology of thin silk ionomer films assembled under different conditions and with different compositions. Changes in pH value both during assembly and post assembly will change the organization of the silk ionomer chains and thus change intermolecular interactions and morphology.
- Construct three-dimensional microcapsule structures based on low grating density silk ionomers as comparison to previously reported values of Young's modulus and diffusion coefficient reported for high grafting density silk ionomers. In addition, explore how the addition of neutral, hydrophilic molecules (i.e. PEG) to the grafted chains will further affect these properties.
- Create a complex, responsive system that makes use of the swelling behavior of silk ionomers in the form of self-rolling microarrays. Such structures should be examined to determine how microstructural and mechanical behaviors coordinate to lead to macroscale responses.
- Incorporate a magnetically responsive element into biocompatible multilayered structures through the addition of segmented magnetic nanorods. By using an angle dependent optical material, this composite material can be used to demonstrate a

metal/polymer with an optical-magnetic response with constrained degrees of freedom.

2.2 Overview of Thesis

Chapter 1 is an overview elucidating the need for biocompatible materials and providing the rationale for using silk fibroin, in addition to a discussion about the synthesis, applications, and properties of microcapsules. The chapter concludes with a general overview of responsive materials including selected examples from the recent literature.

Chapter 2 describes the ultimate goals and specific technical objectives accomplished as a part of this thesis work. In addition, it lays out the organizational structure of the thesis itself.

Chapter 3 covers the major techniques used during the course of the work in this thesis, including the synthesis of materials, the assembly of structures, the characterization of samples, and the computational techniques that were essential for obtaining the results in the following sections.

Chapter 4 contains a study focused on the evaluation of several models related to the determination of mechanical properties of thin films using AFM derived force distance curves (FDCs). In particular, the study demonstrates the validity of models pertaining to various tip geometries at different penetration depths by using selected materials systems.

Chapter 5 contains work performed on the interfacial properties and friction between oppositely layers of silk ionomers. The study looks at the effect of PEGylation on the adhesion and friction coefficient between silica substrates coated with the silk ionomers.

Chapter 6 looks at the role of various treatments in the final properties of microcapsules assembled from silk ionomers. The work studies the effect of prelayers, pH, and PEGylation on the stiffness, swelling, and permeability of crosslinked silk microcapsules.

Chapter 7 details the mechanics of self-rolling tri-layer microarrays containing silk ionomers. The work in this section analyzes the role various geometric and mechanical properties on the statistics of the final rolled shape assumed by these photopatterned films.

Chapter 8 describes a study that combines silk fibroin with bacterial cellulose as a natural means of cell encapsulation. The cells are used as chemical detectors, giving the whole assembly a chemically responsive fluorescent behavior. The section focuses on the effectiveness of the cell encapsulation, as well of the changes in morphology and stiffness induced in the cellulose matrix through the addition of silk proteins.

Chapter 9 demonstrates how nanoscale multilayer assembled polymer films can be given magnetically responsive behavior that is confined to the film-polymer interface. In particular, the study focuses on how the optical properties of segmented nanorods can be magnetically controlled using in situ pinning via polymer interactions.

Chapter 10 presents final conclusions about the results presented in the thesis and gives insight into further avenues of research that should be considered.

CHAPTER 3. EXPERIMENTAL TECHNIQUES AND MATERIALS

In the course of completing the research needed to complete this thesis, a number of techniques were employed to synthesize materials, characterize samples, and analyze data. The following sections highlight some of the primary techniques that have been used, though later chapters will deal with the specific techniques used in that chapter.

3.1 **Porous Alumina Membrane Synthesis**

Porous alumina membranes (PAMs) are attractive as template materials because they can be fabricated in such a way as to have well-ordered pores of diameter ~10^1 - 10^2 nm and lengths of several microns. By depositing materials into these pores, nanorods and nanowires may be readily obtained by dissolving the sacrificial template material[167]. In this study, electrodeposition of metals (nickel, gold, and silver) into a PAM (purchased from Whatman) is used to grow a metallic (made of 1-2 of the aforementioned metals) nanorod

Figure 3.1 Flowchart of nanorod synthesis. A porous alumina membrane (1) is plated with metal (2), which serves as electrode. Next, silver (3), nickel (4), and gold (5) are electroplated. The membrane is dissolved (6) and the nanorods are released (7) from the sacrificial silver layer to be dispersed into a suspension (8).

with a diameter set by the alumina pore diameter and a length set by the deposition time (Fig. 3.1). Unless otherwise noted, all nanorods are grown in a matching electrolyte solution (nickel sulfamate, sodium dicyanoaurate, and silver cyanide) with voltages provided by a Keithley source meter against a standard calomel electrode. The counter electrode for the synthesis is a platinum foil and the working electrode is a sputtered gold contact (typically nickel plated) placed on the backside on the PAM.

3.2 **Nanorod Synthesis**

Nanorods were prepared by electrodeposition into a porous alumina template as described previously[168]. Gold was deposited via Potassium Aurocyanide (Orobrite 24 RTU Rack; Technic Inc.) and nickel via Nickel Sulfamate (Technic Inc.), and a sacrificial silver layer was used to facilitate nanorod release. The nanorods were released by dissolved the

alumina template and the sacrificial layer, and were dispersed in a solution of PVP (360,000 molecular weight, Sigma Aldrich) as surfactant.

3.3 **Piranha Cleaned Silicon Substrates**

Polished single crystal silicon is used as a substrate for much of the work in this study due to smooth, chemically inert surface of the silicon. All silicon is prepared, according to the standard protocol in the laboratory[169], by rinsing and sonication in ultrapure deionized water, followed by immersion into piranha solution (210 mL sulfuric acid:90 mL hydrogen peroxide) for one hour, and finally are subsequently rinsed and dried under a stream of dry air to be stored in clean glass vials until future use.

3.4 **Preparation of Functionalized AFM tips**

First, amino terminated silane groups were grafted to the tip as described previously.[35] Briefly, the tips were placed into an argon filled desiccator along with 10ul trimethylamine (TEA) and 30 ul 3-aminopropyl-triethoxysilane (APTES) which were placed separately into small plastic containers. After two hours of this vapor treatment, the APTES and TEA were removed and the tips were kept in the desiccator for two days to allow for "curing". To attach the silk ionomers to the tip, glutaric dialdehyde was used as a linker between the amine groups[36] in the protein and on the APTES. These tips were then incubated in 5 wt% glutaric dialdehyde for 30 minutes and subsequently washed to remove excess solution. Finally, the tips were submerged in a 1 mg/ml solution of the appropriate silk ionomer for 30 minutes and then thoroughly rinsed to remove weakly adsorbed protein. Ellipsometry testing on planar silicon samples showed a Cauchy film thickness of 0.23 and 1.98 nm after the APTES and silk ionomer treatments, respectively.

3.5 **LbL deposition**

Thin films are easily fabricated through the assembly of sequentially adsorbed material bilayers[170]. Typically, these materials must have a sufficient affinity for each other to allow for stable growth of the film. In a dip coating process, the material deposition can be performed by dipping a substrate into a solution of the target material, followed by a subsequent solvent rinsing step, and repeating the process with another material. A spin-assisted (SA) LbL process is useful for obtaining ultra-thin films with well-defined thickness. In the SA-LbL process, a small amount of solution of the target material is placed on the film's substrate, which is then rotated a high speed (typically 2000-4000 revolutions per minute in this study), followed by solvent rinsing and subsequent depositions. These methods are standard, facile techniques for the production of planar thins films.

3.6 **Assembly of microcapsules**

Nanoshells can be fabricated unto spherical templates also using the LbL method. Instead of a planar silicon wafer, this can be performed on dispersions of silica microspheres. These coated silica cores are then dissolved using a buffered oxide etch (typically 14 M NH4F 1 M HF) for one hour. The resulting suspension is dialyzed over the course of two days against either DI water or a weakly acidic solution. In general, silk ionomers are crosslinked prior to core removal using EDC (30 mM) for 1-24 hours.

3.7 **Atomic Force Microscopy**

AFM provides exceptional topography data from a substrate with a (lateral) resolution down to a few nm. Due to the interaction of the sample and probe tip used in AFM

scanning, mechanical data is readily obtained from the instrument[171]. Of particular interest is the ability to collect detailed force-distance curves, which contain a wealth of information of the sample's mechanical properties. In this study, AFM is used to obtain information about the sample roughness, adhesiveness, and stiffness. Most scans are performed in either "tapping mode", in which the tip is made to vibrate at 50-100 kHz and gently contact the sample, or in "quantitative nanomechanical mapping mode", in which the piezoelectric element of the AFM scanner oscillates at 1-2 kHz and the tip indents into the surface with a controlled force. The AFM used in this study is a Dimension Icon from Bruker Corporation and the standard probes (HQ:XSC11, Mikromasch USA) used have a radius of curvature around 8-10 nm and spring constants ranging from 0.2 – 42 N/m across the four different cantilevers. Scans are typically performed at pixel resolutions between 256 – 1024 px^2 with scan areas of 1-20 μm^2. Ambient air scans are performed using a standard tip holder, while fluid scans are performed using a fluid cell tip holder in either deionized water or an appropriate buffer.

3.8 **Surface Force Spectroscopy**

The deflection of an AFM probe and the movement of the piezo tube can be used to construct FDCs. These FDCs can be used to obtain the stiffness of the surface and the adhesive force between the AFM probe and substrate. When performed for each pixel, this can be used to obtain a mapping of the micromechanical properties of the surface. Typical measurements are calibrated by first obtaining a deflection sensitivity from a silicon or sapphire substrate, and then the force constant for the probe's cantilever is determined by a thermal tuning method. The tip radius of curvature is determined by blind tip estimation using scans obtained from a TiO_2 roughness standard.

3.9 **Colloidal Probe Microscopy**

Instead of standard AFM probes, AFM probes with attached silica microspheres can be used for the probe tip. This allows for the averaging of mechanical properties over larger areas, which can aid in the removal of roughness effects, particularly for porous samples. The large size of the tips leads to a poor lateral resolution, however, so these AFM probes are not typically suitable for imaging.

3.10 **Contact Mechanics**

Force-distance curves (FDCs) extracted from the AFM enabled indentation experiments are not generally interpretable in their raw force. Indentation experiments are well described in the contact mechanics models developed by Hertz and Sneddon (and others), which allow for analytical relations between force, penetration, and elastic modulus for specific indenter tip geometries[172]. This research uses a software package developed by the Tsukruk research group which fits these analytical models to data sets and returns the fitted elastic modulus.

3.11 **Finite Difference Time Domain Simulation**

Finite Difference Time Domain (FDTD) simulations are used to solve Maxwell's Equations numerically for a given system. The simulations have the advantage of being able to view electromagnetic behaviors for materials with arbitrary geometries over a wide range of excitation frequencies. This technique is used to both predict and understand the optical properties (in particular, scattering and absorption) for known materials systems[173] and will enable the study of both near-field electric field enhancement and the (frequency-

wavenumber) dispersion relations for the plasmonically active gold segmented nanorods. The FDTD simulations performed in this work are modelled via FDTD Solutions, which is a commercially available software package from Lumerical Solutions, Inc.

3.12 **Confocal Scanning Laser Microscopy**

Confocal microscopes are generally used for the imaging of fluorescently labeled specimens and offer unmatched z-resolution for optical imaging. This high z-resolution can be used with computer assisted image stitching to build a 3-dimensional representation of specimens. This capability is utilized in this study as a means of ensuring microcapsule integrity and assessing changes in microcapsule volume under different environmental conditions. Another benefit of the high z-resolution is the ability to track florescence intensity in thin plane. When coupled with controlled photobleaching, a florescence recovery after photobleaching (FRAP) experiment can be performed[174]. The diffusion of florescent molecules is tracked through intensity changes and a mass transport model can be applied to a time series of data to determine the diffusion coefficient of the molecules in a particular area. This enables this work to analyze the effect of environmental conditions on the permeability of responsive microcapsules in a direct way. The microscope used for this section of the study is a Zeiss LSM 700 managed by the Parker H. Petit Institute for Bioengineering & Bioscience. Typical images were collected using a 40-63x oil immersion objective at 1-3% intensity of a 488 nm laser. FRAP measurements were collected after 20-30 bleaching cycles using 100% intensity of a 405 nm laser. These images were collected every 500 ms for one minute, with 5 frames for the pre-photobleached reference.

3.13 **Optical Spectroscopy**

Optical spectroscopy gives information about a material's absorption, scattering, and extinction (simply the sum of scattering and absorption) over the range of visible wavelengths. This can be performed in a number of ways, but in this study, microscopes using lamps with a broad range of wavelengths (i.e. tungsten halogen lamps) are used to illuminate the sample and the collected light is passed through a spectrometer for wavelength based analysis. Hyperspectral spectroscopy is a technique which obtains optical data (scattering or extinction) across the visible spectrum for every pixel in an image[175]. This allows for the simultaneous analysis of optical properties in different regions of an image and allows for filtering based on unique spectral characteristics. These techniques are used to quantify the change in spectral properties for certain materials systems, particularly plasmonically active metal nanorods. The instruments used in this study are an Olympus BX51 with hyperspectral capabilities from Cytoviva, inc. and a Leica DM4000 M with a CRAIC spectrophotometer.

3.14 **Ellipsometry**

Ellipsometry utilizes elliptically polarized light at a range of wavelengths and incident angles to determine thickness and refractive index for planar layered materials[176]. Briefly, the change in intensity and phase on the incident light is recorded and the material is modelled using either real material data or an idealized "model "material, which is then used to fit parameters (notably, thickness). This is useful for quickly characterizing the thickness of layers of known materials or to determine optical properties of uncharacterized materials. In this study, a Woolam M-2000U ellipsometer areused with a spectral range of 300 – 1000nm. All scans are obtained under ambient conditions and utilize data collected from three angles of incidence: 65°, 70°, and 75°.

3.15 **Scanning Electron Microscopy**

Confocal Scanning Electron Microscopy (SEM) is a technique that fires a tightly focused beam of electrons at a specimen and records the deflection of the electrons as a function of the position of the rastering beam[177]. This technique is often used in secondary electron detection mode, which gives exceptional contrast for topographical features. Due to the small wavelength of energetic electrons, the diffraction limited feature size of an SEM is much smaller than that of a traditional optical light microscope, giving nanoscale resolution. In addition, the electron-material interaction can produce characteristic x-rays which is utilized in energy-dispersive x-ray spectroscopy (EDS) to obtain details of elemental composition. The microscope used in the study is a Hitachi S-3400N. Most imaging was conducted using a 5-10 keV accelerating voltage, 7-10 mm working distance, and 5-30k x magnification. EDS was conducted using 10-15 keV accelerating voltages, a 10 mm working distance, and at least 5 minutes of integration time. Most samples were sputtered with 1-3 nm of gold prior to imaging to prevent charging, with some exceptions for samples in which EDS was used to determine the localization of gold in the sample.

3.16 **Silk Ionomers**

Silk ionomers were generously provided by Prof. D.L. Kaplan, and were synthesized according to the following protocol. Silk fibroin is isolated from silkworm (Bombyx mori) cocoons (also provided by Prof. Kaplan) according to well established protocols[178],[179].

In brief, cocoons were degummed for 20 minutes in a boiling solution of 0.02M Na2CO3 and then rinsed in ultrapure deionized water (R = 18.2 MΩ·cm) to remove sericin

molecules. The remaining silk fibroin in placed into a 9.3M LiBr solution at 60 C for 4h hours. This solution is dialyzed exhaustively against deionized water for three days.

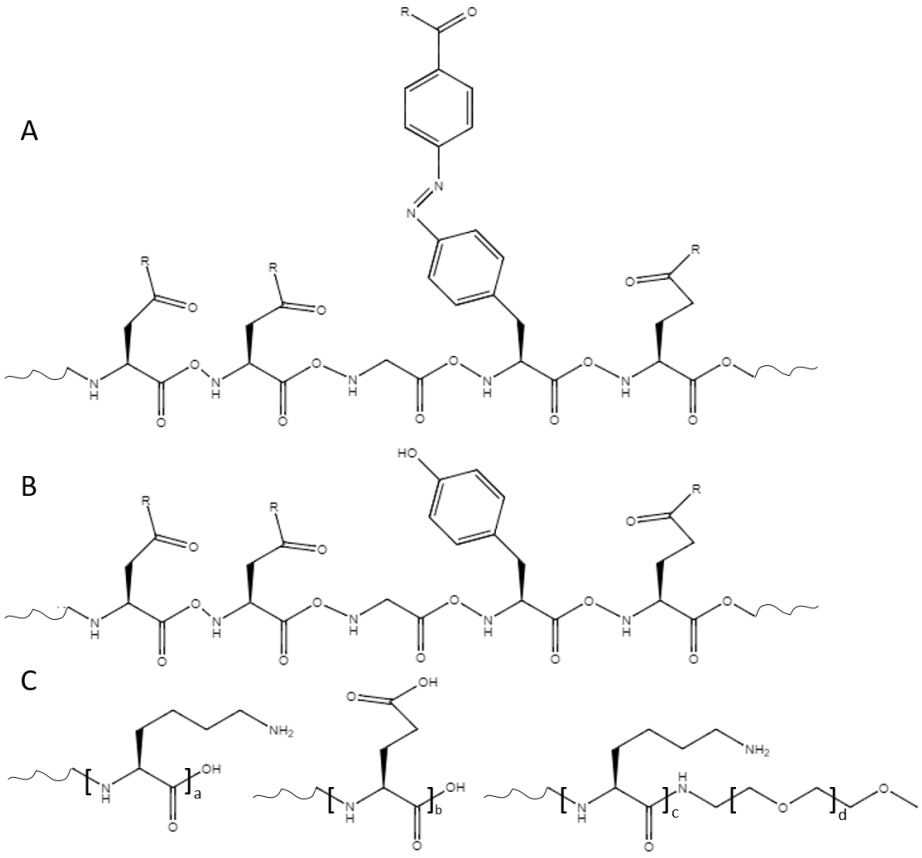

Figure 3.2 (A) SDGYE sequence in Silk Fibroin modified to activate tyrosine and serine residues. (B) The same sequence with only serine residues activated. (C) R groups for silk ionomers: (Left to Right) poly-l-lysine, poly-l-glutamic acid, poly-l-lysine-b-PEG. For high grafting density a ≤ 100, b ≤ 100, while for low grafting density a = 20, b = 20, c = 10, d = 22.

Silk fibroin is modified with either poly-l-lysine, poly-l-glutamic acid, or poly-l-lysine-b-poly ethylene glycol according to an established protocol.[60] In brief, the serine residues of the silk fibroin are modified via reaction with diazonium to give them carboxylic acid groups. These are then targeted with 1-ethyl-3-[3-(dimethylamino)propyl] carbodiimidehydrochloride chemistry to couple the desired protein to the silk fibroin chain (Figs. 3.2 and 3.3).

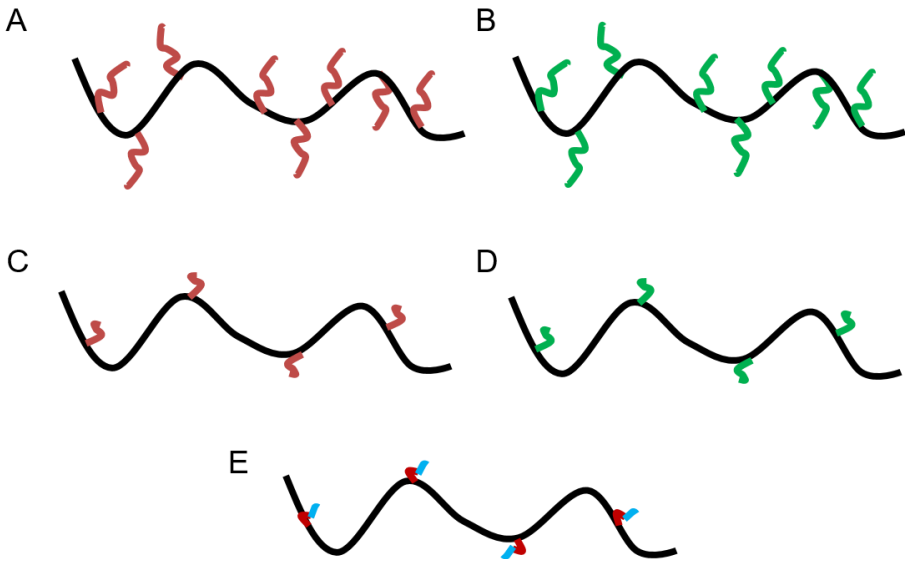

Figure 3.3: Idealized schematic of high (A,B) and low (C,D) grafting density cationic (A,C) and anionic (B,D) silk ionomers. (E) Low grafting density cationic silk ionomer with PEG blocks grafted.

3.17 *Collaborative Work*

In addition, the following work was essential in performing the research detailed in the following chatpers. Dr. M. Chyasnavichyus provided the mathematical modeling and software found in Chapter 4. Dr. C. Ye fabricated the self-rolling films that are examined in Chapter 5. Dr. I. Drachuk fabricated the cellulose-silk composites found in Chapter 6 and performed much of the measurements related to cell viability. Dr. S. Kim performed most of the AFM measurements and calibrations found in Chapter 7. Dr. J Geldmeier performed the FDTD simulations found in Chapter 9.

CHAPTER 4. PROBING ELASTIC PROPERTIES OF SOFT MATERIALS WITH AFM: DATA ANALYSIS FOR DIFFERENT TIP GEOMETRIES

4.1 Introduction

As is known, AFM methods provide a variety of tools to access mechanical properties by measuring the interactions of a sharp probe with a specimen surface, and can often produce topographical images with near atomic resolution.[180] Furthermore, the technique's unmatched force sensitivity allows one to non-destructively investigate a variety of materials ranging from very compliant live cells to extremely stiff cellulose fibrils and rigid polymers.[181,182,183,184] However, experimental routines as well as data analysis for the successful extraction of accurate, quantitative data is not always a straight forward process. Calculations of surface mechanical properties involve specific contact mechanics models which closely resemble actual tip-sample contact geometry. It is known that even for the simplest cases of semi-infinite elastic half-spaces and axisymmetric punch indentations, the calculated elastic modulus will strongly vary with the size of the probe and punch profile shape.

In this study, we discuss several aspects of measurements of elastic properties of materials with AFM. We examine effects of tip shape variation on FDC fitting and elastic modulus extraction as well as importance of characterization of actual tip shape for elastic modulus measurements. In particular, we will discuss parabolic, spherical, and conical models and will examine specific cases where these models should be used. In addition, we will

introduce improved algorithm for fast fitting of FDCs for spherical tip shape approximation, as spherical model is the only model, where there is no analytical equation for tip-sample contact area dependence on penetration. In addition, we discuss how probe size affects results of FDC fitting. For that purpose, we used silicon probes annealed at high temperature to achieve higher tip curvature.

4.2 **Experimental**

4.2.1 Materials

The silk ionomers used in this study are the high grating density silk discussed in section 3.16. These ionomers were made into films through spin-assisted LbL deposition by alternating casting of aqueous solutions of the polycationic and polyanionic silks onto polystyrene coated silicon wafers.

In this study, we also use examples from a commercially available soft contact lens, Balafilcon A (Purevision, Bausch & Lomb Inc.). The lens was measured immediately after removal from its original blister pack containing saline solution and discarded after one day of measurements. The lens was sectioned as described in detail in an earlier study in order to create a flat region conducive to AFM measurements.[172] The lens was then attached to a metal sample disks (Ted Pella Inc.) using double sided tape for AFM measurements on the lens surface. A small droplet of the saline solution taken from the blister pack was placed at the scanning surface and measurements with the AFM were made inside of this.

In one example, we use polystyrene (PS, weight-average molecular weight ~250000 g/mol, Sigma-Aldrich), which is a well-known amorphous polymeric material with values of elastic modulus frequently reported in the literature to be ~3 GPa. A saturated PS solution (150 mg/mL) in chloroform was cast in a glass Petri dish and held under vacuum for several days to remove solvent. The final thickness of this substrate was on the order of 1-2 mm. AFM measurements were made directly on the top surface of the PS substrate without removing from the glass Petri dish.

4.3 **Discussion**

4.3.1 Spherical versus parabolic tip shape

The equation for the elastic modulus calculation developed by Hertz fits well only for small indentations. It was shown by Sneddon[185] that a simple analytical solution can be solved which inversely relates the elastic modulus to $\delta^{3/2}$ for a rigid paraboloidal indenter, according to eq. (1):

$$F = \frac{4\sqrt{R}}{3}\frac{E}{1-\upsilon^2}\delta^{3/2} \qquad (1)$$

where F is the applied force, R is the effective tip-sample radius of curvature, and ν is the samples Poisson's ratio. From this it the penetration depth can also be related to the radius of the contact area circle, a, by eq. (2):

$$\delta = \sqrt{aR} \qquad (2)$$

For the case of truly spherical contact, these equations become much more complicated as there is no analytical solution which relates applied force to penetration depth. In this case the applied force is related to the contact area radius via eq. (3):

$$F = \frac{E}{1-\upsilon^2}\left[(a^2 + R^2)ln\left(\frac{R+a}{R-a}\right) - 2aR\right] \quad (3)$$

while the penetration depth is separately related to the contact area radius by eq. (4):

$$\delta = \frac{a}{2} ln\left(\frac{R+a}{R-a}\right) (4)$$

This difference in contact behavior is related to the fact that the contact area for the spherical indenter is finite and cannot exceed the radius of the indenter, which can be the case for many probes tips (for example, see Fig. 1A,B), whereas for the parabolic indenter this area increases indefinitely and is proportional to the square root of penetration (see eq. (2)). Although for wide variety of materials very deep penetrations will cause plastic deformations and cannot be fitted with the elastic model for some soft polymeric materials, large penetrations (δ on the order of several R) are easily achieved in the elastic regime.[186]

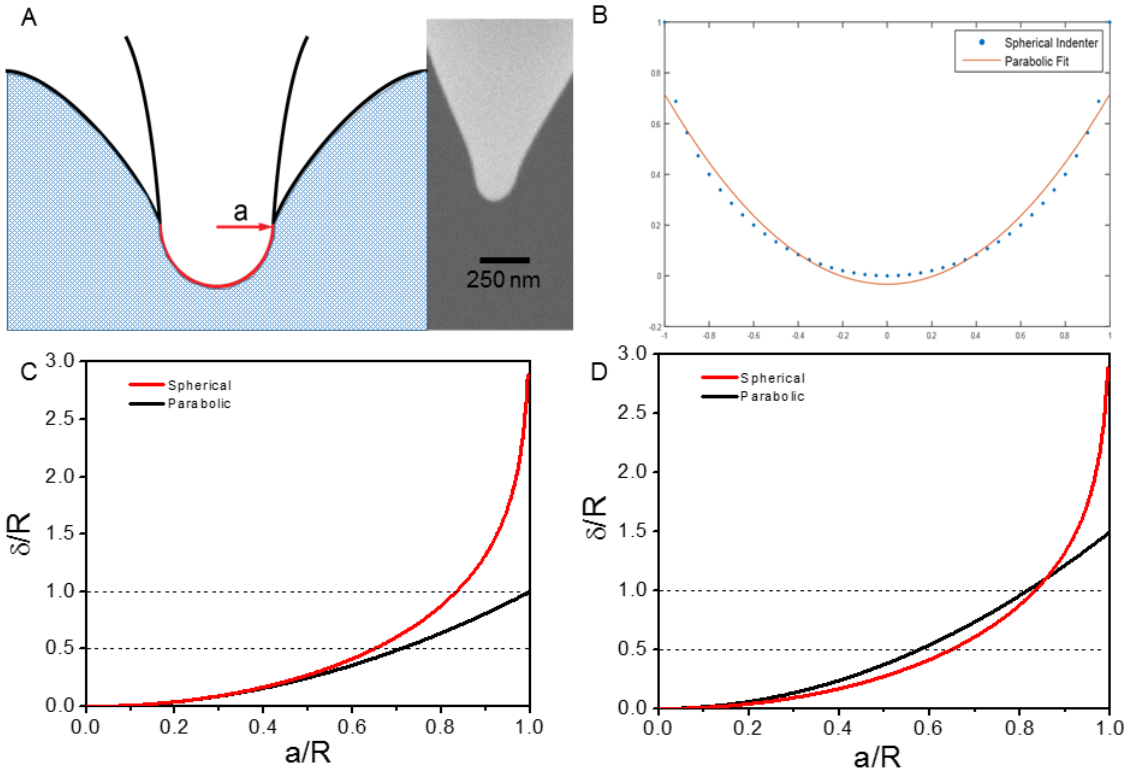

Figure 4.1 (A) Graphical schematic showing an example of how a the end of an AFM tip could behave as a spherical indenter wherein the maximum contact radius does not exceed the radius of the spherical cap. Also shown is an SEM of an annealed AFM tip which displays a similar shape to the schematic. (B) Example of fitting of the spherical indenter with the parabolic models. (C) Differences between the contact area changes with penetration for the spherical indenter with radius R and parabolic indenter with the apex curvature 1/R. (D) Comparison between parabolic and spherical models with radius of curvature for the apex of parabola equals to 0.6675R

Fig. 1C shows penetration depth versus contact area radius both normalized to indenter radius, which allows for the examination of the difference in the contact area between the two models. For simplicity in the following discussion, we assume the radius of the spherical punch, R, to be the same as the radius of curvature of the apex of a paraboloidal punch. The initial regions of the penetration curve for both models show the same δ/R versus a/R. This is a consequence of eq. (4) being the limiting case of eq. (2) for small a (or for small δ). However, there is a large discrepancy between parabolic and spherical model in the terms of contact area for larger penetrations. It is ~9% for $\delta = 0.5R$ and

grows to ~20% at $\delta = 1.0R$ (See Fig. 1C, and Fig. 1A for visualization of physical reason for such deviation). Therefore, under relatively large indentation depths, incorrect selection of the fitting model can result in substantial errors in the calculated elastic modulus value. This is especially true for some annealed tips with larger radius and for used AFM tips, which each have a unique shape (Fig. 1A). In general, if one would try to approximate a spherical indenter with a parabolic profile under conditions of moderate to high penetration depth, the radius of curvature at the apex of the parabola would be smaller than R, thus increasing discrepancy between the two models even more than discussed above. As an example, we have assumed a dimensionless perfect sphere with a radius of $R = 1$ (Fig. 1B). Fitting this profile using points up to $0.7R$ with the general formula for a parabolic profile, $y = ax^2 + b$ gives the values $a = 0.7491$ and $b = -0.0334$, which gives $R_{parabolic} = \frac{1}{2a} = 0.6675$. In this case the curves of δ/R versus a/R are different than those shown previously (see Fig. 1D), with 22% discrepancy at $\delta = 0.5R$ and just 2% at $\delta = 1R$. But in both cases error dramatically grows after $\delta \cong 1.5R$.

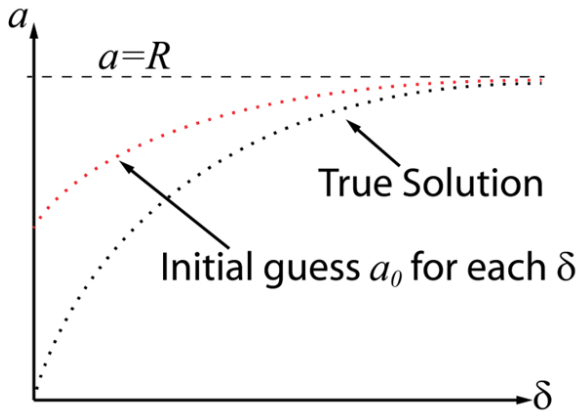

Figure 4.2 True solution to be found via Newtons method (black dots) and initial guess a_0 for each value of δ, which will give values close to the true solution after several iterations (red dots).

In terms of elastic modulus calculation, the main difference between the parabolic and spherical model is absence of an analytical equation which directly relates force and penetration (i.e. the experimental values that are easily acquired from FDCs). This is in contrast to the parabolic and conical models (discussed below), where force is proportional to the penetration through the power law and the elastic modulus is calculated through the constant of proportionality. In order to calculate modulus using a truly spherical indenter, it is thus required to first calculate contact area corresponding to each penetration in the experiment through eq. (4) and then use eq. (3) to calculate the modulus. Since eq. (3) is nonlinear and does not have an analytical solution, solving for a can take considerable amounts of time using simple minimization algorithms, especially for gathering statistics for multiple curves with high numbers of data points. Another problem of the simple minimization algorithm is the precision in the contact area calculation for high penetration values (see Fig. 1C, D), since large changes in penetration produce only minute changes in the contact area.

In order to get around this complication, we have developed fast calculation algorithm in our *MMA Software* which allows for real-time calculations of elastic modulus. The algorithm exploits the monotonic behavior of eq. (3) as well as the fact that the function $a(\delta)$ has limit at $a = R$. Values of penetration δ are known, so a can be calculated from eq. (5) to get the parameter in the brackets in eq. (3). and this value should be calculated for each a. In order to easily perform this calculation, we propose Newton's method for developing values of a from δ. Given an initial guess a_0, the value of $a(\delta)$ can be calculated iteratively:

$$a_1 = 1 + \frac{\delta(a_0)}{\delta'(a_0)} \qquad (5)$$

…

$$a_n = 1 + \frac{\delta(a_{n-1})}{\delta'(a_{n-1})} \quad (6)$$

The formula for the first iteration of finding of the contact radius becomes:

$$a_1 = a_0 + \frac{a_0 ln\left(\frac{R+a_0}{R-a_0}\right) - 2\delta}{ln\left(\frac{R+a_0}{R-a_0}\right) + 2\frac{Ra_0}{(a_0^2+R^2)}} \qquad (7)$$

However, this method requires values of a_0 as an initial guess. The nature of the eq. (4) (i.e. that $\delta(a)$ is monotonically increasing function and contact area a has the limit $a = R$) necessitates that the initial guess, a_0, should always be bigger than the precise value of $a(\delta)$, but smaller than the tip radius R. We propose the following algorithm to find a vector of initial guess values (See Fig. 4.2).

The general formula for such a guess will be:

$$a_0(n) = -\frac{1}{n^2} + R \qquad (8)$$

where n changes from $k_1 = \sqrt{R/2}$ to $k_2 = \sqrt{\frac{1}{R-a'R}}$ with the step $s = (k_2 - k_1)/N$, where N is the total number of points in the vector. As mentioned, the values of a' should then lie somewhere between the true solution (see Fig. 4.1, true solution for the biggest penetration value δ_{max}), but remain smaller than R. The value of the last point depends on penetration: the bigger the penetration is – the closer this point will be to the value of

R. Therefore, the values of a' can be pre-calculated for preset ratios of δ_{max}/R and stored for future use. This pre-calculation step requires a high precision true solution for $a(\delta_{max})$ and requires considerable amount of time but needs to be performed only once.

Thus, for each penetration experiment the following procedure is applied:

The ratio δ_{max}/R is calculated for maximum penetration and depending on this value, a' is selected from the preset data array.

Values of the initial guess $a_0(n)$ are calculated using eq. (8).

Newton's method is applied for 7 iterations using eq. (7) and a high precision true solution $a(\delta)$ is found.

The elastic modulus of the sample surface is then calculated from the slope of the F vs $\left[(a^2 + R^2)ln\left(\frac{R+a}{R-a}\right) - 2aR\right]$ plot.

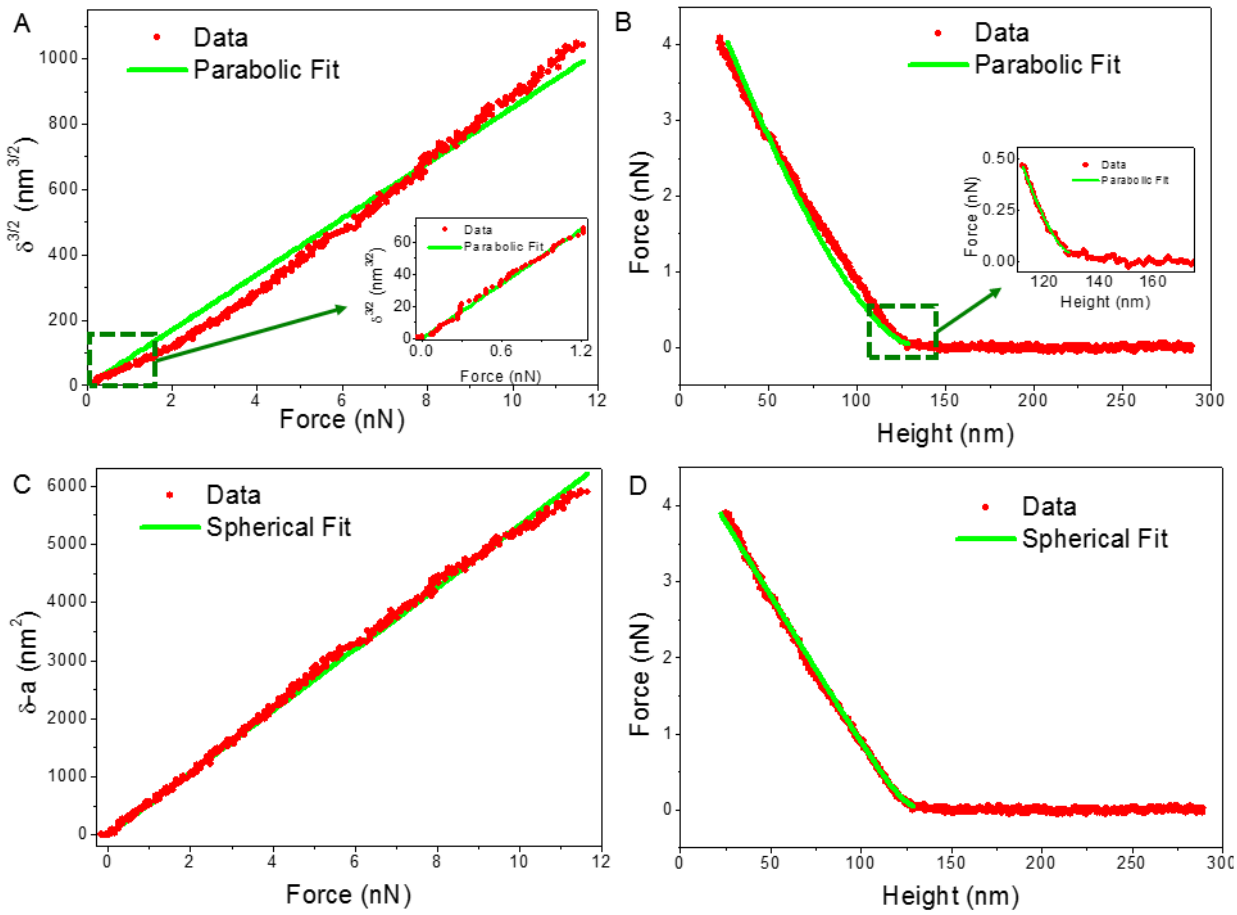

Figure 4.3 FDCs taken on Balafilcon A contact lens surfaces in fluid and fit with either Sneddon's model for a rigid paraboloidal punch (A and B) or for a rigid spherical punch (C and D). Inset in A and B are initial regions of the FDC which have been fitted separately with the parabolic model, exhibiting how well only the very first portion of indentation in this case can be considered parabolic.

As a practical example, Fig. 4.3 shows FDCs taken on commercially available soft contact lenses, Balafilcon A (PureVision, Bausch and Lomb). Fig. 4.3A shows $\delta^{3/2}$ versus F fit with Sneddon's model for a rigid parabolic punch. From this, one can see that instead of a linear dependence of $\delta^{3/2}$ on F, there is significant observable curvature. Back calculating and superimposing onto the original FDC (Fig. 3B) shows different characteristic FDC shape. As mentioned, in the initial stages of indentation the parabolic and spherical models correspond quite closely. Inset in Fig. 3A and Fig. 3B is the initial portion of the FDC also fitted with Sneddon's model for a rigid parabolic punch. From

this it can be seen that the parabolic model fits very closely with the experimental data with minimal deviation. Fig. 4.3C shows a plot of $(a^2 + R^2)ln\left(\frac{R+a}{R-a}\right) - 2aR$ (denoted as δ-a, with units of nm^2) versus F, which has significantly lower fitting error than the parabolic model. As can be seen in Fig. 3D, the same back calculation and superimposition results in a much closer fit over the entire FDC.

To summarize, Sneddon's model for a rigid parabolic punch and spherical punch give very similar results for small indentation depths, with the calculation for the parabolic tip shape being much less cumbersome. As a result, for many users the parabolic model is employed (either knowingly or unknowingly) in preference to the truly spherical model. However, as can be seen in Fig. 1A and Fig. 3C, the shape of AFM tips is not always exactly parabolic, and can actually more closely resemble a more cylindrical punch capped with a hemispherical shape.

4.3.2 Conical versus parabolic tip shape

For soft materials, especially in the case when materials are in the swollen state, very high deformations can be achieved without inducing plastic deformation. Such large indentations require fitting with contact mechanics model which considers a rigid conical indenter on a semi-infinite half-space. During measurements involving large penetration depths, the initial parabolic shape of the tip makes very small contribution to the overall contact area increase, thus the tip can be considered conical in shape. Fig. 4 shows an indentation experiment performed on silk ionomer layers. The parabolic model can be used only for the small initial portion (<20 nm) where contact force changes as $\delta^{3/2}$, after which the penetration changes as δ^2, signifying a different indentation regime.

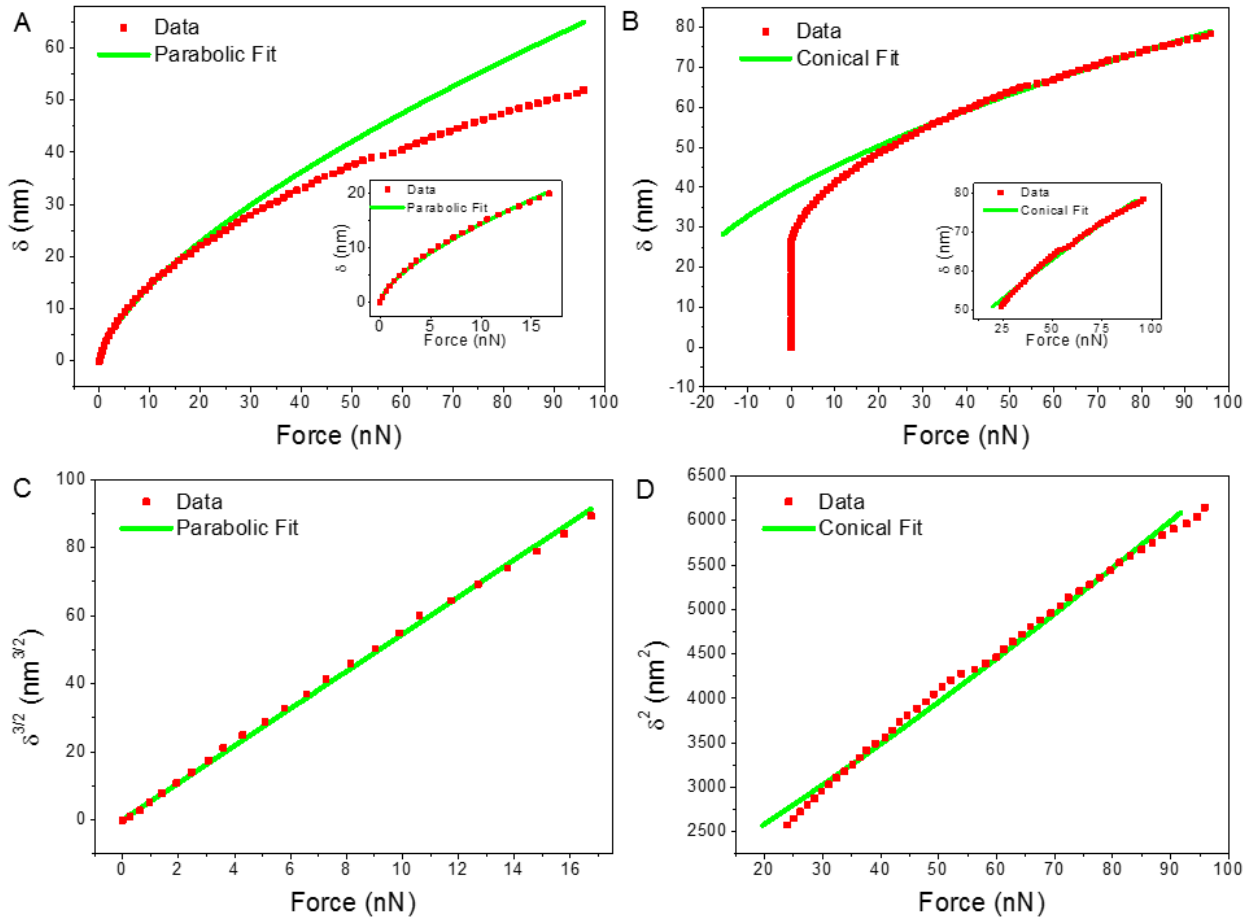

Figure 4.4 A comparison of FDC fitting using the equations for a parabolic punch (A & C) and the equations for a conical punch in our silk ionomer system (B & D). The top row shows the fit of our model function to the whole dataset, while the inset shows the fit in a smaller region more appropriately suited for the specific model (i.e. early in the FDC for parabolic model, and later in the FDC for conical model). Note that the second row is the fitted region plotted as $\boldsymbol{\delta^{3/2}}$ or $\boldsymbol{\delta^2}$ to show linearity.

This view is something of a simplification, as the real tip shape is generally more complex than the simple geometric shapes used in the general approaches. This can be particularly troublesome in the case of surfaces with complex morphologies: establishing a suitable model for the tip-sample interaction is daunting for sharp tips[187]. Various attempts[188] have been made to correct for the tip modelling errors when testing on homogeneous materials. The analytical approaches to these corrections have focused on the inclusion of a small parabolic region at the base of a tip and a smooth transition to a conical or pyramidal region.

Numerical methods have also been utilized[189,190] which can be used to obtain a very detailed picture of the effect of tip shape. While exceptionally accurate, the solutions to these methods can be quite cumbersome and do not lend themselves well to a rapid solution algorithm.

An intriguing compromise between a naïve conical model (that is, one which uses the snap-in point for the penetration starting point) and a more complex tip shape consideration can be used. In general, the determination of tip shape is performed through either electron microscopy[191] or blind estimation.[192] While possible to obtain an accurate reconstruction down to a few nm, obtaining an accurate estimate of tip opening angle generally requires less resolution than determining the tip radius at the apex, which allows for better determination of the tip-sample interaction. Additionally, tip damage or contamination of the tip apex does not generally impact the behavior of a conical tip at sufficiently deep penetrations (since the defect might contribute to only a fraction of the penetration behavior). In the geometric analysis performed by Berla et al.,[193] we see that a real tip can be modeled as a combination of a conical tip with a parabolic terminus defect (often called a "blunted tip"). The projected conical tip will overshoot the real end of the tip by an amount found to be $h = kRm^2$, where k is a constant specific to this equation determined by Berla et al., R is the radius of curvature of the AFM probe, m is the slope of the line parallel to the side angle of the AFM tip.

In order to obtain a picture of our tip profile, we scanned over a roughness standard obtained from Bruker and performed a blind tip estimation. By fitting the profile of the tip apex in our *MMA Software* with a parabolic function, we determined that our probe tip had a radius of about 7 nm, which corresponds well with the manufacturer's stated estimate of

8 nm. The conical profile of the tip was obtained by taking a linear fit of the reconstructed tip profile further away from the tip apex (roughly 15-20 nm away) and lead to a cone semiangle of 25.3°. In our case, this leads to projected cone height which extends roughly 26 nm past the real tip. In our analysis, we compare the results for a parabolic tip, which is fit to small penetrations (0-20 nm), and a conical tip, which is fit to deeper penetrations (15-50 nm) and has its starting point adjusted to account for the 26 nm of the "phantom" tip height.

Because we do not correct for the effects of the blunted tip, the region of small penetration is not accurately fit by this model. As a result, a significant number of points past this initial region is required to obtain a suitable fit for our conical model. In some materials, this constraint coupled with the sharp tips used in this study can be problematic because the large indentations can lead to a significant degree of plastic deformation in the sample[194]. With a swollen thin film of modified silk fibroin, we were able to achieve relatively large penetrations (50 nm) with a negligible amount of plastic deformation as indicated by a lack of hysteresis in the approach and retract curves, and no changes in sample topography after indentation experiments.

For these films, we fit a parabolic indenter with radius of curvature of 7.09 nm and a conical indenter with an opening semiangle of 25.3°. In Fig. 4, the fitting results obtained from our in-house *MMA Software* are displayed. As can be seen in the two graphs, the obtained fitting is quite good for both models and the results obtained for the modulus calculation is comparable. By analyzing 25 of such FDCs, we found that a modelling of the data based on a paraboloid geometry gave an elastic modulus of 47.1 ± 9.3 MPa, whereas modelling a conical geometry led to an elastic modulus of 52.7 ± 5.2 MPa, with errors reported as 1

standard deviation. Given the observed similarity of these values (within the experimental error), the approach used in this study seems to be valid. Of note, the conical model appears to exceed the parabolic model by an average of 15%, though such a deviation is not statistically significant. Considering the relatively high degree of uncertainty in the parabolic fits, we suggest that our model suffers from a degree of uncertainty in the tip-sample interaction within the first few nanometers (particularly, a precise tip profile and starting point location). This can complicate the choice of the starting point adjustment needed to accommodate the conical model, and thus further investigation is warranted.

4.3.3 Tip size variation

For many surface force spectroscopy experimental setups, the use of very sharp probes (~10s of nm radius of curvature) is advantageous as it provides higher lateral resolution facilitating the discernment of different phases of a heterogeneous material surface, or it can allow for the measurement of the micromechanical properties of small structures such as fibrils. We present two examples in which higher resolution is needed in Fig. 5. In Fig. 5A-C the surface of regenerated silk fibroin macromolecules deposited on a silicon wafer is shown with the corresponding adhesion image taken in Bruker's PeakForce QNM mode. As can be seen, the silk fibroin macromolecules interact with the AFM tip differently than the silicon surface, resulting in distinct surface adhesion behavior. An AFM tip with a large radius would be far less discriminant between the two materials at the surface. Furthermore, larger radii tips are more prone to capillary forces due to the presence of a thin water layer at the surface, which would make crisp adhesion mapping shown in Fig. 5B nearly impossible.

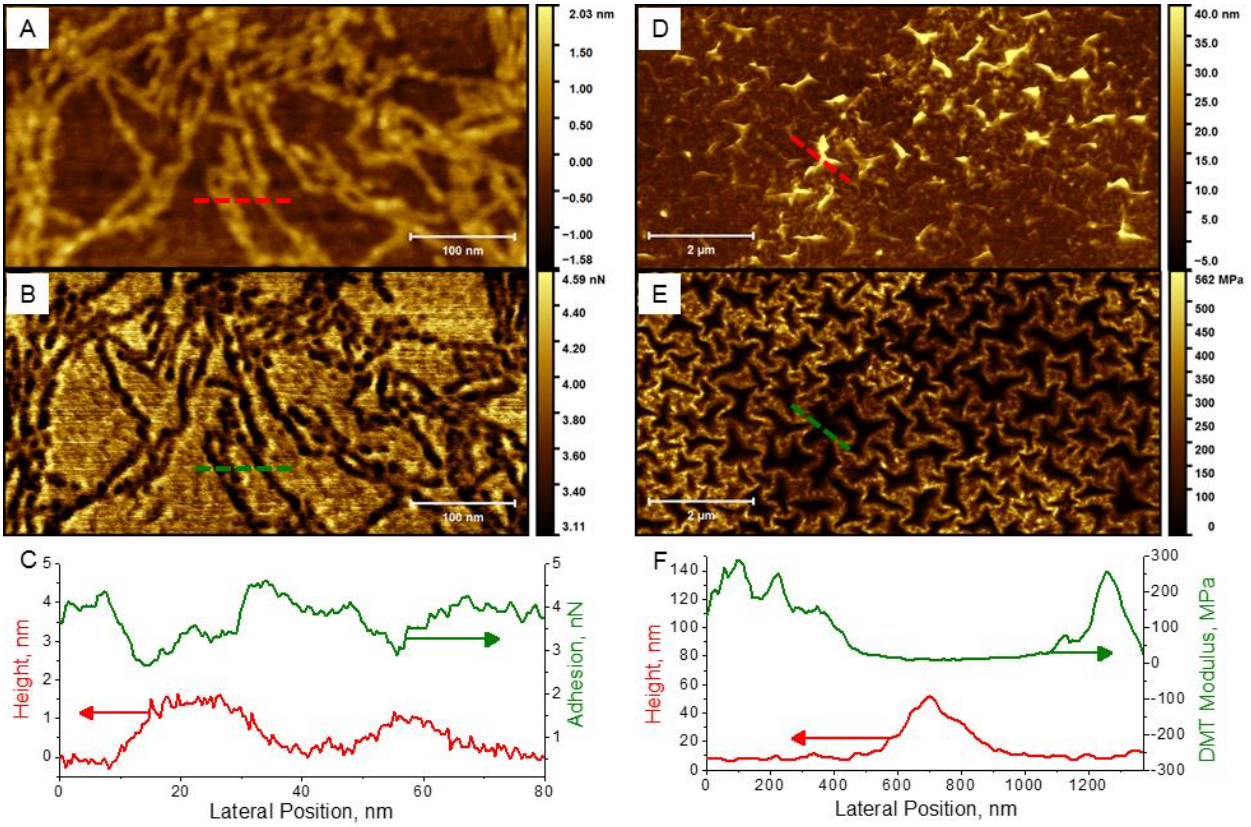

Figure 4.5 (A) Height image of single-few strands of regenerated silk fibroin biomacromolecules cast on a clean silicon wafer. (B) Surface adhesion collected simultaneously, showing a distinct difference between the silk and the silicon ssurface. (C) Sectional profiles of height and adhesion data taken from the locations in A and C denoted by dashed lines. (D) Topography of silk ionomer surface with raised regions occuring as the result of buckling. (E) DMT modulus image acquired simultaneously which highlights the need for a sharp probe as the unsupported buckled regions give unrealisticly low values of modulus while the supported regions can be used for accurate estimation of mechanical properties. (F) Sectional profiles of height and adhesion data taken from the locations in D and E denoted by dashed lines.

As another example, Fig. 5D-F show a buckled silk ionomer surface with the corresponding DMT Modulus (taken using PF QNM). In this case the raised buckled regions are generally between 45 and 90 nm (Fig. 5F shows sectional profile) and are not supported by the underlying substrate. Consequently, these structures are extremely compliant when force is applied by an approaching AFM tip. Because a large radius probe would contact many of these high features first it would be extremely cumbersome to determine true contact area, resulting in high error in calculating the sample elastic modulus. Furthermore, any calculated modulus for FDCs taken with a large radius probe on these samples would be a

composite value of the extremely complaint buckles and the stiffer material. However, scanning with a sharp probe allows for access to substrate-supported regions of the silk ionomer surface, and more accurate measurement of the surface mechanical properties (here the apparent DMT Modulus shows 100-300 MPa for supported regions and ~0 MPa for buckled regions).

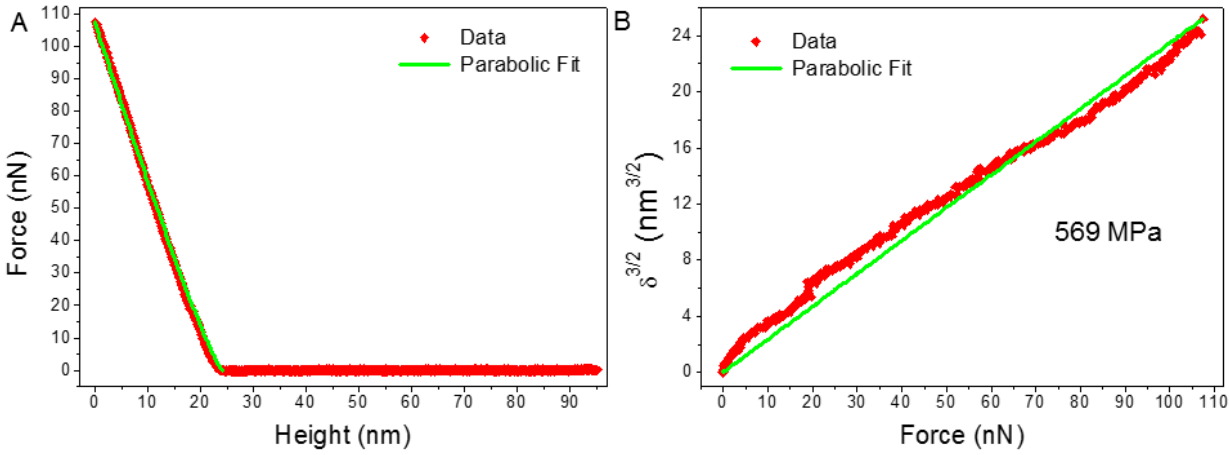

Figure 4.6 (A) Force-distance curve taken with a sharp probe (radius of curvature ~20 nm) on a cast polystyrene substrate. In this measurement, the maximum sample penetration depth is 9 nm. (B) $\boldsymbol{\delta^{3/2}}$ versus applied force used for fitting with Sneddon's model for a rigid parabolic punch. In this curve the elastic modulus was calculated to be 569 MPa.

However, in many cases, the use of probes with large tip radius or colloidal beads can be advantageous over sharp probes. Foremost, it is known that larger tip radii reduce the maximum stress on the material in the area just blow the tip-sample contact point, and thus the use of probes with larger tip radii significantly reduces the possibility of inducing plastic deformation during FDC collection. Quick examination of the simple Sneddon model of a rigid paraboloidal punch shown in eq. (1) reveals that, for a given applied force F, penetration depth (as $\delta^{3/2}$) and tip radius of curvature (as $\sqrt{R}$) are inversely proportional. As a result, one can see that for extremely soft samples such as loosely networked hydrogels or other compliant biomaterials, increasing tip size can significantly

reduce the penetration depth for a given applied force, thus diminishing the probability of inducing plastic deformation on the sample surface.

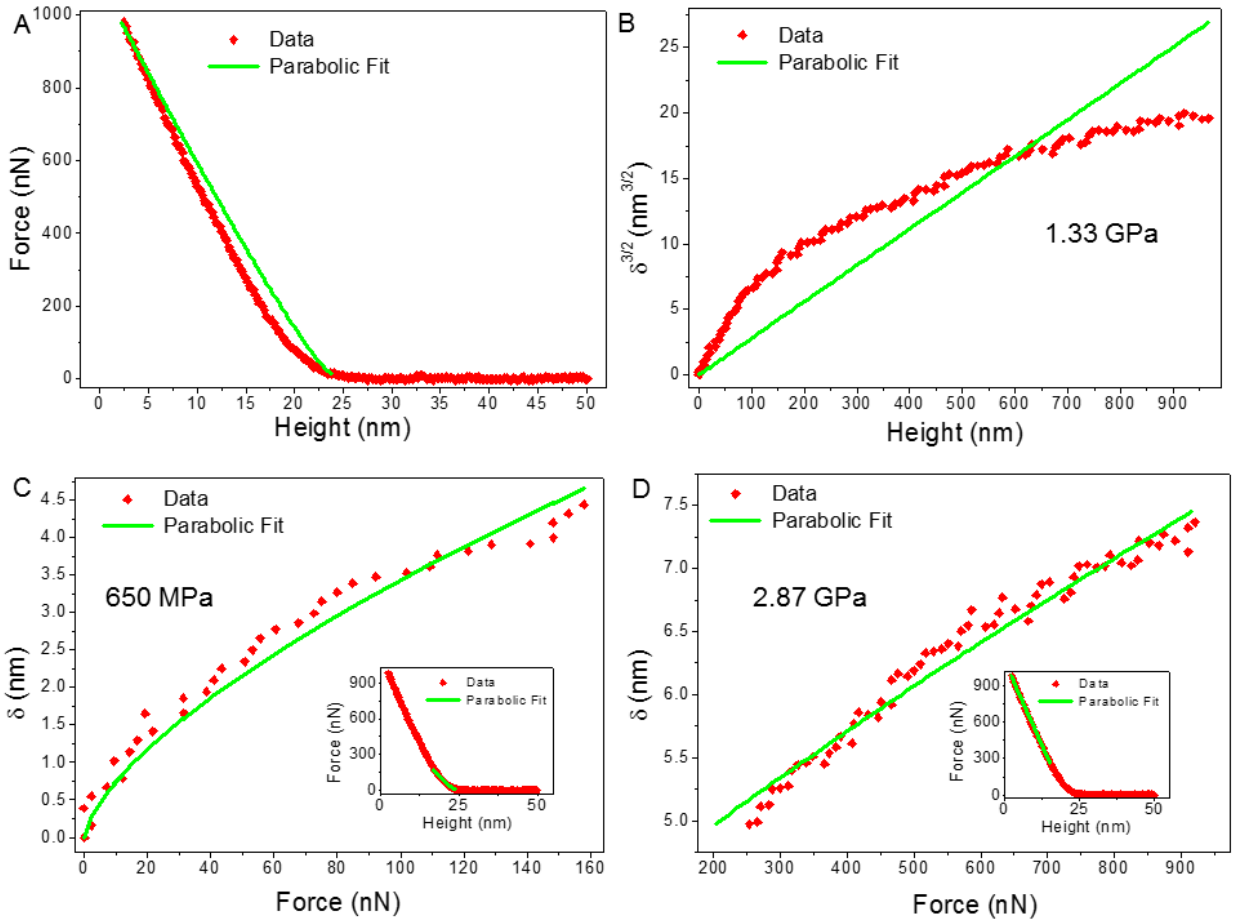

Figure 4.7 (A) Force-distance curve taken with a large, annealed probe (radius of curvature ~330 nm) on the same cast polystyrene substrate as the measurements in Fig. 6. In this measurement the maximum sample penetration depth is 8 nm. (B) $\boldsymbol{\delta^{3/2}}$ versus applied force used for fitting with Sneddon's model for a rigid parabolic punch with the calculated elastic modulus of approximately 1.3 GPa. The bottom two panels show the fitting of $\boldsymbol{\delta}$ (used here to show actual deformation levels) versus applied force for initial penetration (C) and final penetration depths (D). Inset is the original FDC and fitting for the corresponding portion of the curve.

Furthermore, because of this inverse proportionality, in cases where high lateral resolution is not required (e.g. thick, homogeneous material surface), much higher force resolution can be achieved with large radii probes because larger much larger forces can be applied to the surface while maintaining low penetration depths. This can serve to significantly reduce data analysis errors associated with few data points, and can also be used to

overcome the snap-in instabilities associated with large probes as the snap-in forces becomes negligible compared to the overall applied force.

In some cases, even with well-known polymeric materials, processing conditions can create the possibility for high surface roughness, or perhaps a more mobile surface layer which can affect measurements taken with exceedingly sharp probes. We present here several micromechanical measurements taken on a thick polystyrene (PS) film made by casting a highly concentrated solution dissolved in chloroform. FDCs were taken in fluid for both as received AFM tips (R = ~20 nm, Fig. 6), and for thermally annealed tips (R = ~330 nm, Fig. 7). PS is a common polymer system with a well characterized elastic modulus of ~3 GPa. However, in this specific case an abnormally low surface elastic modulus was observed. Fig. 6 shows a representative FDC collected using a sharp probe (spring constant = 6.9 N/m), with a total maximum penetration depth of approximately 8 nm. Fitting the $\delta^{3/2}$ versus applied force data obtained from the FDC in Fig. 6A resulted in a calculated elastic modulus of 569 MPa. Examination of >20 FDCs from different locations along the surface resulted in an average modulus of 479 ± 111 MPa.

When this same surface is probed using an annealed AFM tip with a large radius of curvature (~330 nm tip radius) the FDC behavior is different. Fig. 7A and 7B show a representative FDC and $\delta^{3/2}$ versus applied force plots. In this case the applied force was adjusted by using a stiffer cantilever (spring constant = 65.8 N/m) such that a similar penetration depth could be reached as compared to the FDCs taken with the small radius probe. In this case the maximum penetration depth was ~7.5 nm (Fig. 7D has raw penetration depths determined from the experiment). As can be seen in Fig. 7B, there is

some significant fitting error associated with using the parabolic model for these curves. This is a result of the apparent "layered" behavior seen in the plot of $\delta^{3/2}$ vs. F (Fig. 7B), as one linear slope transitions gradually to another, representing a change from a lower modulus to a higher modulus. Fitting the overall curve, therefore, represents a composite value of the two separate moduli, giving a calculated modulus of 1.3 GPa in this example.

However, this curve was also analyzed in at different penetration depths using the *MMA Software*. For low penetration depths (e.g. ~4 nm seen in Fig. 7C) the sample surface appears much more compliant with a modulus of approximately 650 MPa, which is much more closely associated with the value determined from FDC analysis with a sharp probe. If the region of the FDC corresponding to higher penetration depths is fit the calculated elastic modulus is determined to be 2.8 GPa, which corresponds well with reported values of PS elastic modulus. The primary stress from the applied force from the tip onto the surface extends farther into the subsurface as the tip radius increases for a given penetration depth.[195] Therefore, in this case the large tip radius probe is able to better probe the bulk material away from the compliant surface. Facilitated by a simple fitting algorithm embedded into *MMA Software*, this routine could perhaps be very useful in exploring different mechanical responses with penetration depth. It should be noted here that the explanation of this soft outermost layer for our PS substrate was not examined, however we suggest that it is still useful and relevant to the type of analysis described about.

Further examples of the usefulness of varying tip size when making micromechanical measurements of soft materials is the ability to switch between strictly surface modulus (with a depth of 10s of nm) while using small radii probes, to examining the structural rigidity of a sample of with a large tip radii. There are several examples in the literature in

which the structural rigidity of small cells is measured by examining their mechanical properties with large colloidal probes.[187]

4.4 **Conclusions**

As AFM-based force spectroscopy takes an even more prominent role in determining the micromechanical properties of soft materials, biomaterials, and nanocomposites the precision of data analysis routines should also be refined. Here we have described in detail several contact mechanics models for commonly encountered tip geometries: paraboloidal, conical, and spherical, and used a variety of soft materials to exemplify situations in which each model should be employed. Additionally, we have demonstrated the usefulness of our home-built analysis program, *MMA Software*, in calculating micromechanical properties of soft materials from FDC data.

In this study, we showed how quickly results could deviate after simple misassumption of tip geometry, and use of the equations of a paraboloidal punch rather than those for a spherical punch for FDC analysis. FDCs collected on the soft elastic surface of a commercial contact lens were observed to exhibit behavior that is not fitted very well with the parabolic model. As a result, we suggest that in some cases the sharp tip of a probe could actually resemble more a hemispherically-capped cylindrical punch with a finite limit to contact radius than a paraboloidal punch which has a contact radius that can continuously increase. Unfortunately, there is no analytical solution to the spherical equations and numerical analysis can be very cumbersome. However, we have described our simple algorithm for working with spherical equations, which will be available to users in some capacity via our *MMA Software* package.

Analysis routines for utilizing the conical model here showed that the initial portions of FDCs could be used with the parabolic model, but as indentation depth grows, the blunt tip apex plays a decreasing role in the overall contact area. Thus, calculations using the initial indentation with the parabolic model and the latter stages of indentation with the conical model gave results within on standard deviation. However, the caveat to this approach is that a significant amount of data points need to be collected (i.e. high enough indentation depths need to be achieved) in order to reduce the effect of the blunted tip apex for the conical model to fit well.

Finally, the effect of tip radius were briefly discussed. In general, it is well known that larger probes facilitate mechanical properties determination while reducing the probability of plastic deformation occurring. We have also shown some specific examples of when a sharp probe could be preferential to a dull probe, especially in the case where precise positioning is required for the determination of the properties of extremely fine surface features. In the case of a large radius probe, the stress distribution immediately below the tip-sample contact point extends farther into the subsurface. As a result, the FDC behavior observed on the same material surface may be different when probed with a different radii probes. Here we used an example of a PS surface in which the very top layers were abnormally compliant. By probing farther into the bulk using a large radius probe, we could detect a modulus which more closely matched literature values for PS. As a result, we suggest this method along with the data analysis routines employed in our *MMA Software* as a means to carefully probe some multilayered materials.

CHAPTER 5. INTERFACIAL SHEAR STRENGTH AND ADHESIVE BEHAVIOR OF SILK IONOMER SURFACES

5.1 Introduction

Thin-shell microcapsules have been widely studied for encapsulation due to their favorable transport performance and outstanding mechanical properties.[97,196,197] The LbL assembly approach has attracted attention for fabricating microcapsules with superior encapsulation capabilities.[198,199] Biocompatibility is a critical issue in building nontoxic LbL-based microcapsules; however, in many polymeric microcapsules based on electrostatic interactions, bio-compatibility is compromised by the cytotoxicity of synthetic cationic components.[200] To overcome this issue, natural components such as SFs have been utilized as materials for fabricating LbL microcapsules that are biocompatible and biodegradable.[201] Specifically, silk ionomers with a low content of ionic side groups have been utilized to enhance the encapsulation of cells with retention of high viability.[60,61,202]

Strong mechanical properties are required for thin-shell LbL microcapsules in order to ensure their encapsulation functionalities in various environments, with high mechanical stability, controlled transport, and robustness important. Previous studies determined the elastic modulus of polymer-based microcapsule. Specifically, the elastic modulus of polyelectrolyte multilayer microcapsules has been determined to vary in the range of 0.15−1.9 GPa.[203,204] Additionally, our previous study reported that silk ionomer based microcapsules showed the elastic modulus in the range of 1.1-1.8 GPa.[63] In general, debonding/delamination is prone to occur at interfaces with weaker load transfer capability,

resulting in the loss of overall mechanical properties of LbL microcapsules. Specifically, the mechanical properties of LbL microcapsules are governed by the complementary molecular interactions at the interfaces between the alternating layers and their composition and morphology. The chemical interactions and ionic pairings are the main determinants of mechanical properties.[202,205]

Understanding interfacial shear properties, which is dominated by the transfer of shear load between adjoining surfaces, is critical for quantifying the robustness of multi-layered structures and micro/nanocomposites. As such, various methods have been employed to determine the interfacial shear strength of multicomponent materials.[206] Gallant *et al.* measured the interfacial shear strength of silicon microwires embedded in Nafion membranes through uniaxial wire pull-out experiments.[205] Sakhavand *et al.* performed tensile experiments with platelet–matrix nanocomposites and stacked heterostructures to determine interfacial shear strength between adjacent layers in the platelet–matrix system.[207] Single-fiber push-out tests were conducted to investigate interfacial shear strength between glass fiber/epoxy composites using a microindentation system.[208] However, previous studies have focused on identifying interfacial shear strength of matrix/reinforcements-based nanocomposites through conventional methods such as tensile tests[207,209], which are not suitable for determining an interfacial shear strength of ultrathin (<100 nm) LbL shells.

To evaluate the interfacial properties of various LbL nanocomposites, nanoscratching and nanoindentation have been widely used as effective probing approaches.[210,211] However, these methods are destructive in nature and need severe plastic deformation such as permanent scratches and indents. Polymer and biopolymer LbL shells, which are

frequently composed of ultrathin layers below 3 nm thickness and soft biomaterials are not suitable for nanoscratch and nanoindentation tests. Even though some studies have examined the interfacial interaction between adjacent surfaces of LbL components, [212,213] the interfacial interactions in these systems were only indirectly determined.

As known, the nanoscale and microscale dimensions of functionalized AFM tips allow for probing the influence of topography and the chemically modified surfaces to determine the role of chemical interactions on the interfacial shear strength. **Error! Bookmark not defined.**[202,205,214,215] Colloidal AFM probes have been widely used to measure the friction and adhesive surface properties of materials.[216,217] Surface properties can be measured by using colloidal AFM probes under low uniform contact pressure in the elastic deformation regime. In contrast, with the colloidal tip the standard sharp AFM tip can locally penetrate the target surface due to the high localized pressure.[218,219]

In the present study, we use functionalized AFM tips to perform a shearing experiment in the lateral force microscopy (LFM) regime[220,221] and to conduct force spectroscopy data for measuring adhesive forces (pull-off forces). We select two different types of silk ionomer pairings, a SF-Glu/SF-Lys pair with direct complementary ionic pairing between anionic and cationic materials, and a SF-Glu/SF-Lys[PEG] pair with coulombic interactions partially screened by the presence of PEG segments (Scheme 1). These silk ionomeric materials are the main biopolymer components of silk ionomer-based LbL microcapsules reported earlier.[202,222] The interfacial shear strength of LbL silk ionomers was determined under natural conditions, in the swollen state in fluid.[223]

5.2 **Experimental Details**

5.2.1 Frictional and adhesive force tests

In the contact mode, frictional and adhesive forces between different types of LbL silk ionomers can be derived from LFM data and FDCs, respectively under both dry (in ambient condition) and fluid conditions (in deionized water) (Scheme 2a, b).[224,225,180] By using SF-Glu functionalized AFM tips and the (SF-Glu/SF-Lys)$_5$ silk ionomer LbL film, the interfacial interaction between two different silk surfaces, SF-Glu on AFM tip and SF-Lys on the LbL coating can be investigated (Scheme 2c). Similarly, interfacial properties between SF-Glu and SF-Lys[PEG] were identified by SF-Glu functionalized AFM tips and the (SF-Glu/SF-Lys[PEG])$_5$ silk ionomer films. Furthermore, two different types of SF-Glu functionalized AFM tips, standard sharp AFM tip and colloidal AFM tip, were used to perform the measurements on LbL silk ionomer coatings (Fig. 38c).

The deflection sensitivities of the AFM cantilevers were calibrated by acquiring the FDC data on a sapphire surface.**Error! Bookmark not defined.** The spring constants of the AFM c antilevers were determined by the thermal tuning method[226] with calibrated deflection sensitivities (colloidal AFM cantilever: 0.36 ± 0.08 N/m, sharp AFM cantilever: 0.18 ± 0.05 N/m). To investigate radii of AFM tips, a titanium dioxide (TiO_2) nanospike arrays (RS-15M, Bruker) and a standard AFM calibration grating (Bruker, APCS-0099) were scanned by the sharp AFM tip and the colloidal AFM tip, respectively, and radii of AFM tips were determined by deconvoluting the scanned images: colloidal AFM tip radius: 1.05 ± 0.28 μm, sharp AFM tip radius: 10.8 ± 1.5 nm.**Error! Bookmark not defined.**

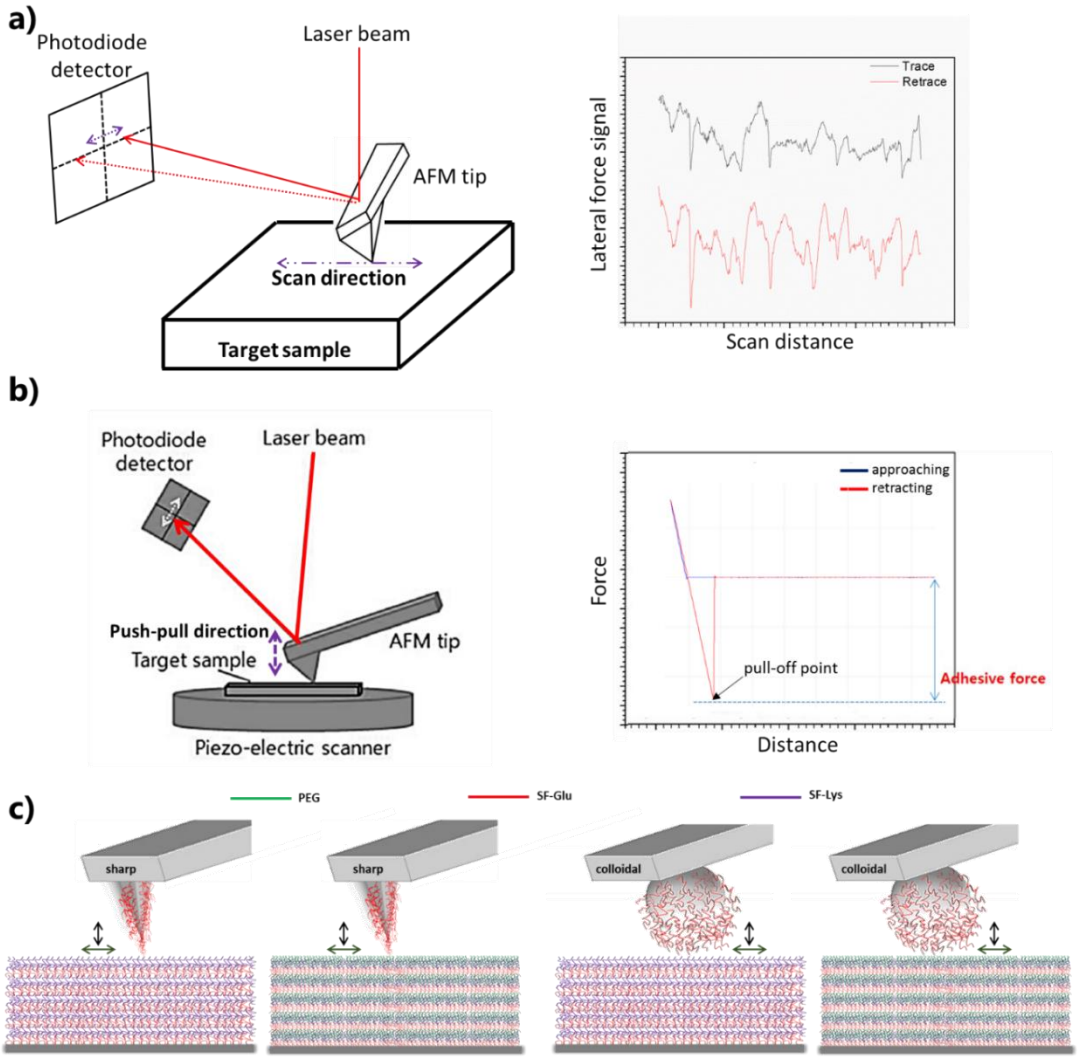

Figure 5.1 (a) Frictional force test with lateral force signal (LFS) and (b) adhesive force test with FDC. (c) Two types of SF-Glu functionalized AFM tips (sharp and colloidal types: red color) located on the target surface of $(SF\text{-}Glu/SF\text{-}Lys)_5$ and $(SF\text{-}Glu/SF\text{-}Lys[PEG])_5$ LBL silk ionomers for nanotribological tests.

In order to obtain LFM data, tip sliding tests (friction loops) were conducted with functionalized and calibrated AFM tips. The torsional stiffness of AFM cantilevers was calibrated using standard AFM calibration grating (Bruker, APCS-0099), and the obtained LFS were converted to the lateral forces with the friction force conversion factor of AFM cantilevers.[227] The scanning rate for sliding tests was fixed as 0.3 Hz. LFSs were obtained using a twisted cantilever within a sliding test performed with LFM, and two different types

of friction signals, namely trace and retrace signals, were generated as a friction loop through forward and backward scanning (Fig. 38a). A range of friction signals were collected by applying different normal forces. Friction images have been obtained through LFM, as well.

Based on the acquired friction signals, friction images were produced representing varying frictional behavior on the scanned surface. The friction signals increased in tandem with the increase of normal force, and the contrast of the friction images corresponds to the alteration of friction signals within so called friction loops. [228] The adhesive forces defined as pull-off forces between the functionalized AFM tip with silk ionomer and the surface of silk ionomer film can be determined according to the product of the spring constant and the maximum (negative) deflection of the AFM cantilever from the FDC retracting portion.[229,230]

5.3 **Results and discussion**

5.3.1 Functionalized AFM tip verification

Both the bare and functionalized AFM tips were examined by XPS for their surface chemical composition. In these spectra, the functionalized AFM tip showed strong nitrogen signal associated with the amine group on the silk fibroin backbone structure, while the untreated AFM tip did not show a nitrogen signal but showed oxygen, carbon, and silicon signals as expected for bare silicon materials. In addition, the survey spectrum revealed that sulfur, which can be originated from traces of sulfur in silk proteins on the functionalized tip.[231] The presence of trace sulfur and nitrogen proved that silk fibroin

material was attached to the AFM tip, as sulfur was not present in the native silicon dioxide or in the organic linkers (APTES SAM and glutaraldehyde).

Additionally, scanning electron microscopy (SEM) images and EDX maps were collected from both the functionalized AFM tips and the untreated AFM tips. EDX results indicated an increased amount of carbon and oxygen (relative to the silicon signal) on the functionalized AFM tips. Overall, these XPS and EDX results indicated that the silk ionomers coated the AFM tips through the functionalization process. The functionalization

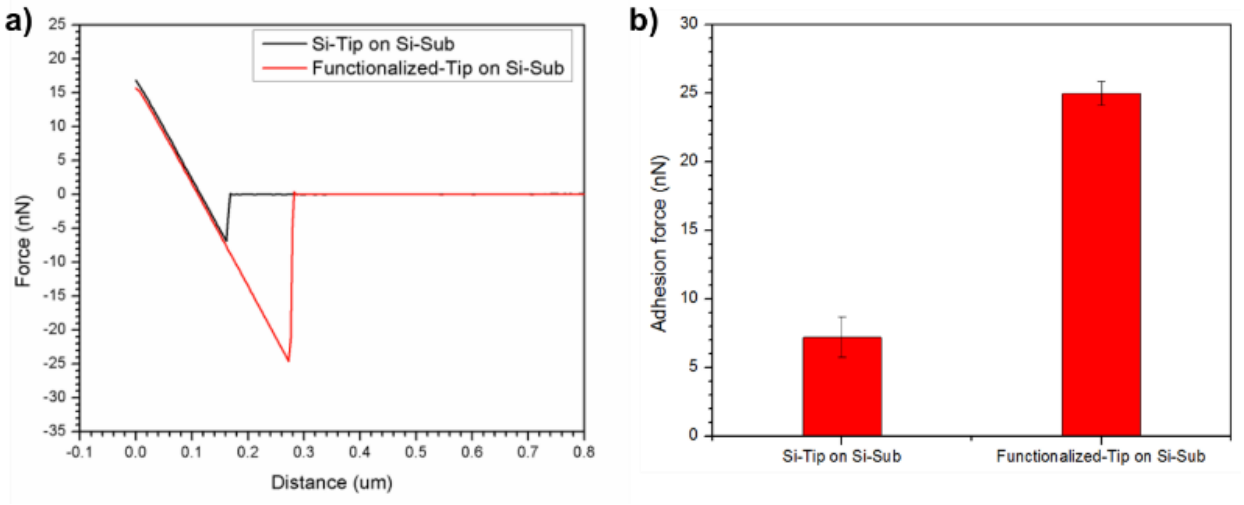

Figure 5.2 (a) Force-distance curves (retracting data) on bare silicon (Si) substrates with functionalized AFM tip and untreated (Si) AFM tip. (b) Adhesive forces on Si substrates with functionalized AFM tip and untreated (Si) AFM tip. Each bar is represented as means with ± STD, n = 10.

of AFM tips was further confirmed by using force spectroscopy measurements between the AFM tips and the silicon oxide substrate. When comparing the adhesive force between a silicon oxide substrate and two different kinds of tips, specifically a non-functionalized, bare silicon tip and a silk ionomer-functionalized tip, a significant difference in pull-off forces was found (Fig. 5.2a). Overall, the functionalized tip demonstrated a much higher adhesive force than the untreated silicon tip (Fig. 5.2b).

The adhesive force of the untreated silicon AFM tip and the functionalized AFM tip were 7.2 nN and 25.0 nN, respectively. Strong adhesion is a general intrinsic property of proteins such as the silk fibroin due to the physical interlocking and chemical interactions by tethering amine-groups on the silk fibroin backbone structure.[232,233,234] The range of measured adhesive force results on the silicon substrate matched other published data.[235,236] Thus, the adhesive force of the functionalized AFM tip was almost fourfold greater than that found for the untreated silicon AFM tip, further confirming tip functionalization.

Next, the effective elastic modulus values of the topmost coatings were evaluated by fitting indentation models (as discussed in subsection 3.10) to FDCs.[237,238,239,104,240] The elastic modulus of the LbL silk ionomer 5 bilayers in the dry state determined from this analysis was 4.2 ± 1.3 GPa. The elastic modulus was determined in dry conditions at 2 nm indentation depth, which is about 10% of the total for 5 bilayers $(SF\text{-}Glu/SF\text{-}Lys[PEG])_5$ thickness and constitutes a fraction of the individual bilayer thickness (4 nm). The value obtained here was close to that obtained for other silk materials in solid films with standard β-sheet content in our previous report and further confirmed the presence of the silk coating on the functionalized tips.[78]

5.3.2 AFM images of silk ionomer LbL coatings

The surface morphologies of two different LbL silk ionomer coatings were investigated in both the dry and swollen states using AFM (Fig. 5.3).**Error! Bookmark not defined.** The surfaces o

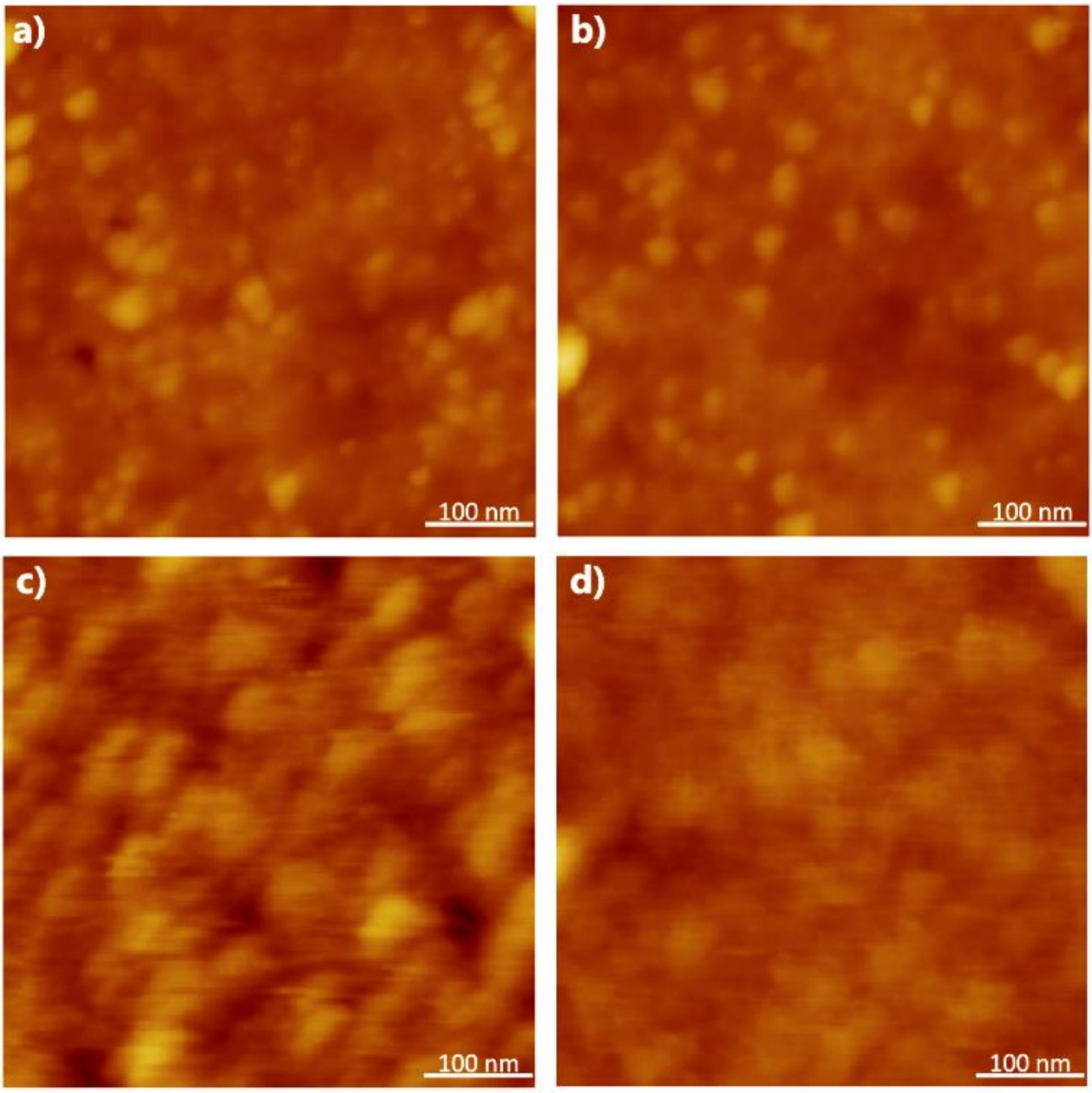

Figure 5.3 Zoomed-in topographical AFM images (Z-scale: 40 nm) of LbL silk ionomer coatings (a) (SF-Glu/SF-Lys[PEG])$_5$ in dry state, (b) (SF-Glu/SF-Lys)$_5$ in dry state, (c) (SF-Glu/SF-Lys[PEG])$_5$ in swollen state, and (d) (SF-Glu/SF-Lys)$_5$ in swollen state.

f both LbL silk ionomers are quite smooth in dry condition (Fig. 5.3a, b). In fluid condition, 5 bilayer (SF-Glu/SF-Lys[PEG])$_5$ becomes rough while the surface of 5 bilayer (SF-Glu/SF-Lys)$_5$ is still smooth (Fig. 5.3c, d). The surface microroughness of each LbL silk ionomer was measured within an area of 500 nm x 500 nm. In the dry condition, the 5

bilayer $(SF\text{-}Glu/SF\text{-}Lys[PEG])_5$ coating possessed a low surface microroughness of 1.4 ± 0.3 nm, similar to the LbL coating $(SF\text{-}Glu/SF\text{-}Lys)_5$, which was 1.7 ± 0.4 nm. These values are comparable to those reported in literature for uniform thin glassy films from synthetic and biopolymers.[241,242] On the other hand, in hydrated conditions, the surface microroughness of the $(SF\text{-}Glu/SF\text{-}Lys[PEG])_5$ LbL coating increased to 3.5 ± 0.9 nm while that of $(SF\text{-}Glu/SF\text{-}Lys)_5$ LbL coating remained almost the same as in the dry conditions (1.9 ± 0.7 nm).

The surface microroughness of the LbL silk ionomers is in good agreement with the data demonstrated for other LbL silk ionomer films.[241,243] On the other hand, it is known that PEG segments swell well in phosphate buffer[244,245] and thus, swollen PEG loops can result in the significant increase of surface microroughness of the $(SF\text{-}Glu/SF\text{-}Lys[PEG])_5$ LbL coatings and the appearance of about 50 nm grainy surface features in contrast to the purely anionic-cationic paired silk ionomers (Fig 5.3).

The energy dissipation, in general, depends on the sliding rate, and larger energy dissipation can be occurred at very high sliding velocities with deformation at the contacting area.246 In this study, we used relatively low 0.3 Hz fixed scanning rate for friction measurements in order to prevent the higher deformation of the silk ionomers LbL structures at the contacting interface. While the topographical images showed no contrast difference with varying normal forces, the contrast in the friction images shifted as the amount of normal force was increased from 50 nN to 150 nN (Fig. 4.4a, b). The brighter contrast regions represent a higher frictional force than the darker regions as quantified by friction loops (Fig 4.4c). It is worth noting that applying a relatively low normal force during the sliding test produced no plastic deformation or surface damage as revealed by

unconverted AFM topography images, despite the increasing normal load.247

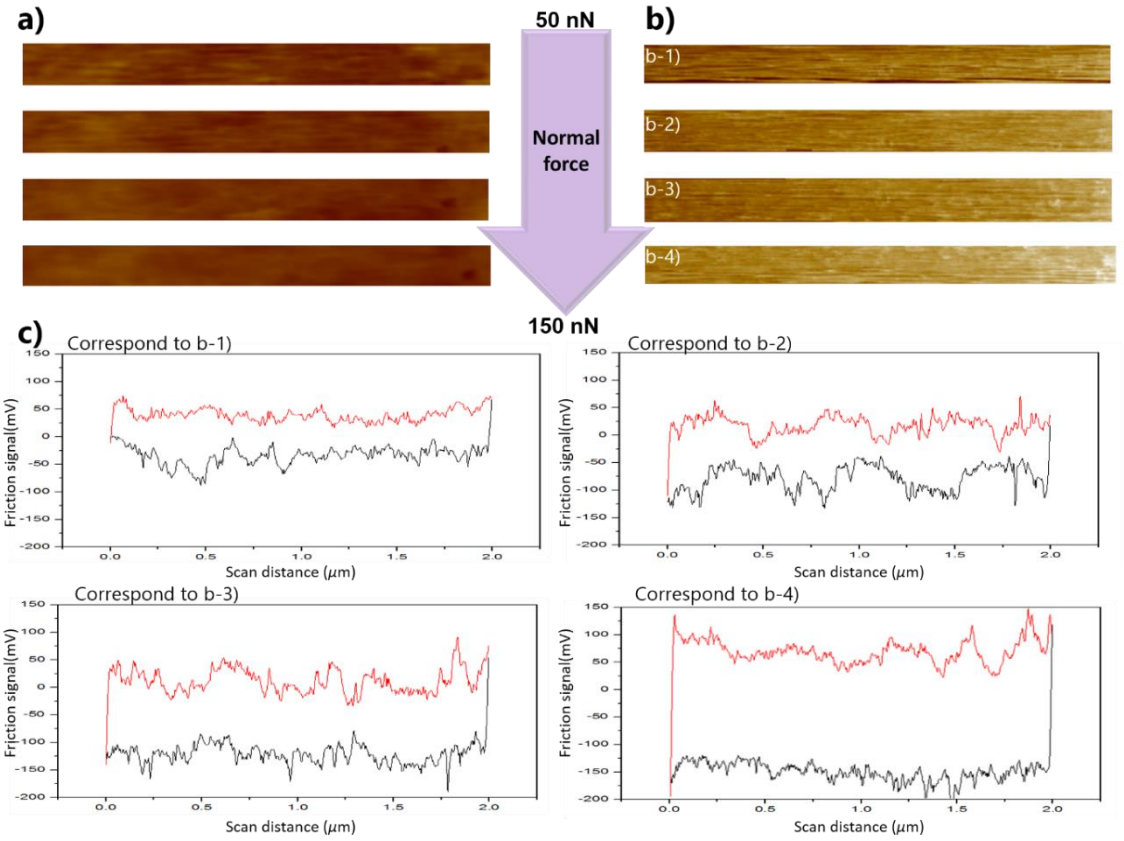

Figure 5.4 (a) Topographical AFM images of $(SF\text{-}Glu/SF\text{-}Lys)_5$ in fluid conditions (Z-scale: 50 nm), (b) AFM friction images of SF-Glu/SF-Lys in fluid conditions (Z-scale: 0.5 V) on $(SF\text{-}Glu/SF\text{-}Lys)_5$ in fluid conditions with applying various normal force from 50 to 150 nN. (c) Friction loops correspond to the friction images (b-1, b-2, b-3, and b-4).

Under all different sliding conditions, frictional force generally increased as normal force was increased in a linear fashion (Fig. 5.5a). In this simplified case, the friction force (F_f) behavior in the elastic deformation regime can be analyzed by using modified Amonton's law:

$$F_f = F_0 + \mu F_n \quad (1)$$

where F0 is the residual force (friction force at zero normal force), μ is the friction coefficient determined as $\mu = \partial Ff / \partial Fn$.[169] The values of residual force can be determined from an intersection of the linear fitting with the horizontal y-axis and the friction coefficient was determined from the slope of the linear fits (Fig. 5.5a).

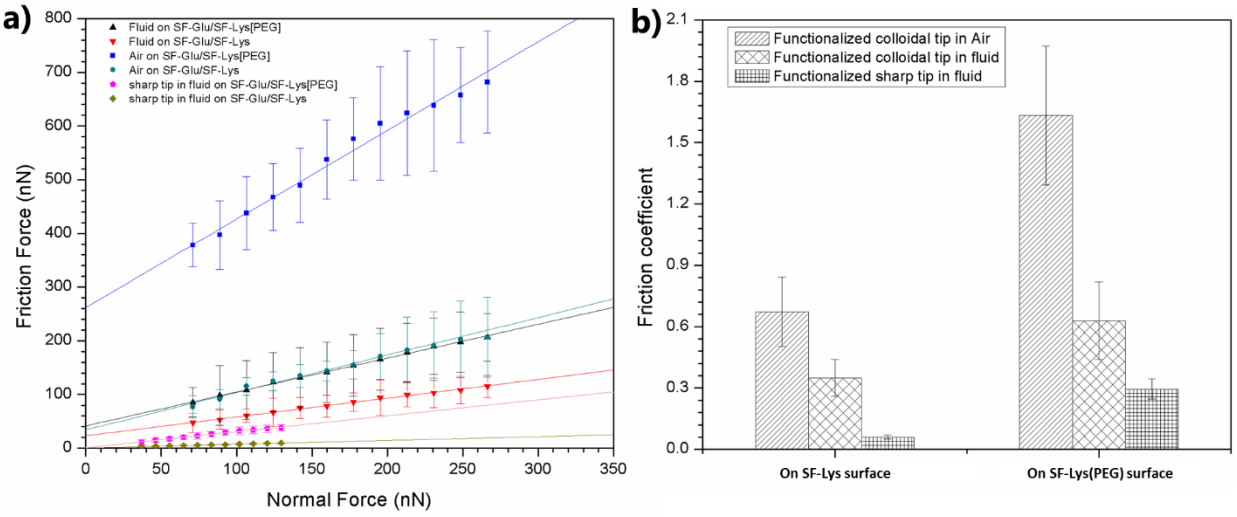

Figure 5.5 Frictional force analysis using SF-Glu functionalized colloidal and sharp AFM tips: a) frictional force versus normal force with different surface of silk-ionomers in both air and fluid conditions, b) friction coefficient of each different condition. Each bar is represented as means ± STD, n = 10.

The frictional force plots show a significant difference of overall friction behavior between different mating surfaces. With the SF-Glu functionalized colloidal AFM tip, the friction coefficient of SF-Lys[PEG] surface was much higher than that of the SF-Lys surface, with an extremely high value of 1.63, versus 0.67, respectively. The friction coefficient between mating surfaces (SF-Glu (tip)) in the fluid condition was reduced significantly to 0.63 and 0.35 for SF-Lys[PEG] and SF-Lys surfaces, respectively (Fig. 5.5b).

Similar trends were observed for sharp SF-Glu functionalized AFM tips but with lower absolute values: 0.07 for the SF-Lys surface and 0.29 for the SF-Lys[PEG] surface (Fig. 5.5b). It is worth noting that much higher friction coefficients were determined with the functionalized colloidal AFM tips, which can be related to the much higher contact area

(of a few μm^2) causing much higher adhesive forces and excessive capillary forces contributions.[248]

Overall, both LbL silk ionomers showed relatively high friction due to strong interactions between complementary silk surfaces with oppositely charged amino acids, similarly to those observed for synthetic cationic-anionic mating SAMs. Indeed, typical friction coefficient for functional organic SAMs are varied in the range of 0.1-0.5 with very low values of 0.01-0.1 observed for hydrophobic SAMs from silanes and some higher values above 1 can be caused by extremely high adhesive forces between complementary chemical groups with ionic pairing or strong hydrogen bonding.[249] Notably, the adhesive forces between the AFM tip and the substrate surface tend to decrease significantly in fluid due to the elimination of the dominating capillary interactions (Fig. 5.5b).[223,250,251] In any case, a significant increase of the friction coefficient for surfaces with PEG segments can be related to increased adhesion as well as to the addition of the plowing component for sliding the tip in loose PEG from the top surface environment.[252]

5.3.3 Adhesive forces between AFM tip and silk ionomer surfaces

The adhesive forces between the functionalized AFM tips and different silk ionomer surfaces were determined by using FDC data in fluid conditions (Fig. 5.6). The adhesive forces with SF-Lys[PEG] surfaces were found to be much higher than that for SF-Lys surfaces: 0.9 ± 0.1 nN vs 0.4 ± 0.1 nN for sharp tips vs 1.6 ± 0.4 nN and 1.0 ± 0.2 nN for colloidal probes (Fig. 5.6). This trend follows those found for residual forces obtained from the friction data, but with absolute values much higher due, probably, to deeper tip penetration under higher normal forces and shearing of the top layer. Derjaguin-Müller-Toporov (DMT) contact model was used to determine the radius of contact between two different interacting silk ionomer pairs.[253,254,255]

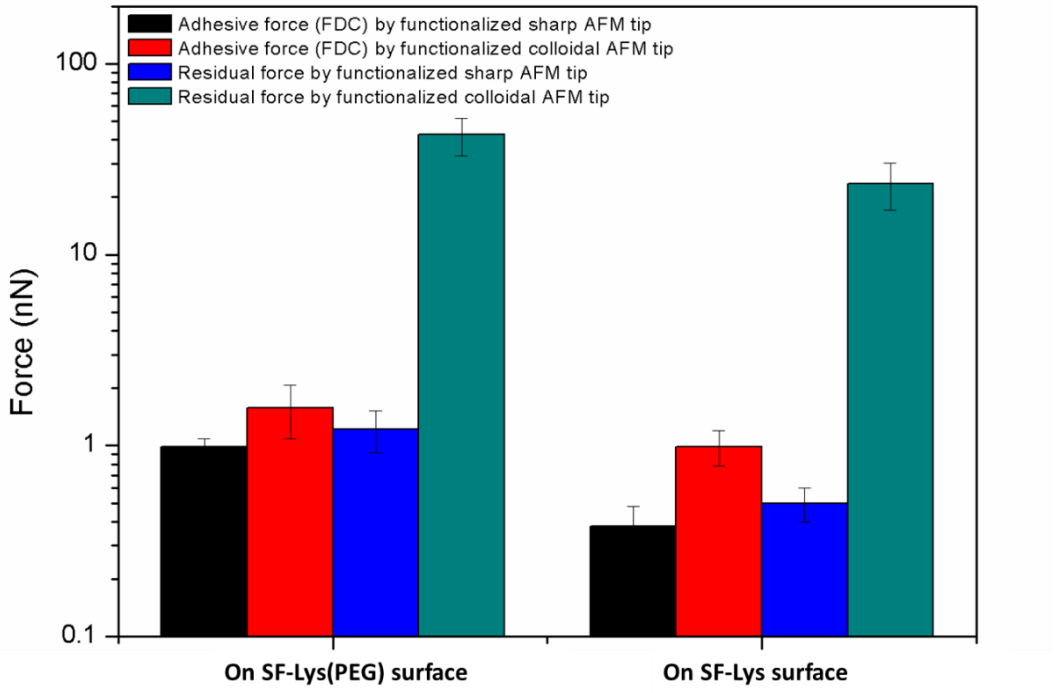

Figure 1.7 Adhesive forces and residual forces between the functionalized colloidal and sharp AFM tips and each target silk ionomer surface SF-Lys[PEG] and SF-Lys in the fluid condition. Each bar is represented as means ± STD, n = 10.

Under liquid-film, the interfacial energy of SF-Lys[PEG] surface and SF-Lys surface as measured with the functionalized sharp AFM tip were 15.1 ± 1.6 mJ/m^2 and 6.4 ± 0.52 mJ/m^2, respectively, while the same values measured with the functionalized colloidal AFM probe were much lower, 0.24 ± 0.08 mJ/m^2 and 0.16 ± 0.03 mJ/m^2 (Fig. 5.8a). Additionally, the interfacial strength was much higher for SF-Lys[PEG] surfaces due to the presence of the loose loopy PEG topmost layer which contributes into energy dissipation during the disjoining process.[256]

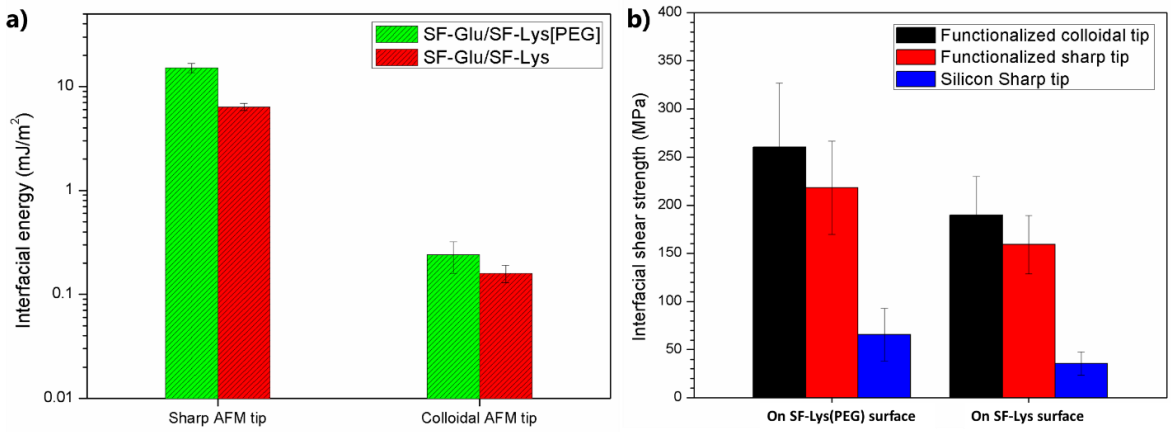

Figure 5.8 a) Interfacial energy of two different SF-Glu functionalized AFM tips (sharp and colloidal tips) on $(SF\text{-}Glu/SF\text{-}Lys[PEG])_5$ and $(SF\text{-}Glu/SF\text{-}Lys)_5$ in fluid condition. b) Interfacial shear strength of $(SF\text{-}Glu/SF\text{-}Lys[PEG])_5$ and $(SF\text{-}Glu/SF\text{-}Lys)_5$ determined by silicon sharp AFM tip, functionalized colloidal AFM tip, and functionalized sharp AFM tip in fluid condition. Each bar is represented as means ± STD, n = 10.

A significant reduction of the measured values for colloidal tips can be related to the lower contribution of the uneven surface topography with grainy texture to the contact areas (fraction of microns) that results in overvaluation of the true contact area under very low local pressure and minute silk surface deformations with colloidal probes.[257,258,259] Another possibility is that the effective tip contact area was overestimated using the DMT model due to the effect of substrate interactions. In the case of large contact areas relative to film thickness, it has been shown[260] that the adhesion mechanism between a film and indenter can depart dramatically from typical adhesion models, though such considerations are beyond the scope of this study.

The overall values of interfacial energies measured here are lower than the values of common polymer surfaces such as SF itself in of 41.0 mJ/m^2, Poly(methyl methacrylate) (PMMA)=38.1 mJ/m^2, Polybutylene succinate (PBS)= 57.2 mJ/m^2, and Polydimethylsiloxane (PDMS)=20.0 mJ/m^2.[261,262,263,264] Moreover, the presence of amine groups in the silk backbone with specific group surface energy contribution of 50.0 mJ/m^2

and PEG segments with group contribution of 58.2 mJ/m^2 should increase the effective surface energy even more.[265,266]

On the other hand, it is important to note that in our experiments we measured interfacial energy related to surface energy at the solid-liquid interface, in contrast to solid-vapor energy which is usually measured and reported in literature. In fact, the interfacial energy of SAMs exhibits lower values in the range of 0.5-8 mJ/m^2 in liquid[169] and the interfacial energy of some natural composites such as starch and cellulose-based materials showed values as low as 0.6-2.3 mJ/m^2.[267,268]

In addition, the interfacial shear strength can be calculated as a function of the contact area, which was determined through the DMT contact model.[254] In this theory, the interfacial shear strength τ was determined by:

$$\tau = \frac{F_0}{\pi a_0^{\,2}} \quad (2)$$

where τ is the interfacial shear strength, F_0 is the residual force (frictional force at zero load), and a_0 is the radius of contact at zero load.[269]

The calculated values of interfacial shear strength, determined by this approach using SF-Glu functionalized AFM tips, varied by the type of LbL silk ionomer surfaces (Fig. 5.8b). First, the overall interfacial shear strength of silk ionomer surfaces was 3 to 6 times higher than that measured for mating stiff silicon oxide surfaces due to the presence of intimately interacting silk surfaces. The shear strength measured here was in the range of 150-250 MPa, comparable to those reported for a variety to different biopolymer nanocomposites

in the range of 20-700 MPa[270,271] or for the shear strength of carbon nanotubes (CNTs)-reinforced polymer nanocomposites in the range of 35-380 MPa.[208,209,272,273]

Next, we observed that SF-Lys[PEG] surfaces had a higher interfacial shear strength than SF-Lys surfaces, for either colloidal or sharp probes (Fig. 5.7b). Similar to the differences in adhesive forces, we suggest that the higher shear strength of PEG-enriched surfaces was caused by the interactions of the overlapped swollen and loopy PEG segments and shearing of asperities of grainy surfaces from opposite surfaces during shearing deformation, in addition to strong ion pairing of oppositely charged surfaces. Additional contributions can come PEG groups acting as hydrogen bond acceptors to various amino acid residues (e.g. serine, tyrosine) side groups of SF-Glu surfaces or the amides in the silk fibroin backbones. Such complementary interactions can add a strength component to the adhesion across the mating interfaces.[274]

5.4 **Conclusions**

In conclusion, we measured the adhesive properties and interfacial shear strength of two different LbL silk ionomers, positively charged SF-Lys and the same ionomer modified with PEG, SF-Lys[PEG], as major components for building biopolymer LbL microcapsules with each other and negatively charged silk ionomer, SF-Glu. The role of the ionic pairing between cationic and anionic side groups of silk backbones and the topological interactions of PEG segments has been tested with chemically modified functionalized AFM tips in the normal compression deformation mode and in the shearing sliding mode.

The interfacial shear strength of silk ionomer surfaces determined by the functionalized colloidal AFM tip was in an agreement with those expected for various synthetic and biopolymer surfaces reported to date. We observed that strong interactions between cationic and anionic silk ionomers resulted in extremely high values of the friction coefficient (above 1 in dry state and 0.6 in the liquid environment) and enhanced adhesive interactions. Moreover, we observed that the modification of silk ionomer surfaces with PEG segments resulted in greatly enhanced adhesive forces and the interfacial shear strength up to 300 MPa in comparison with the interacting surfaces mediated only by complementary Coulombic interactions without any presence of the PEG loops. These observations will be important for selection of natural components and conducting their functionalized modifications for the fabrication of LbL coatings, films, and thin-shell microcapsules with enhanced mechanical stability, shear strength, robustness, and delamination limits for cell engineering and synthetic cell engineering.

CHAPTER 6. TUNABLE INTERFACIAL PROPERTIES IN SILK IONOMER MICROCAPSULES FROM TAILORED MULTILAYER INTERACTIONS

6.1 Introduction

Despite the wide range of microcapsules made from synthetic materials, the possibility of utilizing microcapsules in biological settings have driven a need for materials that are both biocompatible and biodegradable, particularly for any potential in vivo (e.g. medical) application[275]. Some biopolymers (such as proteins), however, are incredibly complex, consisting of hundreds or thousands of precisely ordered residues[276,277], as opposed to most commonly used synthetic polymers, which consist of 1-2 repeat units arranged in a comparatively simple ordering. This can cause complex protein secondary and tertiary structures, leading to major changes in physical properties which can be challenging to predict a priori. In contrast, effective microcapsules need to have controlled, predictable properties in order to release their payloads at specific points.

This work makes use of silk ionomers, as they have shown a great deal of potential as biocompatible encapsulation materials. The silk ionomers in this study utilized chains of poly-L-glutamic acid to generate an anionic silk ionomer species (SF-PG) and chains of poly-L-lysine to generate a cationic silk species (SF-PL). In addition, we utilize a variant of the SF-PL silk ionomer that has been modified with an additional block of polyethylene glycol (PEG) to create a cationic silk ionomer with partially blocked positive charge sites (SF-PL-b-PEG). This cationic silk ionomer variant has been demonstrated to be

substantially more cytocompatible than the unmodified cation silk ionomer, likely due to the PEG block preventing adherence of the poly-l-lysine chain to wall of cells.

PEG has long been used as an antibiofouling coating because it resists the adsorption of free proteins in serum.[278,279] However, while there have been some studies that address the effect of PEGylation on the properties of responsive structures,[280,281,282] there has been less focus on how PEG copolymers affect the performance of polyelectrolyte multilayers as responsive devices. In particular, the impact of PEGylation on the organization of the multilayers and the subsequent effect on mechanical strength and toughness is largely unexamined in the majority of reports that utilize the technique. This report demonstrates the results of PEGylation and contrasts it to variations due to changes in processing parameters using low grafting silk ionomers as a model system.

These silk ionomers are used to fabricate nanoshells through a solution-based LbL process. We studied the effect of various preparation methods on the final properties of the microcapsules. First we prepared microcapsules using a synthetic polyelectrolyte pre-layer, which is a commonly used method to promoted adhesion to a silica core. Next, we compared the effect of using a standard neutral pH (pH 7) buffer vs using a mildly acidic buffer (pH 4) during the deposition of the multilayers. The radius of the swollen microcapsules was observed under optical microscopy and the permeability of the microcapsules was measured by fitting the results from a fluorescence recovery after photobleaching experiment in a variety of different buffers. The stiffness of the microcapsules was determined via atomic force microscopy-assisted indentation experiments. The results of these various tests indicate that the microcapsules have a relatively open microstructure that becomes denser at acidic pH, where some of the anionic

charge can be reduced. In the addition, the different processing strategies to produce the microcapsules lead to different microstructures, which play a critical role in determining the ultimate properties of the microcapsules. ‘

6.2 **Results and Discussion**

6.2.1 Silk ionomers

The materials chosen to build the microcapsules in this study were chemically modified silk fibroin molecules. These silk fibroin species are grafted with short, oligomeric chains consisting of an amino acid with either an amine or carboxyl group as it’s R group. Because these polypeptides sequences are weak polybases or polyacids (depending on the species), and thus contain a cationic or anionic charge, these materials are referred to as silk ionomers. In this study, we use silk fibroin grafted with poly-l-lysine (SF-Lys) and silk fibroin grafted with poly-l-glutamic acid (SF-GLU), which form positively and negatively charged molecules, respectively. In addition, we use a variant of the positively charged silk ionomer species that consists of silk fibroin grafted to poly-l-lysine-block-polyethylene glycol (SF-Lys-PEG). In this work, all of the grafted poly-l-lysine and poly-l-glutamic acid groups are made from 20 repeat units of their component amino acids, and are all grafted to the serine and glutamic acid residues of the silk fibroin backbone. This length and grafting density is significantly shorter than silk ionomer species that have previously been utilized in making microcapsules, and thus have a lower charge density per molecule. These molecules have been shown to be significantly more cytocompatible when used as cellular coatings and have around 1-2 orders of magnitude less substituted amino acids than the highly grafted silk ionomer species.

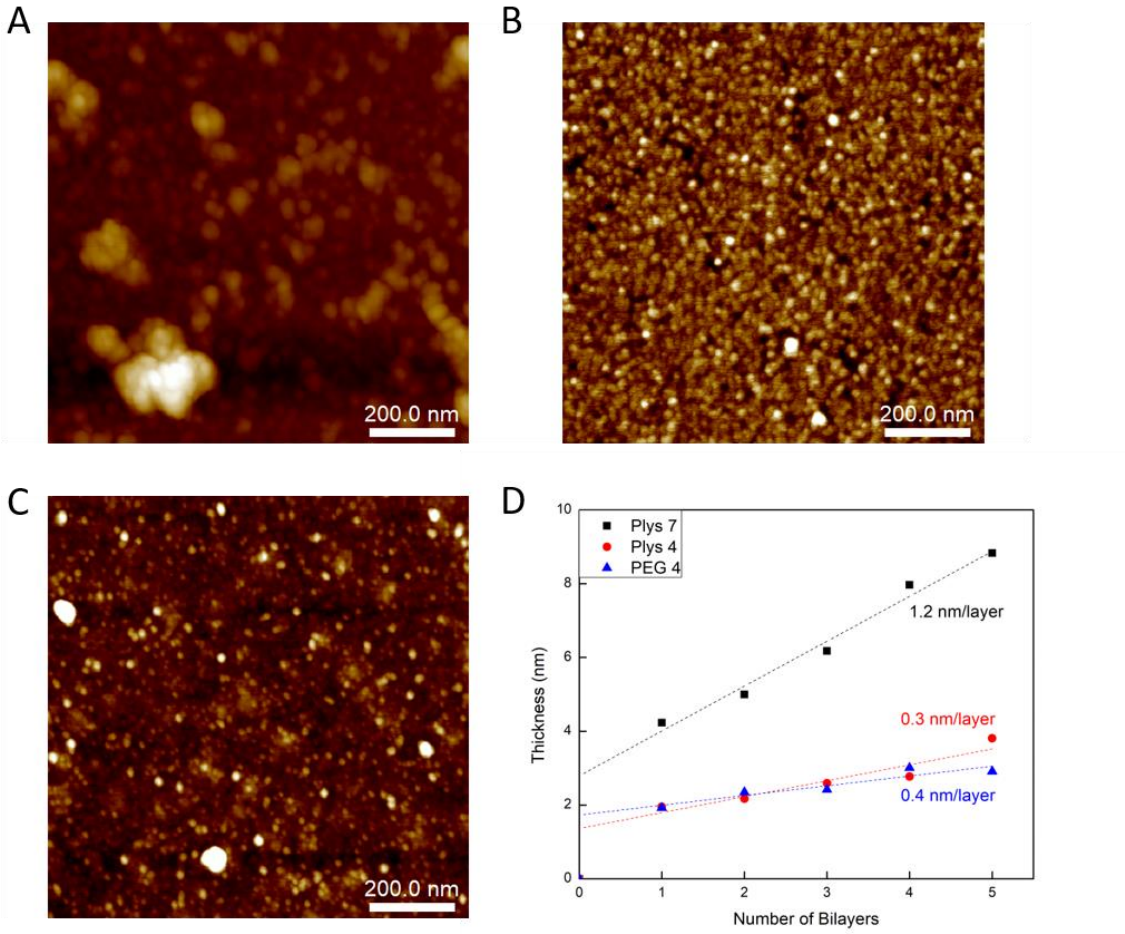

Figure 6.1 Planar films consisting of 5-bilayers of A) SF-PL,SF-PG prepared in pH 7 buffer, B) SF-PL,SF-PG prepared in pH 4 buffer, C) SF-PL-PEG,SF-PG prepared in pH 4 buffer. D) Thickness of these films as determined by spectroscopic ellipsometry.

These silk ionomers were formed into multilayered structures on planar silicon substrates. These multilayers began with the cationic silk ionomer species (SF-PL or SF-PL-PEG), followed by the anionic silk ionomer species (SF-PG). We tested the effect of buffer condition as well, using either pH 7 buffer or pH 4 buffer in both the silk ionomer solutions and the rinsing solution. It was found that using deionized water for the silk ionomer solution lead to a patchy film structure, indicating weak adsorption to the silica, in addition to a significantly more porous morphology. After deposition of the anionic silk ionomer

solution, the films were rinsed in either deionized water (for the pH 7 buffer films) or 0.1 mM HCl solution (for the pH 4 buffer films) to remove excess salt ions, and the film thickness was determined using a spectroscopic ellipsometer. The morphology obtained from the non-PEGylated silk ionomers in pH 7 buffer show a significant degree of roughness (~10.9 nm RMS over 1 μm^2) with a large number of aggregates present on the film surface. By instead using a pH 4 buffer, the films morphology shifts significantly to significantly smoother structure (~0.9 nm RMS over 1 μm^2) with finer features and few aggregates. The PEGylated silk ionomer films show an intermediate morphology with the fine features and low surface roughness (~1.4 nm RMS over 1 μm^2), but a larger degree of aggregates. By plotting the growth of the films, we see a similar trend amongst all species: a larger initial bilayer, followed by a relatively shallow growth of the layers. In addition, it of interesting to note that both silk ionomers grown in pH 4 buffers have a similar growth rate that is much smaller than the growth rate associated with the bilayers grown in the pH 7 buffer. This may be the cause of the finer morphology seen in the AFM images, though previous reports typically have indicated that hydrogen-bonded films typically have smother morphologies in general.

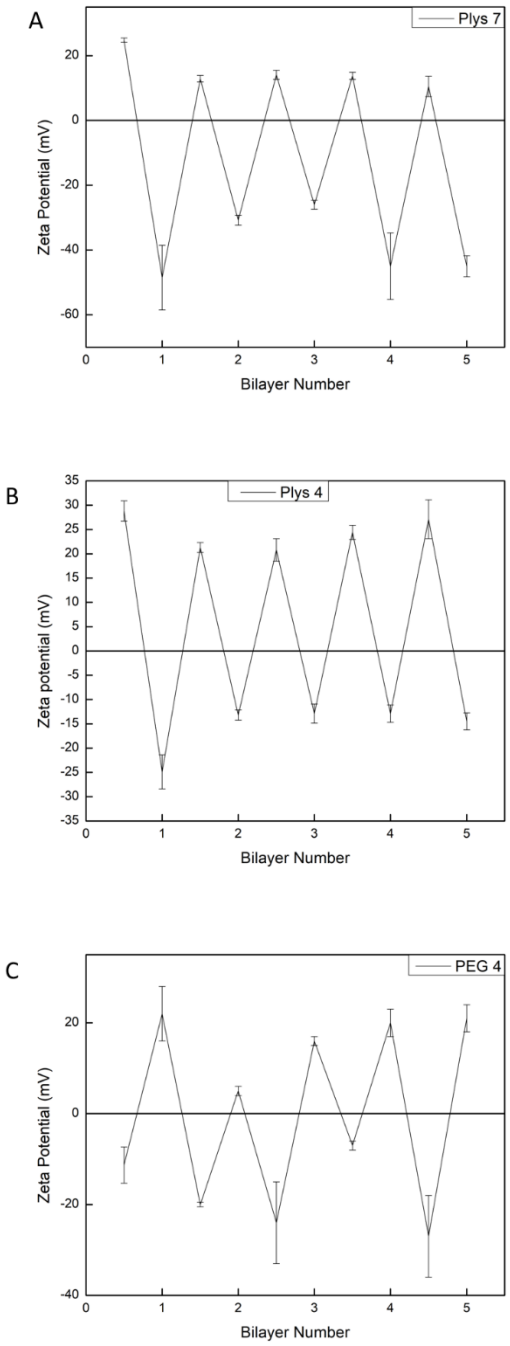

Figure 6.2 Zeta potential measurements for the assembly of (A) Plys-7,(B) Plys-4, and (C) PEG 4 5 bilayer nanoshells onto silica cores.

6.2.2 pH-Responsive Modulus Behavior of 2-bilayer Microcapsules

In the course of designing a microcapsule structure, careful consideration must be given to the minute details of processing conditions. From our previous reports on silk ionomer microcapsules, our group had determined that PEI prelayers can assist with the deposition of silk ionomer films onto silica cores and that acidic pH conditions would lead to an increase in the planar film thickness deposited onto silicon. It is a mistake, however, to suppose that one can alter the processing conditions without any impact in the final performance of the microcapsules.

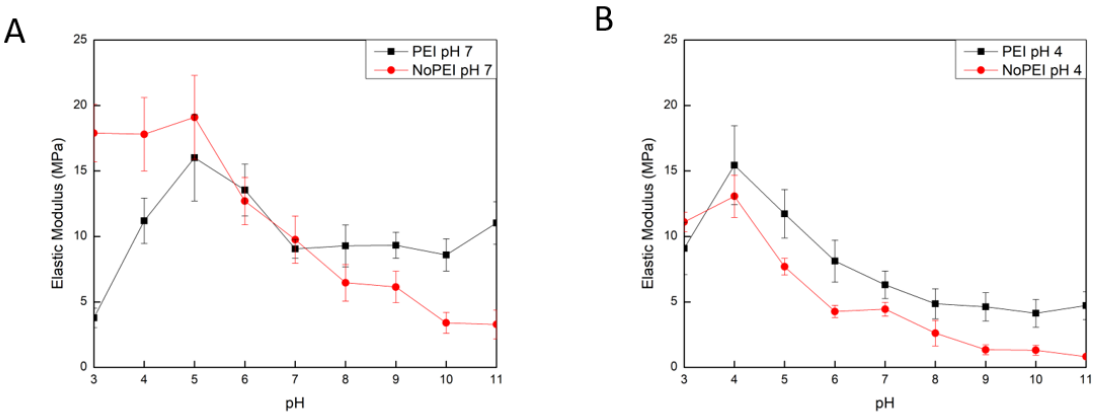

Figure 6.3 Elastic modulus response to pH conditions for 2-bilayer microcapsules prepared in A) pH 7 buffer and B) pH 4 buffer (n = 10).

Indeed, from a study on the stiffness of hydrated microcapsules, we can see that the pH responsive behavior of the microcapsules can vary dramatically depending on their deposition conditions. The range of modulus for all tested conditions is relatively large, from a high of 19.1 MPa in the "NoPEI pH 7" sample at pH 5, to a low of 0.8 MPa in the "NoPEI pH 4" sample at pH 11, which translates to a softening of ~24x. The modulus range within individual samples is much smaller, typically around 3-6x from the minimum to the maximum modulus, but the "NoPEI pH 4" sample is a notable exception in that it

has a modulus shift of more than 15x from its peak to its lowest measured modulus. All microcapsules were found to have a peak modulus when measured in either a pH 4 or pH 5 buffer, which corresponds to the isoelectric point for the silk ionomers.

The presence of a PEI prelayer appears to lead to an overall decrease in the responsive range of the microcapsules, a trend that is particularly noticeable in the samples prepared in pH 4 buffer. Surprisingly, the PEI layer does not confer a substantial increase in the modulus, which might be expected due the increase in amine-carboxyl bonds possible in the microcapsules. This result likely has a simple explanation, however, because the PEI layer is expected to be exceptionally thin in comparison with the overall microcapsule thickness (less than 5%). Despite this, the PEI-primed microcapsules prepared in pH 11 buffer demonstrate a substantially stiffer modulus (at least double, and often much more) than all other microcapsules at pH 11. At this pH, much of the excess charge from the PEI layer will begin to weaken as the amine groups are further deprotonated. This likely leads to a stronger interaction between the anionic silk ionomers and the PEI prelayer, causing a stiffening in the entire microcapsule. This effect can be observed in the PEI-primed microcapsules deposited in the pH 4 buffer as well, but the magnitude of the modulus is significantly reduced. In this case, the PEI prelayer is much more limited in its ability to influence the highly negatively silk ionomers.

The effect of the deposition pH buffer likewise demonstrates a dramatic impact of the microcapsule properties. At most pH environments, microcapsules deposited in pH 4 are more compliant than those deposited at pH 7. This is likely due to an increase in the amount of uncompensated anionic silk ionomers. Evidence for this this explanation can be seen in the position of the peak moduli for the different samples. While all microcapsules reach

their peak modulus near the Pka of the polyglutamic acid, the microcapsules prepared in the pH 7 buffer have peaks at pH 5, while the microcapsules prepared in the pH 4 buffer have peaks at pH 4. This indicates that more of the polyglutamic acid must be protonated in the latter microcapsules in order to reach the optimum charge concentration, suggesting that the microcapsule pH-responsive mechanical properties are dictated by the ratio of anionic to cationic silk ionomers deposited in the membrane.

6.2.3 Swelling and Roughness of Microcapsules

To observe the effects of pH on the morphology of microcapsules, microcapsules with 5 bilayers were assembled. These microcapsules had a larger membrane wall thickness, which allowed for a more accurate determination of the roughness and thickness of a sample under AFM. The swelling experiments were performed by comparing the effect of two different buffer environments on the microcapsules. The first buffer is a buffered oxide etch with a concentration of 14 M NH_4F and 1 M F, which is the etchant used to etch the silica cores. This buffer has a large ionic strength and a pH near the isoelectric point of the silk ionomer multilayers (~pH 4-5). This solution is expected to lead to the largest contraction of microcapsule diameter. The other solution is deionized water, which is used to thoroughly rinse the microcapsules to remove excess ions prior to drying. Because the water has a pH of 7, the silk ionomer multilayers should present a highly negative charge, and because the solvent lacks any counterions, the charge should thus be highly repulsive. In this state, the microcapsules should be highly swollen.

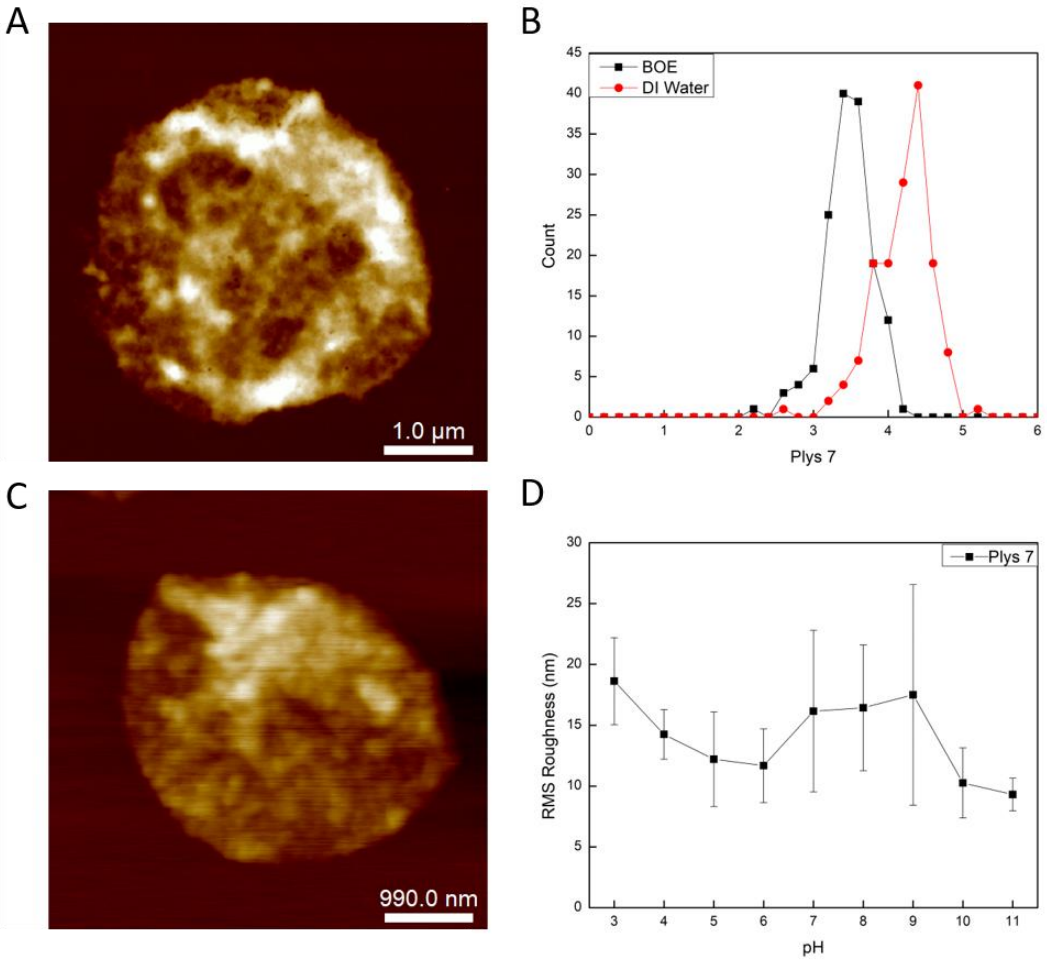

Figure 6.4 Results of 5-bilayer SF-PL,SF-PG (prepared in pH 7 buffer) microcapsules. AFM topography of microcapsules scanned in A) ambient conditions and C) DI water. B) Histogram of microcapsule diamter after core removal and after rinsing in DI water. D) Roughness of microcapsule surface under different pH conditions.

The first sample tested is the 5-bilayer microcapsule batch of unmodified silk ionomers prepared in a buffer with a pH of 7. Immediately after the silica cores are dissolved, the microcapsules shrink from a diameter 4 um (the diameter of the silica cores) to a diameter of 3.4 +/- 0.32 um. Upon heavy rinsing with DI water, the microcapsules swell to a diameter of 4.1 +/- 0.37 um, which is very close to the original size. This effect indicates that the

silk ionomers exist in an extended conformation at pH 7 (even at the microcapsule surface) and undergo a shift towards a more compact conformation at lower pH conditions. Previous reports have demonstrated the shift of poly-l-glumatic acid from an extended, globular state to a more compact form composed of a-helices and b-sheets at neutral and acidic conditions, respectively. The overall trend in the roughness of these microcapsules is not entirely clear, but a general downwards trend from the acidic pH conditions can be observed.

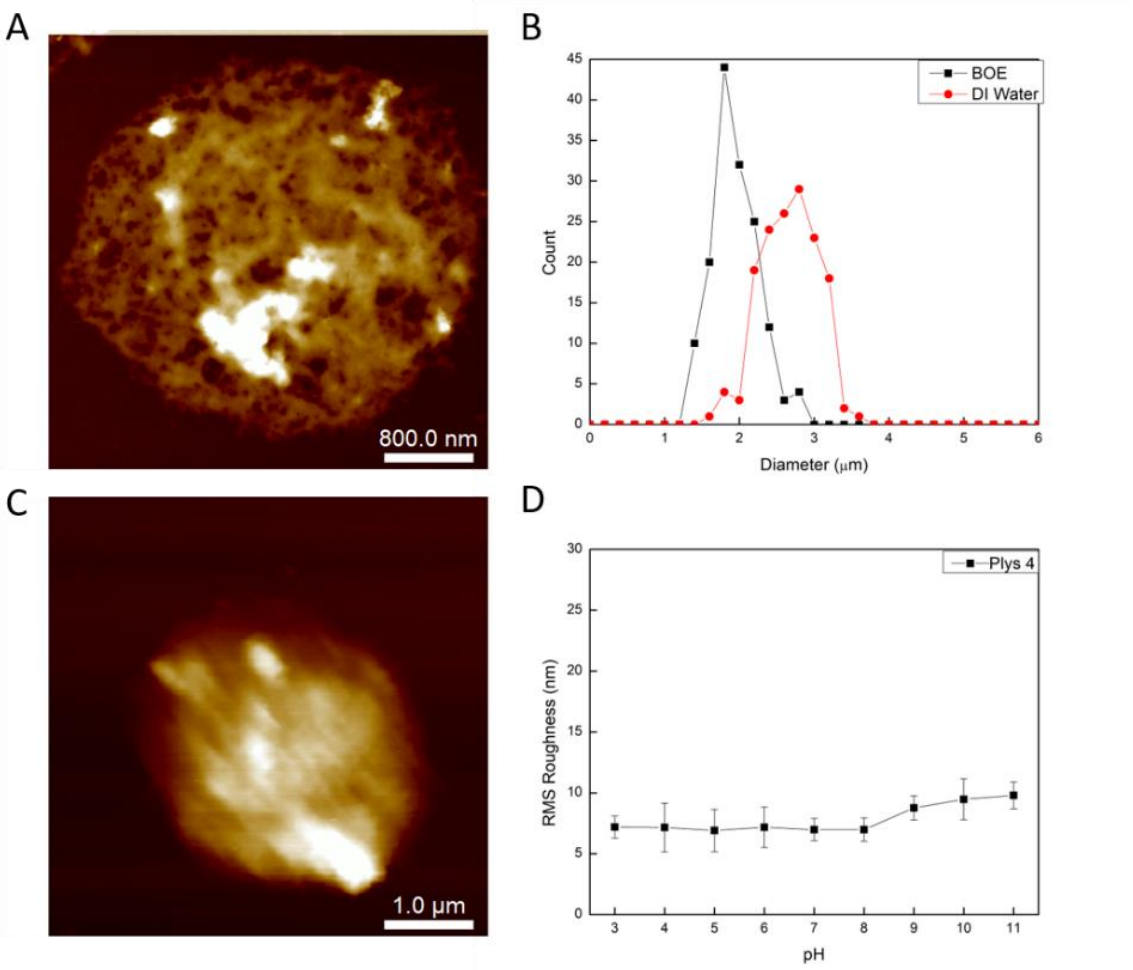

Figure 6.5 Results of 5-bilayer SF-PL,SF-PG (prepared in pH 4 buffer) microcapsules. AFM topography of microcapsules scanned in A) ambient conditions and C) DI water. B) Histogram of microcapsule diamter after core removal and after rinsing in DI water. D) Roughness of microcapsule surface under different pH conditions.

The next sample is the 5-bilayer microcapsules of unmodified silk ionomers prepared in an acidic buffer with pH 4. In these microcapsules as well, we notice an immediate shrinkage of the capsule diameter once the silica is dissolved in the etchant down to an average diameter of 1.8 +/- 0.3 um. Likewise, there is a considerable degree of swelling after being rinsed by DI water, but only to a diameter of 2.6 +/- 0.3 um, which is even lower than the shrunken diameter found in the pH 7 prepared microcapsules. This effect is likely caused by the high degree of uncompensated anionic charge in the microcapsule layers. Because the microcapsules are prepared in an acidic buffer, the amount of carboxyl-bearing silk ionomers deposited is higher than in neutral buffer due to the reduction in self-repulsion. Once these capsules are crosslinked and exposed to DI water, the multilayer structure swells until the force from the charge repulsion is opposed by the strain in the microcapsule crosslinks. This helps to explain why these microcapsules are quite unstable and require a longer crosslinking time to maintain integrity through the release process. Interestingly, the apparent trend in the microcapsules roughness is inverted from the trend in the pH 7 prepared microcapsules. Here we see that the roughness is fairly uniform up until the higher pH buffers (pH ~9). This is likely due to the additional contribution of the amine groups becoming deprotonated and thus losing their cationic charge.

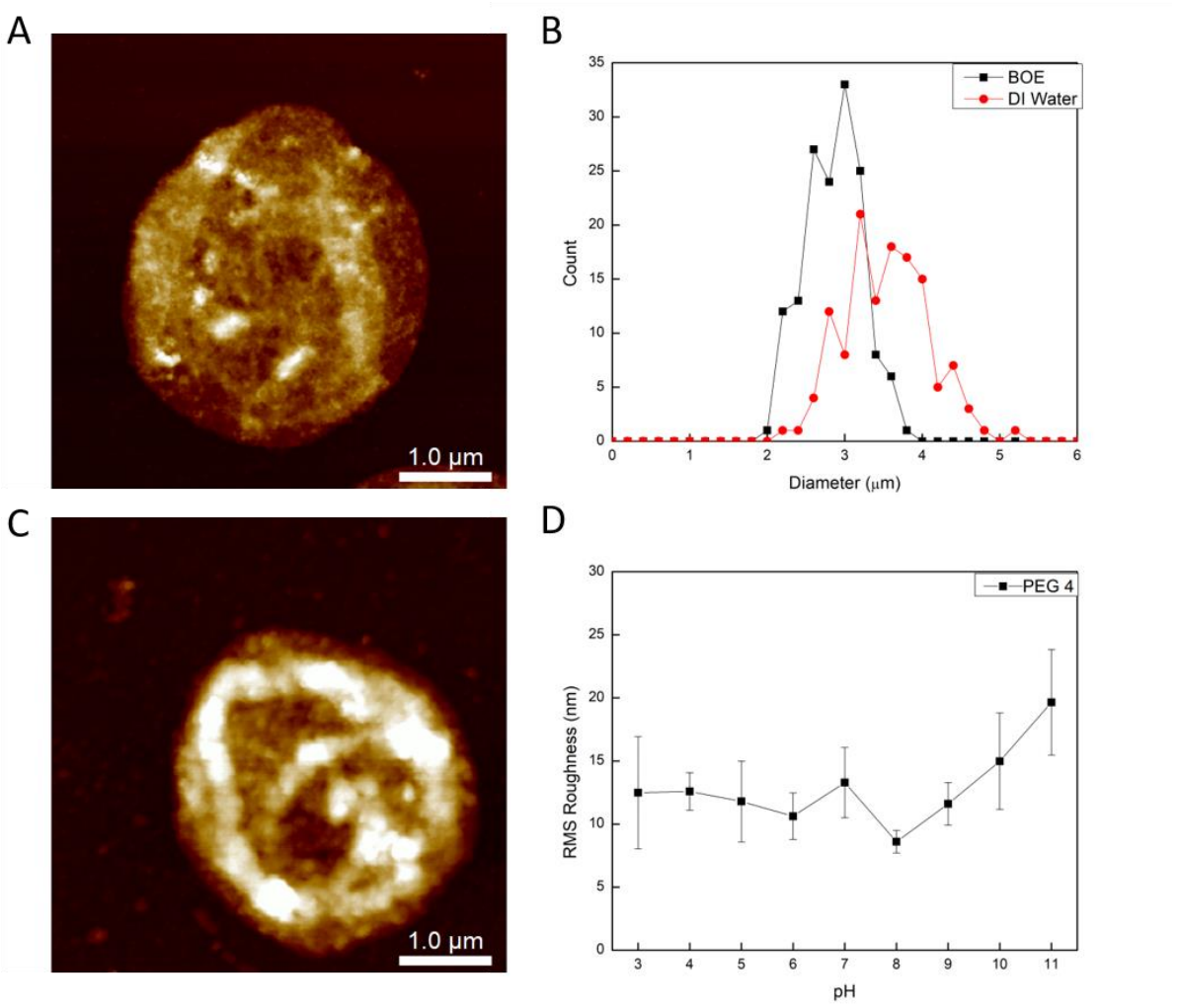

Figure 6.6 Results of 5-bilayer SF-PL-PEG,SF-PG (prepared in pH 4 buffer) microcapsules. AFM topography of microcapsules scanned in A) ambient conditions and C) DI water. B) Histogram of microcapsule diamter after core removal and after rinsing in DI water. D) Roughness of microcapsule surface under different pH conditions.

The final case studied is that of the 5-bilayer microcapsules made from the PEG-grafted silk ionomers in a pH 4 buffer. Like the other two samples, these microcapsules also demonstrate a substantial shrinkage after the silica cores are dissolved, with an average diameter of 2.8 +/- 0.4 um. And again mimicking the other cases, after rinsing with DI water, the microcapsules exhibited a modest degree of swelling to 3.4 +/- 0.5 um. It is interesting to note that both the shrunken and swollen diameters fall between the diameters of the previous two cases. This indicates that the PEG group prevents a large degree of SF-

Glu adsorption during the LbL deposition process, likely by screening the cationic charge of the amine groups and thereby limiting the electrostatic attraction to the anionic silk ionomer species. These microcapsules also exhibit a similar roughness trend to that of the pH 4 prepared microcapsules, but it should be noted that the PEG modified microcapsules exhibited a substantially higher roughness (and indeed, the highest roughness of all three cases tested).

6.2.4 pH-Responsive Modulus Behavior of 5-bilayer Microcapsules

Now we can compare how the mechanical properties of the microcapsules change at higher numbers of bilayers. First, we can see that the SF-Lys/SF-Glu sample prepared in a pH 7 buffer demonstrates a similar trend as was observed for the thinner microcapsules. In addition, the magnitude of the modulus is roughly the same for the 2 bilayer and 5 bilayer samples, indicating that the two microcapsules are likely structurally similar (i.e. the deposition of silk ionomers does not vary significantly with bilayer number).

The SF-Lys/SF-Glu microcapsules prepared in a pH 4 buffer also show a similar trend to their 2-bilayer versions, but there exist a number of key differences. First, we can see that the peak modulus value occurs at a lower pH value than previously observed (pH 3 vs pH 4). This is likely due to the increase in uncompensated SF-Glu anionic charge, which requires an increasingly acidic environment to shift the microcapsules towards charge neutrality. Second, we note that the overall modulus has been reduced across the whole pH range, and in fact has a lower modulus than any other tested microcapsule across the entirety of the pH range. This result indicates that the microcapsule microstructure is not

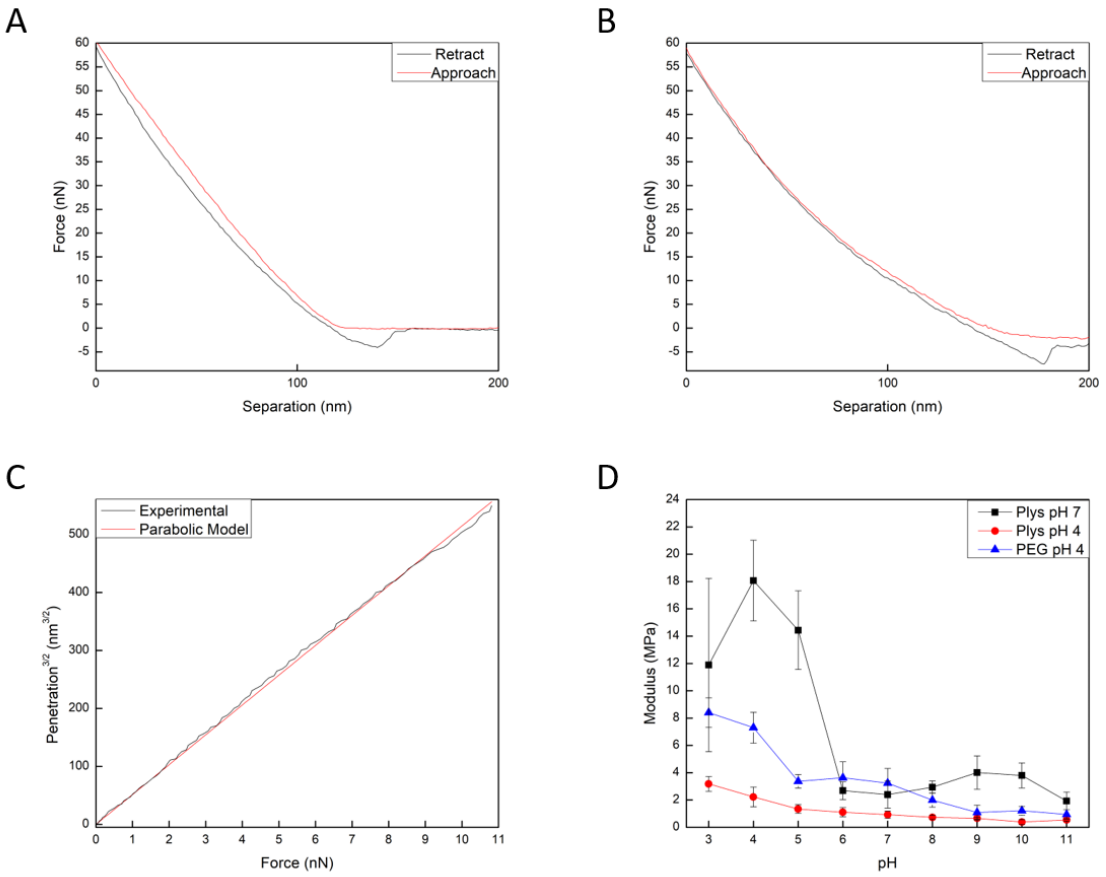

Figure 6.7 Force-separation curves for Plys-7 samples in a (A) pH 4 and (B) pH 11 buffer. (C) Penetration$^{3/2}$ vs force curve for Plys-7 with applied Hertzian fit. (D) Comparison of modulus for different pH values (n = 10).

tightly held together despite the long crosslinking times used to prepare these microcapsules. The highly swollen silk ionomers will naturally exhibit a lower modulus due to the increased water content of the hydrogel structure.

Here we also compare the effect of the addition of PEGylation in the final properties of the microcapsules. First, it should be noted that PEGylated microcapsules prepared in a pH 7 buffer were found to be exceptionally unstable and were not able to be stabilized in deionized water (even with crosslinking). This is thought to be due to the increased charge screening provided by the PEG branching of the cationic silk ionomers, which may lead to

an overall reduction of polylysine groups available for crosslinking. Thus, the microcapsules studied here are formed in a pH 4 buffer. These were also found to be relatively unstable in DI water, so the crosslinking time for these samples was increased to 1 day.

The PEGylated microcapsules formed under pH 4 conditions were found to exhibit a noticeable pH dependent stiffness, though the magnitude of stiffness change was still less than that found in the case of the two bilayer samples. Here the stiffness appears to monotonically decrease as the pH is increased, with values ranging from 3 MPa at pH 3 to 0.5 MPa at pH 11. The most likely cause for this change is the increasing negative charge density in the microcapsules due to an excess in the amount of SF-L-polyglutamic acid. This implies that the dominant factor in the stiffness determination is the degree of charge repulsion within the crosslinked network, which is minimized at low pH conditions. It is interesting to note that the mechanical behavior of the PEGylated microcapsules show a similar trend to the microcapsules prepared in pH 4 buffer, though the magnitude is much higher in the PEGylated microcapsules. It seems likely that the buffer used during preparation controls the overall pH-responsive modulus curve shape, and that the additional grafting of PEG molecules mitigates the large drop in stiffness. This latter effect is either due to the screening of the poly-l-lysine charge from the poly-l-glutamic acid (thus caused less anionic silk ionomer deposition) or through the engagement of a hydrogen-bonding type growth regime due to the PEG acting as hydrogen bond acceptors for the protonated poly-l-glutamic acid.

6.2.5 Permeability Study

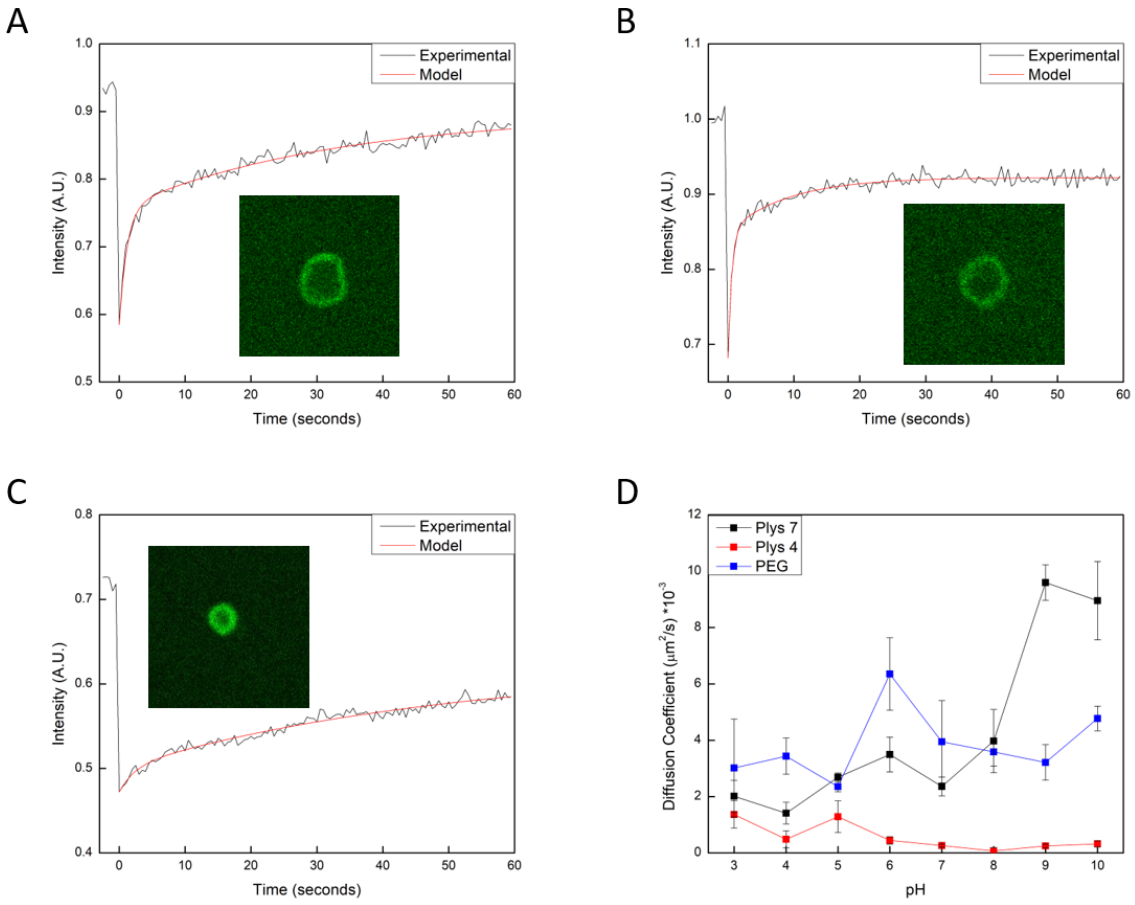

Figure 6.8 FRAP recovery curves for (A) Plys-7, (B) PEG-4, and (C) Plys-4 at pH 4. Inset: Corresponding unbleached microcapsules. (D) Diffusion recovery times obtained from modelling FRAP data at different pH (n = 3).

These five bilayered structures were studied using fluorescence recovery after photobleaching (FRAP) experiments to assess their permeability. Data from low molecular weight dyes (~4-20kDa Dextran with FITC label) demonstrated diffusion times that were too fast to be captured using this setup, which likely indicates a rather porous structure in the microcapsules. 70kDa dextran with FITC label could probe the pH dependent permeability for the microcapsules. Interestingly, the Plys pH 7 samples were found to demonstrate a pH-dependent diffusion resistance response curve that is reminiscent of the

stiffness response curve for the two bilayer samples (i.e. a peak near the isoelectric point of the silk ionomers). This indicates that these capsules have an increase in effective path length through the membrane, which is potentially caused by an increase in density at pH 4.

PEGylated microcapsules demonstrate a relatively small diffusion resistance across the entirety of the pH range. One interesting feature of these microcapsules is that the diffusion resistance does not appreciably change over the entire pH range (though a small, but statistically significant uptick can be seen around pH 9). It is possible that this behavior is due to the charge screening provided by the PEG, which may prevent the cationic silk ionomers from binding tightly to the anionic silk ionomers and allow the dextran molecules to temporarily disrupt these bonds.

The results obtained from the non-PEGylated silk ionomers prepared in pH 4 buffer exhibit a stark contrast to the other microcapsules. The most immediately apparent feature is the large increase in the diffusion resistance on the Plys 4 microcapsules, which are ~5x (at their peaks) more resistant to diffusion than the other microcapsules. In fact, over the majority of the pH range, these microcapsules consistently exhibit a larger diffusion resistance. These microcapsules also exhibit and unexpected deviation from the microcapsules prepared in pH 7 buffer: the peak diffusion resistance occurs at pH 8 rather than pH 4. Interestingly, this behavior likely has the same explanation as for the mechanical properties. When the microcapsules swell, it directly increases the path length of the dextran molecules, which will increase the diffusion resistance as long as the change in thickness more than offsets the effect of the reduction in density. This then explains the drop in resistance above pH 8 as a drop in density that overcomes that increase in thickness.

6.3 **Conclusion**

The results presented in this work demonstrate the challenges and unique properties that can come from seemingly minor process changes in preparing structures from biopolymers. While this suggests that any process involving these biopolymers must deal with several constraints, it also presents the possibility that the properties of a final structure can be modified significantly through minor adjustments in assembly protocol. As shown in this report, changes in surface roughness, swelling, modulus, and diffusion resistance can all be shifted to a relatively large range of values.

Since the silk ionomers presented here are promising biocompatible materials, the authors suggest that future research into these materials will do well to ascertain the desired physical properties of microcapsules for in vivo models. By using the our own (or similar) processing techniques, microcapsules could be created to fit many different required properties. Additional work can build upon our results presented here by further expanding on the range of physical properties through addition of other materials into the membrane (e.g. inorganic fillers, complementary biopolymers) to extend the utility of these materials to a wider range of needs.

CHAPTER 7. BIMORPH SILK MICROSHEETS WITH PROGRAMMABLE ACTUATING BEHAVIOR: EXPERIMENTAL ANALYSIS AND COMPUTER SIMULATIONS

7.1 **Introduction**

Recently, self-reconfigurable structures of micro-origami type emerged as one of the most promising approaches for the rapid and reproducible fabrication of complex objects with tunable properties and morphologies of both exterior and interior surfaces to render these functions. The self-folding of micro-origami can be triggered by changes in environmental conditions, such as temperature, pH, electrical/magnetic field, or optical excitation.[135,283,284,285,286,287]

These systems are usually composed of two dissimilar materials with different swelling properties that results in internal interfacial stresses and shape changes in response to external stimuli. Based on this driving principle, two self-reconfiguration approaches have been developed. One approach utilizes solid patches connected by active hinges, usually employing bimetallic or metal-polymer bilayers, where the patches fold due to the shrinking or expansion of the hinges upon exposure to specific stimuli.[288, 289 ,290] However, this approach is typically achieved using complex, multistep lithographic processes combined with multistep assembly to obtain polyhedral folded structures, and completely sealing the folded patches is also a critical problem for controllable encapsulation and release. The high stiffness and biocompatibility of these 3D structures also limit the application in the biological field. In order to overcome these limitations, another simple

approach has been explored by introducing variable degrees of photo-crosslinking either vertically (bilayer film)[291] or in-plane (patterned films)[292,293] of thermo-responsive gels with reversible bending/unbending behavior.[294] However, this approach usually employs photo-polymerization or utilizes organically soluble polymers to prepare the films, which in turn, limits the applicable materials and processes. The fabricated films are usually hydrogels with hundreds of micrometer thicknesses, limiting biological applications. Therefore, the choice of biocompatible "smart" components for autonomous re-configuration is limited, and easy fabrication with programmable morphology is rarely reported.

In this study, micro-scale autonomous rolling constructs with programmable shape behavior were fabricated from layered, bimorph silk fibroin microsheets, which consist of the highly grafted silk ionomer species discussed in section 3.16. We focus on programming the morphology of the silk-on-silk microstructures and understanding the mechanism of complex self-rolling behavior. Both experimental analysis and theoretical modeling demonstrated how the geometry of the self-rolled structures can be tuned by the layer thickness ratio, aspect ratio and shape of the planar microsheets. We demonstrated that the biaxial distribution of the mismatched stress within the non-uniformly swollen microsheets controls the reconfiguration process and the formation of the final 3D morphology, providing a better understanding and guidelines for the rational design of micro-origami nanomaterials.

7.2 **Experimental**

7.2.1 Materials

Polystyrene (PS) with M_W=250,000 was obtained from Polysciences, Inc. Fluorescent isothiocyanate (FITC), sodium phosphate dibasic and sodium phosphate monobasic were from Sigma-Aldrich. The cross-linker, 1-ethyl-3-[3-dimethylaminopropyl] carbodiimide hydrochloride (EDC), was purchased from TCI. Sodium hydroxide was obtained from EMD. Negative photoresist kit OSCoR 2313 was supplied by Orthogonal, Inc. All the chemicals were used without further purification. The water used in this study was Nanopure water with resistivity of 18.2 MΩ cm (Synergy UV-R, EMD Millipore). Single-side polished silicon wafers of the {100} orientation (University Wafer Co) were cut to a typical size of 10 nm x 20 nm and cleaned in a piranha solution.[295]

7.2.2 Fabrication of silk ionomers-silk fibroin bimorphs

All multilayered films were prepared by the spin-assisted LbL (SA-LbL) technique on a sacrificial substrate.[296,297,298,75] First, a PS pre-layer was deposited on a silicon wafer by spinning a PS solution with different concentration in toluene at 3000 rpm for 30s to stabilize the LbL process. Next, silk-poly-L-glutamic acid (SF-PG), 1 mg/mL prepared in 0.05 M phosphate buffer at pH 5.5, was spun on the PS layer with the same condition, followed by silk-poly-L-lysine (SF-PL) layer deposition as spinning with a 1 mg/mL SF-PL solution in the same solvent. A multilayer $(SF\text{-}PG/SF\text{-}PL)_n$ thin film was obtained by repeating the alternating spinning process. After each layer, 2 wash cycles with phosphate buffer and nanopure water were applied.

The $(SF\text{-}PG/SF\text{-}PL)_n$ films were cross-linked with 1-ethyl-3-[3-dimethylaminopropyl] carbodiimide hydrochloride (EDC) according to established procedures.[299] The film was immersed in 5 mg/mL EDC solution (prepared in 0.05 M phosphate buffer at pH 5.5) for 40 min, then washed with Nanopure water to remove excess coupling agent and spin-dried. Then, silk fibroin aqueous solution (1 mg/mL) was spun on the $(SF\text{-}PG/SF\text{-}PL)_n$ layers at 3000 rpm for 30s, followed by a methanol treatment to transfer the silk coil morphology to silk II structure with β-sheets and a washing cycle with Nanopure water. The β-sheet multilayer was built up by repeating this routine until the desired film thickness was obtained. The thickness of the films and individual layers was measured by a M2000 ellipsometer (Woollam).

7.2.3 Fabrication and treatment of silk microsheets.

Silk micro-patterns were fabricated via single exposure photolithography under cleanroom conditions (Fig. 7.1).[300] A layer of negative photoresist OSCoR 2313 was spun on to the silk film, followed by exposure to UV light with a photomask to facilitate selective crosslinking the exposed portion of the photoresist layer. Followed by further development, the photoresist layer formed inverted micro-patterns on the silk film, working as a shade mask during the following aluminum deposition.

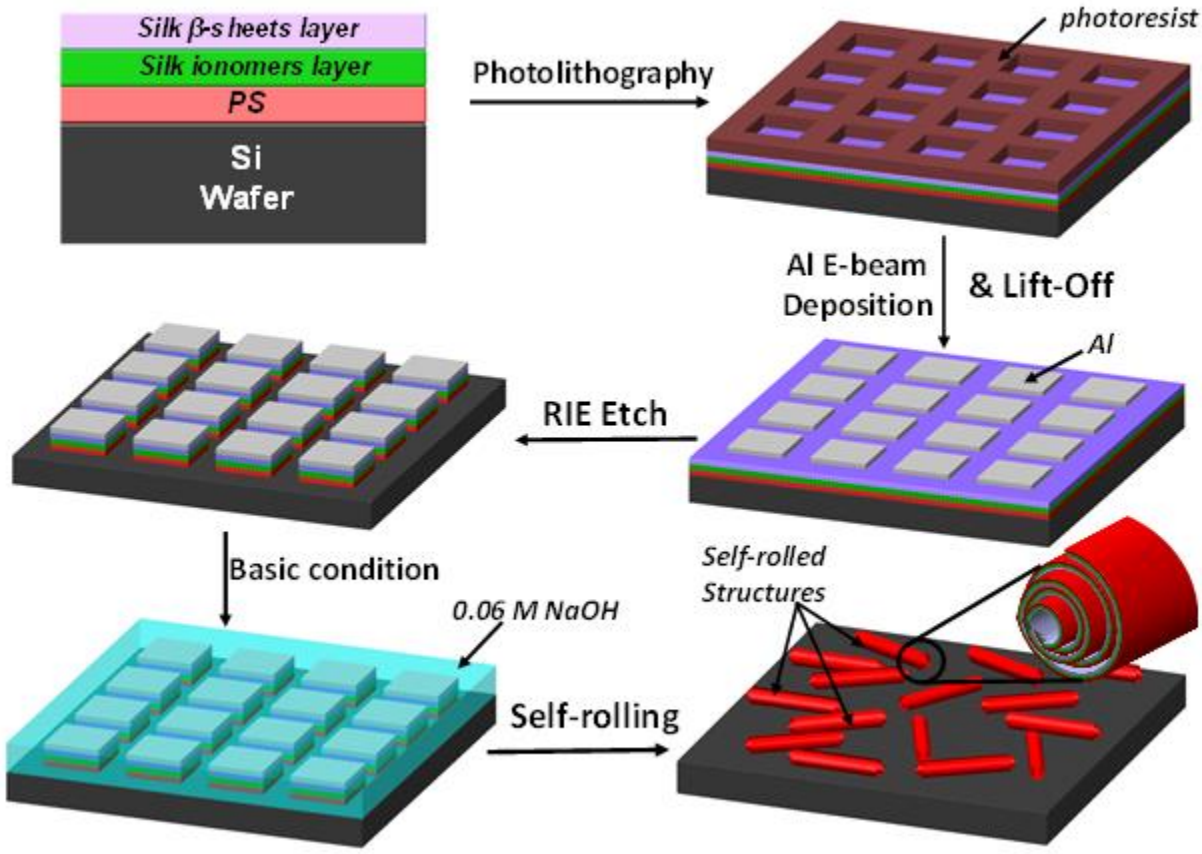

Figure 7.1 Fabrication of silk-on-silk microsheets and self-rolling structures after release. The self-rolled tubes has three layers in the shell, from external to internal are PS pre-layer, silk ionomer layer and β-sheet layer, correspondingly.

A 100 nm aluminum (Al) layer was deposited onto the film using electron-beam evaporator (CHA Industries). Next, a lift-off process was employed to dissolve the photoresist, resulting the Al micro-patterns on the silk film, which protected the covered parts of silk as the film was subject to plasma thermal reactive-ion-etching (RIE), obtained multilayer silk-on-silk micro-patterns. Photomasks with different pattern design were used to fabricate silk micro-sheets with various geometries. Finally, the bimorph silk microsheets were immersed in 0.06 M NaOH solution to selectively induce the swelling of the silk ionomers layer and trigger the self-rolling of the 2D microsheets after the Al protecting layer was dissolved by immersing into the NaOH solution (Fig. 7.1).

In this work, microsheets with various thickness and aspect ratio (thickness ratio of PS layer/ silk ionomers layer: 0.45 to 4.0, β-sheet/ silk ionomers layer thickness ratio: 0.2-1.0 and microsheet with an aspect ratio: 1:1, 1:2, 1:4 1:8) were fabricated to explore the tuning of the shape reconfiguration from planar microfilms to 3D constructs.

7.2.4 Confocal Laser Scanning Microscopy (CLSM) and Optical Microscopy

Confocal images were obtained by LSM 510 Vis confocal microscope equipped with 63x1.4 oil immersion objective lens (Zeiss). Silk self-rolling structures were visualized by adding FITC solution, 1 mg/mL prepared in phosphate buffer with pH 5.5, to the microtube suspension in Lab-Tek chambers (Electron Microscopy Science). Excitation/emission wavelengths were 488/515. To investigate the reversible pH-triggered rolling/unrolling property, a droplet of micro-tube suspension with FITC in 0.06 mol/L NaOH was added to a Lab-Tek chamber. After CLSM images were taken, the liquid in the chamber was removed. Then, the chamber was refilled with phosphate buffer with pH 5.5 and allowed to settle for 20 min before taken CLSM images. This alternative pH treatment cycle was repeated several times to test the repeatability of the shape-changing process. Optical images were collected during the self-rolling process using a Leica DM4000 M optical microscope to record the formation of micro-tubes. All the images were acquired under bright field microscopy conditions with 10x, 20x, or 50x magnifications.

7.2.5 Neutron reflectometry (NR)

Neutron reflectivity measurements were conducted on dry and hydrated SA-LbL films in neutral and basic conditions at the Spallation Neutron Source Liquids Reflectometer (SNS-LR) in Oak Ridge National Lab (ORNL).[301] The SNS-LR collected specular reflectivity

data in a continuous-wavelength band several different incident angles according to procedures established earlier.[241] The reflectivity data were collected using a sequence of 3.25-Å-wide wavelength bands (selected from 2.63 Å < λ < 16.6 Å) and incident angles (ranging over 0.60° < θ < 1.97°), thereby spanning a total wavevector transfer ((Q= 4π sinθ)/λ) range of 0.08 nm^{-1} < Q < 1.6 nm^{-1}. The data were collected at each angle with incident-beam slits set to maintain the relative wavevector resolution constant at δQ/Q=0.05, which allowed the six different angle and wavelength data sets to be stitched together into a single reflectivity curve.

Neutron reflectivity data were collected from dry films in air as well as in a 100% D_2O vapor environment by sealing in a humidity cell with D_2O on the bottom. The silk films in a swollen state, treated with phosphate buffer of pH 11.5, were sealed in the humidity cell with D_2O on the bottom to maintain the hydration. These two hydrated silk films were allowed to equilibrate in the humidity cell overnight before measurement. Isotopic substitution of protium with deuterium is frequently utilized as a contrast variation method due to the large SLD difference between deuterated and protonated water, enabling a distinction between structural inhomogeneity in the liquid state which cannot otherwise be revealed. [302,303]

The experimental data were analyzed using a model analysis software developed at ORNL with conventional NR data fitting techniques, as described previously.[304] To fit the data, the multiple $(SF\text{-}PG/SF\text{-}PL)_n$ layers were considered as a single layer due to the absence of neutron scattering contrast between the components, and likewise for the silk *β*-sheet multilayers. An idealized layered structure featuring sharp interfaces between adjacent layers was first utilized to start the modelling, then modified by introducing layer-to-layer

intermixing to accommodate the physically measured structures via adjusting layer thicknesses, scattering length densities (SLD) and roughnesses to best fit the collected data in all states. Initial individual layer thicknesses for simulations were taken from ellipsometry measurements and then adjusted during NR data analysis. SLD varies as a function of the mass density as well as the local composition in the film. Standard SLD values were used for common materials including D_20 (6.34 x 10-6 $Å^{-2}$) and silicon oxide (3.4 x 10-6 $Å^{-2}$).[305]

7.2.6 Computer simulations

Simulations of actuating behavior are based on computational method with the lattice spring model (LSM), a modeling technique for simulation of deformable solids, which were utilized to simulate the self-rolled microsheets. [306] In the simulation, a single microsheet was constructed using a regular network of interconnected beads placed on a simple square lattice. Each bead in the network was connected by stretching springs (bonds) to its closest and next-closest neighbors. The bulk elastic properties were set by adjusting the stiffness of lattice springs to match the mechanics of polymer layers. Thus, the network consisted of three different regions, corresponding to the polystyrene (PS), silk ionomers layer and β-sheets layer.

The thickness ratios and lateral aspect ratios of the networks were set to match the experimental system. In particular, the rhomboid silk sheets were created from initially rectangular network by removing beads outside the region of interest. The swelling response of the active silk ionomers layer was simulated by change the equilibrium length of the bonds in the "active" network region, in which the length of the bonds gradually

increased by 1% steps until the equilibrium lengths was 1.6 of the initial length. To include the effect of thermal fluctuations on the bending, dissipative particle dynamic thermostat was employed. A viscous damping was imposed to mimic the effect of solvent viscosity. The dissipative force was set proportional to the bead velocity with a proportionally constant equal to 0.2.

7.3 **Results and Discussion**

7.3.1 Fabrication of silk-on-silk microsheets

Silk ionomers were deposited via SA-LbL assembly to obtain a multilayer structure. After cross-linking, the silk-ionomers multilayers were stable over a wide pH range, from extreme acidic to basic conditions, and indicated a remarkable degree of reversible swelling/deswelling by exposing to pH below 2.0 and above 11.0.[202] On the other hand, a physical crosslinked silk β-sheets layer, prepared by transformation silk coil molecular to silk II structure (β-sheets) with methanol treatment, was utilized as a passive layer, as it does not have responsive property at various pHs.[307] The uniform bimorph silk films without patterning (used for ellipsometry and neutron reflectivity measurements) were composed of an active silk ionomer layer and a passive silk β-sheet layer.

7.3.2 Morphology of the 3D self-rolled silk-on-silk structures.

A variety of silk-on-silk bimorph microsheets could be obtained by designing different photomasks. Large scale, highly ordered arrays of tens of nanometers thickness silk microsheets with precisely controlled position, shape and micrometer scale lateral dimensions were prepared in this study (Fig. 7.2a).

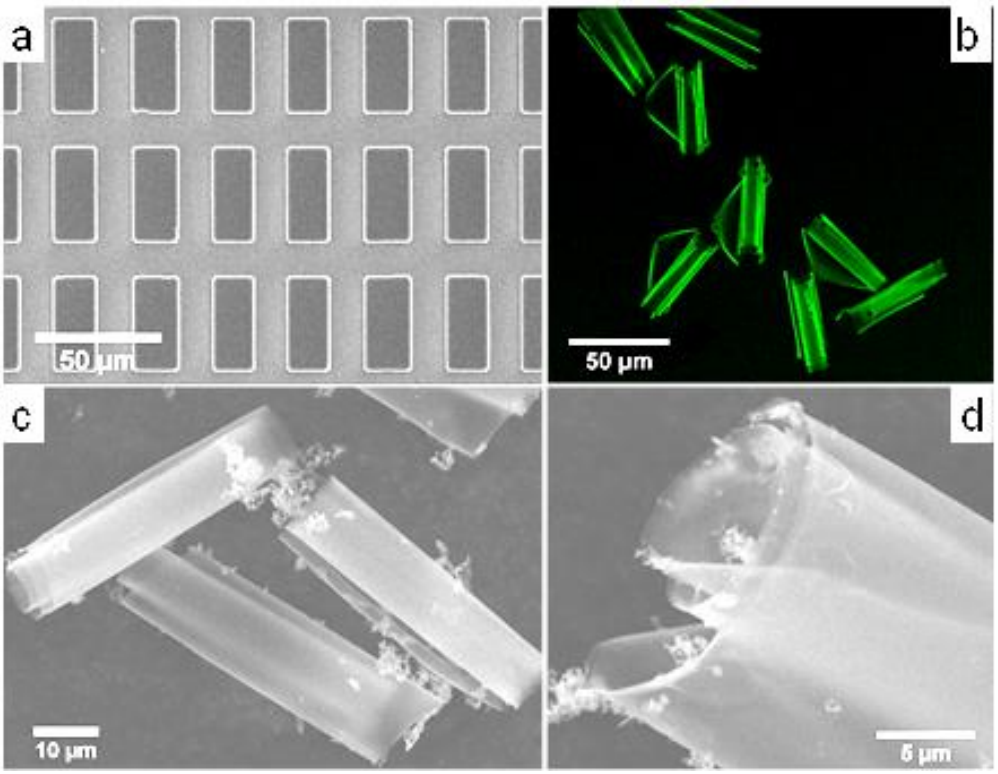

Figure 7.2 (a) SEM image of large scale patterned silk sheet array. (b) Confocal image of self-rolled silk tubes stimulated by basic conditions (staining with FITC). (c) SEM image of conserved 3D structures of the silk tubes after freeze drying. (d) High resolution SEM images of the cross-section of hollow tube with multi-layered wall.

Upon immersion of the composite planar silk microsheets into a 0.06 M NaOH solution, the silk ionomers layer underwent significant swelling, due to the reduction of the ionic bonding in the LbL thin film at extreme basic conditions,[63] while the silk β-sheet layers remained a constant volume, due to the physical cross-linked β-sheet. The structure and shape of the silk-on-silk microtubes were revealed using confocal microscopy by staining with FITC, indicating closed tubes with multilayer shells (Fig. 7.2b). The observation was also confirmed by SEM images of freezing-dried microtubes, demonstrating 3D hollow structures with nanometer thin shell (Fig. 7.2c, d). These stimuli silk self-rolling structures are reversible, unrolling to planar film by adjusting the pH back to neutral condition.[300]

The direction of self-rolling strongly depended on the geometry and dimension of the planar microsheet as well as the thickness of different layers, which will be discussed in

details below. The self-rolled microtubes were distinguished into four general types: short tubes, double short tubes, diagonal/helical tubes and long tubes, respectively (Fig. 7.3a-d). High-resolution AFM images and corresponding cross-section profiles revealed multi-layered microtube shells and step-wise increase of shell thickness with an average increment of 140 ± 10 nm (Fig. 7.3e, h). This value corresponds to the thickness of the triple-layered PS-silk-silk film.

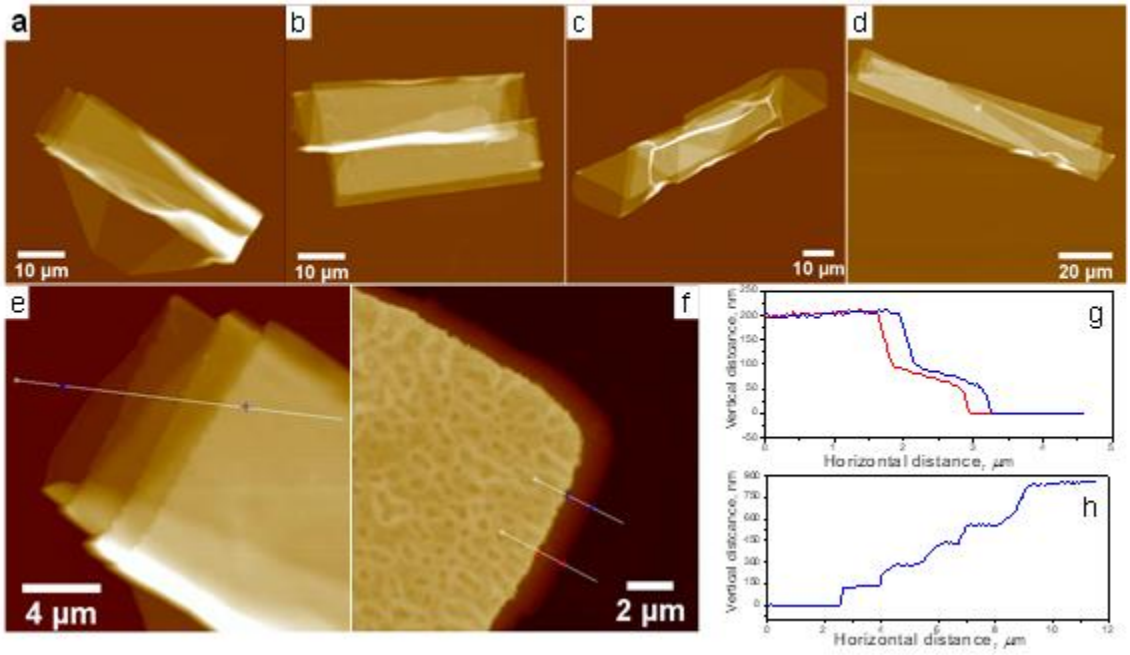

Figure 7.3 AFM topography images of dried self-rolled tubes with various morphologies: (a) short tube (z-scale: 5 μm); (b) double short tube (z-scale: 2.9 μm); (c) diagonal/helical tube (z-scale: 3 μm); (d) long tube (z-scale: 2.5 μm). High resolution AFM image of self-rolled tube (e) (z-scale: 2.5 μm) and unrolled microsheets (f) (z-scale: 400 nm), and corresponding height cross-section profiles (h) and (g) (sections along lines in (e) and (f), respectively.

The unrolled silk sheet, obtained from the reversible "opened" microtube, possess a grainy surface texture, which is consisted with the previously reported morphology of silk materials with partial transformation of silk secondary structure during drying (Fig. 7.3f).[179] It is also worth noting that the supporting PS layer with a thickness of 100 ± 5 nm is clearly visible on this image, indicating that the PS layer is preserved and not delaminated

during transformations. That said, it can be seen that, for planar films, a buckling type effect can be seen in both two and three layered structures (Fig. 7.4 a and b). In addition, the presence of a defect site due to a scratch allows the silk layers to partially delaminate from the PS surface, indicating a weak adhesion between these layers.

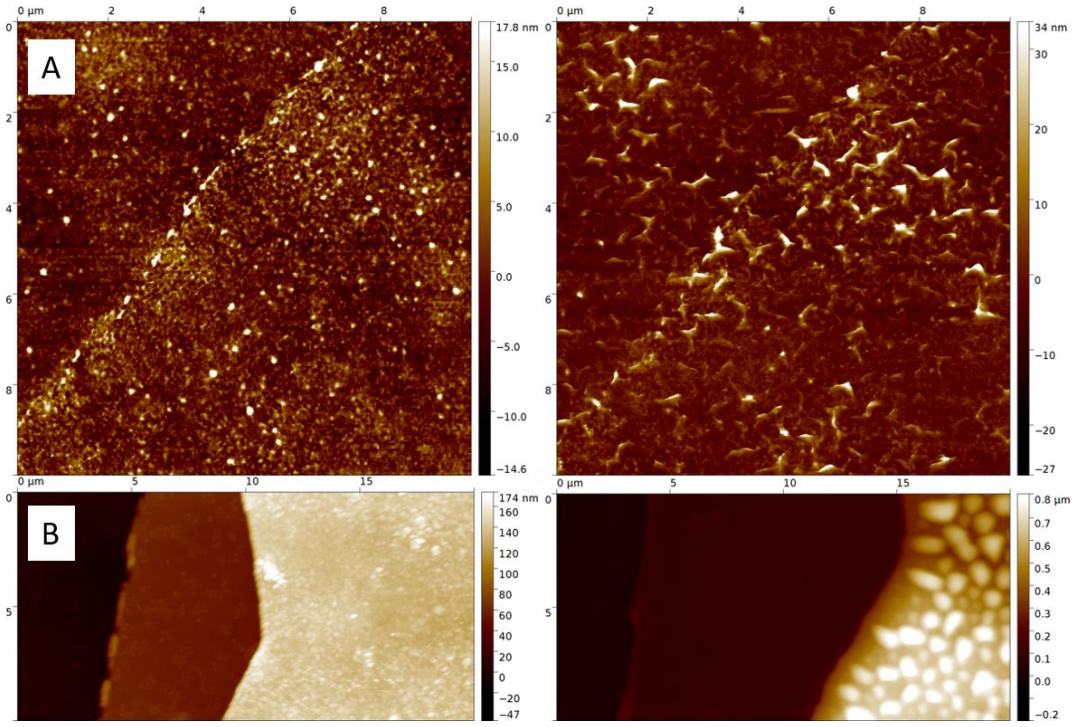

Figure 7.4 AFM profiles for (A) Silk Ionomer film on polystyrene and (B) Composite tri-layer structure. In both set

7.3.3 Microsheet self-rolling process.

In order to monitor the self-rolling process of the silk microsheets, we conducted directly time-resolved observation of microtube formation after immersing into basic solution with optical microscopy (Fig. 7.5).

These *in-situ* observations revealed that the exposure of patterned silk microscopic sheets with aluminum (Al) protection layer to NaOH, an efficient oxidizer for Al, immediately

resulted in the topmost Al layer delamination and dissolution. At the same time, the solution diffused across the periphery of the patterns, causing significant volume expansion of the active silk ionomers layer, due to the decreased ionic bonding between (SF-PG/SF-PL)$_n$ as the amine groups on the SF-PL deprotonated in basic conditions (pKa of polylysine is around 9).[308] The silk microsheets buckled and curved starting from the corners according to the color contrast of patterns and, at the later stage of self-rolling, the planar microsheets delaminated from the substrate, followed by rolling up into 3D microtubes.

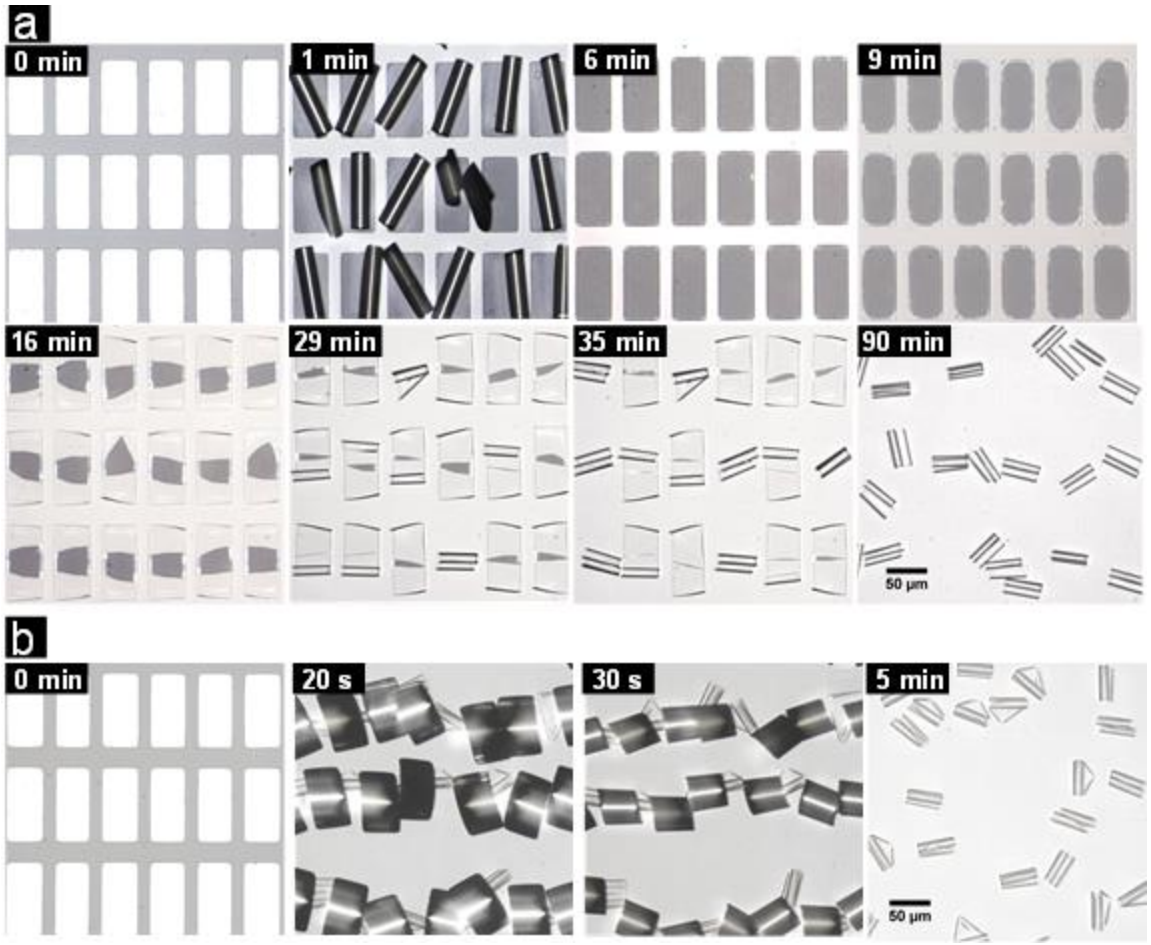

Figure 7.5 Time-resolved optical images of self-rolling process of the silk-on-silk micro-sheets under basic conditions. (a) Rolling process of silk microsheets composed of PS-(SF-PG/SF-PL)$_{12}$-(β-sheet)$_1$, PS layer with a thickness of 88±2 nm. (b) Rolling of silk microsheets composed of PS-(SF-PG/SF-PL)$_{12}$-(β-sheet)$_{10}$, PS layer with a thickness of 68±2 nm.

Silk microsheets with same lateral dimension (50 μm x 100 μm) and active layer thickness, but different thicknesses of PS and topmost passive silk *β*-sheet layer, showed remarkable difference in the self-rolling speed (Fig. 7.5a, b). The time to form a final stable microtube was reduced from 90 min to 5 min as the PS layer thickness decreased from 88 nm to 68 nm, revealing that the self-rolling process is damped by the presence of thicker supporting glassy polymer layer and the rate of rolling can be tuned by changing the film design.

7.3.4 Control of the self-rolling microtube morphology.

Next, we exploited different approaches to control the self-rolling direction, rolling percentage (number of rolled tubes/total number of silk microsheets) and the diameter of the rolled microtubes. First, the different self-rolling scenarios were investigated by varying the PS pre-layer thickness for the patterned silk sheets with same dimension (50 μm x 100 μm) and constant thickness of silk ionomer (48.5 ± 2.5 nm) and silk *β*-sheets layer (34 ± 4.5 nm) (Fig. 7.6). It is worth to note none of the rolling, curving or even buckling was observed for the microscopic sheets with a thick PS layer (207 nm) due to a requirement of a strong bending critical stress for such very thick supporting glassy polymer layer (Fig. 7.6a).

In a striking contrast, silk microsheets with thinner PS prelayer (below 100 nm) self-rolled completely into microtubes (Fig. 7.6b-e). Correspondingly, statistical analysis based-on more than 1000 self-rolled silk microsheets revealed that the rolling-up percentage dramatically increased from 0 to 100% as the thickness of PS layer falls below 40% of original active silk ionomer layer with three types of tubes observed in this case: long-tubes, short-tubes and diagonal-tubes (Fig. 7.6b, g). Decreasing the thickness ratio of PS-

silk ionomers layer to just below 1.4 resulted in the short-tubes (Fig. 7.6d, h). A further decrease of the PS layer thickness (ratio below 0.5) resulted in incomplete tube rolling (Fig. 7.6e, h). Moreover, the diameter of microtubes depends on the PS layer thickness and decreased from 20 ± 2 μm to 7 ± 2 μm with the decreased PS layer thickness (Fig. 7.6f).

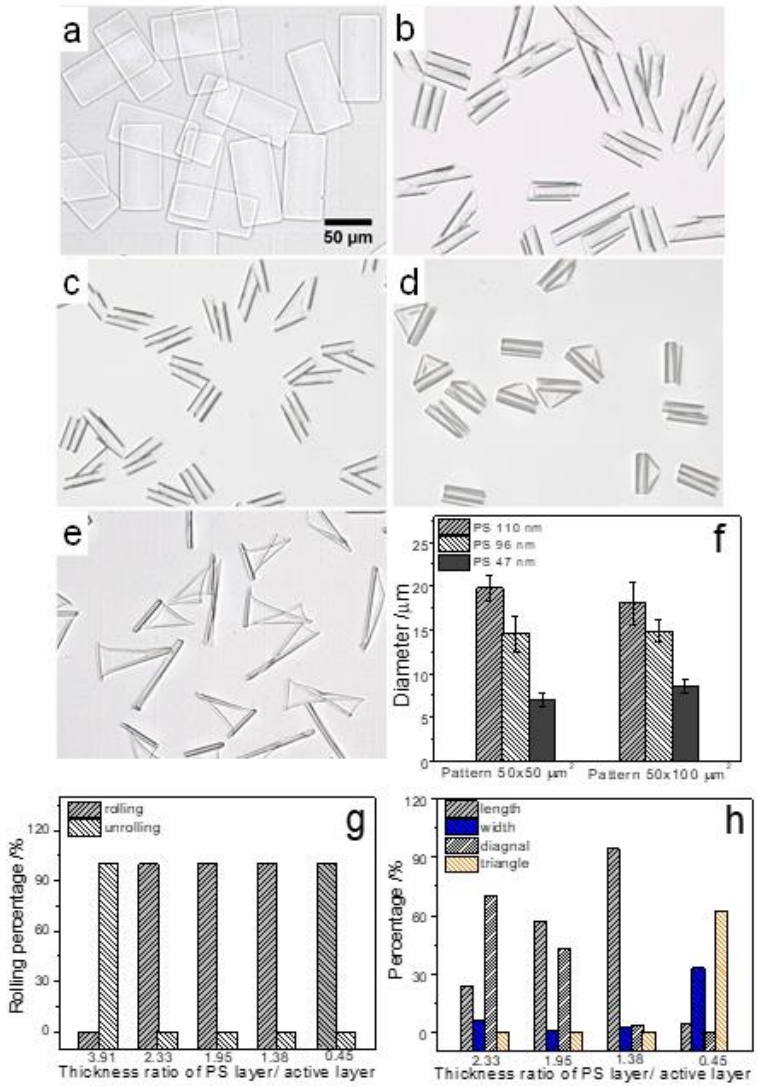

Figure 7.6 Self-rolling of PS-(SF-PG/SF-PL)$_{12}$-(β-sheet)$_{10}$ microsheets with different PS thickness (microsheet lateral dimension: 50 μm x 100 μm, silk ionomers layer: 48.5 ± 2.5 nm, silk β-sheets: 34.5 ± 4.5 nm). PS thickness: (a) 207 nm, (b) 110 nm, (c) 95 nm, (d) 68 nm, (e) 20 nm. (f) The diameter of silk self-rolling microtube as a function of PS layer thickness. (g, h) Statistical analysis of the microsheets rolling/unrolling percentage (g) and the ratio of various rolling direction (h) as a function of the thickness ratio of PS layer/active silk ionomers layer. (*In the panel h, 4 rolling directions were indicated: 1) length: rolled along the microsheet length direction (tubes shown in panel d); 2) Width: rolled along the width of microsheets; 3) diagonal: rolled from the opposite corners, 4) triangle: morphology is shown in panel e.)

In the bimorph model developed for computer simulation, the thicknesses of active silk ionomer layer and passive β-sheet layer was kept constant, and the variation of thickness ratio (PS pre-layer : active silk ionomers layer) was obtained by changing the PS pre-layer thickness. Overall, the experimentally observed self-rolling behavior is in a close agreement with the simulations for different PS layer thicknesses (Fig. 7.7).

For example, our computer simulation suggested that no noticeable rolling should be triggered the swelling of active silk ionomer layer for the microsheets with the PS/silk ratio of 1.6 and higher (Fig. 7.7a1, a2), and no further change was observed by increasing simulation time (Fig. 7.7a3, a4). In contrast, microsheets with decreased thickness ratio (~0.4), which in turn had a thinner PS prelayer, rolled from corners (Fig. 7.7b1, b2) and formed 3D microtubes (Fig. 7.7b3, b4).

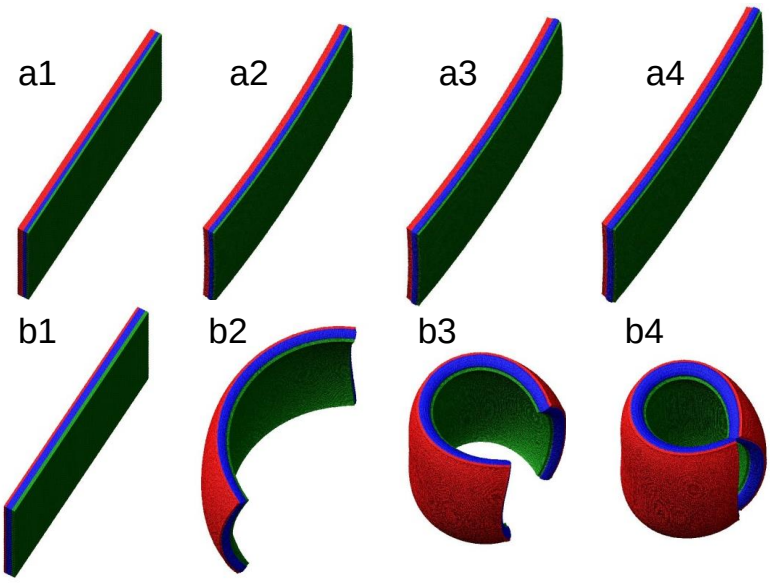

Figure 7.7 Simulated self-rolling of microsheets with aspect ratio of 1:2 as controlled by the thickness ratio of PS prelayer/passive silk layer/silk ionomer layer at increasing time (from left to right). The thickness ratios were set as 1.6 for a1- a4 and 0.4 for b1- b4, respectively.

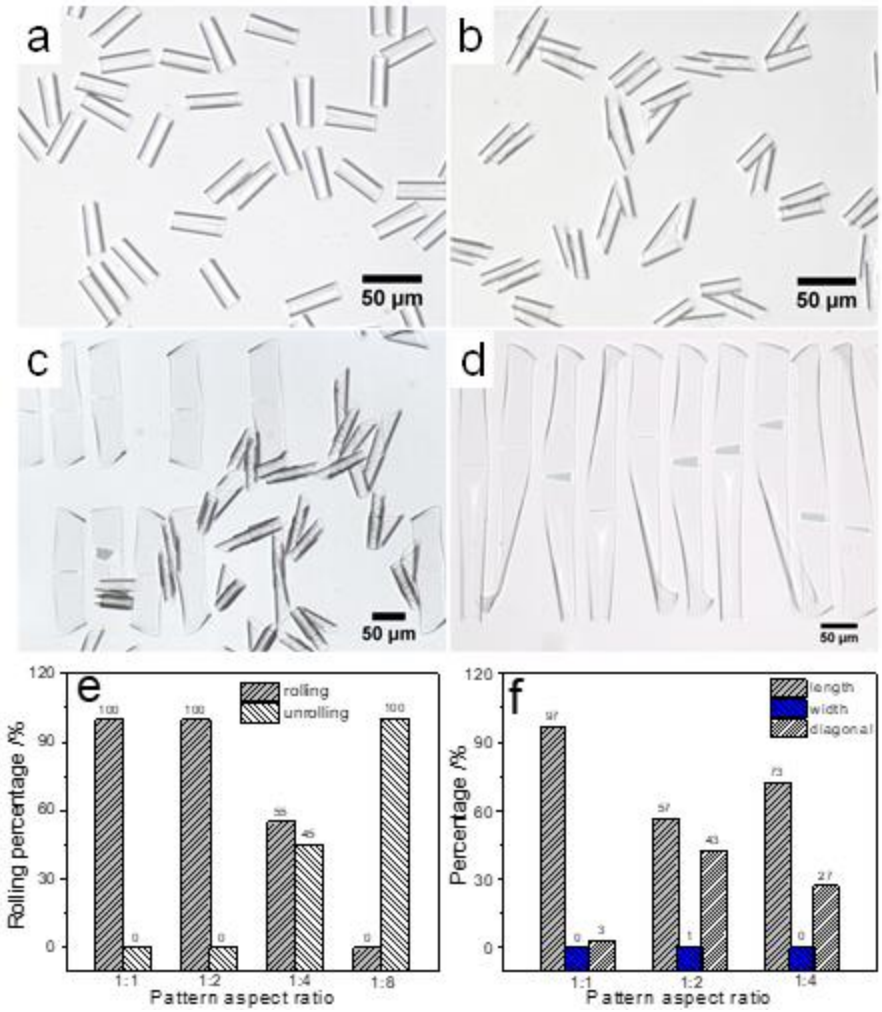

Figure 7.8 Self-rolling behavior of PS-(SF-PG/SF-PL)$_{12}$-(β-sheet)$_{10}$ microsheets as a function of the aspect ratio (silk sheet width: 50 μm, PS: 97.3 ± 8.7 nm, silk ionomer layer: 50.5± 2.0 nm, β-sheet: 34.2 ± 5.0 nm): (a) 1:1, (b) 1:2, (c) 1:4, (d) 1:8. (e, f) Statistical analysis of the rolling/unrolling percentage (e) and the ratio of rolling direction (along long, short, and diagonal axis) (f) at different aspect ratios.

Second, silk planar bimorph sheets with aspect ratios varied from 1:1 to 1:8 were prepared to investigate their reconfiguration ability and self-rolling properties experimentally (Fig. 7.8). Uniform rolling-up for all microsheets and consistent morphology was observed for the silk microsheets with an aspect ratio of 1: 1 (PS layer: 97.3 ± 8.7 nm, silk ionomers layers: 50.5 ± 2.0 nm and silk β-sheets layer 34.2 ± 5.0 nm) (Fig. 7.8a). However, the increase of the aspect ratio to 1:2 and 1:4 resulted in a combination of the short and diagonal rolled tubes with hindered self-rolling (Fig. 7.8b, c, f). Finally, none of the silk microsheets

was able to roll up to form a cylindrical tube with only modest bending occurring around the corners at the highest aspect ratio of 1:8 (Fig. 7.8d, e).

The dramatic change of self-rolling behavior as controlled by the lateral aspect ratio of silk microscopic sheets was observed in computer model simulations as well (Fig. 7.9). Curved strips were obtained for microsheets with a high aspect ratio (width/length: 1:8), which is in agreement with experiment (Fig. 7.9a1-a4 and Fig. 7.8d). The reduction of the aspect ratio of the microsheet to 1:2 and 1:1 resulted in cylindrical microtubes (Fig. 7.9b1-b4 and c1-c4). It is worth noting that isotropic deformation was observed for microsheets with an aspect ratio of 1:1, with symmetrically bending occurring at all the corners (Fig. 7.9c2). However, the microsheets eventually rolled over the center and formed tubes due to the increased localized deformation from the perturbations in the system (Fig. 7.9c3, c4).

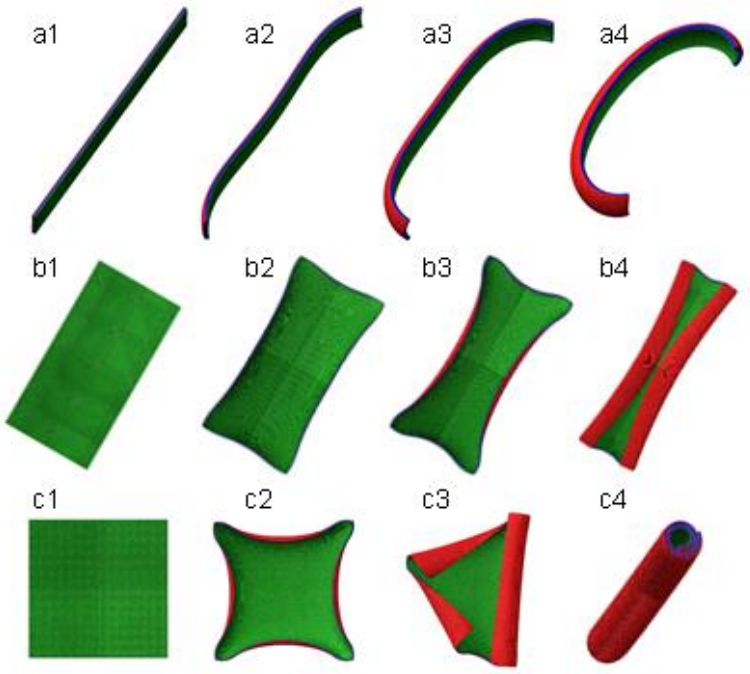

Figure 7.9 Computational modeling of self-rolling of silk microsheets as a function of the aspect ratio (thickness ratio of PS layer/active layer: 1.5). (a-c) at aspect ratios of 1:8 (a); 1:2 (b) and 1:1 (c).

A next set of experiments showed that the thickness ratio of passive layer (silk β-sheets) and active layer (silk ionomers layers) affected the self-rolling behavior as well (Fig. 7.10). For instance, uniform self-rolling of silk-on-silk bimorph microsheets into short-tubes was observed at low thickness ratio (passive β-sheets layer/active silk ionomers layer: 0.16) for the lateral dimensions of 50 µm x 100 µm and constant silk ionomer layer (44.8 ± 5.2 nm) and PS layer (81.6 ± 4.5 nm) (Fig. 7.10a).

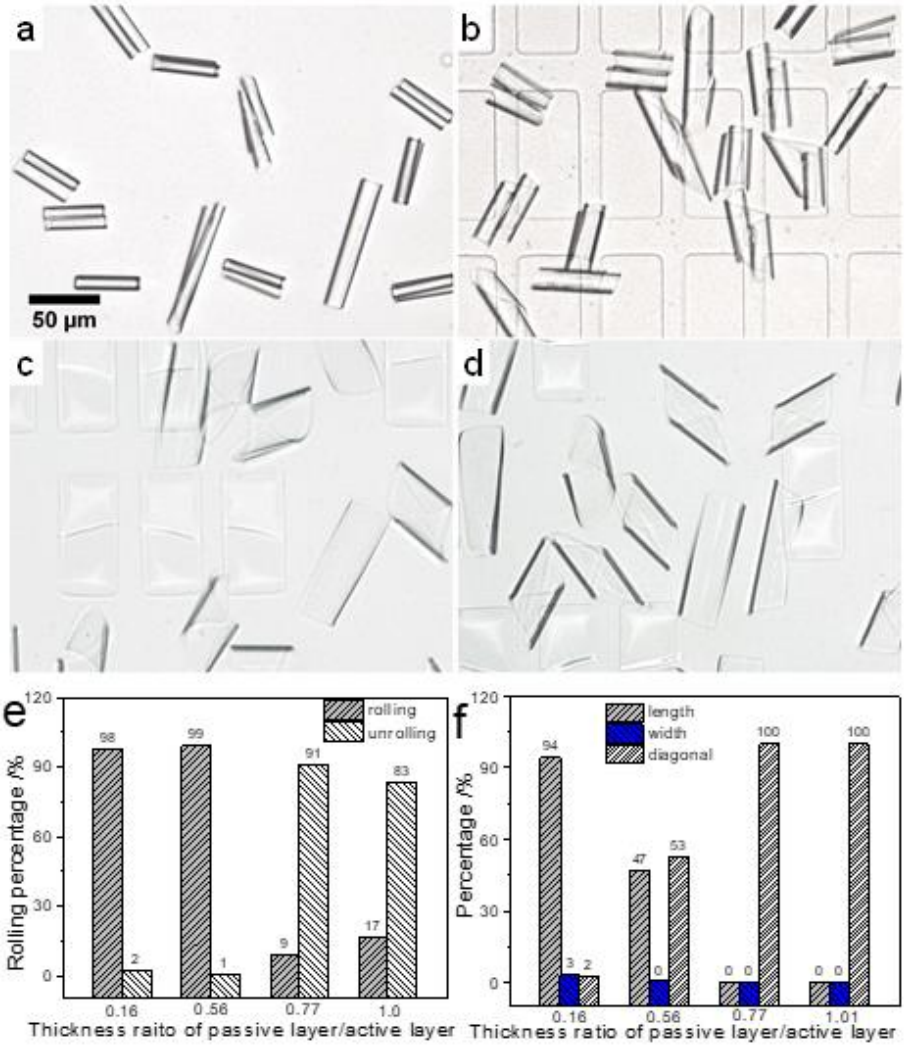

Figure 7.10 Self-rolling behavior of PS-(SF-PG/SF-PL)$_{12}$-(β-sheet)$_n$ microsheets as a function of the thickness ratio between passive β-sheet layer and active silk ionomer layers (sheet dimensions: 50 µm x 100 µm, PS: 81.6 ± 4.5 nm): at β-sheet/silk ionomer thickness ratio of a) 0.16, b) 0.56, c) 0.77, d) 1. e, f) Statistic analysis of the rolling/unrolling percentage (e) and the ratio of various rolling direction (f) at different passive/active layer thickness ratio.

The experimental observations showed that the increase of thickness of passive silk β-sheets results in preferential self-rolling of opposite corners toward each other to form diagonal microtubes in combination with short-tubes at the thickness aspect ratio of 0.56 (Fig. 7.10b). However, silk-on-silk microsheets with an even thicker top most passive silk β-sheet layer showed difficulties in self-rolling. The quantitative analysis of self-rolling/unrolling percentage dropped from 100% to around 10% with a thickness ratio increasing from 0.16 to 0.77, ascribed to the high stress needed for bending thicker silk β-sheets layer.[309]

7.3.5 The internal morphologies of silk-silk microsheets and self-rolling behavior

Selective swelling of the silk layers. Above, we suggested that similarly to those suggested earlier, the non-uniform swelling in the sandwiched planar sheets generated a mismatched interfacial stress, a usual cause discussed in other studies.[310,311,312,313] However, the volume expansion of the active silk layer has not been quantitatively studied in the context of self-rolling of layered biopolymer sheets. Here, in order to assess these effects quantitatively, neutron reflectivity was employed to track the internal structural changes of layered silk films under different conditions (Fig. 7.11). To analyze NR data, the layered silk film components were considered as a single block with variable neutron scattering density, different for PS, silk ionomers and silk β-sheet layers (Table 7.1).[314]

Table 7.1 Film thickness at various conditions characterized by the NR and ellipsometry.

Layers / Thickness	SiO_2 /nm	Polystyrene /nm	Silk ionomers layers /nm	Silk β-sheets /nm
E.S. in air	1.6	36.4	43.7	24.9
NR in air	1.5	37.9	43.6	18.6
NR in D_2O vapor	2.2	37.2	84.2	25.7
NR in D_2O at pH 11.5	2.2	37.8	>300	25.7

*E.S. and NR indicates ellipsometry data and neutron reflectivity, respectively.

The distinct and periodic fringes observed in the neutron reflectivity curve in ambient air indicated the high degree of stratification of the representative PS-(SF-PG.SF-PL)$_{11}$-(β-sheet)$_5$ film which was selected for this experiment (Fig. 7.11a). The corresponding scattering-length-density (SLD) profile that gave the best fit revealed a sharply contrasted and well-defined silicon oxide layer at the surface of Si crystal, followed by polymer layers with different SLD layer as determined by local composition and mass density (Fig. 7.11b). Note that the thicknesses measured by neutron reflectivity in the dry state were 37.9, 43.6 and 18.6 for the PS layer, (SF-PL/SF-PL)$_{11}$ and silk β-sheets, respectively, which are

consistent with the corresponding PS, silk ionomers layer and β-sheet thicknesses derived from the ellipsometry measurements for the same triple-layered system.[305]

In striking contrast to dry films, a larger critical reflection wavevector and higher amplitude fringes were observed upon exposing the films to 100% humidity D_2O, revealing dramatic changes in the internal structure upon solvent diffusion (Fig. 7.11c). A significantly enhanced SLD was observed in association with an increase in the silk ionomer layer thickness to 84.2 nm as compared to the 43.6 nm for the dry state, attributed to the adsorption of D_2O into the porous silk ionomer network, which agrees with the swelling degree observed from AFM measurements for uniform silk ionomer films as was measured earlier (Fig. 7.11d).**Error! Bookmark not defined.**

A drastically different internal morphology was revealed after immersing the silk films in pH 11.5 phosphate buffer and keeping them under 100% D_2O humidity to maintain the swollen state (Fig. 7.11e). In fact, the films exhibited no specular reflectivity below Q = 0.2 nm^{-1}, indicative of an extremely corrugated surface that does not reflect as a single sheet. Only at higher Q values did the neutrons coherently pass through this surface and specularly reflect from the layers below. Correspondingly, the thickness of the silk ionomer layer dramatically increased above 300 nm (corresponding fringes cannot be resolved in NR setup). Increased SLD indicates an extreme volume expansion and porous structure, as demonstrated in Fig. 7.11f. On the other hand, it is worth noting that the thicknesses of the PS pre-layer and silk β-sheets remained almost the same during the various treatments (PS: 37 ± 1 nm and silk β-sheets: 24 ± 3 nm) confirming their passive nature. Such resistance is caused by the fact that water is a bad solvent for the hydrophobic β-sheet fibroin layer with high crystallinity as well as for the glassy PS layer.[315] Overall,

the PS pre-layer and passive silk β-sheets remained at nearly constant volume at all the three cases (dry state in air, dry state in 100% D_2O humidity, and treated with phosphate buffer pH 11.5 at 100% D_2O humidity environment).

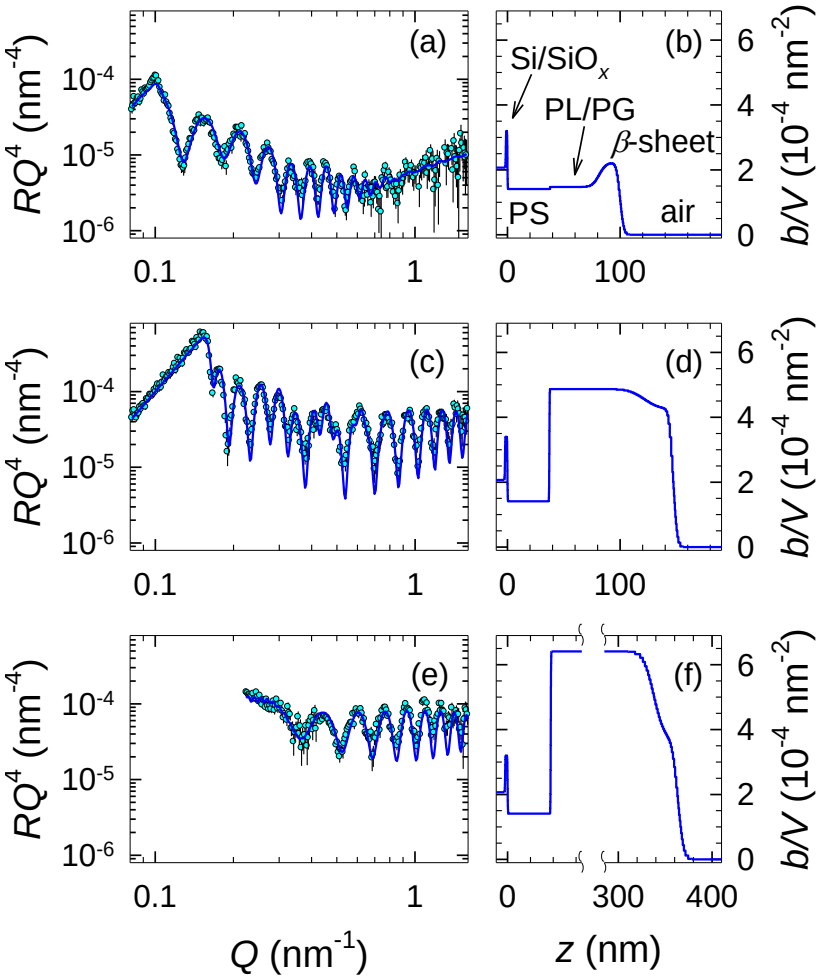

Figure 7.11 Neutron reflectivity (a, c, e) and the corresponding SLD profiles (b, d, f) for PS-(SF-PG/SF-PL)$_{11}$-(β-sheet)$_5$ films at various conditions: ambient air environment (a, b), 100% D_2O vapor humidity (c, d) and treated with pH 11.5 D_2O solution (e, f). Open symbols and solid lines in neutron reflectivity plots stand for the experimental data and fit, respectively.

7.3.6 Discussion of lattice spring model simulations

To verify that the self-rolling of silk-on-silk microsheets can indeed be ascribed to the mismatched interlayer stress generated from the non-uniform swelling of different layers

as exposing to basic aqueous, we employed lattice spring model (LSM) to investigate the developing of the stress throughout the micorsheet by activation the swelling of the silk ionomers layer.[306] First, the stress in each layer of the 3 layered microsheet (PS layer-silk ionomer layer-β sheets) was calculated from corresponding stress field for microscopic silk sheet with various shapes (rectangles aspect ratio: 1:2, 1:8 and 30° parallelograms), in which the negative values of the stress represent tension and positive values represent compression (Fig. 7.12).

The significant swelling of the silk ionomers layer in basic condition triggered a biaxial expansion field within the microsheet, exerting stresses on both PS and β-sheets layers, which in turn, the expansion is constrained on both sides. At each point in time, the fully expanded equilibrium state of silk ionomer layer is inaccessible. Thus, although the silk ionomer layer increases in volume, it constantly remains compressed through the swelling process (Fig. 7.12b). In contrast, both the polystyrene and β-sheet layers remain stretched (Fig. 7.12a, c). The deciding factor in determining which side the structure rolls on is the stiffness of the passive (PS and β-sheet) layers. We can think of each layer as a spring, $F = kx$, where k corresponds to the bulk moduli of each layer. As the silk ionomer swells it enforces a displacement (χ) on both the PS and β-sheet, which in turn, exerting a constraining force. Rolling occurs on the side for which the constraining force is larger. Since the force is governed by the bulk modulus (and displacement is the same for both layers) the structure will always prefer to fold on the stiffer side. The softer side will more easily (less force required) accommodate the displacements imposed by the silk ionomer layer. If the PS layer and β-sheets is roughly the same thickness, rolling will always occur on the beta-sheet side, which is the case in our experimental. It was also confirmed by the

extraction of the $|P_{avg}|$ from computational simulation, the value is larger for β-sheets. This shows that indeed the constraining effect of the β-sheets is greater.

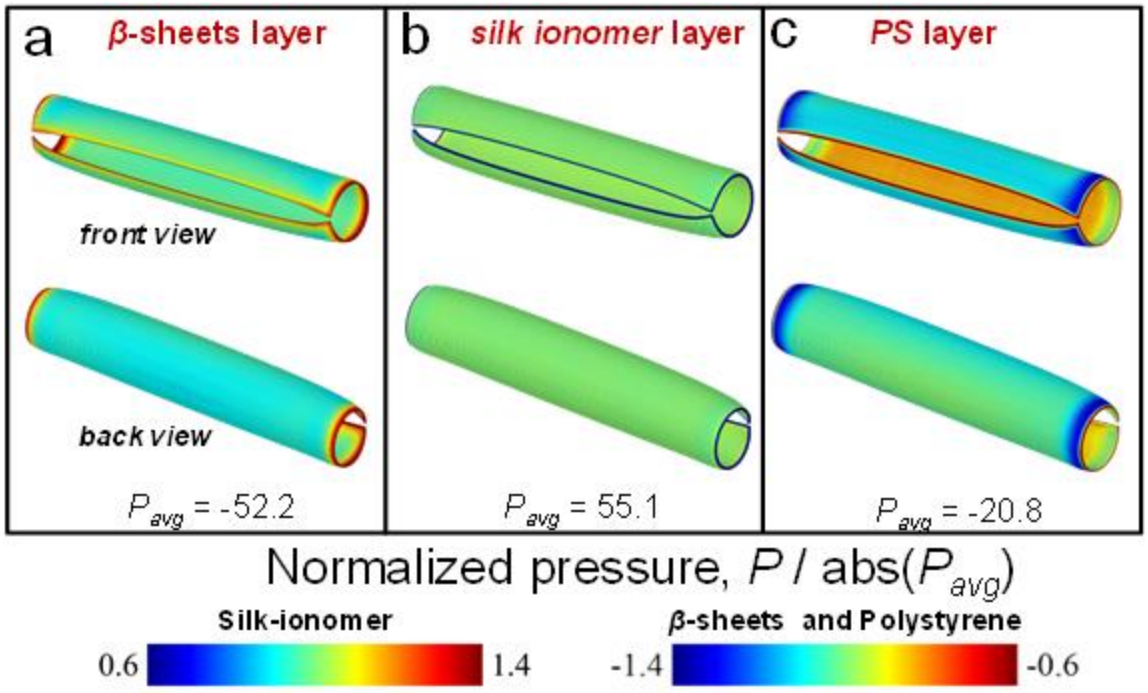

Figure 7.12 Stress map obtained from computational simulations for each individual layer within the sandwiched silk microsheet with an aspect ratio of 1:2. a) β-sheet; b) silk ionomer layer; c) PS layer. Top row indicated front view and the bottom row is the back view for each panel.

By looking at the force map of the PS layer, it is noticeable that along the shorter pair of edges the stress concentration is high (Fig. 7.12c). For understanding this better, next, stress development of individual layers within the microsheets was explored in a time series calculations (Fig. 7.13). For this example, the PS layer from the microscopic sheet with aspect ratio 1:2 was simulated. When the silk ionomer layer is swollen, the computer simulations showed the highly localized stresses in the corners (Fig. 7.13a). These stresses initiated bending at the corners.

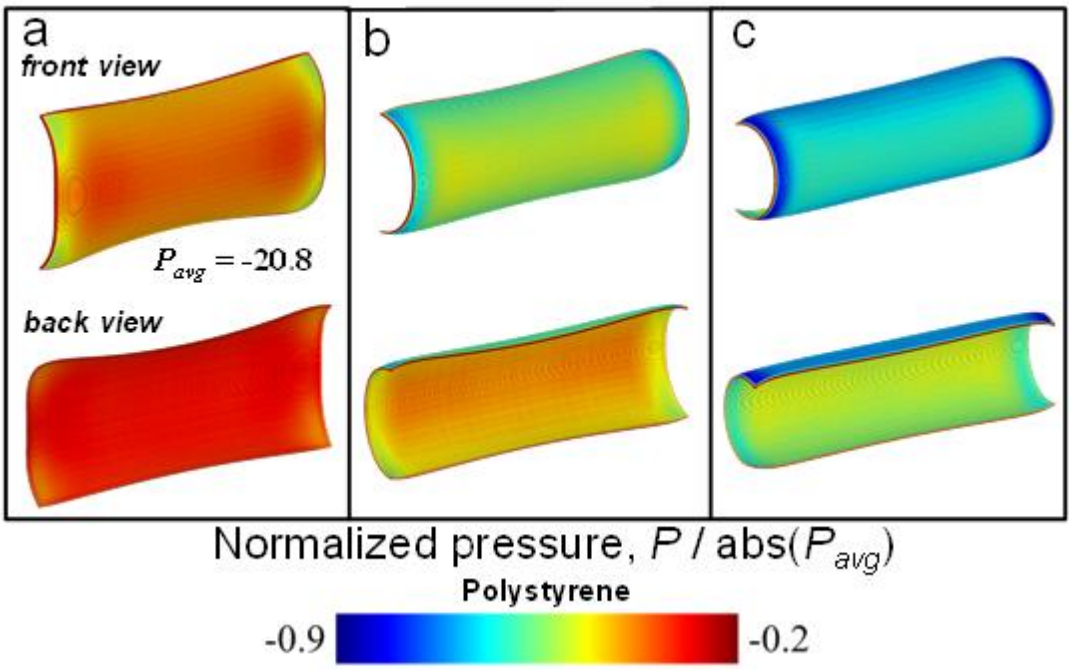

Figure 7.13 Color maps of stress distribution within the PS layer in the sandwiched silk microsheets with an aspect ratio of 1:2 over a time series (a-c). Front views as shown in top row and back views in the bottom row.

Then, as the corners are bent, they pulled and deformed the rest of the sheet. The deformation at the corners causes the moment of inertia along the longitudinal axis to decrease (Fig. 7.13b). This transformation increases the bending moment and drives the deformation even further, thus, rolling sheets into a tube (Fig. 7.13c). It should be noted that the high stress regions in the PS layer correspond to low stress regions in the β-sheet. This happens because β-sheet region is located below the neutral plane and the PS layer is above it. Therefore, any localized bending produces extra tension in the PS layer and extra compression in the β-sheet layer. However, since the β-sheet is strongly stretched by the silk ionomer layer, this localized compressive effect only serves to create areas of low tensional stress.

Furthermore, different stress distribution was revealed for silk microsheets with various shapes via the LSM simulation, which can explain the microtube morphology control by

sheet geometry. For instance, for the microsheet with parallelogram shape, the stress concentrated near the minor angle corners. As a result, the material below the neutral axis (β-sheet layer) experienced the compression stress locally. Meanwhile, material above the neutral axis (PS layer) was locally put in tension. This effect leads to a decrease/increase in tensional stresses for the β-sheet /PS layer near the minor angle corners, producing localized bending. As the deformation progresses, the asymmetry of the structure caused the sheets to roll into helical structures. And, for the onset of folding in 1:1 system, stress concentration near the corners grew significantly and caused the corners to deform at the same time. With time, the thermal fluctuations can cause one of the corners to initiate rolling, which induces the other three corners and sides to rolling to form a tube. However, for the microsheets with an aspect ratio of 1:8, bending along the longitudinal axis is not possible as observed both in the experimental and simulated results (Fig. 7.8d). Furthermore, we also employed a thermomechanical model for bending in composite sections to scaling the final self-rolled tube radius as a function of varied individual layer thickness.[316] The calculated radius matched with the experimental results with the same parameters.

7.4 **Conclusions**

In conclusion, we demonstrated the mass assembling of autonomic self-rolling 3D constructs within micro-scale dimensions from silk-silk layered microsheets. The sheets were composed of pH responsive silk ionomer layer as an active layer and silk β-sheet as a passive layer and supported by uniform polymer layer. We have experimentally shown and theoretically confirmed that the mismatch of the interfacial stress generated from the

non-homogenous swelling of different layers facilitated the rich variety of self-rolling scenarios for the silk-on-silk microsheets with different geometries.

The self-rolling direction, shape and diameter of the self-rolled microsheets can be controlled by biaxial stress distribution, which depends upon lateral dimensions, layer thickness and the aspect ratio of microsheets. In contrast to the previously exploited synthetic hydrogels, the self-rolling ultrathin microsheets demonstrated here are based on biocompatible and biodegradable silk materials with controllable nanoscale thicknesses. Furthermore, beside the biocompatible and biodegradable nature of silk fibroin, it is noteworthy that our silk-on-silk microsheet constructs with fine tunable and reversible rolled morphology are extremely stable in harsh environments. These silk 3D autonomous microstructures upon external stimulus present a further step toward 3D-assembled biomimetic devices for vivo implant applications, such as neutral network monitoring,[317] single cell analyses, capture and position the cells/drugs,[318319] indicating a promising platform for a wide range biological applications.

CHAPTER 8. IMMOBILIZATION OF RECOMBINANT E. COLI CELLS IN A BACTERIAL CELLULOSE-SILK COMPOSITE MATRIX WITH PRESERVATION OF THEIR BIOLOGICAL FUNCTION

8.1 Introduction

Encapsulation of cells and specifically, microbial communities, has attained considerable interest in the field of biotechnology, as combinations of different fabrication processes and biomaterials continues to be explored.[320,321,322,323] The proper entrapment of cells in biocompatible matrix will extend cells storage life, support their sensing and interrogation functions, provide access to signaling molecules, offer protection against environmental variables, and reduce the chance for contamination with engineered microorganisms.[324]

Cellulose, a natural biopolymer, represents a versatile biomaterial that is widely used in biomedical applications due to its unique physical properties.[325] Biocompatibility, excellent mechanical strength, high water absorption capacity and surface area, highly crystalline and refined fiber network structure render biocellulose useful in drug delivery and encapsulation system for living tissues, cellular organisms, enzymes and other types of biocatalysts.[326,327,328,329,330]

In this study, we describe the formation of a composite "living membrane" system consisting of a bacterial cellulose (BC) matrix supplemented with silk fibroin (SF) protein and recombinant bacterial cells that harbor a theophylline synthetic riboswitch (RS) as a model biosensor. With adjusting the composition ratio of SF in BC host matrix, a variety

of BC-based scaffolds were prepared that varied in phototransparency, mechanical stability, porosity, and protection against UV light. The variability in physical properties between pure BC and composite BC-SF scaffolds were analyzed and compared in order to identify a proper microenvironment matrix for the recombinant cells to avoid both uncontrolled proliferation and close-fitting retention of cells in the host hydrogel matrix. Owing to their inherent similarity to the extracellular matrix and mild processing conditions, the composite matrix derived from natural polymers provided proper conditions for the microbial cells to maintain their recombinant functions as reporter cells. Particularly, composite BC-SF matrix with higher content of SF demonstrated direct physical protection of cells from harsh environmental conditions.

8.2 Results and Discussion

Immobilization of one type of bacterial cell in a biocompatible matrix produced by another type of bacteria offers a simple and natural way to encapsulate cells of interest and provide physical protection. In this study, recombinant *E. coli* cells harboring a synthetic riboswitch were encapsulated in the native cellulose matrix produced by *G. xylinus* cells. The goal of this study was to develop an environmentally robust and long-term persistent "living membrane" consisting of bacterial cellulose (BC) matrix and recombinant bacterial strains entrapped within individual cellulosic sheaths. Since the recombinant *E. coli* cells were constructed to host a genetic cellular switch to detect the presence of relevant molecular targets, complete coverage of the recombinant cells and protection of their function were critical for developing "living cell sensor" materials or devices. Although, BC offers remarkable porosity, water absorbency and excellent biological affinity for sustaining the growth of secondary organisms, the permeability of the nanofibril network allows

planktonic cells to escape from the BC matrix. To overcome this shortcoming, BC pellicles were saturated with a second natural polymer, reconstituted silk fibroin protein, forming composite bacterial cellulose–silk fibroin (BC-SF) scaffolds. This approach allowed for the reduction in the porosity BC matrix and prevented the escape of the recombinant cells. Herein we produced and compared several BC-based composite scaffolds that differed in BC and SF composition to examine the compatibility and properties of BC-SF matrix to support the growth and function of the recombinant cells. Moreover, due to well-known natural protective and UV blocking properties of silk fibroin protein, composite BC-SF scaffolds were analyzed for their ability to shield and protect the recombinant bacteria from UV radiation.

8.2.1 Formation of pure BC and composite BC-SF scaffolds

Fig. 8.1 outlines the process for entrapping recombinant *E. coli* cells in either pure BC or composite BC-SF scaffolds, where several procedural steps required optimization. Incubation time necessary to produce the initial cellulose matrix, the amount of *E. coli*, the incubation period during co-culturing of both types of bacterial strains, the amount of SF solution, the viscosity and processing conditions required to initiate sol-gel transitions in silk fibroin structure, were all tested to attain robust composite scaffolds with efficient entrapment of the recombinant cells. Table 8.1 refers to the incubation parameters that were optimized for producing pure and composite pellicles, respectively.

Table 8.1. Procedures for formation of the three types of scaffolds: pure BC, opaque

Type of Scaffold			Incubation parameters for *G. xylinus* cells	Incubation parameters for *E. coli* cells	Processing conditions for SF	Total time
Pure BC scaffolds			3 days, 28°C	3 days, 37 °C	-	6 days
Composite *opaque* BC-SF scaffolds			3 days, 28°C	1 day, 37 °C	SF 3 wt.%, 0.5 mL: 2 days, 30°C	6 days
Composite *transparent* BC-SF scaffolds	3 days, 28°C	1 day, 37 °C	SF 7 wt.%, 0.3 mL: 10 hours, 37°C; 18 hours, 37°C, 0.5 mL PBS		5 days	

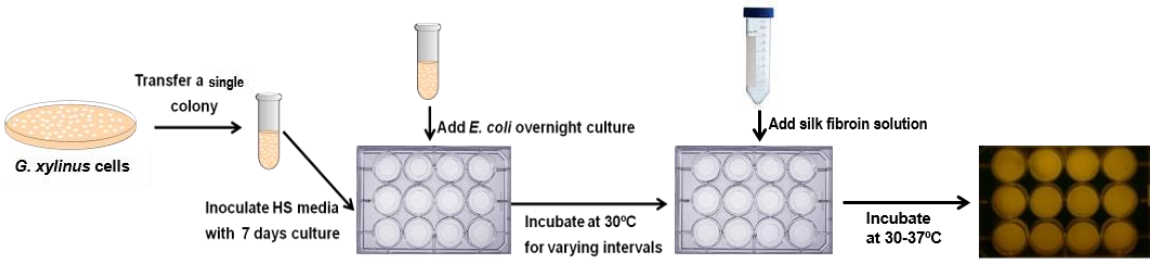

Figure 8.1. Scheme outlining the formation of the primary BC matrix and encapsulation of recombinant *E. coli* cells in pure BC or composite BC-SF matrices.

Initially, the formation of stable BC pellicles had to be established, which required growing a single colony of *G. xylinus* cells for 3 days. Typically, during static cultivation, the cellulose matrix develops into a continuous polymer network of individual membranes accumulated at the air-liquid interface. The pellicle thickness was directly proportional to

the time of cultivation and was mainly limited by media carbon source and level of oxygenation.[331,332] The initial pellicle thickness was controlled to not exceed 2-3 mm thick as other consecutive steps were required for entrapment of recombinant cells. Followed the formation of the initial BC matrix, the pellicles were inoculated with recombinant *E. coli* cells and co-cultured for another 3 days. This allowed a symbiotic relationship to be established between both types of cells and ensure homogeneous distribution of *E. coli* cells within the BC scaffolds. The typical thickness of pure BC scaffolds entrapping the recombinant cells was approximately 6-7 mm. The pellicle continued to accumulate during co-culturing of *E. coli* in *G. xylinus* supportive media, which also demonstrated the compatibility of the technique to entrap secondary organisms within individual BC membranes.

Composite BC-SF scaffolds were produced by adding an aqueous solution of SF to already established colonies of *E. coli* cells (typically after 1 day of inoculation) to yield two types of composite BC-SF scaffolds: opaque and transparent. Opaque composite BC-SF scaffolds were generated by adding 3-3.5% w/w aqueous SF solution in the ratio of 0.6:0.4 BC-SF (w/w) and incubated for additional 3 days (30°C). Transparent composite BC-SF scaffolds were formed by adding 7-7.5% w/w aqueous SF solution in the ratio of 0.4:0.6 BC-SF (w/w) followed by incubation for 28 hours (37°C).

The addition of SF during the growth of recombinant cells in the BC-SF matrix had a significant effect on the physical properties of the composite scaffolds. By controlling drying rate and water content in BC-SF scaffolds, composite scaffolds were produced with different mechanical and optical properties (Fig. 8.2). Fig. 8.2a depicts the differences in absorbance between pure BC, opaque BC-SF and transparent BC-SF scaffolds with

comparable amounts of *E. coli* cells loaded to pre-formed BC matrices (10^8 cells). Regardless of the scaffold composition, there was a linear correlation between *E. coli* loading and optical properties of the scaffold matrix, demonstrating decreased transparency with increased amounts of *E. coli* cells (Fig. 8.2b).

The opacity of pure BC scaffolds was related to the continuous mass accumulation (both cells and cellulose) during longer incubation periods (3 days). Apart from pure BC scaffolds, variability in physical properties of composite BC-SF scaffolds can be explained by the differences in conformational changes of SF secondary structure during sol-gel

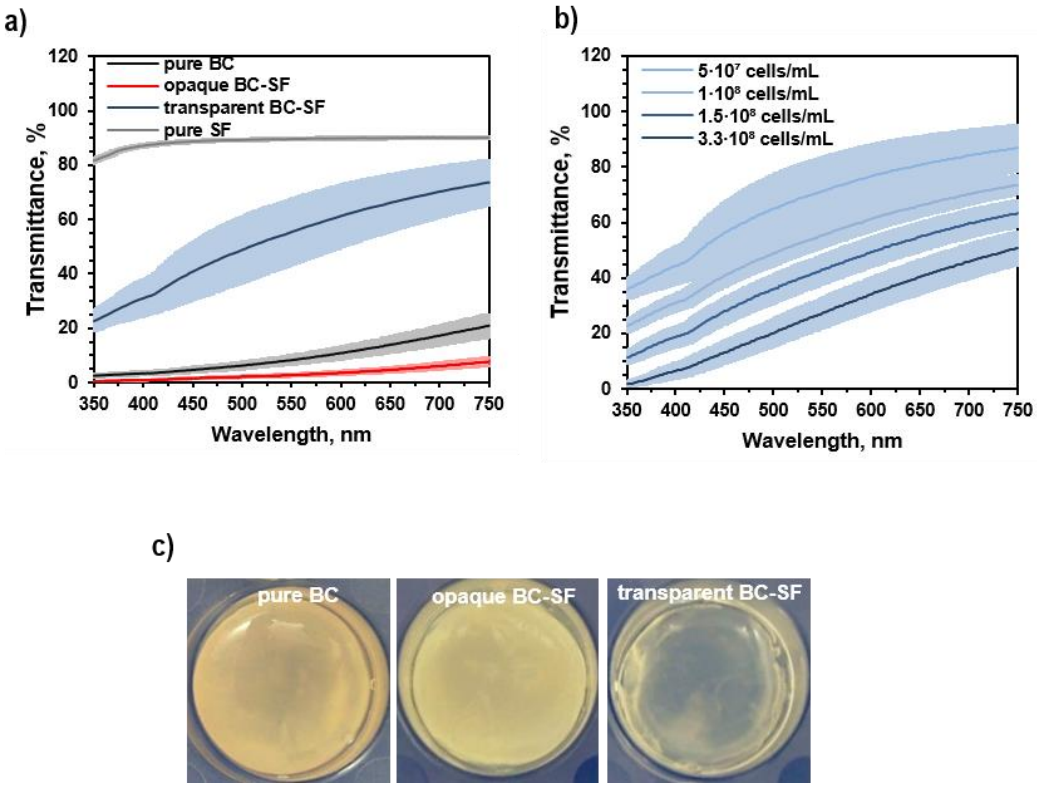

Figure 8.2 UV-Vis spectra of pure BC and SF films, opaque BC-SF and transparent BC-SF scaffolds with comparable *E. coli* cell numbers added initially to the growing BC pellicles ($1{\cdot}10^8$ cells) as a function of secondary structure of SF during processing conditions (a). UV-Vis spectra of transparent BC-SF scaffolds as the function of *E. coli* cells added to growing pellicles prior to adding SF (b) (n=4, ± SD). Typical optical images of pure BC, opaque and transparent BC-SF composite pellicles produced according to the procedures outlined in the Methods (c).

processing. Degradable opaque BC-SF composite scaffolds were produced as the result of

formation of metastable supramolecular fibroin structures comprised of an amorphous bulk structure (random coils, α helixes, β turns and bends) with a low content of β sheets.[333] On the other hand, water-stable transparent BC-SF scaffolds were formed *via* conditions closely matching water annealing.[334,335] These scaffolds were reported to have higher thermodynamically stable silk II content (antiparallel β sheets) than silk I content (hydrated type II β-turns), and were translucent, held more water and were temperature stable.[334,335]

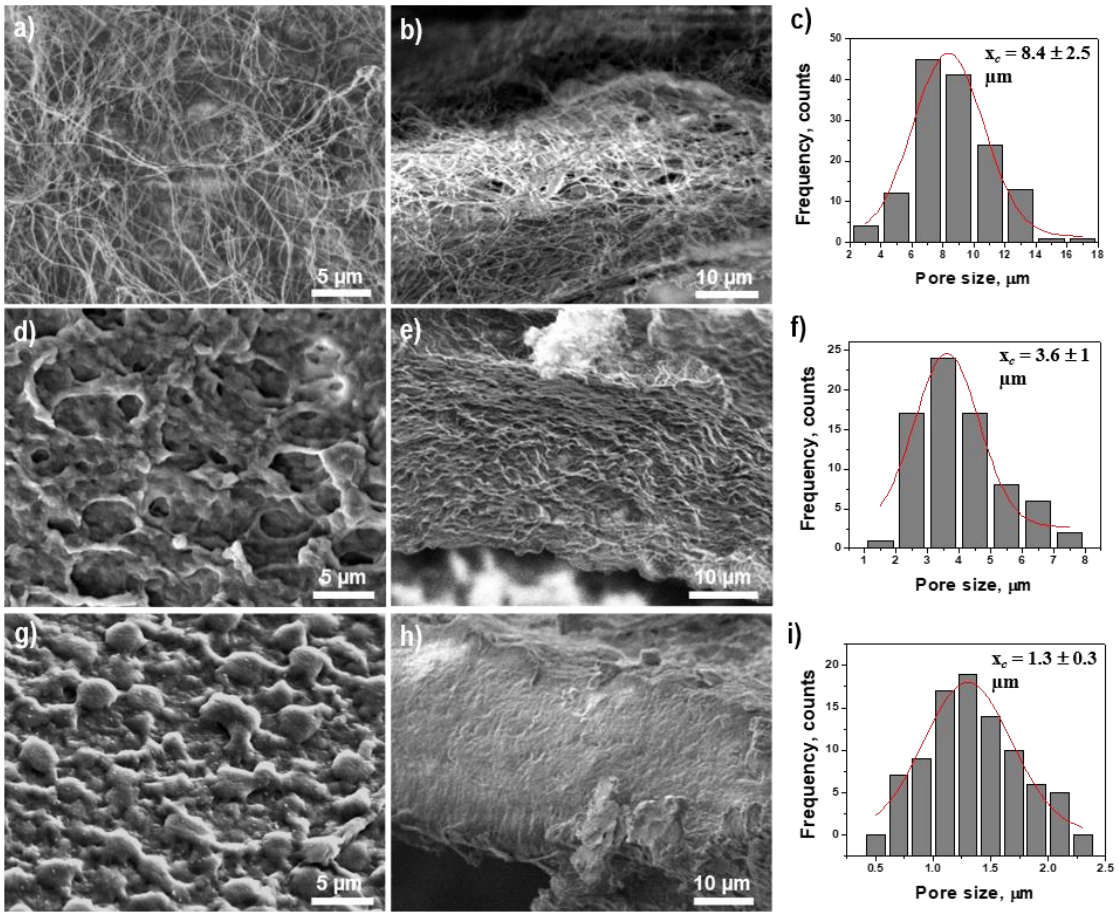

Figure 8.3 SEM images and pore size distribution of pure BC (a-c), composite opaque (d-f) and transparent (e-i) BC-SF scaffolds. The surface topography (a, d, g) and cross-sectional (b, e, h) views were taken from lyophilized scaffolds.

Microstructurally, pure BC and composite BC-SF scaffolds also differed significantly. Fig. 8.3 illustrates the morphology of the nanofibril network arrangement in lyophilized BC and

BC-SF scaffolds and provides the distribution of pore sizes for each type of scaffold. Assessing the pore sizes in all types of the scaffold matrices allowed them to be classified for optimal designs to provide complete entrapment of the cells, as well as to predict permeability of analyte molecules. Pure BC scaffolds formed a continuous 3-D network of intertwined cellulosic nanofibrils with void spaces exceeding the length of rod-shaped *E. coli* bacteria (typically 2 μm in length) (Fig. 8.3a-b). The pore sizes of a mesh-like network structure were 8.4 ± 2.5 μm, through which a transit of individual motile recombinant cells occurred. Composite BC-SF scaffolds formed heterogeneous network structures where cellulose nanofibrils were covered by SF solution. During formation of BC-SF nanocomposite scaffolds with varied amounts of SF, an increased concentration of SF led to decreased porosity, and the mesh size of the network was reduced below 2 μm for BC-SF scaffolds with highest SF concentration (7% w/w). This input effectively allowed the loss of recombinant cells to the surrounding media to be minimized and ensured complete retention of *E. coli* cells, particularly in the transparent BC-SF composite scaffolds.

8.2.2 Water absorbency, water retention and mechanical properties

Measurements of the swelling ratio and water absorption capacity were performed after incubation of the scaffolds in DI water for 24 hours demonstrating the reduction in water uptake capacity across BC and BC-SF scaffolds as SF content increased in the composite scaffolds. Pure BC scaffolds were highly saturated with water (94% of moisture content) and demonstrated up to a 14-fold increase in swelling ratio from the dry weight. Over 90% of the total water content was absorbed within 30 min, emphasizing the highly porous nature of the BC scaffolds.

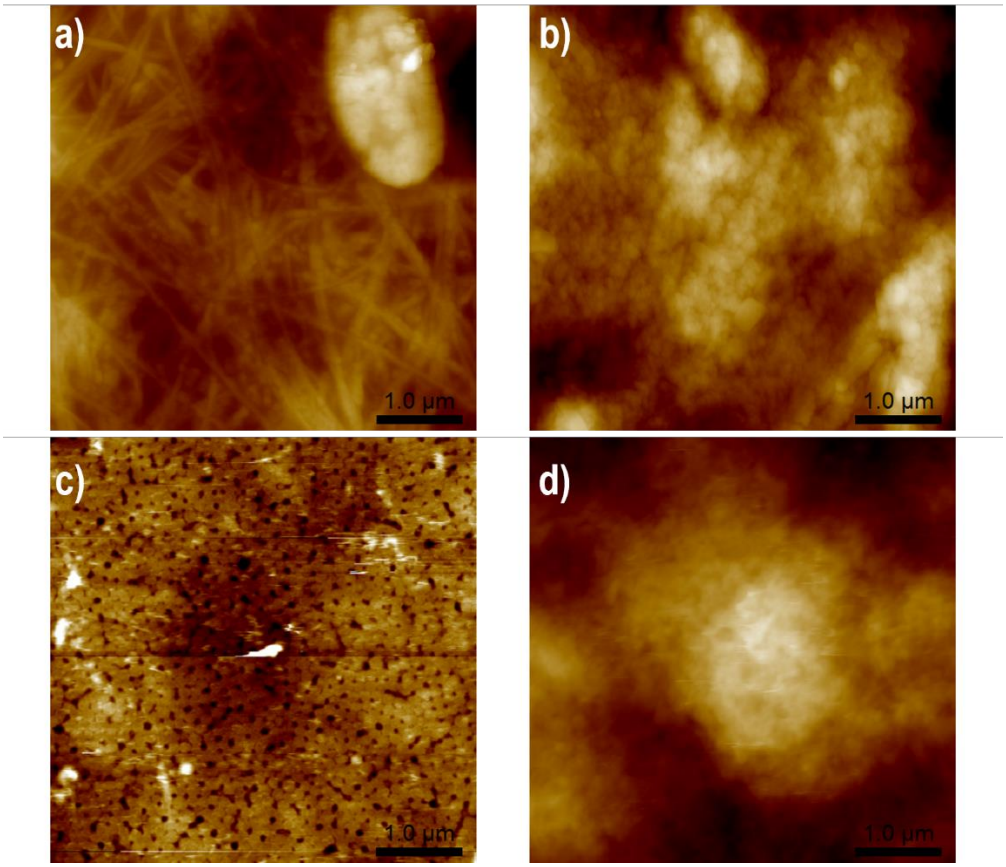

Figure 8.4 AFM topography images of pure BC (a,c) and transparent BC-SF (b,d) scaffolds taken under ambient condition (a,b) and fluid scanning (c,d).

In composite BC-SF scaffolds, the swelling ratio decreased to about half of that for the BC scaffolds, however the water content declined only slightly. Opaque BC-SF scaffolds had a 6.4-fold increase in swelling ratio with a 91% water content. Transparent BC-SF scaffolds showed a 4.6-fold swelling ratio and 86% water content. Mechanically, composite BC-SF scaffolds had significantly improved elastic properties, with an increase in Young's modulus by three orders of magnitude in comparison to pure BC matrix. As can be seen in the AFM topography results obtained from the scaffolds (Fig. 8.4), the addition of silk fibroin causes much of the loosely packed cellulose matrix to be filled with silk, thereby

reducing the amount of space accessible to incoming water. Interestingly, the addition of SF leads to an increase in the RMS roughness of the topography in Fig. 8.4 a,b (58 nm to 78 nm over a 5 μm^2 area). This behavior is even more complicated in the case of hydrated pellicles (Fig. 8.4 c,d). While the roughness of pure BC samples decreases down to ~10 nm, seemingly due to the closure of pores, the roughness of BC-SF composite increases by almost 50% up to ~114 nm once hydrated. A visual comparison of Fig 8.4 b and d suggests that this is due to an increase in the micron scale roughness, perhaps indicating a swelling mismatch in the composites.

Stiffness of pure the BC matrix (in wet state) was derived from the interpretation of FDCs obtained with AFM indentation using colloidal probes. The FDC obtain for the pure BC sample (Fig. 8.5a) demonstrates the extreme compliance of the gel, with virtually no plastic deformation after several microns of indentation and no observable adhesion on the retract curve. By comparison, the result (Fig. 8.5b) from the transparent BC-SF pellicle shows a more typical FDC with moderate penetration, plastic deformation, and adhesion. The results were analyzed (Fig. 8.5c) with a Hertzian contact model to give an effective modulus of 16.1 ± 9.2 kPa for the pure BC. In contrast, indentation results for the BC-SF pellicles indicated a modulus of 9.6 ± 1.9 MPa for the opaque and a modulus of 13.4 ± 3.6 MPa for the transparent scaffolds. The apparent decrease in water absorbency and gain in elastic properties were due to the increased SF content. The astounding changes in the values of stiffness (roughly 3 orders of magnitude) are likely due to the replacement of water with SF in the pore volume and the increased binding provided to limit sliding between the nanofibrils.

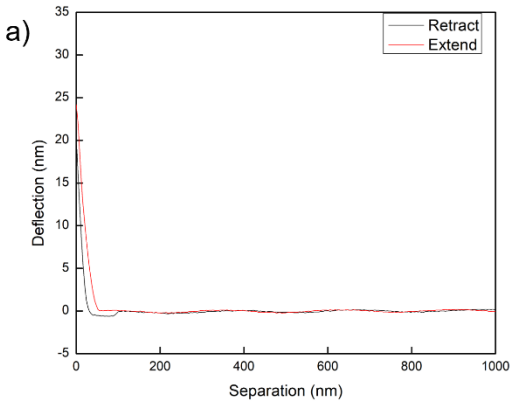

c)

Type of Scaffold	Young's Modulus
Pure BC Scaffolds	16.1 ± 9.2 kPa
Opaque BC-SF Scaffolds	9.6 ± 1.9 MPa
Transparent BC-SF Scaffolds	13.4 ± 3.6 MPa

Figure 8.5 Force distance curves for pure BC (a) and transparent BC-SF (b) scaffolds taken under fluid condition. Comparison of Young's modulus (in swollen state) for pure BC and composite opaque and transparent BC-CF scaffolds (c).

This increase in microscale stiffness also lead to a pronounced reinforcement of the scaffold on the macroscale, causing the dried scaffolds to become more rigid, but also more

brittle. The effect of scaffold affects properties beyond those related to processing the material, however. It has previously been demonstrated[336] that the modulus of a scaffold has a direct impact of the speed of cellular migration through the scaffold material. In addition, there have been several reports demonstrating the effect of scaffold stiffness on the stem cell differentiation fate for mesenchymal stem cells.[337,338] Composite materials have been shown previously to be an effective method of enhancing scaffold modulus for altering cellular gene expression.[339] It should be noted that the bulk modulus of the scaffold material may not correspond with the stiffness encountered by individual cells in non-homogenous materials. The probe size and forces used in the indentation closely match those of *E. coli* cells that have been previously studied, thus the stiffness measurements obtained here are likely good approximations of the stiffness observed at the cellular level.[340]

8.2.3 Activation of dual-color riboswitch in E. coli cells

Co-cultivation of cellulose producing bacteria with secondary catalytic organisms led to the development of a "compatible living membrane". Due to the symbiotic relationship (in terms of viability) between *G. xylinus* and the recombinant *E. coli* cells, co-cultivation of both types of cells allowed the formation of dynamic 3D structures, where differential development of *E. coli* cells was somewhat limited by the cellulose polymer network. Recombinant *E. coli* cells utilized in this study were transformed with a bidirectional reporter system, consisting of recombinase FimE controlled by theophylline synthetic riboswitch and an invertible DNA segment containing a constitutively active promoter placed between two fluorescent protein genes, GFPa1 and mKate2.[341] This system allowed us not only to localize and assess the fitness of encapsulated *E. coli* cells, but also to

monitor the occurrence and propagation of fluorescence signal across the living membrane. In the absence of a target analyte (theophylline), cells expressed GFPa1 protein and hence appeared green and viable, causing the whole pellicle to fluoresce green. However, when the analyte was present, produced FimE recombinase facilitated the inversion of the promoter leading to constitutive expression of mKate2 protein, causing the cells and the scaffold to appear red.

The facultative nature of *E. coli* cells allowed them to achieve flexibility in maintaining baseline populations while supporting cellulose productivity by the *G. xylinus* cells. Since it was not possible to directly estimate the density of recombinant cells in the final pellicles, the dual-color reporter system allowed us to qualitatively assess the amount of viable *E. coli* cells based on the level of GFPa1 intensity. The loading number of *E. coli* cells added to the growing cellulose pellicles had a direct correlation on the cell growth and hence the level of expression for fluorescent proteins. Hence, with the higher number of entrapped cells, the higher level of inducible signal was achieved. On the other hand, with increased loading of *E. coli* cells (typically above 10^9 cells), the crossover in color predominance between non-activated and activated cells was delayed, limiting the sensitivity of the recombinant cells to detect the target analyte. Thus, the optimal loading number of cells was set between $5 \cdot 10^7$ and $1 \cdot 10^8$ cells to balance the two signals.

The high porosity of pure BC scaffolds, along with large amount of water entrained within cellulosic membranes provided fast diffusion for analyte molecules to reach the recombinant cells entrapped in the structures and elicit the response. From a materials point of view, pure BC scaffolds promoting fast activation of cells might seem optimal for the storage of recombinant cells. However, during incubation in the reaction buffer, *E. coli*

cells were able to easily escape from highly porous cellulosic membranes under sheer forces. As illustrated in Fig. 8.3, the microstructure of cellulose membranes consists of loosely intertwined nanofibrils with the mesh pore sizes much greater than the size of recombinant cells. This highly porous scaffold supported continuous efflux of *E. coli* cells into the media where they then proliferated, causing an increase in fluorescence signal and optical density. On the other hand, when the recombinant cells were encapsulated in the composite BC-SF scaffolds, the cell escape was significantly reduced only for the transparent BC-SF matrix. Opaque BC-SF scaffolds demonstrated a modest decrease in efflux of planktonic cells due to the specific microstructure of the composite matrix. The processing of low viscosity SF during the formation of opaque BC-SF pellicles reduced pore size (Fig. 8.3c-d). However, the void dimensions were not reduced sufficiently to hinder the leakage of the cells. With a higher content of SF in the composite BC-SF matrix, a denser network structure was formed, reducing the effective voids (Fig. 8.3e-f) and hindering the escape of *E. coli* cells from BC-SF scaffolds. Hence, only the transparent composite BC-SF scaffolds (with higher content of SF) provided the most effective entrapment matrix that both *supported* catalytic activation and *hindered* diffusion of recombinant cells.

8.2.4 Distribution of activated E. coli cells in cellulose-based scaffolds

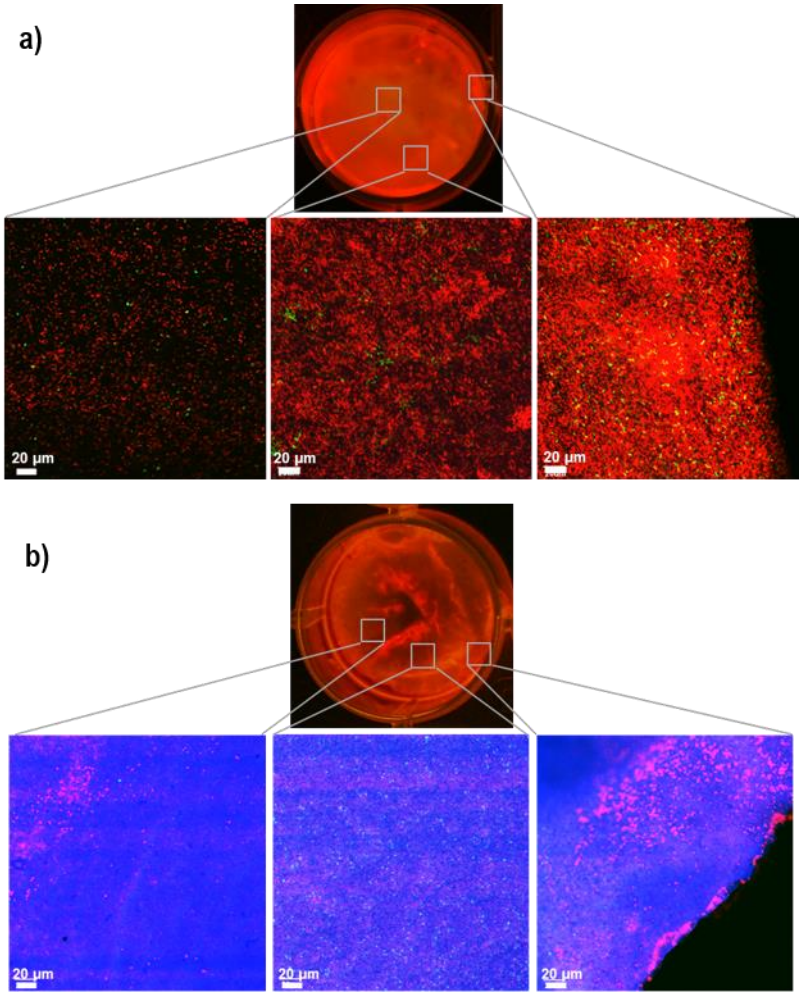

Figure 8.6 Distribution of *E. coli* cells encapsulated in pure BC (a) and transparent BC-SF (b) composite scaffolds after incubation in the reaction media for 48 hours (2.5 mM theophylline, DMSO, 37°C, 110 rpm). Optical fluorescent image of the whole pellicle was combined with three confocal images from the selected areas. Red fluorescence was attributed to *E. coli* cells expressing inducible mKate2 protein (activated cells), green fluorescence was representing *E. coli* cells constitutively expressing GFPa1 protein (non-activated cells) and blue fluorescence was associated with intrinsic fluorescence of SF.

Fig. 8.6 illustrates the differences in spatial distribution of recombinant cells within pure and composite scaffolds after continuous cultivation for 48 hours. Spatial fluctuations of fluorescence intensities were indicative of the preferential density of *E. coli* cells. As shown in localized confocal images, activated *E. coli* cells were radially distributed across pure BC pellicles, with the central region having the lowest cell density and the periphery of the

pellicles the highest (Fig. 8.6a). Such behavior can be explained by the continuous influx of actively proliferating motile bacteria back into the BC matrix. The inward propagation of cells was due to the highly porous microstructure of the pure BC network, which led to a gradual saturation of the pellicle circumference with activated cells.

In contrast to pure BC scaffolds, where the distribution of *E. coli* cells was mainly limited by media resources, the final localization of recombinant cells in the transparent BC-SF scaffolds occurred during sol-gel processing of SF. In the composite scaffolds, recombinant cells were restricted in the movement due to reduced porosity of the matrix. Fig. 8.6b illustrates the spreading of activated *E. coli* cells after 48 hours of cultivation of transparent BC-SF pellicles in reaction media. In a contrast to the BC matrix, the recombinant cells had an even concentration across the composite matrix with some small irregularly distributed high cell density colonies. Since the porosity of the composite matrix was less than the effective radii of the recombinant cells, the formation of local populations might have been occurred during the processing of SF. With time permitted to form several generation of bacterial cells (processing of SF occurred within 10 hours), small populations of *E. coli* cells were formed, which later were confined to the spaces limited by excess of SF. The ability of cells to undergo division during SF processing illustrates the compatibility of the current technique for cell encapsulation process. Hence, composite BC-SF matrices with a higher SF content (~7% w/w) provided preferable conditions for colonization and nesting of bacteria, and for the isolation and activation of recombinant cells.

8.2.5 Protection of BC-SF scaffolds against UV light

The effectiveness of the reconstituted SF protein incorporated into the BC scaffolds to protect recombinant bacteria against UV radiation was investigated. BC-based pellicles (both pure and composite) containing comparable cell loading numbers were exposed to a narrow bandwidth UV light centered at λ=254 nm (dose of irradiation was 380 $J \cdot cm^{-2}$). Time-course studies revealed different levels of bacteria susceptibility to UV radiation under conditions exceeding the recommended doses for inactivation of *E. coli* bacterial populations (~36 $mJ \cdot cm^{-2}$).[342] Particularly, UV-treated suspensions of bacterial cells (positive control) did not proliferate and lost their ability to react to an inducer analyte over the course of study (Fig. 8.7a). Similarly, *E. coli* cells encapsulated in pure BC scaffolds lost their ability to respond to the presence of analyte and did not show RS activation (Fig. 8.7b). In contrast, *E. coli* cells encapsulated in composite BC-SF scaffolds demonstrated response recovery, however, not to the same extent as non-UV treated cells

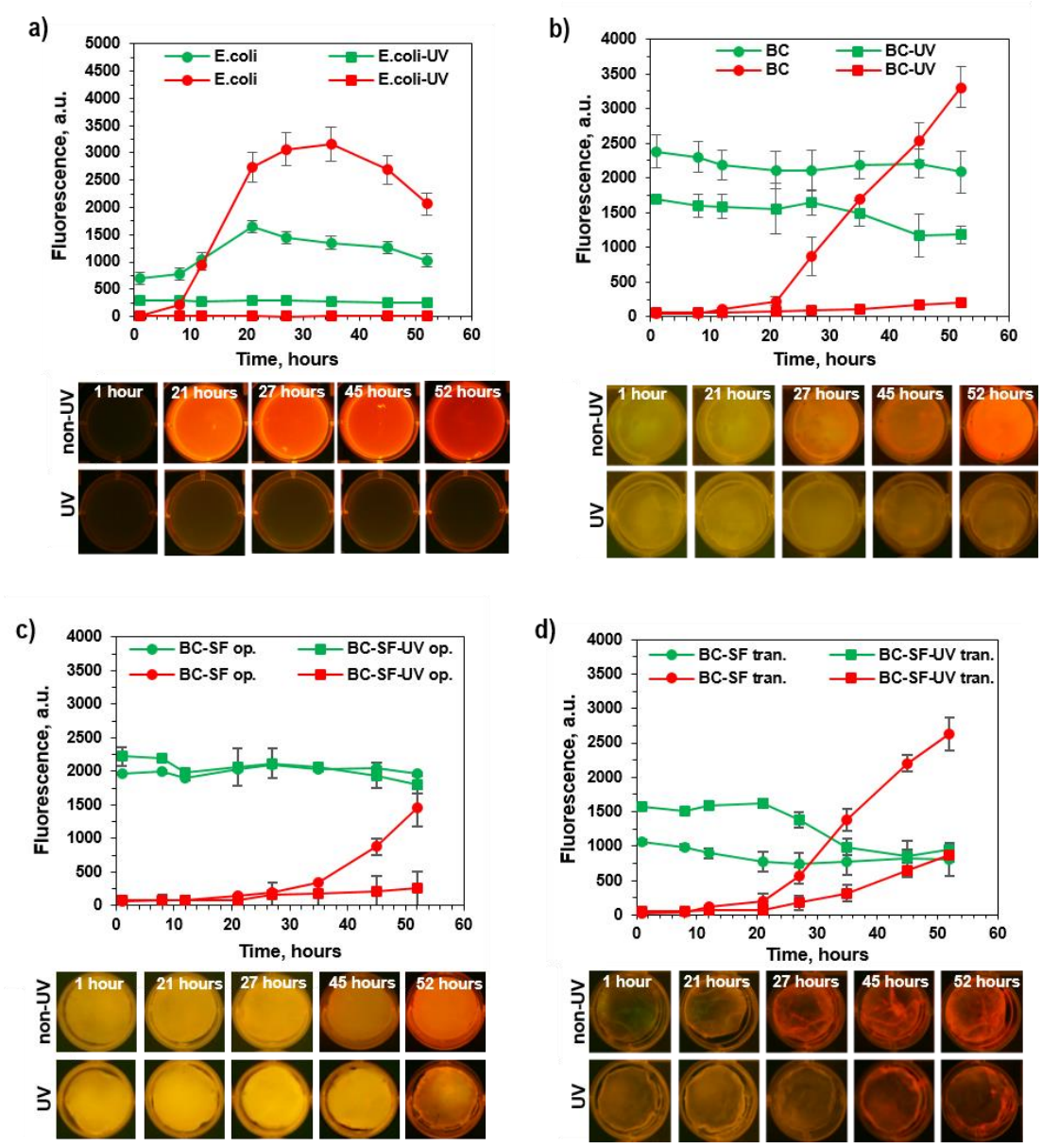

Figure 8.7 Comparison of RS activation in *E. coli* cells after UV irradiation (254 nm, 3.8 MJ·m^{-2}). Non-encapsulated *E. coli* cells (control) (a) were cross-referenced with cells encapsulated in pure BC (b), opaque BC-SF (c) and transparent BC-SF (d) scaffolds. Kinetics of fluorescence accumulation in pellicles (for both GFPa1 (green lines) and mKate2 (red lines) proteins) were compared to optical images captured at specified time points. Cells were induced with 2.5 mM theophylline (100 mM, DMSO) and incubated in LB media (37 °C, 110 rpm). (Data shown as average ± SD (n=8) from two independent experiments).

immobilized in the same type of matrix. Even though, the activation of cells was initiated at the same time point, the response rate was significantly slower. The gain in fluorescence intensity from the recombinant cells encapsulated in opaque BC-SF composite scaffolds

occurred after 52 hours of post-induction (Fig. 8.7c). Maximum fluorescence for *E. coli* cells encapsulated in transparent BC-SF scaffolds reached about half of that for the non-UV treated scaffolds (Fig. 8.7d).

Two factors were attributed to the bacterial survival in BC-SF scaffolds: the ability of SF to absorb light in UV-C region and the confinement of *E. coli* cells in the composite matrix. Absorption of SF protein in 200-280 nm range is accredited to aromatic amino acids residues, tyrosine (Tyr, 5.3 mol.%), tryptophan (Trp, 0.5 mol.%) and phenylalanine (Phe, 0.6 mol.%) that have distinguishable absorption peaks at 228 and 278 nm.[35] Increased *β*-sheet structure during the formation of solidified silk fibroin films can enhance optical responses further.[343] Such an effect was attributed to stronger intra- and inter-molecular hydrogen bond interactions including the aromatic amino acids, specifically $\pi \rightarrow \pi^*$ charge transfer transitions of Tyr and Trp aromatic rings.[344] We observed significant enhancement in absorption peaks for water vapor annealed SF cast films compared to the corresponding SF solutions that also linearly correlated to SF concentration. Alternatively, during the formation of composite BC-SF scaffolds with higher SF content (7% w/w), water-annealing treatment might enhance secondary structure towards thermodynamically stable *β*-sheet conformations, increasing silk II content.[333,335,343] Hence, by inducing *β*-sheet structure during the formation of composite scaffolds, UV–light absorption or blocking can be enhanced, enabling the recombinant cells encapsulated in high content SF composite scaffolds improved protection against UV exposure.

In addition to UV absorption, the protective potential of composite BC-SF scaffolds was indirectly attributed to prompting clustering of *E. coli* cells.

8.3 **Conclusions**

Encapsulation of recombinant *E. coli* cells harboring dual color RS was performed in biocompatible composite scaffolds consisting of a bacterial cellulose matrix supplemented with reconstituted silk fibroin material. The ease and simplicity of the present technique relied upon the symbiotic relationship between both bacterial organisms, where one provided a polymeric matrix for immobilization and storage of the secondary organism. By varying the composition ratio between cellulose and the additive SF, as well as processing conditions and viscosity for SF during the formation of composite scaffolds, matrix properties can be controlled. The optimal encapsulation matrix was accomplished when higher concentration and content ratio of SF was used. It led to the formation of robust and phototransparent composite scaffolds with matrix properties closely matching extracellular environment. The closer-fitted pliable and biomimetic composite scaffolds not only preserved recombinant function of the entrapped recombinant cells, but also improved their metabolic potential. When exposed to UV-light, cells were able to recover, respond and activate analyte-induced heterologous genes. Both factors, the spatially-confined environment and the UV-absorbing properties of SF allowed *E. coli* cells to better maintain their ability to express the recombinant properties and resist additional stress associated with exposure to UV light. Adopting the present immobilization technique on a macroscale level can be beneficial for some of biotechnological applications that require phototransparency of the material host to be surveyed from a long distance.

CHAPTER 9. REMOTE GIANT MULTISPECTRAL PLASMONIC SHIFTS OF LABILE HINGED NANOROD ARRAY VIA MAGNETIC FIELD

9.1 Introduction

The ultimate goal in design effective stimuli-responsive nanomaterials is to fabricate quick, large-scale, easily detectable, and reversible systems by readily-available means.[135] Great interest has focused on the concept of materials whose physical properties can be reversibly controlled through a weak external stimulus such as changes in wettability[345], color[346], and shape[347]. In order to be universally effective, such material responses should be reversible, tunable, and operate on appropriately small time scales. While some of these criteria have been met in recent material designs, it is rare to find a system in which all three are satisfied. Plasmonic materials with local surface plasmon resonance (LSPR) are considered to be excellent candidates for colorimetric responsive systems, since their optical properties (i.e. absorption and scattering) can alter with minor changes to a system[348]. Many successful attempts at responsive LSPR systems have involved incorporating nanoparticles with a polymer gel that undergoes a volume phase transition349 to reposition the load particles and, effectively, change the local refractive index and coupling behavior.350 These gels typically require control over the environmental conditions of a system (e.g. pH[351], light [352], e-field[353], or temperature[354]) in order to direct the phase of the materials. In many cases, these slow responsive (minutes-hours response time) materials have difficulties with producing instant responses, since the transition is controlled by slow diffusion processes.

To date, very few examples of fast responding systems based, for instance, upon liquid crystalline materials have been demonstrated.[355]

Self-assembly of anisotropic metal nanostructures with rich plasmonic properties has been though to yield novel responsive plasmonic structures. [356,357,358] Recent studies have demonstrated the utility of anisotropic nanostructures with reversibly altering plasmonic and photonic properties via particle reorientation and chain aggregation.[153,160,359] However, common shifts in the position of an individual optical band are very modest, usually below 20 nm, which makes difficult to utilize these changes.[360,361] Further, nanorods with magnetic and plasmonic metals have shown promise as building blocks for hybrids nanostructures but their spontaneous bundling prevents reversible behavior.[362] However, the response times for these systems can be rapid, and the stimuli used have the potential to act remotely, at long-range, without altering composition of the material if spontaneous aggregation can be suppressed.

Here, we demonstrate an approach which allows for the rapid and remote manipulation of the optical signature with dramatic and reversible optical shifts concurrently at multiple wavelengths reaching 100 nm with external magnetic field. These changes far exceed current literature examples and are caused by variable coupling of incident light and surface plasmon polariton (SPP) modes of plasmonic-magnetic nanorods. The basis for this unusual phenomenon is precisely controlled reversible reorientation of hybrid nanorods and flexibly hinged to the sticky substrate that prevents spontaneous bundling but leave orientational freedom. This is also in contrast to current designs, in which large-scale responsive behavior is elusive due to the difficulty in dealing with the confined nanostructures with arrested mobility.[363,364,365,366,367]

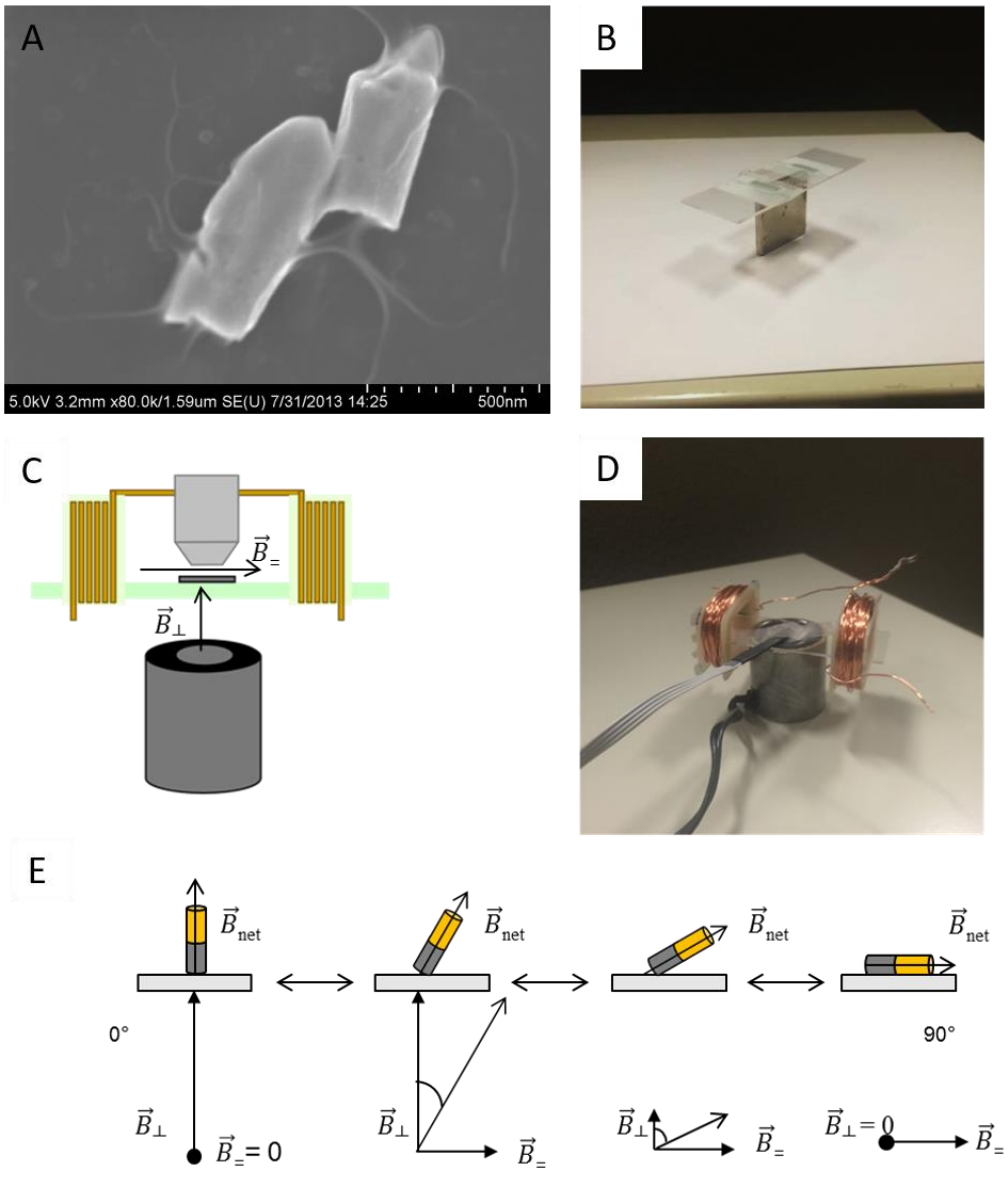

Figure 9.1. A SEM image on nanorods partially tethered by polymer multilayers. **B** Simple rare earth magnet tilting setup. (**C**-**E**) Orthogonal, two magnet tilting system. **C** Idealized operation of two manget system under microscope lens. **D** Actual two magnet system with attached Gauss meter. **E** Mechanism of controlled nanorod tilting under two magnet system.

To facilitate this approach, we synthesized hybrid, segmented, dimer nanorods with a nickel magnetic segment combined with a gold segment (Fig. 9.2A). This design is essential for direct assembly of aligned, uniformly oriented magnetic-plasmonic nanorods into an ordered large-scale monolayer under a magnetic field applied to the dispersed nanorod solution.[368] These segmented nanorods were used as a model system containing both magnetically and optically "active" segments and chosen from different designs.[368]. These nanorods were functionalized with a polyvinyl pyrrilidone (PVP) coating which serves as a means to tether the nanorods to the PVP-coated polymethacrilic acid (PMAA) substrate as shown in Fig. 9.1 A.[369] For these experiments, we utilized symmetrical cylindrical nanorods with a diameter of 250 nm and equal lengths of the gold and nickel segments of 400 nm to assure the location of the SPP in the visible wavelength range (Fig. 9.2 A). Upon assembling the nanorods in a uniformly-oriented vertical fashion onto a polymer coated substrate, the nanorods are hinged with substrate, which allows unconstrained nanorod tilting whilst restricting their lateral translation. Two different methods are used to control this rotation: permanent magnet placement (for angles of 0 (vertical) or 90^{o} (horizontal)) or two orthogonal electromagnets (for variable direction of magnetic field) (Fig. 9.1 B-E).

9.2 **Results and Discussion**

As we observed, under the influence of an external magnetic field, the tethered Au-Ni nanorods are capable of realigning to minimize their magnetostatic potential in a uniform manner. A magnetic field perpendicular to the substrate will tend to align the nanorods in an upright orientation (designated as 0^{o}). Due to the uniform nanorod alignment (magnetic segment in contact with substrate, Fig. 9.2 A), the light scattered by the monolayers appears

as an orange-red hue (Fig. 9.2 C,E). Changing the orientation of the magnetic field by 90^{o} causes the nanorods to preferentially lie flat on the substrate as revealed by SEM from freeze-dried arrays while also occasionally causing nanorod chains to form due to weak tethering. Consequently, a dramatic change in the color appearance of scattered light occurs (Fig. 9.2 D,F). The spectral measurements from individual nanorods show dramatic and reversible changes from three well-defined plasmon peaks to nearly featureless rising scattering after nanorod realignment (Fig. 9.2 B). This unexpected behavior is in contrast to the conventional scenario of changing the ratio of the transverse and longitudinal modes due to the realignment of gold nanorods[370] and can be attributed to the angular dependence of light coupling to SPP modes, as discussed below.

From the optical spectra of the vertical nanorods, three distinct scattering peaks can be observed under transverse electric and magnetic polarization (Fig. 9.2 B). Finite-difference time-domain (FDTD) simulations were used to calculate E-field enhancements that indicate that the different peak positions correspond to the formation of standing waves with 5, 4, and 3 nodes (Fig. 9.2 B). The FDTD simulated spectra are in good agreement with the scattering peaks observed experimentally. These modes are caused by Fabry-Perot interference owing to the finite length of the nanorods as suggested.[371,372,373] The longitudinal and transverse plasmon modes for the flat nanorods were not observed experimentally or in simulations. This appears to be an effect of the silicon substrate, as FDTD simulations on non-substrate bound nanorods indicate major peaks around 770/912 nm (beyond experimentally measurable range) and 624 nm for longitudinal and transverse excitations, respectively.

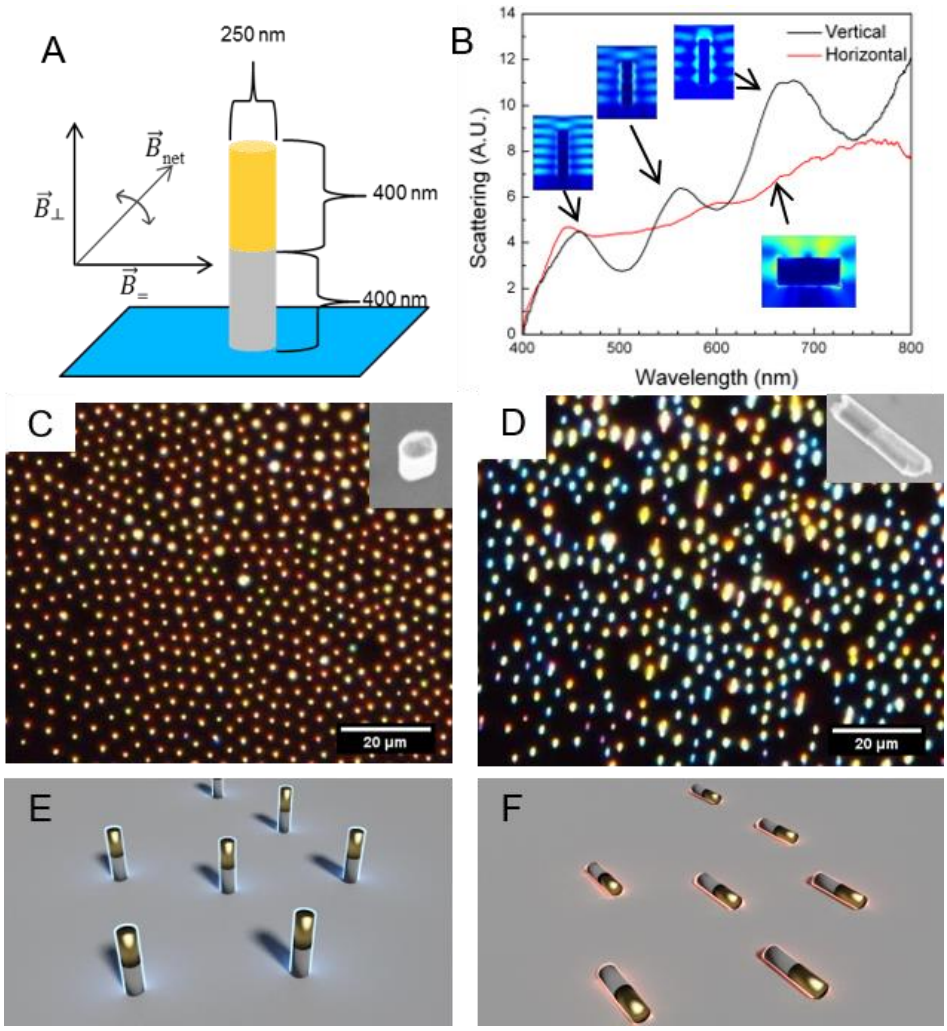

Figure 9.2. A Design of dimer segmented gold-nikel nanorod flexible attached to the substrate and a scheme of two orthogonal magnetic field vectors drawn for reference. **B** Comparison of scattering spectra obtained for the two different nanorod orientations. Insets represent the FDTD calculated E-field plots for the indicated peak positions and non-specific scattering from fully tilted nanorods. **(C, D)** Dark-field microscopy images of nanorod assemblies aligned perpendicular (**C**) and parallel (**D**) to the substrate and corresponding schematics (**E, F**). Insets represent SEM images obtained from freeze-dried sample showing the orientation of individual nanorods.

This phenomenon caused by the coupling of light to nanowires of finite length and is the result of Fabry-Perot interference that occurs due to the repeated reflection of the polariton off the distal end of the nanowire. Due to constructive interference, metal cylinders of finite length will exhibit enhanced SPP formation for certain wavelengths ($\lambda \sim 2l/n$), where l is the effective nanorod length[374].

As known, excited modes in finite nanorods typically exist when the resonance conditions (given above) and the surface plasmon polariton dispersion relations are both satisfied. The coupling of light to an SPP mode is given as, $k_0\sqrt{\varepsilon_2}\sin(\theta) = Re\left(\frac{2\pi}{\lambda}\sqrt{\frac{\varepsilon_1\varepsilon_2}{\varepsilon_1+\varepsilon_2}}\right)$ (k_0 is the wavevector of incident light, λ is the wavelength of the surface plasmon, ε_1 and ε_2 are the permittivities of the metal and dielectric medium, respectively, and θ is the angle of incidence of the light).[375] Due to limitations in the experimental setup, only three of these SPP modes can be observed, but some of the lower order modes appear in the FDTD calculated spectra.

Generally, if the peak scattering wavelengths are shifted, the number of "nodes" formed by the SPP is conserved. This, in turn, implies that the wavevector of the SPP is kept relatively constant (since the wavevector governs the spatial frequency of the maxima). Since the wavevector parallel to the rod axis, k_z, is inversely proportional to $\sin(\theta)$, the wavelength of the incident light must decrease by the same factor in order to keep k_z constant. The allowed wavevector and frequency of an SPP mode is set by its dispersion relations, though, as will be discussed later, multiple SPP modes may be present and have a unique set of allowable wavevector and frequency pairs.

Increasing the tilt angle of the nanorods was found to systematically blue-shift the SPP modes as is apparent from dark-field images of individual nanorods (Fig. 9.3 A) and optical spectra (Fig. 9.3 B) obtained from a modified single magnet approach and a two orthogonal electromagnet setup, respectively.

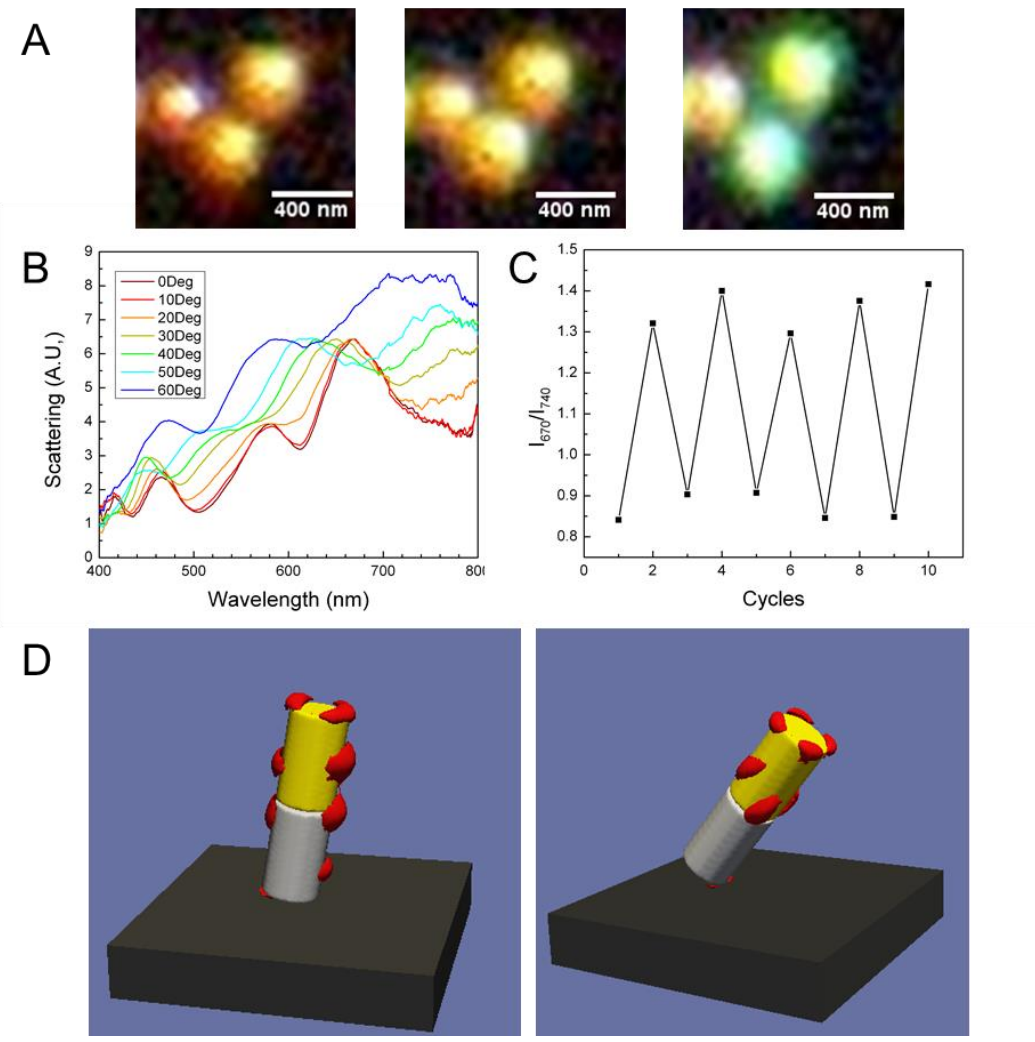

Figure 9.4 A Dark-field optical images of nanorods with increasing tilt obtained as substrate is translated across surface of magnet. **B** Plot of experimental scattering spectra for a single nanorod at 7 different tilt angles as controlled by magnetic field. **C** Reversibility of nanorod tilt (from 0° to 90°) expressed in terms of recovery of peak at 670 nm (normalized to intensity at 740 nm). **D** Generated 3-D E-field plots for nanorod at (left) 10 degree tilt and 652 nm excitation and (right) 10 degree tilt and 628 nm excitation.

To test the reversibility of these dramatic changes of optical spectra, we reoriented the nanorods in a cyclic fashion and monitored spectral response for a single nanorod. Cycling the nanorod orientation shows excellent reversibility and full recovery of initial SPP modes after each reorientation (Fig. 9.3 C). The fully tilted nanorod orientation showed a small degree of spectral hysteresis, but the overall spectral shape is largely recovered. We suggest that this hysteresis may be due to the increased sensitivity of the nanorod spectra to

substrate proximity at high tilting angles. Finally, FDTD simulation of SPP modes at

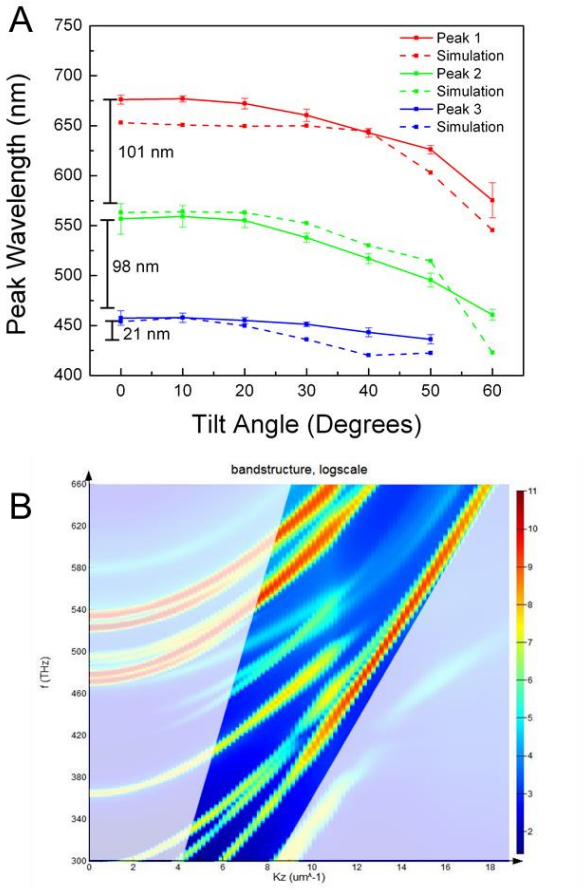

Figure 9.4 A Experimental and simulated peak positions at different tilt angles for three different scattering peaks. **B** Simulated dispersion map for an infinite gold cylinder of radius = 125 nm. Window represents the area traced by the light-water light for tilt angles between 0° and 60° (90° and 30° angle of incidence, respectively) calculated using the expression, $\frac{ck_z}{2\pi n\cos(\theta)}$, where f is the frequency in THz, k_z is the wave vector along the long axis of the cylinder in um^{-1}, c is the speed of light in vacuum (~$3 \cdot 10^8$ m/s), and n is the refractive index of water (~1.33). Z-axis represents the normalized electric field).

different nanorod tilt angles demonstrated redistribution of the surface plasmon modes consistent with experimental observations (Fig. 9.3 D). These 3D simulations show the transition of a dipolar transverse mode to a higher energy quadrupolar transverse mode, increasing the azimuthal number of the mode by 1. This transition in the SPP mode appearance expands the allowed solutions to the resonant conditions in the nanorods, in

turn allowing the nanorods to continue to couple to light effectively at many different angles down to almost horizontal nanorod orientation.

Furthermore, the analysis of the spectral changes for a single nanorod at various tilting angles showed a consistent and very large blue shift for all SPP modes (Figs. 9.3 B, 9.4 A). The peak positions changed dramatically, up to 100 nm, for the two lower-order modes for a tilt angle of 60^{o} (Fig. 9.4 A). Moreover, these changes are virtually instant (faster than a second as limited by the fastest accumulation time in our spectral measurements). Such a dramatic and well-controlled shift of SPP modes in optical spectral changes has been never observed for gold nanorods and their assemblies under different materials designs. Computer simulations of the SPP mode shifts in tilted nanorods showed continuous and significant blue shifts that closely match those observed experimentally (Fig. 9.4 B). The continuous shift in all resonances observed here is in contrast to previous reports[376], which show that the angle of incident light does not change the position of spectral features. We suggest that the larger radii of the nanorods used in this study permit the formation of higher order modes [377,378] (i.e. non-TM_0 modes) under the tested wavelengths, which allow the SPP modes to couple across multiple wavelengths. Moreover, the unchanging modes in these earlier studies were observed for thinner nanowires which lie flat against a substrate that breaks the symmetry of the environment.

A dispersion plot can be generated to analyze the expected intensity of an electromagnetic mode for a given spatial frequency (i.e. wavevector) and temporal frequency (Fig. 9.4 B). Simulations showed that gold nanorods used in this study support a large number of modes in the regime probed by the light-water line (grey area). Because of the large number of possible modes, when the light is swept over a range of incident angles, it is still able to

excite an SPP mode (by matching frequency and wavevector) and therefore satisfy the finite rod resonance condition (by maintaining a nearly constant wavevector). These nanorods are able to support a large number of plasmon modes due to a larger diameter and the symmetry of the local refractive index (the nanorods is surrounded by water on all sides at any tilt angle except 90° tilting angle).

In conclusion, we have demonstrated magnetically enabled, optically tunable hybrid (metal-polymer, plasmonic-magnetic) nanomaterials with very large and reversible shifts in concurrent manner of multiple scattering peaks under remote external stimuli. This plasmonic-magnetic nanomaterials design allows for the fast (<second) alteration of surface plasmon polariton modes of uni-directionally oriented monolayer nanorod array via changed directions of magnetic field in a broad range from UV-vis to near-infrared (concurrently at 450 nm, 550 nm, 670 nm). In addition, the magnitude of changes in the scattering spectra (large, up to 100 nm shift) is the most pronounced for stimuli-responsive plasmonic materials reported to date. Coupled with the high degree of reversibility and the nearly instantaneous switching speed of the structures, these results offer exciting possibilities for both the design of effective new fast-responsive nanomaterials on flexible polymer substrates which can be mediated remotely without interfering with internal materials morphology and environment.

CHAPTER 10. CONCLUSION

10.1 Summary of Major Results

While many varieties of synthetic polymer-based responsive materials have been previously studied, this research has devoted itself to studying the properties of responsive materials based on proteins modified with charged polypeptide sequences. This work has provided a critical look into a novel class of biomaterials that previously had not been vigorously characterized.

For the first time, these silk ionomers have been utilized to fabricate highly complex structures based on the use of silk ionomer multilayers for films, microsheets, and microcapsules. In addition, these applications were all successfully used to demonstrate rapid, reversible mechanical changes due to a shift in pH environment. Additionally, the use of magnetic/plasmonic nanoparticles was shown to be a simple method to bestow complex optical properties driven by magnetic fields for rapid tuning of light scattering.

In addition, we present the one of the first studies of the responsive interfacial properties of two novel varieties of silk ionomer. We have developed a method to determine the interaction between different types of silk ionomers, providing useful and unintuitive information regarding the binding of these species within multilayers. Further, we show how changes in processing conditions and pH environment can cause changes in the mechanical and transport properties of the silk ionomer multilayers, thereby demonstrated a wide range of potential response from closely related materials.

First, we studied the validity of different indentation models when determining the fitting of Young's modulus to FDCs obtained from AFM tests. Analytical models for determining the evolution of two surfaces in contact with each other often rely on simplifying assumptions to derive useful functions. Most notably, these models require the AFM probe tip to be approximated by simple geometric shapes, ranging from cones to sphere to parabolas. In fact, the actual tip geometry can vary dramatically at different positions along the long-axis of the probe, and the work presented here demonstrates the that the validity of different models can vary drastically with the indentation depth.

The Hertzian contact models can be applied to a wide range of polymeric samples, including non-water soluble materials such as polystyrene films and swollen hydrogels such Balafilcon A and silk ionomer multilayers. In particular, our results show that in the low indentation regime (several nm), a statistically significant deviation can be observed between spherical and parabolic indenter models, with the spherical model appearing to fit the data with less error in the very low indentation regime and the parabolic model fitting the experimental data better at slight larger indentations. A similar trend was observed for parabolic and conical indenter models at moderate indentation depths (several tens of nm), in which the parabolic model fit data more accurately at low penetration depths, while the conical model exhibited the opposite.

In addition, the agreement in elastic modulus between the two models could be greatly improved by applying a correction factor to the starting point of indentation for the conical model. Overall, we developed insights into and methods for deriving the mechanical properties of soft polymer films that are widely applicable to many systems and will serve to provide more accurate and reliable results for future AFM-based studies.

Second, we examined the interfacial interactions between silk ionomer components through analysis of mechanical properties. It was shown that silk ionomers could be readily attached to AFM probes with radii of curvature in both the microscale and nanoscale, allowing for different levels of lateral resolution. This modification also allowed for the direct measurement of mechanical interactions between the coated tip (both standard and colloidal probes) and the planar multilayers on a substrate. In particular, the study examined the adhesion and friction between different silk ionomer species and compared the results obtained using a standard nanoscale AFM probe and a specialized microscale colloidal probe.

It was found that the addition silk fibroin-co-polyglutamic acid led to an increase in adhesion between the probe and a silicon substrate, compared to the standard unmodified AFM probe, despite the negative zeta potential expected of the tip and substrate. This indicates that the silk ionomers do not need to rely entirely on electrostatic interactions to adsorb onto a surface (a result in line with the adsorption of the silk ionomer multilayers on polystyrene studied in Chapter 7), and instead may utilize hydrogen bonding or hydrophobic interactions. Adhesion and friction coefficient values calculated from experiments conducted with larger AFM probes and experiments conducted in ambient conditions were larger than those conducted with smaller probes or in DI water, which is in line with standard trends in substrate AFM probe interactions. Surprisingly, an increase in interaction magnitude (both adhesion and friction coefficient) was observed between SF-co-poly glutamic acid and SF-co-polylysine-block-PEG vs the non-PEGylated variant of the same system. These results challenge the expectation of the block-graft PEGylation being an effective broad spectrum antifouling agent, though further studies are required to

understand if the testing conditions in this experiment are applicable to molecular adsorption results. Because of the block copolymer nature of the grafting, this method of PEGylation may lead to a long-range chain extension (i.e. swelling) that leads to increased friction in a way that has not been previous reported.

Third, we demonstrate the assembly of silk ionomer based multilayers onto spherical cores and the subsequent formation of hollow microcapsules. Planar assemblies of silk ionomer multilayers were used to understand the different growth rates of LbL deposited films assembled with different buffers, in addition to revealing differences in the observed nanoscale roughness between the films to dry and swollen conditions. The role of PEGylation on the film morphology was also examined and determined to limit some of the pH responsive behaviors of the microcapsules.

The silk ionomer microcapsules demonstrated pH responsive properties due to the lysine and glutamic acid side groups present within the multilayers. Due to the low degree of derivatization in the silk ionomers used in this work, the microcapsules exhibited a lower degree of stability than typical polyelectrolyte microcapsules, indicating a tradeoff in microcapsule stability for decreased polycationic toxicity. In addition, general trends in pH responsive Young's modulus shifts showed that all silk microcapsules became less stiff at higher pH levels, though the magnitude of the measured stiffness varied heavily with assembly pH and chemical composition. In contrast, the calculated diffusion coefficient for the various microcapsules exhibited a range of pH-responsive behavior including increasing, decreasing, or roughly static diffusion coefficients. These anomalous results indicate that the low grafting density silk ionomers have an extreme sensitivity to their ionic environment. Overall, the work demonstrates that microcapsules with responsive,

tuned permeability and modulus can be fabricated and invites discussion on how further modifications to processing or chemistry may lead to larger, more targeted changes.

Fourth, we investigated the role of silk ionomers as a functional element in a self-rolling multilayer composite, photopatterned arrays. Primarily, this application demonstrated that silk ionomers could induce large-scale, reversible motion that was controlled by changing the pH of the solution In addition, the study demonstrated the role of the thin film geometry, as well as the thickness of various components within the film, on the ultimate rolling pattern.

The multiple types of components showed the difference in the strength of silk ionomer adhesion between the hydrophobic polystyrene layer and the amphiphilic crystallized silk fibroin layers deposited above and below the silk ionomer multilayers, respectively. Despite forming stable multilayers on polystyrene, the silk ionomers demonstrate delamination through blister formation when swollen, though this delamination is somewhat reversible at neutral pH, indicating a degree of adhesion between the two materials. Despite not containing additional ionic amino acid residues (and being treated to create insoluble β-sheets) the crystallized silk fibroin layer demonstrated a remarkable adhesion to the underlying silk ionomer layers at neutral and swollen conditions. These results indicates that the silk ionomers and silk fibroin systems may be compatible as a form of composite structures assembled from the same class of proteins. These structures show promise as a technique for capturing target particles/cells in solution and as a potential platform for three-dimensional ordered assembly of particles.

Fifth, we synthesized porous meshes from bacterial cellulose and introduced regenerated silk fibroin to create a naturally derived composite material. This construct was used to house recombinant bacteria within the porous of the materials and simultaneously entrap the bacteria and protect it from environmental hazards, with increasing concentrations of silk fibroin leading to an improvement in both of these properties. Silk fibroin infiltrated the pores of the cellulose mesh and lead to a reduction in pore size, porosity, and swelling ratio is water. Microstructural analysis demonstrated that the silk fibroin coated the cellulose nanofibers, indicating favorable interactions between the two biopolymers. In addition, the silk fibroin lead to a mechanical reinforcement of the composite, with the stiffness of the material increasing by 3-4 orders of magnitude due to the increased interfacial binding due to the silk. This work provides a working example of a large, mechanically robust cell scaffold and serves as a guide to future studies utilizing modified silk fibroin proteins.

Sixth, we utilize segmented metallic nanorods to create a hybrid magnetically responsive polymer multilayer-nanoparticle system. Because polymeric systems typically lack large magnetic susceptibilities, magnetic particles be embedded into the polymer matrix to create a magnetically active composite film. In contrast to other reports, which utilize bulk magnetic particle infiltration, our work utilizes controlled surface attachment to create a tethered magnetic interface. A balance of forces is required in the polymer-particle interface to confine the spatial translation of particles while allowing virtually unrestrained rotation, while preventing particle detachment and aggregation. While LbL polyelectrolyte multilayers were found to bind the nanoparticles too strongly to exhibit reorientation,

hydrogen bonded multilayers appeared to have the necessary interfacial properties to allow for this balance.

Noble metal nanoparticles are known to exhibit structure dependent optical/plasmonic properties and thus the rotation of the anchored dual magnetic/plasmonic nanoparticles was predicted to produce a shift in the scattering spectrum. The unique geometry presented by the polymer-particle system allows for the strong excitation of plasmonic modes that would be otherwise damped in confined within a substrate. This allowed for the demonstration of an anomalous, seemingly continuous shift in plasmonic excitation modes hypothesized to be the result of hybridization of higher order plasmonic modes. Not only does this provide a new means to understand the formation of sensitive higher order plasmonic modes, it also showcases one of the fastest, reversible color shifting materials based on mechanical reorientation.

10.2 Proposed Future Work and Applications

While the work in this research has achieved its objectives of advancing the understanding of silk ionomer responsive assemblies, there are virtually unlimited permutations and advances to yet consider. In the following paragraphs, some selected avenues of future research will be highlighted.

There remain a great number of questions regarding the long-term biodegradability of materials based on silk ionomers. One issue to resolve is the degradation kinetics of the silk ionomers in vivo, namely the rate and byproducts of the enzymatic breakdown of the proteins in different tissues. Another important issue is the impact of the grafted side chains on the biofouling characteristics of the silk ionomers. Finally, in vivo tests should be

conducted in mammalian specimens to determine the immune response and any potential foreign body response when implanted with a silk ionomer based construct.

The work shown in this research illustrates a number of examples of silk based systems being combined with other classes of materials. While the silks appear to interact favorably with most classes of materials, the exact mechanisms that determine the strength of these interactions have not been rigorously studied. A more detailed model of the silk interactions could, for example, explain the behavior of the PEGylated silks in a number of the studies beyond the level of conjecture. With enough understanding of these interactions, it may become possible to make use of the pH responsive properties to reversibly alter the interaction strengths and thus create large scale changes in the mechanical properties of the composites.

Another possibility is the examination of multifunctional systems with orthogonal stimuli responses. While the research presented here demonstrates the use of pH, chemical, and magnetic stimuli as potential pathways, each stimulus is studied in isolation. Future designs could benefit from an increase in fine control over a response if multiple types of responsive behaviors could be utilized together. This could potentially be achieved through covalent attachment of the silk ionomers to other particles (e.g. iron oxide nanoparticles) to create bi- or tri- responsive, biocompatible materials.

Finally, the results shown in several of the previous chapters indicate that silk based materials interact strongly with each other. This suggests that further modifications of the silk ionomers would potentially be well tolerated and could expand on the functionality of the silk ionomers. One potential application is the covalent inclusion of peptide sequences

that would alter the enzymatic degradation of the silk ionomers by acting as reversible inhibitors. Alternatively, the silk ionomers could be grafted with dyes, antibiotics, or growth factors to augment their capacity as cell encapsulation materials that release useful chemical agents as they degrade.

The work presented in this dissertation has been summarized in the following major publications:

- **R. Geryak**, S. Kim, E. Quigley, V. Korolovych, R. Calabrese, D.L. Kaplan, and V.V. Tsukruk. "Tunable Interfacial Properties in Silk Ionomer Microcapsules from Tailored Multilayer Interactions" **2017** In Preparation.

- S. Zhang, **R. Geryak**, J. Geldmeier, S. Kim, and V.V. Tsukruk. "Synthesis, assembly, and applications of hybrid nanostructures for biosensing" *Chemical Reviews*. **2017** In Print. doi: cr-2017-00088n.R1

- S. Kim, **R.D. Geryak**, S. Zhang, and V.V. Tsukruk. "Interfacial Shear Strength and Adhesive Force of Silk Ionomer LbL-Microcapsules" *Biomacromolecules*. **2017** Accepted. doi: 10.1021/acs.biomac.7b00790

- I. Drachuk, S. Harbaugh, **R. Geryak**, D.L. Kaplan, V.V. Tsukruk, and N. Kelley-Loughnane. "Immobilization of Recombinant E. coli cells in a Bacterial Cellulose-Silk Composite Matrix with Preservation of Their Biological Function". **2017** Submitted

- C. Ye, S. V. Nikolov, **R. D. Geryak**, R. Calabrese, J. F. Ankner, A. Alexeev, D. L. Kaplan, V. V. Tsukruk. "Bimorph Silk Microsheets with

Programmable Actuating Behavior: Experimental Analysis and Computer Simulations" *ACS Applied Materials & Interfaces,* **2016**, 8, 17694

- M. Chyasnavichyus, S.L. Young, **R. Geryak**, V.V. Tsukruk. "Probing elastic properties of soft materials with AFM: Data analysis for different tip geometries" *Polymer*, **2016**, 102, 317

- **R. Geryak**, J Geldmeier, K Wallace, V.V. Tsukruk. "Remote Giant Multispectral Plasmonic Shifts of Labile Hinged Nanorod Array via Magnetic Field" *Nano Letters*, **2015**, 15, 2679

- **R. Geryak** and V.V. Tsukruk. "Reconfigurable and actuating structures from soft materials" *Soft Matter*, **2014**, 10, 1246

- M.K. Gupta, D.D. Kulkarni, **R. Geryak**, S. Naik, V.V. Tsukruk. "A robust and facile approach to assembling mobile and highly-open unfrustrated triangular lattices from ferromagnetic nanorods" *Nano Letters*, **2012**, 13, 36

Conference presentations related to this dissertation:

- **R. Geryak** , J. Geldmeier , K. Wallace , and V. V. Tsukruk. "Remote Giant Multispectral Plasmonic Shifts of Labile Hinged Nanorod Array via Magnetic Field," presented at Magnetically Stimulated Soft Materials conference, Athens, GA (2015)

- **R. Geryak** , J. Geldmeier , K. Wallace , and V. V. Tsukruk. “Remote Giant Multispectral Plasmonic Shifts of Labile Hinged Nanorod Array via Magnetic Field,” presented at American Chemical Society National Meeting, Boston, MA (2015)

- **R. Geryak**, J. Geldmeier, T. Koenig, K. Wallace, V.V. Tsukruk. “Plasmonically Active Segmented Nanorods with Magnetically Actuable Response,” Presented at Materials Research Society National Meeting, Boston, MA (2013)

- **R. Geryak**, M.K. Gupta, D.D. Kulkarni, S. Naik, V.V. Tsukruk. “Ferromagnetic nanoparticle assemblies: highly ordered and tunable lattices,” Presented at GTRIC conference at Georgia Institute of Technology, Atlanta, Georgia (2013)

REFERENCES

1 Whitesides, G. M.; Grzybowski, B. Self-assembly at all scales. *Science* **2002,** *295*, 2418-2421.
2 Forterre, Y.; Skotheim, J. M.; Dumais, J.; Mahadevan, L. How the Venus flytrap snaps. *Nature* **2005,** *433*, 421-425.
3 Tsukruk, V. V. Assembly of supramolecular polymers in ultrathin films. *Prog. Polym. Sci.* **1997,** *22*, 247-311.
4 Luzinov, I.; Minko, S.; Tsukruk, V. V. Adaptive and responsive surfaces through controlled reorganization of interfacial polymer layers. *Prog. Polym. Sci.* **2004,** *29*, 635-698.
5 Lemieux, M.; Minko, S.; Usov, D.; Stamm, M.; Tsukruk, V. V. Direct Measurement of Thermoelastic Properties of Glassy and Rubbery Polymer Brush Nanolayers Grown by "Grafting-from" Approach. *Langmuir* **2003,** *19*, 6126-6134.
6 Drachuk, I.; Shchepelina, O.; Lisunova, M.; Harbaugh, S.; Kelley-Loughnane, N.; Stone, M.; Tsukruk, V. V. pH-Responsive Layer-by-Layer Nanoshells for Direct Regulation of Cell Activity. *ACS Nano* **2012,** *6*, 4266-4278.
7 Strauss, M. B.; Davis, R. K.; Rosenbaum, J. D.; Rossmeisl, E. C. "WATER DIURESIS" PRODUCED DURING RECUMBENCY BY THE INTRAVENOUS INFUSION OF ISOTONIC SALINE SOLUTION. *J. Clin. Invest.* **1951,** *30*, 862-868.
8 Tufa, R. A.; Curcio, E.; van Baak, W.; Veerman, J.; Grasman, S.; Fontananova, E.; Di Profio, G. Potential of brackish water and brine for energy generation by salinity gradient power-reverse electrodialysis (SGP-RE). *RSC Advances* **2014,** *4*, 42617-42623.
9 Walczak, J. J.; Wang, L.; Bardy, S. L.; Feriancikova, L.; Li, J.; Xu, S. The effects of starvation on the transport of Escherichia coli in saturated porous media are dependent on pH and ionic strength. *Colloids and surfaces. B, Biointerfaces* **2012,** *90*, 129-136.
10 Basu, B. In *Biomaterials for Musculoskeletal Regeneration: Concepts*; Springer Singapore: Singapore, 2017, DOI:10.1007/978-981-10-3059-8_8 10.1007/978-981-10-3059-8_8.
11 Yang, L.; Li, J.; Jin, Y.; Li, M.; Gu, Z. In vitro enzymatic degradation of the cross-linked poly(ε-caprolactone) implants. *Polym. Degrad. Stab.* **2015,** *112*, 10-19.
12 Cui, F. Z.; Li, D. J. A review of investigations on biocompatibility of diamond-like carbon and carbon nitride films. *Surf. Coat. Technol.* **2000,** *131*, 481-487.
13 Böstman, O.; Pihlajamäki, H. Clinical biocompatibility of biodegradable orthopaedic implants for internal fixation: a review. *Biomaterials* **2000,** *21*, 2615-2621.
14 Nichols, S. P.; Koh, A.; Storm, W. L.; Shin, J. H.; Schoenfisch, M. H. Biocompatible Materials for Continuous Glucose Monitoring Devices. *Chem. Rev.* **2013,** *113*, 2528-2549.
15 Bhamra, T. S.; Tighe, B. J. Mechanical properties of contact lenses: The contribution of measurement techniques and clinical feedback to 50 years of materials development. *Contact Lens and Anterior Eye* **2017,** *40*, 70-81.
16 Geetha, M.; Singh, A. K.; Asokamani, R.; Gogia, A. K. Ti based biomaterials, the ultimate choice for orthopaedic implants – A review. *Prog. Mater Sci.* **2009,** *54*, 397-425.
17 Tranoudis, I.; Efron, N. Tensile properties of soft contact lens materials. *Contact Lens and Anterior Eye* **2004,** *27*, 177-191.
18 Nguyen, J. K.; Park, D. J.; Skousen, J. L.; Hess-Dunning, A. E.; Tyler, D. J.; Rowan, S. J.; Weder, C.; Capadona, J. R. Mechanically-compliant intracortical implants reduce the neuroinflammatory response. *Journal of neural engineering* **2014,** *11*, 056014.
19 Park, J. H.; Chung, B. G.; Lee, W. G.; Kim, J.; Brigham, M. D.; Shim, J.; Lee, S.; Hwang, C.; Durmus, N. G.; Demirci, U.et al. Microporous Cell-laden Hydrogels for Engineered Tissue Constructs. *Biotechnol. Bioeng.* **2010,** *106*, 138-148.
20 Bysell, H.; Månsson, R.; Hansson, P.; Malmsten, M. Microgels and microcapsules in peptide and protein drug delivery. *Adv. Drug Del. Rev.* **2011,** *63*, 1172-1185.
21 Collins, M. N.; Birkinshaw, C. Hyaluronic acid based scaffolds for tissue engineering—A review. *Carbohydr. Polym.* **2013,** *92*, 1262-1279.

22 Nicodemus, G. D.; Bryant, S. J. Cell encapsulation in biodegradable hydrogels for tissue engineering applications. *Tissue engineering. Part B, Reviews* **2008,** *14*, 149-165.
23 Evans, N. T.; Torstrick, F. B.; Lee, C. S. D.; Dupont, K. M.; Safranski, D. L.; Chang, W. A.; Macedo, A. E.; Lin, A. S. P.; Boothby, J. M.; Whittingslow, D. C.et al. High-strength, surface-porous polyether-ether-ketone for load-bearing orthopedic implants. *Acta Biomater.* **2015,** *13*, 159-167.
24 Passos, M. F.; Dias, D. R. C.; Bastos, G. N. T.; Jardini, A. L.; Benatti, A. C. B.; Dias, C. G. B. T.; Maciel Filho, R. pHEMA hydrogels. *J. Therm. Anal. Calorim.* **2016,** *125*, 361-368.
25 Narayanan, G.; Vernekar, V. N.; Kuyinu, E. L.; Laurencin, C. T. Poly (lactic acid)-based biomaterials for orthopaedic regenerative engineering. *Adv. Drug Del. Rev.* **2016,** *107*, 247-276.
26 Mondal, D.; Griffith, M.; Venkatraman, S. S. Polycaprolactone-based biomaterials for tissue engineering and drug delivery: Current scenario and challenges. *International Journal of Polymeric Materials and Polymeric Biomaterials* **2016,** *65*, 255-265.
27 Sarkar, K.; Xue, Y.; Sant, S. In *The Immune Response to Implanted Materials and Devices: The Impact of the Immune System on the Success of an Implant*; Corradetti, B., Ed.; Springer International Publishing: Cham, 2017, DOI:10.1007/978-3-319-45433-7_5 10.1007/978-3-319-45433-7_5.
28 Kogan, G.; Šoltés, L.; Stern, R.; Gemeiner, P. Hyaluronic acid: a natural biopolymer with a broad range of biomedical and industrial applications. *Biotechnol. Lett* **2007,** *29*, 17-25.
29 Müller, F. A.; Müller, L.; Hofmann, I.; Greil, P.; Wenzel, M. M.; Staudenmaier, R. Cellulose-based scaffold materials for cartilage tissue engineering. *Biomaterials* **2006,** *27*, 3955-3963.
30 Singh, A.; Elisseeff, J. Biomaterials for stem cell differentiation. *J. Mater. Chem.* **2010,** *20*, 8832-8847.
31 Kundu, B.; Rajkhowa, R.; Kundu, S. C.; Wang, X. Silk fibroin biomaterials for tissue regenerations. *Adv. Drug Del. Rev.* **2013,** *65*, 457-470.
32 Mondal, M. The silk proteins, sericin and fibroin in silkworm, Bombyx mori Linn., - a review. *Caspian Journal of Environmental Sciences* **2007,** *5*, 63-76.
33 Yamada, H.; Nakao, H.; Takasu, Y.; Tsubouchi, K. Preparation of undegraded native molecular fibroin solution from silkworm cocoons. *Materials Science and Engineering: C* **2001,** *14*, 41-46.
34 Inoue, S.; Tanaka, K.; Arisaka, F.; Kimura, S.; Ohtomo, K.; Mizuno, S. Silk fibroin of Bombyx mori is secreted, assembling a high molecular mass elementary unit consisting of H-chain, L-chain, and P25, with a 6:6:1 molar ratio. *J. Biol. Chem.* **2000,** *275*, 40517-40528.
35 Murphy, A. R.; Kaplan, D. L. Biomedical applications of chemically-modified silk fibroin. *J. Mater. Chem.* **2009,** *19*, 6443-6450
36 Zhou, C.-Z.; Confalonieri, F.; Jacquet, M.; Perasso, R.; Li, Z.-G.; Janin, J. Silk fibroin: Structural implications of a remarkable amino acid sequence. *Proteins: Structure, Function, and Bioinformatics* **2001,** *44*, 119-122.
37 Asakura, T.; Okushita, K.; Williamson, M. P. Analysis of the Structure of Bombyx mori Silk Fibroin by NMR. *Macromolecules* **2015,** *48*, 2345-2357
38 Lefevre, T.; Rousseau, M. E.; Pezolet, M. Protein secondary structure and orientation in silk as revealed by Raman spectromicroscopy. *Biophys. J.* **2007,** *92*, 2885-2895
39 Hu, X.; Kaplan, D.; Cebe, P. Determining Beta-Sheet Crystallinity in Fibrous Proteins by Thermal Analysis and Infrared Spectroscopy. *Macromolecules* **2006,** *39*, 6161-6170
40 Zhou, C. Z.; Confalonieri, F.; Medina, N.; Zivanovic, Y.; Esnault, C.; Yang, T.; Jacquet, M.; Janin, J.; Duguet, M.; Perasso, R.et al. Fine organization of Bombyx mori fibroin heavy chain gene. *Nucleic Acids Res.* **2000,** *28*, 2413-2419
41 He, Y.-X.; Zhang, N.-N.; Li, W.-F.; Jia, N.; Chen, B.-Y.; Zhou, K.; Zhang, J.; Chen, Y.; Zhou, C.-Z. N-Terminal Domain of Bombyx mori Fibroin Mediates the Assembly of Silk in Response to pH Decrease. *J. Mol. Biol.* **2012,** *418*, 197-207
42 Tanaka, K.; Kajiyama, N.; Ishikura, K.; Waga, S.; Kikuchi, A.; Ohtomo, K.; Takagi, T.; Mizuno, S. Determination of the site of disulfide linkage between heavy and light chains of silk fibroin produced by Bombyx mori. *Biochim. Biophys. Acta* **1999,** *1432*, 92-103
43 Pérez-Rigueiro, J.; Elices, M.; Llorca, J.; Viney, C. Effect of degumming on the tensile properties of silkworm (Bombyx mori) silk fiber. *J. Appl. Polym. Sci.* **2002,** *84*, 1431-1437.
44 Ravitch, M. M. The Operative Treatment of Pectus Excavatum. *Annals of Surgery* **1949,** *129*, 429-444.
45 Rossitch, E.; Bullard, D. E.; Oakes, W. J. Delayed foreign-body reaction to silk sutures in pediatric neurosurgical patients. *Child's Nervous System* **1987,** *3*, 375-378.
46 Bahnson, H. T.; Spencer, F. C.; Bennett, I. L. Staphylococcal Infections of the Heart and Great Vessels Due to Silk Sutures. *Annals of Surgery* **1957,** *146*, 399-406.

47 Chen, X.; Hou, D.; Wang, L.; Zhang, Q.; Zou, J.; Sun, G. Antibacterial Surgical Silk Sutures Using a High-Performance Slow-Release Carrier Coating System. *ACS Applied Materials & Interfaces* **2015,** *7*, 22394-22403.
48 Chen, X.; Hou, D.; Tang, X.; Wang, L. Quantitative physical and handling characteristics of novel antibacterial braided silk suture materials. *Journal of the Mechanical Behavior of Biomedical Materials* **2015,** *50*, 160-170.
49 De Simone, S.; Gallo, A. L.; Paladini, F.; Sannino, A.; Pollini, M. Development of silver nano-coatings on silk sutures as a novel approach against surgical infections. *J. Mater. Sci. Mater. Med.* **2014,** *25*, 2205-2214.
50 Gil, E. S.; Panilaitis, B.; Bellas, E.; Kaplan, D. L. Functionalized Silk Biomaterials for Wound Healing. *Advanced Healthcare Materials* **2013,** *2*, 206-217.
51 Çalamak, S.; Erdoğdu, C.; Özalp, M.; Ulubayram, K. Silk fibroin based antibacterial bionanotextiles as wound dressing materials. *Materials Science and Engineering: C* **2014,** *43*, 11-20.
52 Liu, H.; Fan, H.; Wang, Y.; Toh, S. L.; Goh, J. C. H. The interaction between a combined knitted silk scaffold and microporous silk sponge with human mesenchymal stem cells for ligament tissue engineering. *Biomaterials* **2008,** *29*, 662-674.
53 Fan, H.; Liu, H.; Toh, S. L.; Goh, J. C. H. Anterior cruciate ligament regeneration using mesenchymal stem cells and silk scaffold in large animal model. *Biomaterials* **2009,** *30*, 4967-4977.
54 He, P.; Sahoo, S.; Ng, K. S.; Chen, K.; Toh, S. L.; Goh, J. C. H. Enhanced osteoinductivity and osteoconductivity through hydroxyapatite coating of silk-based tissue-engineered ligament scaffold. *Journal of Biomedical Materials Research Part A* **2013,** *101A*, 555-566.
55 Li, L.; Puhl, S.; Meinel, L.; Germershaus, O. Silk fibroin LbL microcapsules for localized gene delivery. *Biomaterials* **2014,** *35*, 7929-7939.
56 Mottaghitalab, F.; Farokhi, M.; Shokrgozar, M. A.; Atyabi, F.; Hosseinkhani, H. Silk fibroin nanoparticle as a novel drug delivery system. *J. Controlled Release* **2015,** *206*, 161-176.
57 Murphy, A. R.; John, P. S.; Kaplan, D. L. Modification of silk fibroin using diazonium coupling chemistry and the effects on hMSC proliferation and differentiation. *Biomaterials* **2008,** *29*, 2829-2838.
58 Gotoh, Y.; Tsukada, M.; Minoura, N. Effect of the chemical modification of the arginyl residue in Bombyx mori silk fibroin on the attachment and growth of fibroblast cells. *J. Biomed. Mater. Res.* **1998,** *39*, 351-357.
59 Zhang, Y.-Q.; Ma, Y.; Xia, Y.-Y.; Shen, W.-D.; Mao, J.-P.; Zha, X.-M.; Shirai, K.; Kiguchi, K. Synthesis of silk fibroin-insulin bioconjugates and their characterization and activities in vivo. *Journal of Biomedical Materials Research Part B: Applied Biomaterials* **2006,** *79B*, 275-283.
60 Serban, M. A.; Kaplan, D. L. pH-Sensitive ionomeric particles obtained via chemical conjugation of silk with poly(amino acid)s. *Biomacromolecules* **2010,** *11*, 3406-3412.
61 Calabrese, R.; Kaplan, D. L. Silk ionomers for encapsulation and differentiation of human MSCs. *Biomaterials* **2012,** *33*, 7375-7385.
62 Drachuk, I.; Calabrese, R.; Harbaugh, S.; Kelley-Loughnane, N.; Kaplan, D. L.; Stone, M.; Tsukruk, V. V. Silk Macromolecules with Amino Acid–Poly(Ethylene Glycol) Grafts for Controlling LbL Encapsulation and Aggregation of Recombinant Bacterial Cells. *ACS Nano* **2015,** *9*, 1219-1235.
63 Ye, C.; Drachuk, I.; Calabrese, R.; Dai, H.; Kaplan, D. L.; Tsukruk, V. V. Permeability and Micromechanical Properties of Silk Ionomer Microcapsules. *Langmuir* **2012,** *28*, 12235-12244.
64 Siró, I.; Plackett, D. Microfibrillated cellulose and new nanocomposite materials: a review. *Cellulose* **2010,** *17*, 459-494.
65 O'SULLIVAN, A. C. Cellulose: the structure slowly unravels. *Cellulose* **1997,** *4*, 173-207.
66 Kim, J.; Yun, S.; Ounaies, Z. Discovery of Cellulose as a Smart Material. *Macromolecules* **2006,** *39*, 4202-4206.
67 Habibi, Y.; Lucia, L. A.; Rojas, O. J. Cellulose Nanocrystals: Chemistry, Self-Assembly, and Applications. *Chem. Rev.* **2010,** *110*, 3479-3500.
68 Czaja, W.; Krystynowicz, A.; Bielecki, S.; Brown, R. M. Microbial cellulose—the natural power to heal wounds. *Biomaterials* **2006,** *27*, 145-151.
69 Svensson, A.; Nicklasson, E.; Harrah, T.; Panilaitis, B.; Kaplan, D. L.; Brittberg, M.; Gatenholm, P. Bacterial cellulose as a potential scaffold for tissue engineering of cartilage. *Biomaterials* **2005,** *26*, 419-431.
70 Johar, N.; Ahmad, I.; Dufresne, A. Extraction, preparation and characterization of cellulose fibres and nanocrystals from rice husk. *Industrial Crops and Products* **2012,** *37*, 93-99.

71 Iguchi, M.; Yamanaka, S.; Budhiono, A. Bacterial cellulose—a masterpiece of nature's arts. *Journal of Materials Science* **2000,** *35*, 261-270.
72 Zaborowska, M.; Bodin, A.; Bäckdahl, H.; Popp, J.; Goldstein, A.; Gatenholm, P. Microporous bacterial cellulose as a potential scaffold for bone regeneration. *Acta Biomater.* **2010,** *6*, 2540-2547.
73 Yamanaka, S.; Watanabe, K.; Kitamura, N.; Iguchi, M.; Mitsuhashi, S.; Nishi, Y.; Uryu, M. The structure and mechanical properties of sheets prepared from bacterial cellulose. *Journal of Materials Science* **1989,** *24*, 3141-3145.
74 Xiang, Y.; Lu, S.; Jiang, S. P. Layer-by-layer self-assembly in the development of electrochemical energy conversion and storage devices from fuel cells to supercapacitors. *Chem. Soc. Rev.* **2012,** *41*, 7291-7321.
75 Jiang, C.; Markutsya, S.; Tsukruk, V. V. Compliant, Robust, and Truly Nanoscale Free-Standing Multilayer Films Fabricated Using Spin-Assisted Layer-by-Layer Assembly. *Adv. Mater.* **2004,** *16*, 157-161.
76 Wang, Y.; Kozlovskaya, V.; Arcibal, I. G.; Cropek, D. M.; Kharlampieva, E. Highly swellable ultrathin poly(4-vinylpyridine) multilayer hydrogels with pH-triggered surface wettability. *Soft Matter* **2013,** *9*, 9420-9429.
77 Xu, G.; Pranantyo, D.; Xu, L.; Neoh, K.-G.; Kang, E.-T.; Teo, S. L.-M. Antifouling, Antimicrobial, and Antibiocorrosion Multilayer Coatings Assembled by Layer-by-layer Deposition Involving Host–Guest Interaction. *Ind. Eng. Chem. Res.* **2016,** *55*, 10906-10915.
78 Jiang, C.; Wang, X.; Gunawidjaja, R.; Lin, Y. H.; Gupta, M. K.; Kaplan, D. L.; Naik, R. R.; Tsukruk, V. V. Mechanical Properties of Robust Ultrathin Silk Fibroin Films. *Adv. Funct. Mater.* **2007,** *17*, 2229-2237.
79 Urbas, R.; Milošević, R.; Kašiković, N.; Pavlović, Ž.; Elesini, U. S. Microcapsules application in graphic arts industry: a review on the state-of-the-art. *Iranian Polymer Journal* **2017**, DOI:10.1007/s13726-017-0541-1 10.1007/s13726-017-0541-1.
80 Mahdavi, S. A.; Jafari, S. M.; Ghorbani, M.; Assadpoor, E. Spray-Drying Microencapsulation of Anthocyanins by Natural Biopolymers: A Review. *Drying Technol.* **2014,** *32*, 509-518.
81 Xiao, Z.; Liu, W.; Zhu, G.; Zhou, R.; Niu, Y. A review of the preparation and application of flavour and essential oils microcapsules based on complex coacervation technology. *J. Sci. Food Agric.* **2014,** *94*, 1482-1494.
82 van der Zwaag, S.; Grande, A. M.; Post, W.; Garcia, S. J.; Bor, T. C. Review of current strategies to induce self-healing behaviour in fibre reinforced polymer based composites. *Mater. Sci. Technol.* **2014,** *30*, 1633-1641.
83 Zhang, Y.; Chan, H. F.; Leong, K. W. Advanced materials and processing for drug delivery: The past and the future. *Adv. Drug Del. Rev.* **2013,** *65*, 104-120.
84 Sergeeva, A. S.; Gorin, D. A.; Volodkin, D. V. Polyelectrolyte Microcapsule Arrays: Preparation and Biomedical Applications. *BioNanoScience* **2014,** *4*, 1-14.
85 Wang, Y.; Hou, C.; Zhang, Y.; He, F.; Liu, M.; Li, X. Preparation of graphene nano-sheet bonded PDA/MOF microcapsules with immobilized glucose oxidase as a mimetic multi-enzyme system for electrochemical sensing of glucose. *Journal of Materials Chemistry B* **2016,** *4*, 3695-3702.
86 Wang, L.; Ng, W.; Jackman, J. A.; Cho, N.-J. Graphene-Functionalized Natural Microcapsules: Modular Building Blocks for Ultrahigh Sensitivity Bioelectronic Platforms. *Adv. Funct. Mater.* **2016,** *26*, 2097-2103.
87 Kazakova, L. I.; Shabarchina, L. I.; Anastasova, S.; Pavlov, A. M.; Vadgama, P.; Skirtach, A. G.; Sukhorukov, G. B. Chemosensors and biosensors based on polyelectrolyte microcapsules containing fluorescent dyes and enzymes. *Anal. Bioanal. Chem.* **2013,** *405*, 1559-1568.
88 Anu Bhushani, J.; Anandharamakrishnan, C. Electrospinning and electrospraying techniques: Potential food based applications. *Trends Food Sci. Technol.* 2014, 38, 21-33.
89 Byun, A.; Shim, J.; Han, S. W.; Kim, B.; Chae, P. S.; Shin, H. S.; Kim, J. W. One-pot microfluidic fabrication of graphene oxide-patched hollow hydrogel microcapsules with remarkable shell impermeability. *Chem. Commun.* **2015,** *51*, 12756-12759.
90 Richardson, J. J.; Teng, D.; Björnmalm, M.; Gunawan, S. T.; Guo, J.; Cui, J.; Franks, G. V.; Caruso, F. Fluidized Bed LbL Microcapsule Formation. *Langmuir* **2014,** *30*, 10028ibid.ibid.
91 Walter, A.; Rehage, H.; Leonhard, H. Shear induced deformation of microcapsules: shape oscillations and membrane folding. *Colloids Surf. Physicochem. Eng. Aspects* **2001,** *183–185*, 123-132.
92 Walter, A.; Rehage, H.; Leonhard, H. Shear-induced deformations of polyamide microcapsules. *Colloid. Polym. Sci.* **2000,** *278*, 169-175.

93 Wang, W.; Liu, X.; Xie, Y.; Zhang, H. a.; Yu, W.; Xiong, Y.; Xie, W.; Ma, X. Microencapsulation using natural polysaccharides for drug delivery and cell implantation. *J. Mater. Chem.* **2006,** *16*, 3252-3267.
94 Poncelet, D.; Neufeld, R. J. Shear breakage of nylon membrane microcapsules in a turbine reactor. *Biotechnol. Bioeng.* **1989,** *33*, 95-103.
95 Delcea, M.; Möhwald, H.; Skirtach, A. G. Stimuli-responsive LbL capsules and nanoshells for drug delivery. *Adv. Drug Del. Rev.* **2011,** *63*, 730-747.
96 Errico, C.; Pierre, J.; Pezet, S.; Desailly, Y.; Lenkei, Z.; Couture, O.; Tanter, M. Ultrafast ultrasound localization microscopy for deep super-resolution vascular imaging. *Nature* **2015,** *527*, 499-502.
97 Kolesnikova, T. A.; Gorin, D. A.; Fernandes, P.; Kessel, S.; Khomutov, G. B.; Fery, A.; Shchukin, D. G.; Möhwald, H. Nanocomposite Microcontainers with High Ultrasound Sensitivity. *Adv. Funct. Mater.* **2010,** *20*, 1189-1195.
98 Lensen, D.; Gelderblom, E. C.; Vriezema, D. M.; Marmottant, P.; Verdonschot, N.; Versluis, M.; de Jong, N.; van Hest, J. C. M. Biodegradable polymeric microcapsules for selective ultrasound-triggered drug release. *Soft Matter* **2011,** *7*, 5417-5422.
99 Finken, R.; Seifert, U. Wrinkling of microcapsules in shear flow. *J. Phys.: Condens. Matter* **2006,** *18*, L185.
100 Lebedeva, O. V.; Kim, B. S.; Vinogradova, O. I. Mechanical properties of polyelectrolyte-filled multilayer microcapsules studied by atomic force and confocal microscopy. *Langmuir* **2004,** *20*, 10685-10690.
101 Olga, I. V. Mechanical properties of polyelectrolyte multilayer microcapsules. *J. Phys.: Condens. Matter* **2004,** *16*, R1105.
102 Annabi, N.; Nichol, J. W.; Zhong, X.; Ji, C.; Koshy, S.; Khademhosseini, A.; Dehghani, F. Controlling the porosity and microarchitecture of hydrogels for tissue engineering. *Tissue engineering. Part B, Reviews* **2010,** *16*, 371-383.
103 Notley, S. M.; Eriksson, M.; Wågberg, L. Visco-elastic and adhesive properties of adsorbed polyelectrolyte multilayers determined in situ with QCM-D and AFM measurements. *J. Colloid Interface Sci.* **2005,** *292*, 29-37.
104 Shulha, H.; Kovalev, A.; Myshkin, N.; Tsukruk, V. V. Some aspects of AFM nanomechanical probing of surface polymer films. *Eur. Polym. J.* **2004,** *40*, 949-956.
105 Hu, K.; Kulkarni, D. D.; Choi, I.; Tsukruk, V. V. Graphene-polymer nanocomposites for structural and functional applications. *Prog. Polym. Sci.* **2014,** *39*, 1934-1972.
106 Li, J.; Illeperuma, W. R. K.; Suo, Z.; Vlassak, J. J. Hybrid Hydrogels with Extremely High Stiffness and Toughness. *ACS Macro Letters* **2014,** *3*, 520-523.
107 Wang, J.; Dlamini, D. S.; Mishra, A. K.; Pendergast, M. T. M.; Wong, M. C. Y.; Mamba, B. B.; Freger, V.; Verliefde, A. R. D.; Hoek, E. M. V. A critical review of transport through osmotic membranes. *J. Membr. Sci.* **2014,** *454*, 516-537.
108 Fan, X.; Zhao, H.; Liu, Y.; Quan, X.; Yu, H.; Chen, S. Enhanced Permeability, Selectivity, and Antifouling Ability of CNTs/Al2O3 Membrane under Electrochemical Assistance. *Environ. Sci. Technol.* **2015,** *49*, 2293-2300.
109 Padaki, M.; Surya Murali, R.; Abdullah, M. S.; Misdan, N.; Moslehyani, A.; Kassim, M. A.; Hilal, N.; Ismail, A. F. Membrane technology enhancement in oil–water separation. A review. *Desalination* **2015,** *357*, 197-207.
110 Firpo, G.; Angeli, E.; Repetto, L.; Valbusa, U. Permeability thickness dependence of polydimethylsiloxane (PDMS) membranes. *J. Membr. Sci.* **2015,** *481*, 1-8.
111 Huang, L.; McCutcheon, J. R. Impact of support layer pore size on performance of thin film composite membranes for forward osmosis. *J. Membr. Sci.* **2015,** *483*, 25-33.
112 Kirk, K.; Hao, E.; Lahmy, R.; Itkin-Ansari, P. Human embryonic stem cell derived islet progenitors mature inside an encapsulation device without evidence of increased biomass or cell escape. *Stem Cell Research* **2014,** *12*, 807-814.
113 Pereira, M. R.; Yarwood, J. ATR-FTIR spectroscopic studies of the structure and permeability of sulfonated poly(ether sulfone) membranes. Part 1.-Interfacial water-polymer interactions. *J. Chem. Soc., Faraday Trans.* **1996,** *92*, 2731-2735.
114 An, Z.; Möhwald, H.; Li, J. pH Controlled Permeability of Lipid/Protein Biomimetic Microcapsules. *Biomacromolecules* **2006,** *7*, 580-585.
115 Prescott, S. W.; Mulvaney, P. Gold nanorod extinction spectra. *J. Appl. Phys.* **2006,** *99*, 123504.

116 Kabashin, A. V.; Evans, P.; Pastkovsky, S.; Hendren, W.; Wurtz, G. A.; Atkinson, R.; Pollard, R.; Podolskiy, V. A.; Zayats, A. V. Plasmonic nanorod metamaterials for biosensing. *Nat Mater* **2009,** *8*, 867-871.
117 Tokarev, A.; Rubin, B.; Bedford, M.; Kornev, K. G. Magnetic Nanorods for Optofluidic Applications. *AIP Conf. Proc.* **2010,** *1311*, 204-209.
118 Nikoobakht, B.; El-Sayed, M. A. Preparation and Growth Mechanism of Gold Nanorods (NRs) Using Seed-Mediated Growth Method. *Chem. Mater.* **2003,** *15*, 1957-1962.
119 Lee, J. I.; Cho, S. H.; Park, S.-M.; Kim, J. K.; Kim, J. K.; Yu, J.-W.; Kim, Y. C.; Russell, T. P. Highly Aligned Ultrahigh Density Arrays of Conducting Polymer Nanorods using Block Copolymer Templates. *Nano Lett.* **2008,** *8*, 2315-2320.
120 Cozzoli, P. D.; Kornowski, A.; Weller, H. Low-Temperature Synthesis of Soluble and Processable Organic-Capped Anatase TiO2 Nanorods. *J. Am. Chem. Soc.* **2003,** *125*, 14539-14548.
121 Chang, S.; Singamaneni, S.; Kharlampieva, E.; Young, S. L.; Tsukruk, V. V. Responsive Hybrid Nanotubes Composed of Block Copolymer and Gold Nanoparticles. *Macromolecules* **2009,** *42*, 5781-5785.
122 Jones, M. R.; Osberg, K. D.; Macfarlane, R. J.; Langille, M. R.; Mirkin, C. A. Templated Techniques for the Synthesis and Assembly of Plasmonic Nanostructures. *Chem. Rev.* **2011,** *111*, 3736-3827.
123 Martin, C. R. Nanomaterials: A Membrane-Based Synthetic Approach. *Science* **1994,** *266*, 1961-1966.
124 Chakarvarti, S. K. Track-etch membranes enabled nano-/microtechnology: A review. *Radiat. Measur.* **2009,** *44*, 1085-1092.
125 Lee, W.; Ji, R.; Gosele, U.; Nielsch, K. Fast fabrication of long-range ordered porous alumina membranes by hard anodization. *Nat Mater* **2006,** *5*, 741-747.
126 C. Hulteen, J.; Martin, C. R. A general template-based method for the preparation of nanomaterials. *J. Mater. Chem.* **1997,** *7*, 1075-1087.
127 Banholzer, M. J.; Qin, L.; Millstone, J. E.; Osberg, K. D.; Mirkin, C. A. On-wire lithography: synthesis, encoding and biological applications. *Nat. Protocols* **2009,** *4*, 838-848.
128 Bernstein, R. E.; Cruz, C. A.; Paul, D. R.Barlow, J. W. LCST Behavior in Polymer Blends. *Macromolecules* **1977,** *10*, 681-686.
129 Sheiko, S. S.Möller, M. Visualization of MacromoleculesA First Step to Manipulation and Controlled Response. *Chem. Rev.* **2001,** *101*, 4099-4124.
130 J. R. Fried, *Polymer Science & Technology*, Pearson Education Inc., Upper Saddle River, NJ, 2008
131 Khokhlov, A. R.; Starodubtzev, S. G.; Vasilevskaya, V. V. In *Responsive Gels: Volume Transitions I*; Dušek, K., Ed.; Springer Berlin Heidelberg: Berlin, Heidelberg, 1993, DOI:10.1007/3-540-56791-7_3 10.1007/3-540-56791-7_3.
132 Roiter, Y.; Minko, S. AFM Single Molecule Experiments at the Solid−Liquid Interface: In Situ Conformation of Adsorbed Flexible Polyelectrolyte Chains. *J. Am. Chem. Soc.* **2005,** *127*, 15688-15689.
133 Cai, S.; Suo, Z. Mechanics and chemical thermodynamics of phase transition in temperature-sensitive hydrogels. *J. Mech. Phys. Solids* **2011,** *59*, 2259-2278.
134 Neuburger, N. A.; Eichinger, B. E. Critical experimental test of the Flory-Rehner theory of swelling. *Macromolecules* **1988,** *21*, 3060-3070.
135 Stuart, M. A.; Huck, W. T.; Genzer, J.; Muller, M.; Ober, C.; Stamm, M.; Sukhorukov, G. B.; Szleifer, I.; Tsukruk, V. V.; Urban, M.et al. Emerging applications of stimuli-responsive polymer materials. *Nat Mater* **2010,** *9*, 101-113.
136 Dai, S.; Ravi, P.; Tam, K. C. pH-Responsive polymers: synthesis, properties and applications. *Soft Matter* **2008,** *4*, 435-449.
137 *Multilayer Thin Films*, ed. G. Decher and J. Schlenoff, Wiley-VCH, Weinheim, 2012
138 Jinlian, H.; Harper, M.; Guoqiang, L.; Samuel, I. I. A review of stimuli-responsive polymers for smart textile applications. *Smart Mater. Struct.* **2012,** *21*, 053001.
139 Labbé, A.; Carlotti, S.; Deffieux, A.; Hirao, A. Controlled Polymerization of Glycidyl Methyl Ether Initiated by Onium Salt/Triisobutylaluminum and Investigation of the Polymer LCST. *Macromolecular Symposia* **2007,** *249-250*, 392-397.
140 Zarzar, L. D.; Kim, P.; Aizenberg, J. Bio-inspired Design of Submerged Hydrogel-Actuated Polymer Microstructures Operating in Response to pH. *Adv. Mater.* **2011,** *23*, 1442-1446.
141 Thérien-Aubin, H.; Wu, Z. L.; Nie, Z.; Kumacheva, E. Multiple Shape Transformations of Composite Hydrogel Sheets. *J. Am. Chem. Soc.* **2013,** *135*, 4834-4839.
142 Puntes, V. F.; Krishnan, K. M.; Alivisatos, P. Synthesis, self-assembly, and magnetic behavior of a two-dimensional superlattice of single-crystal ε-Co nanoparticles. *Appl. Phys. Lett.* **2001,** *78*, 2187-2189.

143 Lin, J.; Zhou, W.; Kumbhar, A.; Wiemann, J.; Fang, J.; Carpenter, E. E.; O'Connor, C. J. Gold-Coated Iron (Fe@Au) Nanoparticles: Synthesis, Characterization, and Magnetic Field-Induced Self-Assembly. *J. Solid State Chem.* **2001,** *159*, 26-31.
144 Miltenyi, S.; Muller, W.; Weichel, W.; Radbruch, A. High gradient magnetic cell separation with MACS. *Cytometry* **1990,** *11*, 231-238.
145 Maier-Hauff, K.; Ulrich, F.; Nestler, D.; Niehoff, H.; Wust, P.; Thiesen, B.; Orawa, H.; Budach, V.; Jordan, A. Efficacy and safety of intratumoral thermotherapy using magnetic iron-oxide nanoparticles combined with external beam radiotherapy on patients with recurrent glioblastoma multiforme. *Journal of neuro-oncology* **2011,** *103*, 317-324.
146 Thevenot, J.; Oliveira, H.; Sandre, O.; Lecommandoux, S. Magnetic responsive polymer composite materials. *Chem. Soc. Rev.* **2013,** *42*, 7099-7116.
147 Sakurai, Y.; Chiba, N.; Kimishima, Y.; Uehara, M. Electronic and magnetic properties of La4Ni3−xCuxO8 and Nd4−ySmyNi3O8. *Physica C: Superconductivity* **2013,** *487*, 27-30.
148 R. E. Hummel, *Electronic Properties of Materials*, Springer, 2005, pp. 305–364
149 Wood, D. S.; Camp, P. J. Modeling the properties of ferrogels in uniform magnetic fields. *Physical review. E, Statistical, nonlinear, and soft matter physics* **2011,** *83*, 011402.
150 Chung, S. E.; Kim, J.; Choi, S. E.; Kim, L. N.; Kwon, S. In Situ Fabrication and Actuation of Polymer Magnetic Microstructures. *Journal of Microelectromechanical Systems* **2011,** *20*, 785-787.
151 Fuhrer, R.; Athanassiou, E. K.; Luechinger, N. A.; Stark, W. J. Crosslinking metal nanoparticles into the polymer backbone of hydrogels enables preparation of soft, magnetic field-driven actuators with muscle-like flexibility. *Small* **2009,** *5*, 383-388.
152 Tasoglu, S.; Yu, C. H.; Gungordu, H. I.; Guven, S.; Vural, T.; Demirci, U. Guided and magnetic self-assembly of tunable magnetoceptive gels. *Nat Commun* **2014,** *5*, 4702.
153 Wang, M.; He, L.; Hu, Y.; Yin, Y. Magnetically rewritable photonic ink based on superparamagnetic nanochains. *Journal of Materials Chemistry C* **2013,** *1*, 6151-6156.
154 Homola, J.; Yee, S. S.; Gauglitz, G. Surface plasmon resonance sensors: review. *Sensors Actuators B: Chem.* **1999,** *54*, 3-15.
155 Kneipp, K.; Wang, Y.; Kneipp, H.; Perelman, L. T.; Itzkan, I.; Dasari, R. R.; Feld, M. S. Single Molecule Detection Using Surface-Enhanced Raman Scattering (SERS). *Phys. Rev. Lett.* **1997,** *78*, 1667-1670.
156 McNay, G.; Eustace, D.; Smith, W. E.; Faulds, K.; Graham, D. Surface-Enhanced Raman Scattering (SERS) and Surface-Enhanced Resonance Raman Scattering (SERRS): A Review of Applications. *Appl. Spectrosc.* **2011,** *65*, 825-837.
157 Sepúlveda, B.; Angelomé, P. C.; Lechuga, L. M.; Liz-Marzán, L. M. LSPR-based nanobiosensors. *Nano Today* **2009,** *4*, 244-251.
158 Sherry, L. J.; Chang, S.-H.; Schatz, G. C.; Van Duyne, R. P.; Wiley, B. J.; Xia, Y. Localized Surface Plasmon Resonance Spectroscopy of Single Silver Nanocubes. *Nano Lett.* **2005,** *5*, 2034-2038.
159 Jung, I.; Jang, H.-J.; Han, S.; Acapulco, J. A. I.; Park, S. Magnetic Modulation of Surface Plasmon Resonance by Tailoring Magnetically Responsive Metallic Block in Multisegment Nanorods. *Chem. Mater.* **2015,** *27*, 8433-8441.
160 Wang, M.; Gao, C.; He, L.; Lu, Q.; Zhang, J.; Tang, C.; Zorba, S.; Yin, Y. Magnetic Tuning of Plasmonic Excitation of Gold Nanorods. *J. Am. Chem. Soc.* **2013,** *135*, 15302-15305.
161 Savage, T. J.; Dunphy, D. R.; Harbaugh, S.; Kelley-Loughnane, N.; Harper, J. C.; Brinker, C. J. Influence of Silica Matrix Composition and Functional Component Additives on the Bioactivity and Viability of Encapsulated Living Cells. *ACS Biomaterials Science & Engineering* **2015,** *1*, 1231-1238.
162 Huang, C.-W.; Wei, C.-C.; Liao, V. H.-C. A low cost color-based bacterial biosensor for measuring arsenic in groundwater. *Chemosphere* **2015,** *141*, 44-49.
163 Li, F.; Lei, C.; Shen, Q.; Li, L.; Wang, M.; Guo, M.; Huang, Y.; Nie, Z.; Yao, S. Analysis of copper nanoparticles toxicity based on a stress-responsive bacterial biosensor array. *Nanoscale* **2013,** *5*, 653-662.
164 Robinson, C. J.; Vincent, H. A.; Wu, M.-C.; Lowe, P. T.; Dunstan, M. S.; Leys, D.; Micklefield, J. Modular Riboswitch Toolsets for Synthetic Genetic Control in Diverse Bacterial Species. *J. Am. Chem. Soc.* **2014,** *136*, 10615-10624.
165 Kellenberger, C. A.; Wilson, S. C.; Sales-Lee, J.; Hammond, M. C. RNA-Based Fluorescent Biosensors for Live Cell Imaging of Second Messengers Cyclic di-GMP and Cyclic AMP-GMP. *J. Am. Chem. Soc.* **2013,** *135*, 4906-4909.

166 Kellenberger, C. A.; Chen, C.; Whiteley, A. T.; Portnoy, D. A.; Hammond, M. C. RNA-Based Fluorescent Biosensors for Live Cell Imaging of Second Messenger Cyclic di-AMP. *J. Am. Chem. Soc.* **2015,** *137*, 6432-6435.
167 Qin, L.; Park, S.; Huang, L.Mirkin, C. A. On-wire lithography. *Science* **2005,** *309*, 113-115.
168 Osberg, K. D.; Schmucker, A. L.; Senesi, A. J.; Mirkin, C. A. One-Dimensional Nanorod Arrays: Independent Control of Composition, Length, and Interparticle Spacing with Nanometer Precision. *Nano Lett.* **2011,** *11*, 820-824.
169 Tsukruk, V. V.Bliznyuk, V. N. Adhesive and Friction Forces between Chemically Modified Silicon and Silicon Nitride Surfaces. *Langmuir* **1998,** *14*, 446-455.
170 Borges, J.Mano, J. F. Molecular Interactions Driving the LbL Assembly of Multilayers. *Chem. Rev.* **2014,** *114*, 8883-8942.
171 Tsukruk, V. V.; Ahn, H.-S.; Kim, D.Sidorenko, A. Triplex molecular layers with nonlinear nanomechanical response. *Appl. Phys. Lett.* **2002,** *80*, 4825-4827.
172 Chyasnavichyus, M.; Young, S. L.Tsukruk, V. V. Mapping micromechanical properties of soft polymer contact lenses. *Polymer* **2014,** *55*, 6091-6101.
173 Hao, F.Nordlander, P. Efficient dielectric function for FDTD simulation of the optical properties of silver and gold nanoparticles. *Chem. Phys. Lett.* **2007,** *446*, 115-118.
174 Ishikawa-Ankerhold, H. C.; Ankerhold, R.Drummen, G. P. Advanced fluorescence microscopy techniques--FRAP, FLIP, FLAP, FRET and FLIM. *Molecules* **2012,** *17*, 4047-4132.
175 Aaron, J.; Nitin, N.; Travis, K.; Kumar, S.; Collier, T.; Park, S. Y.; José-Yacamán, M.; Coghlan, L.; Follen, M.; Richards-Kortum, R.et al. Plasmon resonance coupling of metal nanoparticles for molecular imaging of carcinogenesis in vivo. *J. Biomed. Opt.* **2007,** *12*, 034007.
176 Hilfiker, J. N.; Singh, N.; Tiwald, T.; Convey, D.; Smith, S. M.; Baker, J. H.Tompkins, H. G. Survey of methods to characterize thin absorbing films with Spectroscopic Ellipsometry. *Thin Solid Films* **2008,** *516*, 7979-7989.
177 Vernon-Parry, K. D. Scanning electron microscopy: an introduction. *III-Vs Review* **2000,** *13*, 40-44.
178 Hu, K.; Gupta, M. K.; Kulkarni, D. D.;Tsukruk, V. V. Ultra-Robust Graphene Oxide-Silk Fibroin Nanocomposite Membranes. *Adv. Mater.* **2013,** *25*, 2301-2307.
179 Gupta, M. K.; Singamaneni, S.; McConney, M.; Drummy, L. F.; Naik, R. R.Tsukruk, V. V. A facile fabrication strategy for patterning protein chain conformation in silk materials. *Adv. Mater.* **2010,** *22*, 115-119.
180 Tsukruk VV and Singamaneni S. *Scanning Probe Microscopy of Soft Matter: Fundamentals and Practices*. 2012: Wiley, Weinheim.
181 Müller, D. J.; Dufrêne, Y. F. Atomic force microscopy: a nanoscopic window on the cell surface. *Trends Cell Biol.* **2011,** *21*, 461-469.
182 Iwamoto, S.; Kai, W.; Isogai, A.; Iwata, T. Elastic Modulus of Single Cellulose Microfibrils from Tunicate Measured by Atomic Force Microscopy. *Biomacromolecules* **2009,** *10*, 2571-2576.
183 Young, T. J.; Monclus, M. A.; Burnett, T. L.; Broughton, W. R.; Ogin, S. L.; Smith, P. A. The use of the PeakForce TM quantitative nanomechanical mapping AFM-based method for high-resolution Young's modulus measurement of polymers. *Meas. Sci. Technol.* **2011,** *22*, 125703.
184 Häberle, W.; Hörber, J. K. H.; Binnig, G. Force microscopy on living cells. *Journal of Vacuum Science & Technology B: Microelectronics and Nanometer Structures Processing, Measurement, and Phenomena* **1991,** *9*, 1210-1213.
185 Sneddon, I. N. The relation between load and penetration in the axisymmetric boussinesq problem for a punch of arbitrary profile. *International Journal of Engineering Science* **1965,** *3*, 47-57.
186 Chyasnavichyus, M.; Young, S. L.Tsukruk, V. V. Probing of Polymer Surfaces in the Viscoelastic Regime. *Langmuir* **2014,** *30*, 10566-10582.
187 Guz, N.; Dokukin, M.; Kalaparthi, V.; Sokolov, I. If Cell Mechanics Can Be Described by Elastic Modulus: Study of Different Models and Probes Used in Indentation Experiments. *Biophys. J.* **2014,** *107*, 564-575.
188 Lin, D. C.; Horkay, F. Nanomechanics of polymer gels and biological tissues: A critical review of analytical approaches in the Hertzian regime and beyond. *Soft Matter* **2008,** *4*, 669-682.
189 Liu, C.-L.; Fang, T.-H.; Lin, J.-F. Atomistic simulations of hard and soft films under nanoindentation. *Materials Science and Engineering: A* **2007,** *452*, 135-141.
190 Poon, B.; Rittel, D.; Ravichandran, G. An analysis of nanoindentation in linearly elastic solids. *International Journal of Solids and Structures* **2008,** *45*, 6018-6033.

191 Kopycinska-Müller, M.; Geiss, R. H.; Hurley, D. C. Contact mechanics and tip shape in AFM-based nanomechanical measurements. *Ultramicroscopy* **2006,** *106*, 466-474.
192Flater, E. E.; Zacharakis-Jutz, G. E.; Dumba, B. G.; White, I. A.; Clifford, C. A. Towards easy and reliable AFM tip shape determination using blind tip reconstruction. *Ultramicroscopy* **2014,** *146*, 130-143.
193 Berla, L. A.; Allen, A. M.; Han, S. M.; Nix, W. D. A Physically Based Model for Indenter Tip Shape Calibration for Nanoindentation. *J. Mater. Res.* **2010**, *25* (4), 735–745.
194 Oliver, W. C.; Pharr, G. M. Measurement of Hardness and Elastic Modulus by Instrumented Indentation: Advances in Understanding and Refinements to Methodology. *J. Mater. Res.* **2004**, *19* (1), 3–20.
195 Johnson KL. *Contact Mechanics*. 1985: Cambridge University Press, Cambridge.
196 Long, Y.; Song, K.; York, D.; Zhang, Z.; Preece, J. A., Engineering the Mechanical and Physical Properties of Organic–Inorganic Composite Microcapsules. *Colloids Surf.,A* **2013**, *433*, 30-36.
197 Korolovych, V.; Grishina, O.; Inozemtseva, O.; Selifonov, A.; Bratashov, D.; Suchkov, S.; Bulavin, L.; Glukhova, O.; Sukhorukov, G. B.; Gorin, D. A., Impact of high-frequency ultrasound on nanocomposite microcapsules: in silico and in situ visualization. *PCCP* **2016,** *18*, 2389-2397.
198 Jiang, C.; Tsukruk, V. V., Freestanding Nanostructures via Layer-by-Layer Assembly. *Adv. Mater.* **2006,** *18*, 829-840.
199 Drachuk, I.; Gupta, M. K.; Tsukruk, V. V., Biomimetic coatings to control cellular function through cell surface engineering. *Adv. Funct. Mater.* **2013,** *23* (36), 4437-4453.
200 Wilson, J. T.; Cui, W.; Chaikof, E. L., Layer-by-Layer Assembly of a Conformal Nanothin Peg Coating for Intraportal Islet Transplantation. *Nano Lett.* **2008**, *8*, 1940-1948.
201 Li, L.; Puhl, S.; Meinel, L.; Germershaus, O., Silk Fibroin Layer-by-Layer Microcapsules for Localized Gene Delivery. *Biomaterials* **2014**, *35*, 7929-7939.
202 Ye, C.; Shchepelina, O.; Calabrese, R.; Drachuk, I.; Kaplan, D. L.; Tsukruk, V. V., Robust and Responsive Silk Ionomer Microcapsules. *Biomacromolecules* **2011**, *12*, 4319-4325.
203 Kim, B.-S.; Lebedeva, O. V.; Kim, D. H.; Caminade, A.-M.; Majoral, J.-P.; Knoll, W.; Vinogradova, O. I., Assembly and mechanical properties of phosphorus dendrimer/polyelectrolyte multilayer microcapsules. *Langmuir* **2005,** *21*, 7200-7206.
204 Dubreuil, F.; Elsner, N.; Fery, A., Elastic properties of polyelectrolyte capsules studied by atomic-force microscopy and RICM. *Eur. Phys. J. E* **2003,** *12*, 215-221.
205 Gallant, B. M.; Gu, X. W.; Chen, D. Z.; Greer, J. R.; Lewis, N. S., Tailoring of Interfacial Mechanical Shear Strength by Surface Chemical Modification of Silicon Microwires Embedded in Nafion Membranes. *ACS Nano* **2015**, *9*, 5143-5153.
206 Wang, J.; Cheng, Q.; Tang, Z., Layered Nanocomposites Inspired by the Structure and Mechanical Properties of Nacre. *Chem. Soc. Rev.* **2012**, *41*, 1111-1129.
207 Sakhavand, N.; Shahsavari, R., Universal Composition–Structure–Property Maps for Natural and Biomimetic Platelet–Matrix Composites and Stacked Heterostructures. *Nature communications* **2015**, *6*.
208 Godara, A.; Gorbatikh, L.; Kalinka, G.; Warrier, A.; Rochez, O.; Mezzo, L.; Luizi, F.; Van Vuure, A.; Lomov, S.; Verpoest, I., Interfacial Shear Strength of a Glass Fiber/Epoxy Bonding in Composites Modified with Carbon Nanotubes. *Composites Sci. Technol.* **2010**, *70*, 1346-1352.
209 Zhang, X.; Fan, X.; Yan, C.; Li, H.; Zhu, Y.; Li, X.; Yu, L., Interfacial Microstructure and Properties of Carbon Fiber Composites Modified with Graphene Oxide. *ACS Appl. Mater. Interfaces* **2012**, *4*, 1543-1552.
210 Mallikarjunachari, G.; Ghosh, P., Analysis of Strength and Response of Polymer Nano Thin Film Interfaces Applying Nanoindentation and Nanoscratch Techniques. *Polymer* **2016**, *90*, 53-66.
211 Yan, Y. X.; Yao, H. B.; Mao, L. B.; Asiri, A. M.; Alamry, K. A.; Marwani, H. M.; Yu, S. H., Micrometer-Thick Graphene Oxide–Layered Double Hydroxide Nacre-Inspired Coatings and Their Properties. *Small* **2016**, *12*, 745-755.
212 Zhu, J.; Cao, W.; Yue, M.; Hou, Y.; Han, J.; Yang, M., Strong and Stiff Aramid Nanofiber/Carbon Nanotube Nanocomposites. *ACS Nano* **2015**, *9*, 2489-2501.
213 Zhao, X.; Zhang, Q.; Hao, Y.; Li, Y.; Fang, Y.; Chen, D., Alternate Multilayer Films of Poly (Vinyl Alcohol) and Exfoliated Graphene Oxide Fabricated Via a Facial Layer-by-Layer Assembly. *Macromolecules* **2010**, *43*, 9411-9416.
214 Mitragotri, S.; Burke, P. A.; Langer, R., Overcoming the Challenges in Administering Biopharmaceuticals: Formulation and Delivery Strategies. *Nat. Rev. Drug discovery* **2014**, *13*, 655-672.

215 Barthelat, F., Architectured Materials in Engineering and Biology: Fabrication, Structure, Mechanics and Performance. *Int. Mater. Rev.* **2015**, *60*, 413-430.
216 Yang, S.; Zhang, H.; Hsu, S. M., Correction of Random Surface Roughness on Colloidal Probes in Measuring Adhesion. *Langmuir* **2007**, *23*, 1195-1202.
217 Halperin, A.; Zhulina, E., Atomic Force Microscopy of Polymer Brushes: Colloidal Versus Sharp Tips. *Langmuir* **2010**, *26*, 8933-8940.
218 Kutnyanszky, E.; Vancso, G. J., Nanomechanical Properties of Polymer Brushes by Colloidal AFM Probes. *Eur. Polym. J.* **2012**, *48*, 8-15.
219 Chyasnavichyus, M.; Young, S. L.; Geryak, R.; Tsukruk, V. V., Probing elastic properties of soft materials with AFM: Data analysis for different tip geometries. *Polymer* **2016,** *102*, 317-325.
220 Daly, M.; Cao, C.; Sun, H.; Sun, Y.; Filleter, T.; Singh, C. V., Interfacial Shear Strength of Multilayer Graphene Oxide Films. *ACS Nano* **2016**, *10*, 1939-1947.
221 Hazel, J.; Tsukruk, V., Friction Force Microscopy Measurements: Normal and Torsional Spring Constants for V-Shaped Cantilevers. *J. Tribology* **1998**, *120*, 814-819.
222 C. Ye, Z.A. Combs, R. Calabrese, H. Dai, D.L. Kaplan, V.V. Tsukruk, Robust microcapsules with controlled permeability from silk fibroin reinforced with graphene oxide, Small, **2014**, *10*, 5087-5097.
223 Brady, R. F., *Comprehensive Desk Reference of Polymer Characterization and Analysis*; An American Chemical Society Publication, 2003.
224 Katsuki, F., Single asperity tribochemical wear of silicon by atomic force microscopy. *J. Mater. Res.* **2009**, *24*, 173-178.
225 Bhushan, B.; Tokachichu, D. R.; Keener, M. T.; Lee, S. C., Nanoscale adhesion, friction and wear studies of biomolecules on silicon based surfaces. *Acta Biomater.* **2006,** *2*, 39-49.
226 Cook, S.; Schäffer, T.; Chynoweth, K.; Wigton, M.; Simmonds, R.; Lang, K., Practical Implementation of Dynamic Methods for Measuring Atomic Force Microscope Cantilever Spring Constants. *Nanotechnology* **2006**, *17*, 2135.
227 Choi, D.; Hwang, W.; Yoon, E., Improved Lateral Force Calibration Based on the Angle Conversion Factor in Atomic Force Microscopy. *J. Microscopy* **2007**, *228*, 190-199.
228 McConney, M. E.; Singamaneni, S.; Tsukruk, V. V., Probing Soft Matter with the Atomic Force Microscopies: Imaging and Force Spectroscopy. *Polymer Reviews* **2010**, *50*, 235-286.
229 Kim, S.; Polycarpou, A. A.; Liang, H., Active Control of Surface Forces Via Nanopore Structures. *APL Materials* **2013**, *1*, 032118.
230 Florin, E.-L.; Moy, V. T.; Gaub, H. E., Adhesion Forces between Individual Ligand-Receptor Pairs. *Science-AAAS-Weekly Paper Edition-including Guide to Scientific Information* **1994**, *264*, 415-417.
231 Shao, J.; Liu, J.; Zheng, J.; Carr, C. M., X-ray photoelectron spectroscopic study of silk fibroin surface. *Polym. Int.* **2002,** *51*, 1479-1483.
232 Dumitru, A. C.; Herruzo, E. T.; Rausell, E.; Ceña, V.; Garcia, R., Unbinding Forces and Energies between a Sirna Molecule and a Dendrimer Measured by Force Spectroscopy. *Nanoscale* **2015**, *7*, 20267-20276.
233 Geisler, M.; Pirzer, T.; Ackerschott, C.; Lud, S.; Garrido, J.; Scheibel, T.; Hugel, T., Hydrophobic and Hofmeister effects on the adhesion of spider silk proteins onto solid substrates: an AFM-based single-molecule study. *Langmuir* **2008,** *24*, 1350-1355.
234 Mahdavi, A.; Ferreira, L.; Sundback, C.; Nichol, J. W.; Chan, E. P.; Carter, D. J.; Bettinger, C. J.; Patanavanich, S.; Chignozha, L.; Ben-Joseph, E., A biodegradable and biocompatible gecko-inspired tissue adhesive. *Proc. Natl. Acad. Sci.* **2008,** *105*, 2307-2312.
235 Tao, Z.; Bhushan, B., Surface Modification of AFM Silicon Probes for Adhesion and Wear Reduction. *Tribol. Lett.* **2006**, *21*, 1.
236 Yoon, E.-S.; Yang, S. H.; Han, H.-G.; Kong, H., An Experimental Study on the Adhesion at a Nano-Contact. *Wear* **2003**, *254*, 974-980.
237 Gorbunov, V.; Fuchigami, N.; Hazel, J.; Tsukruk, V., Probing surface microthermal properties by scanning thermal microscopy. *Langmuir* **1999,** *15*, 8340-8343.
238 Reedy, E., Contact Mechanics for Coated Spheres That Includes the Transition from Weak to Strong Adhesion. *J. Mater. Res.* **2007**, *22*, 2617-2622.
239 Chyasnavichyus, M.; Young, S. L.; Tsukruk, V. V., Recent advances in micromechanical characterization of polymer, biomaterial, and cell surfaces with atomic force microscopy. *Jpn. J. Appl. Phys.* **2015,** *54*, 08LA02.

240 Kovalev, A.; Shulha, H.; Lemieux, M.; Myshkin, N.; Tsukruk, V., Nanomechanical probing of layered nanoscale polymer films with atomic force microscopy. *J. Mater. Res.* **2004,** *19*, 716-728.
241 Wallet, B.; Kharlampieva, E.; Campbell-Proszowska, K.; Kozlovskaya, V.; Malak, S.; Ankner, J. F.; Kaplan, D. L.; Tsukruk, V. V., Silk Layering As Studied with Neutron Reflectivity. *Langmuir* **2012,** *28*, 11481-11489.
242 Weichert, N.; Hauptmann, V.; Menzel, M.; Schallau, K.; Gunkel, P.; Hertel, T. C.; Pietzsch, M.; Spohn, U.; Conrad, U., Transglutamination allows production and characterization of native-sized ELPylated spider silk proteins from transgenic plants. *Plant Biotechnol. J.* **2014,** *12*, 265-275.
243 Posati, T.; Benfenati, V.; Sagnella, A.; Pistone, A.; Nocchetti, M.; Donnadio, A.; Ruani, G.; Zamboni, R.; Muccini, M., Innovative Multifunctional Silk Fibroin and Hydrotalcite Nanocomposites: A Synergic Effect of the Components. *Biomacromolecules* **2013**, *15*, 158-168.
244 Nichols, M. D.; Scott, E. A.; Elbert, D. L., Factors Affecting Size and Swelling of Poly (Ethylene Glycol) Microspheres Formed in Aqueous Sodium Sulfate Solutions without Surfactants. *Biomaterials* **2009**, *30*, 5283-5291.
245 Park, B.-D.; Lee, Y.-S., The effect of PEG groups on swelling properties of PEG-grafted-polystyrene resins in various solvents. *React. Funct. Polym.* **2000,** *44*, 41-46.
246 Tambe, N.S.; Bhushan, B., Friction model for the velocity dependence of nanoscale friction, *Nanotechnology* **2005,** *16*, 2309-2324.
247Bahr, D.; Kramer, D.; Gerberich, W., Non-linear deformation mechanisms during nanoindentation. *Acta Mater.* **1998,** *46*, 3605-3617.
248 Yoon, E.-S.; Singh, R. A.; Oh, H.-J.; Kong, H., The Effect of Contact Area on Nano/Micro-Scale Friction. *Wear* **2005**, *259*, 1424-1431.
249 Tsukruk, V. V., Molecular Lubricants and Glues for Micro-and Nanodevices. *Adv. Mater.* **2001,** *13*, 95-108.
250 Fang, H. H.; Chan, K.-Y.; Xu, L.-C., Quantification of bacterial adhesion forces using atomic force microscopy (AFM). *J. Microbiol. Methods* **2000,** *40*, 89-97.
251 Binggeli, M.; Mate, C., Influence of capillary condensation of water on nanotribology studied by force microscopy. *Appl. Phys. Lett.* **1994,** *65*, 415-417.
252 Bodugoz-Senturk, H.; Macias, C. E.; Kung, J. H.; Muratoglu, O. K., Poly (vinyl alcohol)–acrylamide hydrogels as load-bearing cartilage substitute. *Biomaterials* **2009,** *30*, 589-596.
253 Maugis, D., Adhesion of Spheres: The JKR-DMT Transition Using a Dugdale Model. *J. Colloid Interface Sci.* **1992**, *150*, 243-269.
254 Carpick, R. W.; Ogletree, D. F.; Salmeron, M., A General Equation for Fitting Contact Area and Friction Vs Load Measurements. *J. Colloid Interface Sci.* **1999**, *211*, 395-400.
255 Derjaguin, B. V.; Muller, V. M.; Toporov, Y. P., Effect of Contact Deformations on the Adhesion of Particles. *J. Colloid Interface Sci.* **1975**, *53*, 314-326.
256 Klapper, Y.; Vrânceanu, M.; Ishitsuka, Y.; Evans, D.; Scheider, D.; Nienhaus, G. U.; Leneweit, G., Surface energy of phospholipid bilayers and the correlation to their hydration. *J. Colloid Interface Sci.* **2013,** *390*, 267-274.
257 Jiang, Q.; Li, J.; Chi, B., Size-Dependent Cohesive Energy of Nanocrystals. *Chem. Phys. Lett.* **2002**, *366*, 551-554.
258 Lu, H.; Jiang, Q., Size-Dependent Surface Energies of Nanocrystals. *J. Phys. Chem. B* **2004**, *108*, 5617-5619.
259 Li, Y.; Liu, Y.; Peng, X.; Yan, C.; Liu, S.; Hu, N., Pull-out Simulations on Interfacial Properties of Carbon Nanotube-Reinforced Polymer Nanocomposites. *Computational Materials Science* **2011**, *50*, 1854-1860.
260 Chung, J. Y., Soft and Hard Adhesion. *J. Adhes.* **2005**, *81*, 1119-1145.
261 Zhang, J.; Du, S.; Kafi, A.; Fox, B.; Li, J. L.; Liu, X.; Rajkhowa, R.; Wang, X., Surface energy of silk fibroin and mechanical properties of silk cocoon composites. *RSC Advances* **2015,** *5*, 1640-1647.
262 Ozcan, C.; Hasirci, N., Evaluation of surface free energy for PMMA films. *J. Appl. Polym. Sci.* **2008,** *108*, 438-446.
263 Hallab, N. J.; Bundy, K. J.; O'Connor, K.; Moses, R. L.; Jacobs, J. J., Evaluation of metallic and polymeric biomaterial surface energy and surface roughness characteristics for directed cell adhesion. *Tissue Eng.* **2001,** *7*, 55-71.

264 Fuard, D.; Tzvetkova-Chevolleau, T.; Decossas, S.; Tracqui, P.; Schiavone, P., Optimization of poly-di-methyl-siloxane (PDMS) substrates for studying cellular adhesion and motility. *Microelectron. Eng.* **2008,** *85*, 1289-1293.
265 Thomas, R. C.; Houston, J.; Crooks, R. M.; Kim, T.; Michalske, T. A., Probing adhesion forces at the molecular scale. *J. Am. Chem. Soc.* **1995,** *117*, 3830-3834.
266 Laura, M.; Lu, J. J.; Chiu, I. W.; Leung, K. S.; Chan, Y. W.; Zhang, L.; Policova, Z.; Hair, M. L.; Neumann, A. W., Poly (ethylene glycol) enhances the surface activity of a pulmonary surfactant. *Colloids Surf. B. Biointerfaces* **2004,** *36*, 167-176.
267 Cyras, V. P.; Manfredi, L. B.; Ton-That, M.-T.; Vázquez, A., Physical and Mechanical Properties of Thermoplastic Starch/Montmorillonite Nanocomposite Films. *Carbohydr. Polym.* **2008**, *73*, 55-63.
268 Gardner, D. J.; Oporto, G. S.; Mills, R.; Samir, M. A. S. A., Adhesion and Surface Issues in Cellulose and Nanocellulose. *J. Adhes. Sci. Technol.* **2008**, *22*, 545-567.
269 Hertz, H., Über Die Berührung Fester Elastischer Körper. *J. Reine Angewandte Mathematik* **1882**, *92*, 156-171.
270 Le Duigou, A.; Bourmaud, A.; Balnois, E.; Davies, P.; Baley, C., Improving the Interfacial Properties between Flax Fibres and Plla by a Water Fibre Treatment and Drying Cycle. *Industrial Crops and Products* **2012**, *39*, 31-39.
271 De Silva, R.; Pasbakhsh, P.; Qureshi, A.; Gibson, A.; Goh, K., Stress Transfer and Fracture in Nanostructured Particulate-Reinforced Chitosan Biopolymer Composites: Influence of Interfacial Shear Stress and Particle Slenderness. *Compos. Interfaces* **2014**, *21*, 807-818.
272 Cooper, C. A.; Cohen, S. R.; Barber, A. H.; Wagner, H. D., Detachment of Nanotubes from a Polymer Matrix. *Appl. Phys. Lett.* **2002**, *81*, 3873-3875.
273 Sager, R.; Klein, P.; Lagoudas, D.; Zhang, Q.; Liu, J.; Dai, L.; Baur, J., Effect of Carbon Nanotubes on the Interfacial Shear Strength of T650 Carbon Fiber in an Epoxy Matrix. *Composites Sci. Technol.* **2009**, *69*, 898-904.
274 Raghavan, S. R.; Walls, H.; Khan, S. A., Rheology of silica dispersions in organic liquids: new evidence for solvation forces dictated by hydrogen bonding. *Langmuir* **2000,** *16*, 7920-7930.
275 Reddy, N.; Reddy, R. and Jiang, Q. Crosslinking biopolymers for biomedical applications. *Trends Biotechnol.* **2015,** *33*, 362.
276 Hirayama, K.; Akashi, S.; Furuya, M. and Fukuhara, K.-i. Rapid confirmation and revision of the primary structure of bovine serum albumin by ESIMS and frit-FAB LC/MS. *Biochem. Biophys. Res. Commun.* **1990,** *173*, 639.
277 Bang, M.-L.; Centner, T.; Fornoff, F.; Geach, A. J.; Gotthardt, M.; McNabb, M.; Witt, C. C.; Labeit, D.; Gregorio, C. C.; Granzier, H. and Labeit, S. The Complete Gene Sequence of Titin, Expression of an Unusual ≈700-kDa Titin Isoform, and Its Interaction With Obscurin Identify a Novel Z-Line to I-Band Linking System. *Circul. Res.* **2001,** *89*, 1065.
278 Ma, H.; Hyun, J.; Stiller, P.; Chilkoti, A. "Non-Fouling" Oligo(ethylene glycol)- Functionalized Polymer Brushes Synthesized by Surface-Initiated Atom Transfer Radical Polymerization. *Adv. Mater.* **2004,** *16* (4), 338.
279 Zhang, M.; Ferrari, M. Hemocompatible Polyethylene Glycol Films on Silicon. *Biomed. Microdevices* **1998,** *1* (1), 81.
280 Yao, K.; Meng, Q.; Bulone, V.; Zhou, Q. Flexible and Responsive Chiral Nematic Cellulose Nanocrystal/Poly(ethylene glycol) Composite Films with Uniform and Tunable Structural Color. *Adv. Mater.*, DOI:10.1002/adma.201701323 10.1002/adma.201701323, 1701323.
281 Gumel, A. M.; Annuar, M. S. M. Poly-3-hydroxyalkanoates-co-polyethylene glycol methacrylate copolymers for pH responsive and shape memory hydrogel. *J. Appl. Polym. Sci.* **2014,** *131* (23), 41149.
282 Peng, T.; Cheng, Y.-L. Temperature-responsive permeability of porous PNIPAAm-g-PE membranes. *J. Appl. Polym. Sci.* **1998,** *70* (11), 2133.
283 Lendlein, A.; Jiang, H. Y.; Junger, O.; Langer, R.; Light-Induced Shape-Memory Polymers. *Nature* **2005**, *434*, 879-882.
284 Russell, T. P. Surface-Responsive Materials. *Science* **2002**, *297*, 964-967.
285 Sidorenko, A.; Krupenkin, T.; Taylar, A.; Fratzl, P.; Aizenberg, J. Reversible Switching of Hydrogel-Actuated Nanostructures into Complex Micropatters. *Science* **2007**, *315*, 487-490.
286 Leong, T. G.; Randall, C. L.; Benson, B. R.; Bassil, N.; Stern, G. M.; Gracias, D. H. Tetherless, Thermobiochemically Actuated Microgrippers. *Proc. Natl. Acad. Sci. U.S.A.* **2009**, *103*, 703-708.

287 Pokroy, B.; Epstein, A. K.; Persson-Gulda, C. M.; Aizenberg, J. Fabrication of Bioinspired Actuated Nanostructures with Arbitrary Geometry and Stiffness. *Adv. Mater.* **2009**, *21*, 463-469.
288 Randhawa, J. S.; Keung, M. D.; Tyagi, P.; Gracias, D. H. Reversible Actuation of Microstructures by Surface-Chemical Modification of Thin-Film Bilayer. *Adv. Mater.* **2010**, *22*, 407-410.
289 Leong, T. G.; Gu, Z.; KOH, T.; Gracias, D. H. Spatially Controlled Chemistry Using Remotely Guided Nanoliter Scale Containers. *J. Am. Chem. Soc.* **2006**, *128*, 11336-11337.
290 Leong, T. G.; Benson, B. R.; Call, E. K.; Gracias, D. H. Thin Film Stress Driven Self-Folding of Microstructured Containers. *Small* **2008**, *4*, 1605-1609.
291 Zakharchenko, S.; Puretskiy, N.; Stoychev, G.; Stamm, M.; Ionov, L. Temperature Controlled Encapsulation and Release Using Partially Biodegradable Thermo-Magneto-Sensitive Self-Rolling Tubes. *Soft matter* **2010**, *6*, 2633-2636.
292 Klein, Y.; Efrati, E.; Sharon, E. Shaping of Elastic Sheets by Prescription of Non-Euclidean Metrics. *Science* **2007**, *315*, 1116-1120.
293 Kim, J.; Hanna, J. A.; Byun, M.; Santangelo, C. D.; Hayward, R. C. Designing Responsive Buckled Surfaces by Halftone Gel Lithography. *Science* **2012**, *35*, 1201-1205.
294 Ionov, L. Soft Microorigami: Self-Folding Polymer Films. *Soft matter* **2011**, *7*, 6786-6791.
295 Kozlovskaya, V.; Kharlampieva, E.; Jones, K.; Lin, Z.; Tsukruk, V. V. pH-Controlled Assembly and Properties of LbL Membranes from Branched Conjugated Poly(alkoxythiophene sulfonate) and Various Polycatons. *Langmuir* **2010**, *26*, 7138-7147.
296 Kim, U.-J.; Park, J.; Li, C.; Jin, H.-J.; Valluzzi, R.; Kaplan, D. L. Structure and Properties of Silk Hydrogels. *Biomacromelecules* **2004**, *5*, 786-792.
297 Jiang, C.; Markutsya, S.; Pikus, Y.;Tsukruk, V.V. Freely Suspended Nanocomposite Membranes as Highly Sensitive Sensors. *Nature Mater.* **2004,** *3*, 721-728.
298 Jiang, C.; Markutsya, S.; Shulha, H.; Tsukruk, V. V. Freely Suspended Gold Nanoparticle Arrays. *Adv. Mater.* **2005,** *17*, 1669-1673.
299 Kozlovskaya, V.; Kharlampieva, E.; Mansfield, M. L.; Sukhishvili, V. Poly(methacrylic acid) Hydrogel Films and Capsules: Response to pH and Ionic Strength, and Encapsulation of Marcromolecules. *Chem. Mater.* **2006**, *18*, 328-336.
300 Ye, C.; Nikolov, S. V.; Calabrese, R.; Dindar, A.; Alexeev, A.; Kippelen, B.; Kaplan, D. L. Tsurkruk, V. V. Self-(Un)rolling Biopolymer Microstructures: Rings, Tubules, and Helical Tubules from the Same Material. *Angew. Chem. Int. Ed.* **2015**, *54*, 8490-8493.
301 Kozlovskaya, V.; Zavgorodnya, O.; Wang, Y.; Ankner, J. F.; Kharlampieva, E. Tailoring Architecture of Nanothin Hydrogels: Effect of Layering on pH-Triggered Swelling. *ACS Macro Lett.* **2013**, *3*, 226-229.
302 Jean, B.; Dubreuil, F.; Heux, L.; Cousin, F. Structural Details of Cellulose Nanocrystals /Polyelectrolytes Multilayers Probed by Neutron Reflectivity and AFM. *Langmuir* **2008**, *24*, 3452-3458.
303 Russell, T. P.; Karim, A.; Mansour, A.; Felcher, G. P. Specular Reflectivity of Neutrons by Thin Polymer Films. *Macromolecules* **1988**, *21*, 1890-1893.
304 Kharlampieva, E.; Kozlovskaya, V.; Ankner, J. F.; Sukhishvili, S. A. Hydrogen-Bonded Polymermultilayers Probed by Neutron Reflectivity. *Langmuir* **2008**, *24*, 11346-11349.
305 Jomaa, H. W.; Schlenoff, J. B. Salt-Induced Polyelectrolyte Interdiffusion in Multilayered Films: A Neutron Reflectivity Study. *Macromolecules* **2005**, *38*, 8473-8480.
306 Buxton, G. A.; Care, C. M.; Cleaver, D. J. A Lattice Spring Model of Heterogeneous Materials with Plasticity. *Modell. Simul. Mater. Sci. Eng.* **2001**, *9*, 485-497.
307 Shchepelina, O.; Drachuk, I.; Gupta, M. K.; Lin, J. Tsukruk, V. V. Silk-on-Silk LbL Microcapsules. *Ad. Mater.* **2011**, *23*, 4655-4660.
308 Yu, A.; Gentle, I. R.; Qing, G. Biocompatible Polypeptide Microcapsules via Templating Mesoporous Silica Spheres. *J. Colloid Interface Sci.* **2009**, *333*, 341-345.
309 Timoshenko, S. P.; Gere, J. M. Theory of Elastic Stability. McGraw-Hill, Singapore, **1963**. PP 348-360.
310 Shim, T. S.; Kim, S-H.; Heo, C-J.; Jeon, H. C.; Yang, S-M. Controlled Origami Folding of Hydrogel Bilayers with Sustained Reversibility for Robust Microcarries. *Angew. Chem. Int. Ed.* **2012**, *51*, 1420-1423.
311 Thérien-Aubin, H.; Wu, Z. L.; Nei, Z.; Kumacheva, E. Multiple Shape Transformation of Composite Hydrogel Sheets. *J. Am. Chem. Soc.* **2013**, *135*, 4834-4839.
312 Stoychev, G.; Zakharchenko, S.; Turcaud, S.; Dunlop, J. W. C.; Ionov, L. Shape-Programmed Folding of Stimuli-Responsive Polymer Bilayers. *ACS Nano* **2012**, *5*, 3925-3934.

313 Wu, Z. L.; Moshe, M.; Greener, J.; Thérien-Aubin, H.; Nie, Z.; Saron, E.; Kumacheva, E. Three-Dimensional Shape Transformations of Hydrogel Sheets Induced by Small-Scale Modulation of Internal Stresses. *Nat. Commun*. **2013**, *4*, 1586-1592.
314 Pan, J.; Heberle, F. A.; Carmichael, J. R.; Ankner, J. F.; Katsara, J. Time-of-Flight Brag Scattering from Aligned Stacks of Lipid Bilayers Using the Liquids Reflectometer at the Spallation Neutron Source. *J. Appl. Cryst.* **2012**, *45*, 1119-1227.
315 Vepari, C.; Kaplan, D. L. Silk as a Biomaterial. *Prog. Polym. Sci.* **2007**, *32*, 991-1007.
316 Nayfeh, A. H.; Baker, S. R. Thermomechanical Distortion of Composite Panels. *Fiber Sci. and Tech.* **1977**, *10*, 139-149.
317 Karnaushenko, D.; Münzenrieder, N.; Karnaushenko, D. D.; Koch, B.; Meyer, A. K.; Baunack, S.; Petti, L.; Tröster, G.; Makarov, D.; Schmidt, O. G. Biomimetic Microelectonics for Regenerative Neuronal Cuff Implants. *Adv. Mater.* **2015**, *27*, 6797-6805.
318 Malachowski, K.; Jamal, M.; Jin, Q.; Polat, B.; Morris, C. J.; Gracias, D. H. Self-Folding Single Cell Grippers. *Nano Lett.* **2014**, *14*, 4164-4170.
319 Magdanz, V.; Guix, M.; Hebenstreit, F.; Schmidt, O. G. Dynamic Polymeric Microtubes for the Remote-Controlled Capture, Guidance, Release of Sperm Cells. *Adv. Mater.* **2016**, DOI: 10.1002/adma.201505487.
320 Drachuk, I.; Gupta, M. K.; Tsukruk, V. V., Biomimetic coatings to control cellular function through cell surface engineering. *Adv. Funct. Mater.* **2013,** *23* (36), 4437-4453.
321 Yang, S. H.; Hong, D.; Lee, J.; Ko, E. H.; Choi, I. S. Artificial Spores: Cytocompatible Encapsulation of Individual Living Cells within Thin, Tough Artificial Shells. *Small* **2013,** *9*, 178-186.
322 Fakhrullin, R. F.; Lvov, Y. M. "Face-Lifting" and "Make-Up" for Microorganisms: Layer-by-Layer Polyelectrolyte Nanocoating. *ACS Nano* **2012,** *6*, 4557-4564.
323 Fakhrullin, R. F.; Zamaleeva, A. I.; Minullina, R. T.; Konnova, S. A.; Paunov, V. N. Cyborg cells: functionalisation of living cells with polymers and nanomaterials. *Chem. Soc. Rev.* **2012,** *41*, 4189-4206.
324 Jen, A. C.; Wake, M. C.; Mikos, A. G. Review: Hydrogels for cell immobilization. *Biotechnol. Bioeng.* **1996,** *50*, 357-364.
325 Pértile, R. A. N.; Moreira, S.; Gil da Costa, R. M.; Correia, A.; Guãrdao, L.; Gartner, F.; Vilanova, M.; Gama, M. Bacterial Cellulose: Long-Term Biocompatibility Studies. *Journal of Biomaterials Science, Polymer Edition* **2012,** *23*, 1339-1354.
326 Sokolnicki, A. M.; Fisher, R. J.; Harrah, T. P.; Kaplan, D. L. Permeability of bacterial cellulose membranes. *J. Membr. Sci.* **2006,** *272*, 15-27.
327. Lin, W. C.; Lien, C. C.; Yeh, H. J.; Yu, C. M.; Hsu, S. H. Bacterial cellulose and bacterial cellulose-chitosan membranes for wound dressing applications. *Carbohydr. Polym.* **2013,** *94*, 603-611.
328. Almeida, I. F.; Pereira, T.; Silva, N. H.; Gomes, F. P.; Silvestre, A. J.; Freire, C. S.; Sousa Lobo, J. M.; Costa, P. C. Bacterial cellulose membranes as drug delivery systems: an in vivo skin compatibility study. *Eur. J. Pharm. Biopharm* **2014,** *86*, 332-336.
329 Trovatti, E.; Freire, C. S.; Pinto, P. C.; Almeida, I. F.; Costa, P.; Silvestre, A. J.; Neto, C. P.; Rosado, C. Bacterial cellulose membranes applied in topical and transdermal delivery of lidocaine hydrochloride and ibuprofen: in vitro diffusion studies. *Int. J. Pharm.* **2012,** *435*, 83-87.
330 Choi, Y.; Cho, S. Y.; Heo, S.; Jin, H.-J. Enhanced mechanical properties of silk fibroin-based composite plates for fractured bone healing. *Fibers and Polymers* **2013,** *14*, 266-270.
331. Setyawati, M. I.; Chien, L. J.; Lee, C. K. Expressing Vitreoscilla hemoglobin in statically cultured Acetobacter xylinum with reduced O(2) tension maximizes bacterial cellulose pellicle production. *J. Biotechnol.* **2007,** *132*, 38-43
332. Mohammadkazemi, F.; Azin, M.; Ashori, A. Production of bacterial cellulose using different carbon sources and culture media. *Carbohydr. Polym.* **2015,** *117*, 518-523.
333. Matsumoto, A.; Chen, J.; Collette, A. L.; Kim, U. J.; Altman, G. H.; Cebe, P.; Kaplan, D. L. Mechanisms of silk fibroin sol-gel transitions. *J. Phys. Chem. B* **2006,** *110*, 21630-21638.
334. Jin, H. J.; Park, J.; Karageorgiou, V.; Kim, U. J.; Valluzzi, R.; Cebe, P.; Kaplan, D. L. Water-Stable Silk Films with Reduced β-Sheet Content. *Adv. Funct. Mater.* **2005,** *15*, 1241-1247.
335. Lu, Q.; Hu, X.; Wang, X.; Kluge, J. A.; Lu, S.; Cebe, P.; Kaplan, D. L. Water-insoluble silk films with silk I structure. *Acta Biomater.* **2010,** *6*, 1380-1387.
336. Harley, B. A. C.; Kim, H.-D.; Zaman, M. H.; Yannas, I. V.; Lauffenburger, D. A.; Gibson, L. J. Microarchitecture of Three-Dimensional Scaffolds Influences Cell Migration Behavior via Junction Interactions. *Biophys. J.* **2008,** *95*, 4013-4024.

337. Ryan, A. J.; O'Brien, F. J. Insoluble elastin reduces collagen scaffold stiffness, improves viscoelastic properties, and induces a contractile phenotype in smooth muscle cells. *Biomaterials* **2015,** *73*, 296-307.
338. Sun, H.; Zhu, F.; Hu, Q.; Krebsbach, P. H. Controlling stem cell-mediated bone regeneration through tailored mechanical properties of collagen scaffolds. *Biomaterials* **2014,** *35*, 1176-1184.
339. Kang, S.; Park, J. B.; Lee, T.-J.; Ryu, S.; Bhang, S. H.; La, W.-G.; Noh, M.-K.; Hong, B. H.; Kim, B.-S. Covalent conjugation of mechanically stiff graphene oxide flakes to three-dimensional collagen scaffolds for osteogenic differentiation of human mesenchymal stem cells. *Carbon* **2015,** *83*, 162-172.
340. Deng, Y.; Sun, M.; Shaevitz, J. W. Direct measurement of cell wall stress stiffening and turgor pressure in live bacterial cells. *Phys. Rev. Lett.* **2011,** *107*, 158101.
341. Harbaugh, S. V.; Goodson, M. S.; Dillon, K.; Zabarnick, S.; Kelley-Loughnane, N. Riboswitch-Based Reversible Dual Color Sensor. *ACS Synthetic Biology* **2017,** *6*, 766-781.
342. Masschelein, W. J., and R. G. Rice. **2002**. Ultraviolet light in water and wastewater sanitation, p. 3-4. Lewis Publishers, Boca Raton, Fla.
343. Lee, B.; Kwon, H.; Kim, S.; Rotermund, F. Natural silk protein as a new broadband nonlinear optical material. *Opt. Mater. Express* **2016,** *6*, 993-1002.
344. Oladepo, S. A.; Xiong, K.; Hong, Z.; Asher, S. A.; Handen, J.; Lednev, I. K. UV Resonance Raman Investigations of Peptide and Protein Structure and Dynamics. *Chem. Rev.* **2012,** *112*, 2604-2628.
345 Azzaroni, O.; Brown, A. A.; Huck, W. T. UCST wetting transitions of polyzwitterionic brushes driven by self-association. *Angew. Chem. Int. Ed. Engl.* **2006,** *45*, 1770-1774.
346 Kang, J.-H.; Moon, J. H.; Lee, S.-K.; Park, S.-G.; Jang, S. G.; Yang, S.; Yang, S.-M. Thermoresponsive Hydrogel Photonic Crystals by Three-Dimensional Holographic Lithography. *Adv. Mater.* **2008,** *20*, 3061-3065.
347 Stoychev, G.; Puretskiy, N.; Ionov, L. Self-folding all-polymer thermoresponsive microcapsules. *Soft Matter* **2011,** *7*, 3277-3279.
348 Ghosh, S. K.; Pal, T. Interparticle Coupling Effect on the Surface Plasmon Resonance of Gold Nanoparticles: From Theory to Applications. *Chem. Rev.* **2007,** *107*, 4797-4862.
349 Tokarev, I.; Minko, S. Tunable plasmonic nanostructures from noble metal nanoparticles and stimuli-responsive polymers. *Soft Matter* **2012,** *8*, 5980-5987.
350 Tokarev, I.; Tokareva, I.; Gopishetty, V.; Katz, E.; Minko, S. Specific Biochemical-to-Optical Signal Transduction by Responsive Thin Hydrogel Films Loaded with Noble Metal Nanoparticles. *Adv. Mater.* **2010,** *22*, 1412-1416.
351 Tokareva, I.; Minko, S.; Fendler, J. H.; Hutter, E. Nanosensors Based on Responsive Polymer Brushes and Gold Nanoparticle Enhanced Transmission Surface Plasmon Resonance Spectroscopy. *J. Am. Chem. Soc.* **2004,** *126*, 15950-15951.
352 Zhu, Z.; Senses, E.; Akcora, P.; Sukhishvili, S. A. Programmable Light-Controlled Shape Changes in Layered Polymer Nanocomposites. *ACS Nano* **2012,** *6*, 3152-3162.
353 König, T. A. F.; Ledin, P. A.; Kerszulis, J.; Mahmoud, M. A.; El-Sayed, M. A.; Reynolds, J. R.; Tsukruk, V. V. Electrically Tunable Plasmonic Behavior of Nanocube–Polymer Nanomaterials Induced by a Redox-Active Electrochromic Polymer. *ACS Nano* **2014,** *8*, 6182-6192.
354 Karg, M.; Pastoriza-Santos, I.; Pérez-Juste, J.; Hellweg, T.; Liz-Marzán, L. M. Nanorod-Coated PNIPAM Microgels: Thermoresponsive Optical Properties. *Small* **2007,** *3*, 1222-1229.
355 Wang, C.; Du, Y.; Wu, Q.; Xuan, S.; Zhou, J.; Song, J.; Shao, F.; Duan, H. Stimuli-responsive plasmonic core-satellite assemblies: i-motif DNA linker enabled intracellular pH sensing. *Chem. Commun.* **2013,** *49*, 5739-5741.
356 Smoukov, S. K.; Gangwal, S.; Marquez, M.; Velev, O. D. Reconfigurable responsive structures assembled from magnetic Janus particles. *Soft Matter* **2009,** *5*, 1285-1292.
357 Nie, Z.; Fava, D.; Kumacheva, E.; Zou, S.; Walker, G. C.; Rubinstein, M. Self-assembly of metal-polymer analogues of amphiphilic triblock copolymers. *Nat Mater* **2007,** *6*, 609-614.
358 Osberg, K. D.; Rycenga, M.; Harris, N.; Schmucker, A. L.; Langille, M. R.; Schatz, G. C.; Mirkin, C. A. Dispersible Gold Nanorod Dimers with Sub-5 nm Gaps as Local Amplifiers for Surface-Enhanced Raman Scattering. *Nano Lett.* **2012,** *12*, 3828-3832.
359 Tokarev, A.; Gu, Y.; Zakharchenko, A.; Trotsenko, O.; Luzinov, I.; Kornev, K. G.; Minko, S. Reconfigurable Anisotropic Coatings via Magnetic Field-Directed Assembly and Translocation of Locking Magnetic Chains. *Adv. Funct. Mater.* **2014,** *24*, 4738-4745.

360 Kozlovskaya, V.; Kharlampieva, E.; Khanal, B. P.; Manna, P.; Zubarev, E. R.; Tsukruk, V. V. Ultrathin Layer-by-Layer Hydrogels with Incorporated Gold Nanorods as pH-Sensitive Optical Materials. *Chem. Mater.* **2008,** *20*, 7474-7485.
361 Stewart, M. E.; Anderton, C. R.; Thompson, L. B.; Maria, J.; Gray, S. K.; Rogers, J. A.; Nuzzo, R. G. Nanostructured Plasmonic Sensors. *Chem. Rev.* **2008,** *108*, 494-521.
362 Love, J. C.; Urbach, A. R.; Prentiss, M. G.; Whitesides, G. M. Three-Dimensional Self-Assembly of Metallic Rods with Submicron Diameters Using Magnetic Interactions. *J. Am. Chem. Soc.* **2003,** *125*, 12696-12697.
363 Peng, L.; Mortensen, N. A. Plasmonic-cavity model for radiating nano-rod antennas. **2014,** *4*, 3825.
364 Lee, S. J.; Baik, J. M.; Moskovits, M. Polarization-Dependent Surface-Enhanced Raman Scattering from a Silver-Nanoparticle-Decorated Single Silver Nanowire. *Nano Lett.* **2008,** *8*, 3244-3247.
365 Yoon, I.; Kang, T.; Choi, W.; Kim, J.; Yoo, Y.; Joo, S.-W.; Park, Q. H.; Ihee, H.; Kim, B. Single Nanowire on a Film as an Efficient SERS-Active Platform. *J. Am. Chem. Soc.* **2009,** *131*, 758-762.
366 Encina, E. R.; Coronado, E. A. Plasmonic Nanoantennas: Angular Scattering Properties of Multipole Resonances in Noble Metal Nanorods. *The Journal of Physical Chemistry C* **2008,** *112*, 9586-9594.
367 Li, Z.; Bao, K.; Fang, Y.; Huang, Y.; Nordlander, P.; Xu, H. Correlation between Incident and Emission Polarization in Nanowire Surface Plasmon Waveguides. *Nano Lett.* **2010,** *10*, 1831-1835.
368 Gupta, M. K.; Kulkarni, D. D.; Geryak, R.; Naik, S.; Tsukruk, V. V. A Robust and Facile Approach To Assembling Mobile and Highly-Open Unfrustrated Triangular Lattices from Ferromagnetic Nanorods. *Nano Lett.* **2013,** *13*, 36-42.
369 Ofir, Y.; Samanta, B.; Rotello, V. M. Polymer and biopolymer mediated self-assembly of gold nanoparticles. *Chem. Soc. Rev.* **2008,** *37*, 1814-1825.
370 Damm, S.; Lordan, F.; Murphy, A.; McMillen, M.; Pollard, R.; Rice, J. H. Application of AAO Matrix in Aligned Gold Nanorod Array Substrates for Surface-Enhanced Fluorescence and Raman Scattering. *Plasmonics* **2014,** *9*, 1371-1376.
371 Barnard, E. S.; Coenen, T.; Vesseur, E. J. R.; Polman, A.; Brongersma, M. L. Imaging the Hidden Modes of Ultrathin Plasmonic Strip Antennas by Cathodoluminescence. *Nano Lett.* **2011,** *11*, 4265-4269.
372 Rossouw, D.; Couillard, M.; Vickery, J.; Kumacheva, E.; Botton, G. A. Multipolar Plasmonic Resonances in Silver Nanowire Antennas Imaged with a Subnanometer Electron Probe. *Nano Lett.* **2011,** *11*, 1499-1504.
373 Douillard, L.; Charra, F.; Korczak, Z.; Bachelot, R.; Kostcheev, S.; Lerondel, G.; Adam, P.-M.; Royer, P. Short Range Plasmon Resonators Probed by Photoemission Electron Microscopy. *Nano Lett.* **2008,** *8*, 935-940.
374 Gómez-Medina, R.; Yamamoto, N.; Nakano, M.; Abajo, F. J. G. d. Mapping plasmons in nanoantennas via cathodoluminescence. *New Journal of Physics* **2008,** *10*, 105009.
375 Salihoglu, O.; Balci, S.; Kocabas, C. Plasmon-polaritons on graphene-metal surface and their use in biosensors. *Appl. Phys. Lett.* **2012,** *100*, 213110.
376 Schider, G.; Krenn, J. R.; Hohenau, A.; Ditlbacher, H.; Leitner, A.; Aussenegg, F. R.; Schaich, W. L.; Puscasu, I.; Monacelli, B.; Boreman, G. Plasmon dispersion relation of Au and Ag nanowires. *Physical Review B* **2003,** *68*, 155427.
377 Schmidt, M. A.; Russell, P. S. J. Long-range spiralling surface plasmon modes on metallic nanowires. *Opt. Express* **2008,** *16*, 13617-13623.
378 Zhang, S.; Wei, H.; Bao, K.; Håkanson, U.; Halas, N. J.; Nordlander, P.; Xu, H. Chiral Surface Plasmon Polaritons on Metallic Nanowires. *Phys. Rev. Lett.* **2011,** *107*, 096801.